SIReNa - Sciences et Ingénierie des Ressources Naturelles /GeoRessources

Thèse

Présentée et soutenue publiquement pour l'obtention du titre de

DOCTEUR DE l'UNIVERSITÉ DE LORRAINE

Mention : Géosciences

Présentée par

Farah AL SAHYOUNI

Sous la direction de : **Fabrice GOLFIER**
Dragan GRGIC

Impact Thermo-Hydro-Bio-Chemio-Mécanique du stockage géologique de H_2

Thermo-Hydro-Bio-Chemo-Mechanical impact of geological storage of H_2

Soutenanue le 9 Décembre 2021

Membres du jury :

President de la jury :	M. Philippe COSENZA	Professeur, IC2MP, Université de Poitiers
Directeur de these:	M. Fabrice GOLFIER	Professeur, GeoRessources ENSG, Université de Lorraine
Co-Directeur de these:	M. Dragan GRGIC	Maitre de conférences HDR, GeoRessources ENSG, Université de Lorraine
Rapporteur:	M. Frederic Victor DONZE	Professeur, ISTerre, Université Grenoble-Alpes
Rapporteur:	M. Frédéric SKOCZYLAS	Professeur, LaMcube, Université de Lille
Examinatrice :	Mme Catherine NOIRIEL	Maitresse de conférences, GET, Université de Toulouse
Examinatrice :	Mme Anne -Julie TINET	Maitresse de conférences, GeoRessources ENSG, Université de Lorraine

Dedicated to my Mother's soul
My guarding angel in the hand of God

"*The struggle itself towards the heights is enough to fill a man's heart. One must imagine Sisyphus happy.*"

— ***Albert Camus***

Abstract

Renewable energies (like wind, hydraulic and solar) are highly demanded in order to meet the goal of greenhouse emissions reduction to 20% by 2050 according to the Paris agreement. Hydrogen produced from water electrolysis appears to be the best candidate for large-scale geological storage to cover the intermittence production of these renewable energies. It can be stored either in salt caverns or in porous rocks like saline aquifers and depleted reservoirs of oil and gas. But the sealing integrity and capacity of these storage sites reveal concerns due to the mechanical, chemical and thermal constraints, related to in-situ conditions but also to the operating processes, that apply. This thesis proposes an evaluation of the risk of gas leakage in the case of salt cavities, and the risk of biogeochemical alteration (in presence of hydrogenotrophic bacteria) of the gas stock in the case of porous reservoir rocks.

Rock salt is a polycrystalline material mainly made of individual grains of NaCl (halite). In-situ intrinsic permeability of undisturbed halite is very low (around 10^{-21} m^2), which gives an excellent sealing capacity. The flow through rock salt can only occur through the interconnected cracks. These cracks, located in the near field of salt caverns and caused by the severe increase in deviatoric stresses due to the excavation and temperature variations (due to the high-frequency cycling of gas pressure), can be responsible for a significant increase in permeability. Then, understanding the complex relationship between the permeability evolution and the mechanical and thermal solicitations is of highest importance to survey any possible risk of fluid permeation or leakage through the salt formation. The complexity is due to the specific features of the mechanical behaviour (large plastic deformation capacity, good creep properties, microcracking damage, cracks healing) of rock salt and gas flow in such unconventional reservoir (Klinkenberg effect). Then, we performed a complete set of laboratory experiments on a rock salt specimen (salt bed of the Alsace potash mines in the East region of France). The porosity of the studied rock salt is very low (~1%) and the initial permeability varies over 4.5 orders of magnitude. The Klinkenberg effect is only observed for the less permeable and damaged samples. The poroelastic coupling is almost negligible in our samples. Deviatoric loading under low confining pressure (1 MPa) induces a moderate increase in gas permeability from the dilatancy threshold due to microcracking. Measurement of ultrasonic wave velocities during uniaxial compression showed an almost irreversible closure of pre-existing microcracks and the opening of axial microcracks that are perpendicular and parallel, respectively, to the uniaxial stress direction and allowed a precise determination of the dilatancy threshold. Under higher confining pressure (5 MPa), no increase in permeability was measured because the material becomes fully plastic which practically eliminates microcracking and thus dilatancy. Under hydrostatic loading, gas permeability decreases because of cracks closure and this decrease is irreversible due to the time-dependent self-healing process. Permeability increases slightly during dynamic mechanical and thermal fatigue due to microcracking, while it reduces during static fatigue (creep) thanks to the self-recovery process. All these results give strong confidence in the underground hydrogen storage in salt caverns which remains by far the safest solution because the different mechanisms (viscoplasticity with strain hardening, microcracking and cracks healing) involved in material deformation act in a competitive way to annihilate any significant permeability evolution.

In the case of porous reservoir rocks, hydrogen injection can induce geochemical redox reactions between the fluids and minerals. This might change the porosity structure and permeability and increase leakage risks, and also induce an unwanted consumption of the hydrogen resource. Fluid-rock interactions in sandstone reservoir are minor but they could be catalyzed by the biological activity. Indeed, microorganisms can tolerate the extreme conditions of deep saline aquifers and reservoirs. To study these phenomena, we developed a new experimental device to simulate the biochemical activity under conditions (T=35°C, PH_2=50bar, Pconfinement=200bar) representative of storage reservoirs on cylindrical core samples containing bacteria in a triaxial compression cell. The outflow gas was automatically sampled with a HP-LP valve and the concentration was measured with a micro-gas chromatograph to quantify biological processes of hydrogen consumption. We chose to work on the Vosges sandstone (formation of lower Triassic), a very porous and permeable rock. The strain chosen for this purpose is Shewanella putrefaciens bacteria which reduces iron in the presence of hydrogen to produce energy. Its metabolism and performance as hydrogenotrophic bacteria were first tested in batch condition on a rock powder. Results showed that this type of bacteria can tolerate anaerobic environments. It can reduce the iron present in the medium using endogenous source of electrons. However, it can also use the hydrogen in the medium to execute this reaction and prefers available dissolved hydrogen in the water pores rather than in gaseous phase. Under triaxial conditions (i.e., with stresses, gas pressure and temperature applied on a cylindrical rock sample), which better mimic in-situ conditions, the bacterial activity doesn't seem to impact enough the hydrogen concentration in the system, whatever the initial hydrogen concentration (70% or 5%) and the sampling frequency

(one or three days). Many hypotheses are proposed to explain the observed differences between batch and triaxial conditions: the scarcity of dissolved hydrogen in residual water which is preferentially consumed by bacteria, the low exchange surface for biogeochemical reactions in the case of solid core samples, the slow kinetic of hydrogen consumption by *S. putrefaciens* when reducing iron in a solid core sample, the short duration of the experiments in the triaxial cell, and the detection limit of measuring instruments given the low reactivity of the biogeochemical reaction. Despite the remaining uncertainties related to our experiments, our preliminary results suggest that the underground storage of pure hydrogen in porous reservoir rocks is not severely threatened by the activity of *Shewanella putrefaciens* bacteria. In-situ conditions are not favorable for the growth of such bacteria and for a significant consumption of the hydrogen resource. Therefore, the hydrogen storage under these conditions can be considered safe.

Acknowledgment

First, I would like to express my deepest gratitude to my supervisors: *Pr. Fabrice GOLFIER* and *Dr. Dragan GRGIC* for all their support and guidance throughout this thesis journey. Without their understanding, patience and involvement in every step throughout the process, this would have never been accomplished. I am grateful for all the knowledge I have gained from you over these years in Geosciences especially in Hydrogeology and geomechanics. Words fail to describe my gratitude for your acceptance to supervise my PhD thesis, to answer my questions even at late night hours, your recommendations to urge me to follow a scientific rigor in analysis and conclusions. Your insightful notes helped to sharpen my thinking, formulating my methodology and fine-tuning my results and redaction till this final report of the thesis defense.

I Thank ANR –Géodenergies –Air Liquide and Région Grand-Est for the financial support that made this work possible. Also, I would like to express a respected acknowledgement to the members of the Jury for their acceptance to read the manuscript and evaluate this work.

I wish to thank all Professional members, technicians and engineers of the team Hydrogéomecanique Multi-échelle-GeoRessources, *Laurent, Patrick, Mohamed, Eric, Clément, Elise*, with whom I shared knowledge, and experience, success and failures of the experiments. I am infinitly grateful for their inexorable help and support to teach me new laboratory techniques, assisting me to realize my heavy experimental trials, and their presence to solve any technical problem at any time. I thank you for your modesty, for understanding my moods, my thoughts, my foolish behavior, and my clumsiness sometimes. I also appreciate every word, every comment and every wisdom I've heard from you. I will never forget the good times, the field trips, the taughtful discussions, the sweet jokes and laughters, and the words of love and encouragement. This work would not have been possible without your great contribution and your precious expertise.

My thanks also go to all the technicians of the lab's imaging team who helped me with the X-ray tomography and SEM-EDX techniques: *Christophe and Andrei*.

I would also like to give special thanks to *Catherine LORGEOUX* for her immense help in the biogeochemistry part of the thesis especially in implementing the micro-GC technique. Thank you for the time you gave me to teach me about the micro-GC, your enthusiasm to make the experiment work no matter the obstacles, and to answer my questions and my reflexions and any time I call. I admire your outstanding passion for your work, your kindness, and your sens of humour.

Furthermore, I acknowledge the great contribution of the Laboratoire LCPME expecially Dr. *Fréderic JORAND* and the intern *Elodie MARTET* in the microbiology part and their assistance in bacterial solution preparation and incubation and the batch experiment part.

I thank all other Colleagues/friends at HGM-Georessources for their support, good times and good humor, good food, good pause café, *Wilfried, Arash, koko, Ahmad, Dong, Kassem, Fabrice, Franck, Cedric, Sourena, Marvin* and those whom I had the chance to know here and through all the process of this work. I thank also my friends in Nancy for the beautiful getaway, nights out, dinners, and stress release time. Especially, *Sirina* for standing by my side when I felt so down.

Finally, I would like to extend a most grateful acknowledgement for my father for having trusted me, for his big heart, and for having accompanied me throughout this year with fervent prayers. I would like to express my sincere thanks and gratitude to my little brother *Adonis*, who always stands by my side and encourages me. I always see the feeling of pride in his eyes. I cannot express how much I love him and I am proud of him, especially for standing by my mother in times of illness, when I was far away, studying to achieve my dreams.

Lastly, I dedicate this work to the soul of my mother who always dreamed of my graduation day and who always encouraged me to the mointains and dream big, but she passed away before she could read these lines. She taught perseverance, strength and dedication. She will always be my inspiration.

Table of Content

Table of figures

Table of Tables

Résumé de la thèse

1. Contexte générale de la thèse

L'hydrogène est un vecteur d'énergie renouvelable propre et durable offrant des perspectives prometteuses pour la transition énergétique. Récemment, la volonté d'aller vers les énergies alternatives vertes (comme le vent, l'eau et le solaire) pour décarbonner les systèmes énergétiques s'est accrue. Les gouvernements cherchent à promouvoir une énergie durable et verte pour assurer les exigences économiques et environnementales. Le but est de proposer un mix énergétique et atteindre les objectifs de l'accord de Paris et le pacte vert de l'Union européenne qui visent à réduire les émissions de gaz à effet de serre responsables du réchauffement climatique de 20 % à 30 % si les conditions sont favorables pour 2050 (European Commission. Directorate-General for Energy, 2012). Cependant, l'émergence des énergies renouvelables suscite des inquiétudes importantes quant à leur intermittence et la fiabilité de leur production en toutes saisons. C'est ainsi que l'approvisionnement de l'énergie à long terme devient un besoin indispensable pour contribuer aux besoins du marché et avoir une flexibilité et une expansion de la production. Plusieurs techniques de stockage d'énergie sont apparues comme le stockage d'électricité dans les batteries, le stockage en souterrain à grand échelle et long terme de l'énergie géothermique, le stockage d'air comprimé, etc. Aussi, le stockage souterrain des gaz comme le dioxyde de carbone, le gaz naturel, l'air comprimé et l'hydrogène, ce dernier étant considéré comme la technologie la plus prometteuse. L'hydrogène étant un gaz polyvalent et vert produit par l'électrolyse de l'eau en utilisant l'énergie générée à partir d'énergies renouvelables, son stockage souterrain à grande échelle est favorisé. Il se fait à l'échelle mondiale soit sous forme de liquide comprimé, soit sous forme solide adsorbée, soit sous forme gazeuse.

Le stockage de l'hydrogène se fait soit dans les roches poreuses des aquifères ultra-salins et des réservoirs épuisés de pétrole et gaz, soit dans des cavités salines selon l'utilisation, le coût, la disponibilité des structures géologiques appropriées et les capacités économiques et le taux de productibilité. Mais, des questions et des inquiétudes subsistent quant à la fiabilité, la capacité et l'étanchéité de ces types de stockage sous l'effet de contraintes mécanique, chimique, thermique liées aux conditions in-situ mais aussi au processus d'opération de la cavité (Fig.1).

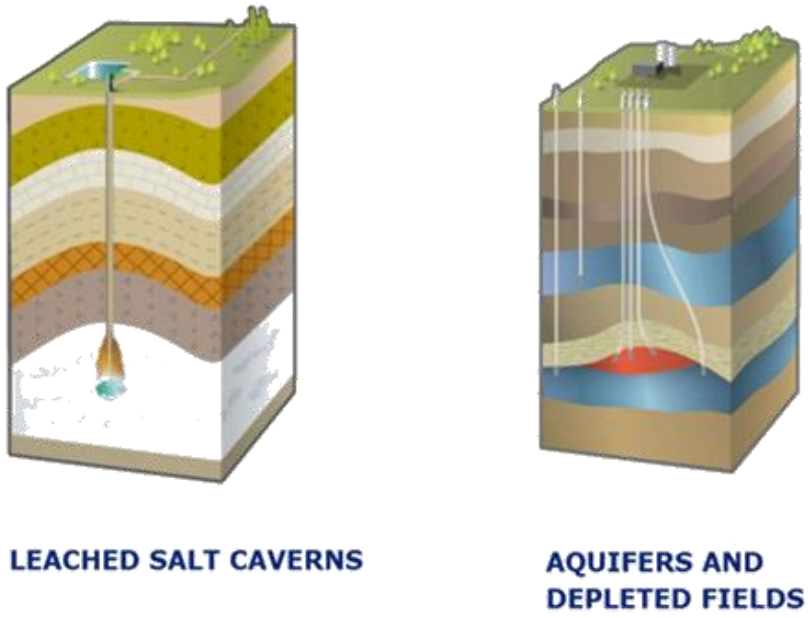

Fig.1: Les différents types de stockage souterrain d'hydrogène dans le monde (source :Geostock)

Le stockage géologique dans le sel est actuellement l'option la plus viable en raison de la facilité d'utilisation, de la grande capacité de livraison et, surtout, de l'intégrité de son étanchéité (Zivar et al., 2021). Les cavités sont creusées dans les strates profondes de sel formées par les dépôts cycliques des sédiments ou dans les dômes de sel générés par halokinèse des couches sous l'effet de la haute pression et température. Actuellement, quatre grandes cavernes d'hydrogène fonctionnent dans le monde : Teesside au Royaume-Uni est un site de trois cavernes elliptiques à une profondeur de 350-450 m et un volume total de 210 000 m3 qui fonctionne depuis les années

1970. Les trois autres sont situés aux États-Unis (Texas) et construits dans des dômes de sel pur (Clemens Dome, Moss Bluff, Spindletop), Spindeltop étant la plus grande caverne de sel au monde (Caglayan et al., 2020). D'autres projets pilotes ou de recherche existent également en Europe (ex. Etrez et Beynes en France). Cependant, étant donné la spécificité et la nature de ce gaz, il faut absolument caractériser et évaluer les processus hydrodynamiques qui peuvent nuire à l'intégrité du stockage (Tarkowski, 2019). La roche sel est une roche polycristalline composée de grains individuels de NaCl (halite), dont la taille des cristaux varie généralement entre 2 et 20 mm, mais comprend aussi d'autres impuretés solides en phases minérales secondaires (calcite, anhydrite, argiles) ou des fluides piégés dans des inclusions dans les joints de grains ou dans les pores (Roedder, 1984; Urai et al., 1987; Cosenza et al., 1999; Schoenherr et al., 2007). La perméabilité intrinsèque in situ de l'halite non endommagé est très faible, environ 10^{-21} m^2 (Peach & Spiers, 1996b; Popp et al., 2001), ce qui lui confère une excellente capacité d'étanchéité. L'écoulement à travers le sel gemme se produit uniquement à travers les fissures ou les fractures interconnectées et non pas au travers des cristaux eux-mêmes (Gloyna & Reynolds, 1961), ce qui est à l'origine de la très faible perméabilité des formations salines. Les fissures, causées par la relaxation des contraintes et l'augmentation sévère des contraintes déviatoriques dans la zone endommagée par l'excavation des cavernes de sel, sont responsables d'une augmentation significative de la perméabilité. Ainsi, comprendre la relation entre le développement des fractures réparties dans le massif de sel et les changements des propriétés pétrophysiques est de la plus grande importance pour estimer les risques possibles de perméation des fluides ou des fuites à travers la formation de sel.

Le stockage d'hydrogène dans les roches poreuses, quant à lui, est favorisé dans le cas du long terme (sur des mois ou des saisons) pour fournir de l'énergie pour le chauffage urbain ou les besoins industriels. Bien que son étude soit encore restreinte, il existe quelques projets pilotes dans le monde (exemple : Lauchstadt en Allemagne, Lobodice en république et Beynes en France. Il s'agit de la technique la plus prometteuse compte tenu de sa capacité de stockage et de la grande distribution géologique de ce type de formation à travers le monde, de sa facilité d'opération et un savoir-faire déjà existant. Une caractéristique typique d'un réservoir poreux est qu'il est scellé par une roche de couverture et une structure de piégeage (Stone et al., 2009; Lord et al., 2014; Heinemann et al., 2021). L'injection d'hydrogène dans un réservoir poreux stable pourrait provoquer des interactions géochimiques entre le gaz, les fluides et les minéraux présents dans le milieu. L'hydrogène injecté déplace les fluides in-situ des pores et répand l'hydrogène dans la structure dans un écoulement multiphasique. De plus, le point d'injection entraîne un panache d'hydrogène hautement saturé dans la zone proche du puits et dans la partie supérieure du réservoir par une ségrégation gravitaire des fluides affectant la pureté du gaz sortant et l'homogénéité du réservoir (Sáinz-García et al., 2017; Hagemann, 2018; Luboń & Tarkowski, 2020). Cette interaction entre l'hydrogène, le milieu et l'eau stimule la dissolution et la précipitation minérales. Elle pourrait modifier la perméabilité et la porosité du milieu (Ganzer et al., 2013; Truche et al., 2013). Ceci peut se faire par dissolution et précipitation d'anhydrite et de carbonates remplissant les pores (Flesch et al., 2018). D'autre part, les milieux poreux (aquifères et réservoirs) sont majoritairement un biotope pour les microorganismes. Ainsi, la bioconsommation d'hydrogène peut également conduire à une altération importante des stocks (Varjani & Gnansounou, 2017; Dopffel et al., 2021). La vie microbienne souterraine dans les aquifères et les réservoirs épuisés se trouve à plusieurs kilomètres de profondeur dans des conditions de température et de pression dites « extrêmes » (Kirchman, 2018). Dans les conditions anaérobies des environnements extrêmes, l'hydrogène peut remplacer les donneurs d'électrons pour la respiration des bactéries hydrogénotrophes produisant de l'énergie cellulaire (Wait, 2011; Gregory et al., 2019; Dopffel et al., 2021). Ainsi, l'élévation artificielle de la concentration en H_2 stimule leur croissance, consommant ainsi le stock d'hydrogène ou le convertissant sous d'autres formes comme le dioxyde de carbone ou le méthane (Dopffel et al., 2021).

Dans ce cadre général, cette thèse propose une évaluation du comportement thermo-hydro-biochimio-mécanique du stockage souterrain d'hydrogène dans les cavités salines et les roches aquifères poreuses afin d'évaluer les risques de fuite et d'altération du gaz. Une partie des recherches a été menée dans le cadre du projet Rostock-H qui vise à analyser les conditions technico-économiques, réglementaires et sociales du déploiement de la technologie de stockage souterrain d'hydrogène (UHS) dans les cavités salines en France et en Europe. Le projet est financé par l'ANR (Agence Nationale de Recherche, France) à travers le Groupement d'Intérêt Scientifique Géodenergies (Géodénergies, 2016). Un financement complémentaire de thèse a été assuré par le conseil régional de la région de la Lorraine.

2. Objectifs

La première partie de cette thèse est dédiée à la caractérisation de la relation complexe entre la perméabilité et le comportement mécanique du sel sous l'effet du chargement mécanique. Pour cela, nous effectuerons un ensemble complet d'expériences hydromécaniques sur des échantillons de sel. Dans un premier temps, la microstructure initiale du sel gemme sera identifiée avec différentes méthodes de porosité et avec la tomographie 3D aux rayons X, permettant ainsi la détermination de la proportion de vides (pores et fissures) à différentes échelles. Ensuite, différents essais mécaniques à court terme (essais de compression hydrostatique, essais de compression uniaxiale et triaxiale, essai de compression uniaxiale avec mesure des vitesses d'ondes ultrasonores P et S) seront effectués sur de grandes carottes pour caractériser le comportement poromécanique (mécanismes de déformation, propriétés élastiques, coefficient de Biot) de notre spécimen de sel gemme. Des mesures de perméabilité au gaz (hélium) seront effectuées à différents niveaux de contraintes pour analyser l'impact des mécanismes de déformation sur l'évolution de la perméabilité, et à différentes pressions de gaz pour caractériser l'effet de glissement (Klinkenberg) et obtenir la perméabilité intrinsèque réelle du sel gemme aux faibles pressions de gaz. L'impact de la fatigue mécanique, sous chargement triaxial dynamique/cyclique et chargement triaxial statique (essai de fluage), et de la fatigue thermique cyclique sur la perméabilité du sel sera également analysé.
La deuxième partie concerne le stockage de l'hydrogène dans les aquifères ou les réservoirs de pétrole et de gaz épuisés. L'objectif est d'identifier les principaux phénomènes microbiens capables d'altérer la ressource H_2 stockée et de quantifier ce mécanisme. En effet, l'activité bactérienne est susceptible de produire d'autres gaz (par exemple, H_2S) en consommant H_2. Celle-ci sera réalisée par des tests de percolation (c'est-à-dire des tests d'écoulement dans une cellule mécanique triaxiale) sur des échantillons cylindriques partiellement saturés en présence de bactéries hydrogénotrophes afin d'évaluer les processus bactériens susceptibles de favoriser la dégradation de H_2. Un dispositif expérimental sera construit pour essayer de quantifier l'importance de l'activité biologique dans les conditions de pression et de température du stockage aquifère. Des expérimentations seront menées sur des échantillons de grès vosgien, choisi comme roche réservoir analogue.

3. Le stockage d'Hydrogène dans les cavités salines

3.1 Problématique

La très faible perméabilité du sel est essentiellement liée à la structure des minéraux constitutifs (essentiellement l'halite) et à sa texture. L'halite est le minéral principal et le plus abondant dans les gisements sous formes pur ou avec des impuretés intercalaires d'anhydrite, calcite et des minéraux d'argile et autres. Ces minéraux peuvent aussi présenter des inclusions et des intrusions de fluides entre les joints des grains. Ces inclusions influencent la ductilité et la rigidité du sel, mais aussi ils peuvent contribuer à l'élargissement des fissures ou leur scellage (Roedder, 1984; Urai et al., 1987; Cosenza et al., 1999; Schoenherr et al., 2007; Thorel, 1994a).

L'étanchéité des cavernes de sel utilisées pour le stockage souterrain dépend fortement de la perméabilité du sel au gaz et à la saumure. Ce paramètre est fortement couplé aux mécanismes de déformation (endommagement, plasticité, fluage) qui influencent les propriétés d'écoulement des fluides au sein d'un milieu très peux poreux et très peu perméable. Ainsi, il est important de comprendre l'interaction entre l'écoulement des fluides et la rhéologie du sel. De plus, lors des mesures de perméabilité, l'augmentation de la pression du gaz interstitielle pourrait induire une expansion volumique et diminuer la contrainte moyenne via le concept de contrainte effective, ce qui complique l'analyse de l'effet des pressions interstitielles et de confinement sur l'évolution de la perméabilité. Pour déterminer si le concept de contrainte effective s'applique dans le sel gemme, ce qui n'est pas aussi évident que pour les milieux poreux classiques du fait de sa très faible porosité connectée, le coefficient de couplage poroélastique de Biot doit être évalué.

D'autre part, le sel intact est considéré comme un réservoir non conventionnel étanche aux gaz en raison de sa très faible perméabilité et de ses pores micrométriques à nanométriques. Toutefois, la précision des mesures de perméabilité, réalisées *in situ* ou en laboratoire sur différents spécimens de sel, est affectée par le lieu d'échantillonnage de ce sel, son hétérogénéité et la variabilité de la structure des pores due à différentes contraintes, mécanique ou hydraulique. On distingue alors deux zones : la zone non perturbée (ou saine) et la zone endommagée (EDZ : Excavation Damaged Zone) proche de la paroi de l'excavation. En général, la perméabilité des échantillons non perturbés est inférieure de plusieurs ordres de grandeur à celle de la zone endommagée, car constituée de pores non-connectés ou remplis par du ciment recristallisé servant d'étanchéité pour le transport

des fluides. Quant au sel endommagé, *in situ* par l'excavation (mécanique ou par dissolution) ou au laboratoire par les techniques d'échantillonnage, il présente une connectivité plus importante liée à la présence de fissures/fractures à différentes échelles. D'autre part, l'écoulement de gaz dans des pores d'un diamètre très petit à basse pression induit un choc moléculaire avec les parois du milieu ce qui provoque un effet de glissement. Plus la taille des pores et la pression du gaz sont faibles, plus l'effet de glissement du gaz sera important. La conséquence est que la perméabilité apparente (ka) au gaz mesurée au laboratoire par la loi de Darcy sera supérieure à la perméabilité intrinsèque (k_∞) liée à la porosité géométrique connectée. Ainsi, l'étude de l'écoulement du gaz dans un tel matériau doit prendre en compte cet effet également appelé effet Klinkenberg (Klinkenberg, 1941; Letham & Bustin, 2016). Cela a été étudié plusieurs fois dans la littérature à partir d'essais effectués sur le sel dans des conditions de chargement hydrostatique et triaxiale mais essentiellement avec la méthode transitoire ou pulse test (Peach & Spiers, 1996; Popp et al., 2001; Schulze et al., 2001; Sutherland & Cave, 1980; Zhang et al., 2020). Pour s'affranchir de cet effet de glissement, ces auteurs ont utilisé des pressions de gaz élevées (une pression de gaz moyenne de 1 MPa est suffisante). Très peu d'études (e.g., Gloyna & Reynolds, 1961) ont considéré la méthode d'écoulement en régime permanent. La correction de l'effet Klinkenberg est nécessaire lors de l'utilisation de faibles pressions de gaz, ce qui est le cas lorsque de faibles pressions de confinement sont appliquées. Elle se fait par des méthodes analytiques en considérant le régime d'écoulement du gaz selon l'échelle de Knudsen (Fig.2).

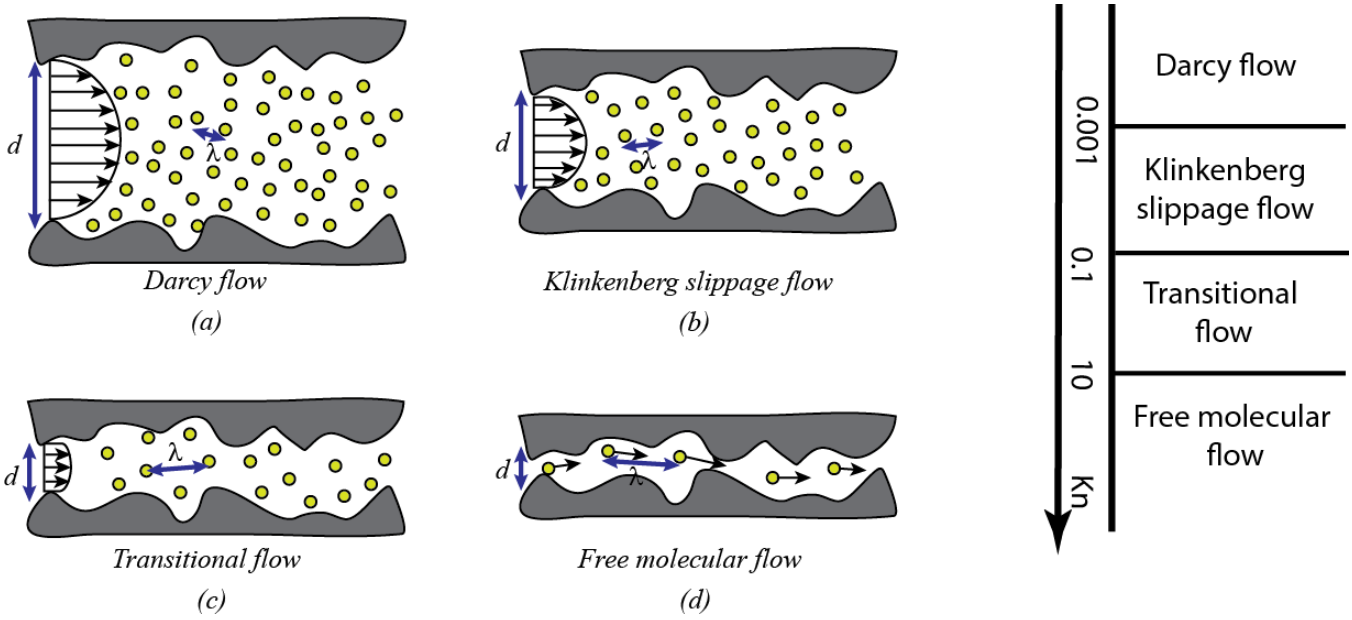

Fig.2: Les différents régimes de transfert de gaz dans les milieux poreux non-conventionnel selon les gammes de nombre de Knudsen

Le comportement mécanique du sel gemme est dominé par les processus de déformation plastique durcissante et de fluage important. À faible contrainte moyenne effective, la dilatance liée à l'ouverture de fissures en extension peut se produire au cours de la déformation du sel, induisant ainsi une augmentation très significative de la perméabilité de plusieurs ordres de grandeur (Popp et al. 2001 ; Peach et Spiers 1996). Le seuil de dilatance, qui correspond à l'endommagement par microfissuration instable, est souvent utilisé comme seuil pour la conception des cavernes de sel (ex. Labaune et al. 2018). Cependant, de nombreuses études (par exemple, Sutherland et Cave 1980 ; Peach 1991 ; Chen et al. 2013 ; Zhu et Arson 2015, Drury et Urai 1990) ont déjà montré que les microfissures peuvent être auto-cicatrisées sous des conditions appropriées de température et pression. Du point de vue microscopique, le processus d'auto-guérison/cicatrisation correspond à la recristallisation des cristaux du sel gemme. Ce processus de cicatrisation des joints de grains est similaire à celui de la cicatrisation des fissures intragranulaires (Smith et Evans, 1984). Le processus de fermeture/cicatrisation des fissures peut ainsi contribuer à la restauration de la rigidité et de la perméabilité initiales du sel.

De nos jours, le cyclage de la pression de gaz dans les cavernes de sel se fait à haute fréquence afin de répondre aux besoins des marchés de l'énergie. Mais ce mode opératoire est plus agressif car les changements de pression, et les changements de température et de contraintes associés, peuvent générer des fractures dans la roche environnante (Rouabhi et al. 2017). Même si l'épaisseur de cette zone endommagée par l'excavation est relativement faible, l'intégrité du projet de stockage pourrait être affectée négativement.

3.2 Matériau et méthodes expérimentales

Du fait des spécificités du comportement mécanique (grandes déformations plastique et de fluage, endommagement par microfissuration, cicatrisation des fissures) du sel gemme et de l'écoulement de gaz dans un tel réservoir non conventionnel (effet Klinkenberg), la relation entre l'évolution de la perméabilité et le chargement mécanique est très complexe. Nous proposons donc un ensemble complet d'expériences de laboratoire sur un spécimen de sel gemme issu des mines de potasse d'Alsace, afin d'étudier l'évolution de la perméabilité sous différents types de conditions de chargement :

- Caractérisation de la microstructure initiale (pores, fissures) du sel avec différentes méthodes porosimétriques et par tomographie 3D aux rayons X.
- Essais mécaniques à court terme (essais de compression hydrostatique, essais de compression uniaxiale et triaxiale, essai de compression uniaxiale avec mesure des vitesses d'ondes ultrasonores P et S) afin de caractériser le comportement poromécanique (mécanismes de déformation, propriétés élastiques, coefficient de Biot).
- Mesure de la perméabilité au gaz (hélium) en régime permanent sous compression hydrostatique et sous compression triaxiale avec différentes pressions de confinement (Fig.3). Les mesures de perméabilité sont réalisées à différents niveaux de contrainte afin d'analyser l'impact des mécanismes de déformation, et à différentes pressions de gaz afin de caractériser l'effet de glissement et obtenir la perméabilité intrinsèque réelle du sel aux faibles pressions de gaz. Des mesures de perméabilité seront également réalisées de manière continue au cours d'essais de compression triaxiale afin de limiter la guérison de l'endommagement qui peut se produire si la durée de l'essai est trop longue.
- Etude de l'impact de la fatigue mécanique, sous chargement triaxial dynamique/cyclique et sous chargement triaxial statique (essai de fluage), et de l'impact de la fatigue thermique cyclique sur la perméabilité du sel sera également analysée.

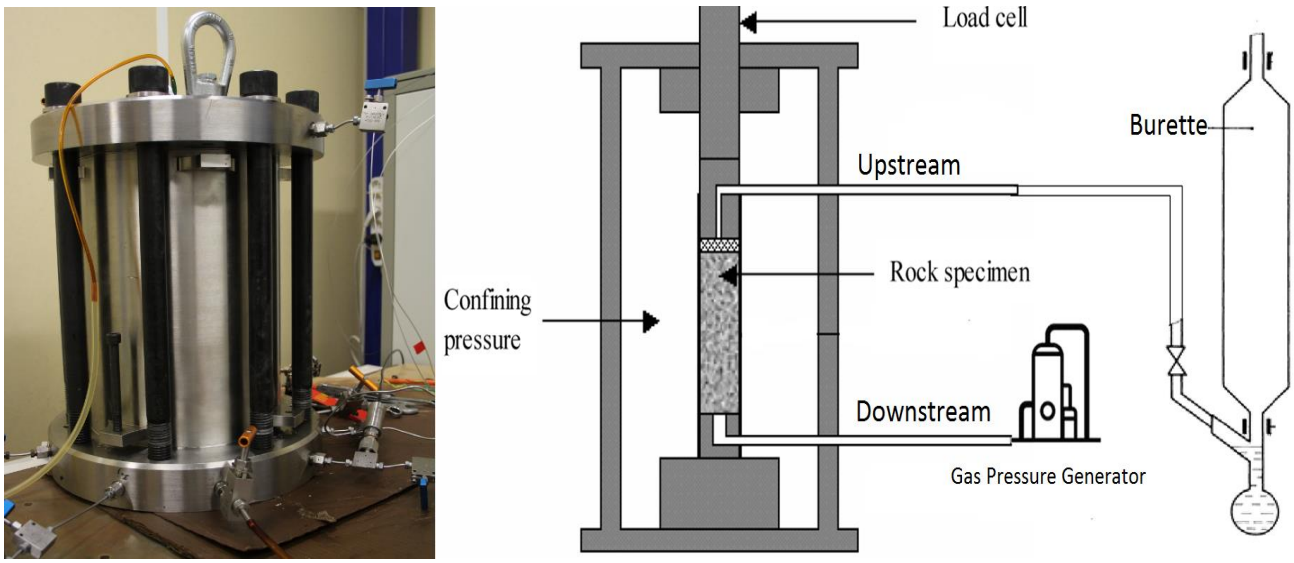

Fig.3: Essai de compression traixiale couplé à l'injection de gaz pour suivre l'évolution de la perméabilité en fonction du chargement mécanique

Les expérimentations sont menées sur des échantillons de sel prélevés à 530 m de profondeur dans les mines de potasse d'Alsace (MDPA) dans l'Est de la France (site de Stocamine). Cette roche saline, relativement impure, est considérée comme un analogue naturel des cavernes salines utilisées pour le stockage souterrain de H_2. La plupart des expériences a été réalisée sur de grandes éprouvettes cylindriques (50 à 100 mm de diamètre, élancement 2).

3.3 Résultats et discussions

La porosité du sel étudié est très faible (~1%) et est principalement composée d'infrapores (de taille nanométrique) qui connectent des macropores et fissures dispersés (Fig. 4). Ce large spectre poreux correspond à un milieu poreux multi-échelle qui impacte l'écoulement de gaz. Les valeurs de perméabilité initiale de notre spécimen de sel sont très dispersées et varient sur 4.5 ordres grandeur (10^{-16}-5×10^{-21} m^2). Certaines valeurs de perméabilité sont très

importantes comparé à celles couramment attendues pour un échantillon sain (i.e., non endommagé) de sel gemme (de 10^{-20} à 10^{-21} m^2). Cette gamme de perméabilité très large dans les échantillons prélevés *in situ* est principalement due à la présence de fissures causées par la relaxation des contraintes (induite par le carottage des sondages ou l'excavation de la cavité) et la préparation des éprouvettes d'essai. L'effet Klinkenberg (i.e., diminution de la perméabilité avec l'augmentation de la pression de gaz) est observé seulement sur les échantillons les moins perméables (et donc les moins endommagés initialement). Lorsque cet effet est observé, la correction empirique exponentielle donne la meilleure estimation de la perméabilité intrinsèque, ce qui signifie que l'écoulement de gaz se situe dans le régime transitionnel pour le sel quasi intact (Fig. 4).

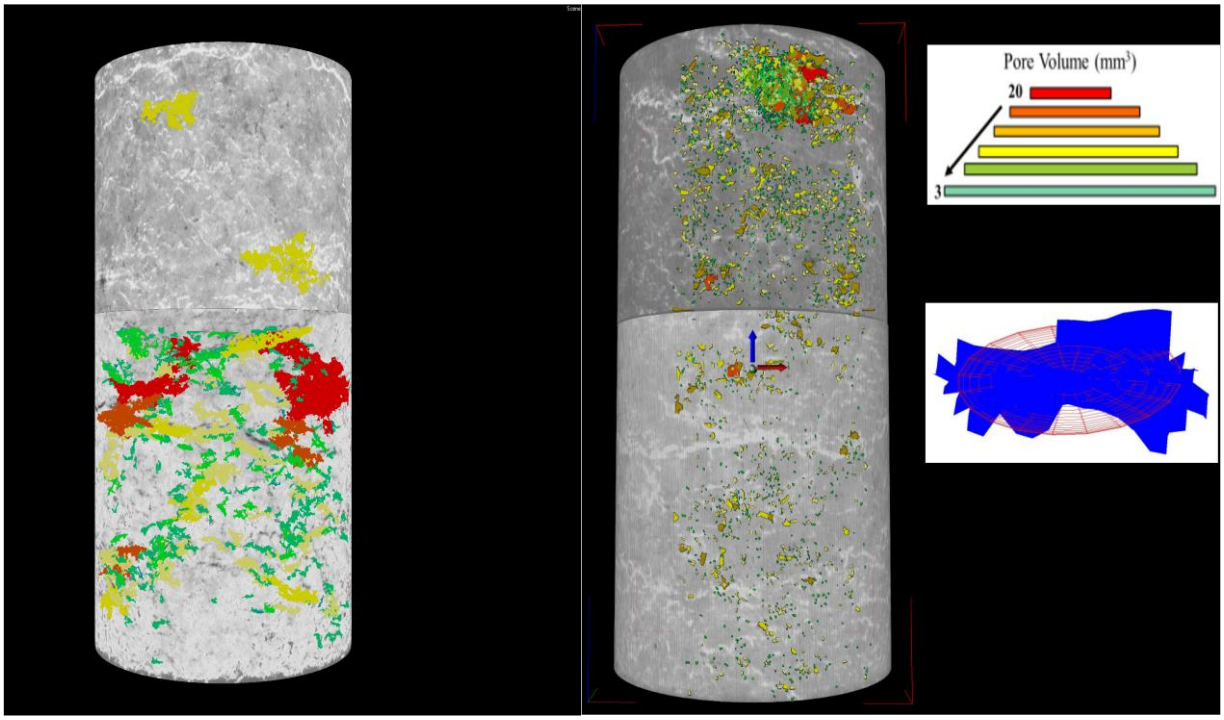

Fig.4: Distribution des pores sur des larges échantillons cylindriques de sel gemme obtenue à partir de la tomographie 3D à rayons X.

Le comportement mécanique du sel est isotrope et élastique linéaire (jusqu'à 30 MPa) sous chargement hydrostatique. Le chargement hydrostatique induit une fermeture irréversible des vides initiaux, augmentant ainsi la raideur du matériau. Le coefficient de Biot est égal à zéro pour un échantillon initialement très perméable (~10^{-18} m^2) et demeure pratiquement égal à zéro après avoir été endommagé au cours d'un essai de compression uniaxiale (jusqu'à une contrainte déviatorique de 16 MPa). Ainsi, on peut considérer que le couplage poroélastique est pratiquement négligeable pour nos échantillons de sel, ce qui signifie que la contrainte moyenne effective est pratiquement égale à la contrainte moyenne totale. Sous chargement déviatorique, le sel présente les caractéristiques suivantes (Fig.5) qui diffèrent sensiblement de celles de roches fragiles ou semi-fragiles largement décrites dans la littérature (e.g., Bieniawski 1967 ; Martin and Chandler 1994 ; Hoek and Martin 2014, Eberhardt et al. 1998) mais qui sont similaires à celles d'autres types de sel: limite élastique (seuil de plasticité) très basse, les seuils d'initiation des fissures et de propagation instable des fissures (i.e., seuil de dilatance) tendent à augmenter avec la pression de confinement, l'endommagement par microfissuration (dilatant et irréversible) se développe principalement aux faibles pressions de confinement (0 et 1 MPa), le comportement devient pratiquement plastique parfait (ductile) à partir d'une pression de confinement de 5 MPa. La mesure des cinq vitesses d'onde P et S ultrasonores au cours d'un essai de compression uniaxiale a montré la fermeture préférentielle de microfissures et pores aplatis préexistants qui sont normales (ou pratiquement perpendiculaires) à la direction de la contrainte uniaxiale, ainsi que l'ouverture de microfissures axiales dont la direction est parallèle (ou pratiquement parallèle) à la direction de la contrainte uniaxiale appliquée. La fermeture des microfissures est pratiquement irréversible ce qui est vraiment spécifique au sel, contrairement donc à une roche calcaire par exemple (Eslami et al. 2010). Du fait de ces mécanismes de déformation, le sel, initialement isotrope, devient légèrement anisotrope (isotrope transverse). La méthode ultrasonore permet une détermination plus précise du seuil de dilatance (11 MPa sous chargement uniaxial) qu'avec les jauges de déformation. Le seuil de dilatance, qui est une limite très importante à partir de laquelle des changements importants dans les propriétés du sel gemme peuvent se produire (i.e., augmentation importante de la perméabilité due à l'accumulation de l'endommagement par microfissuration).

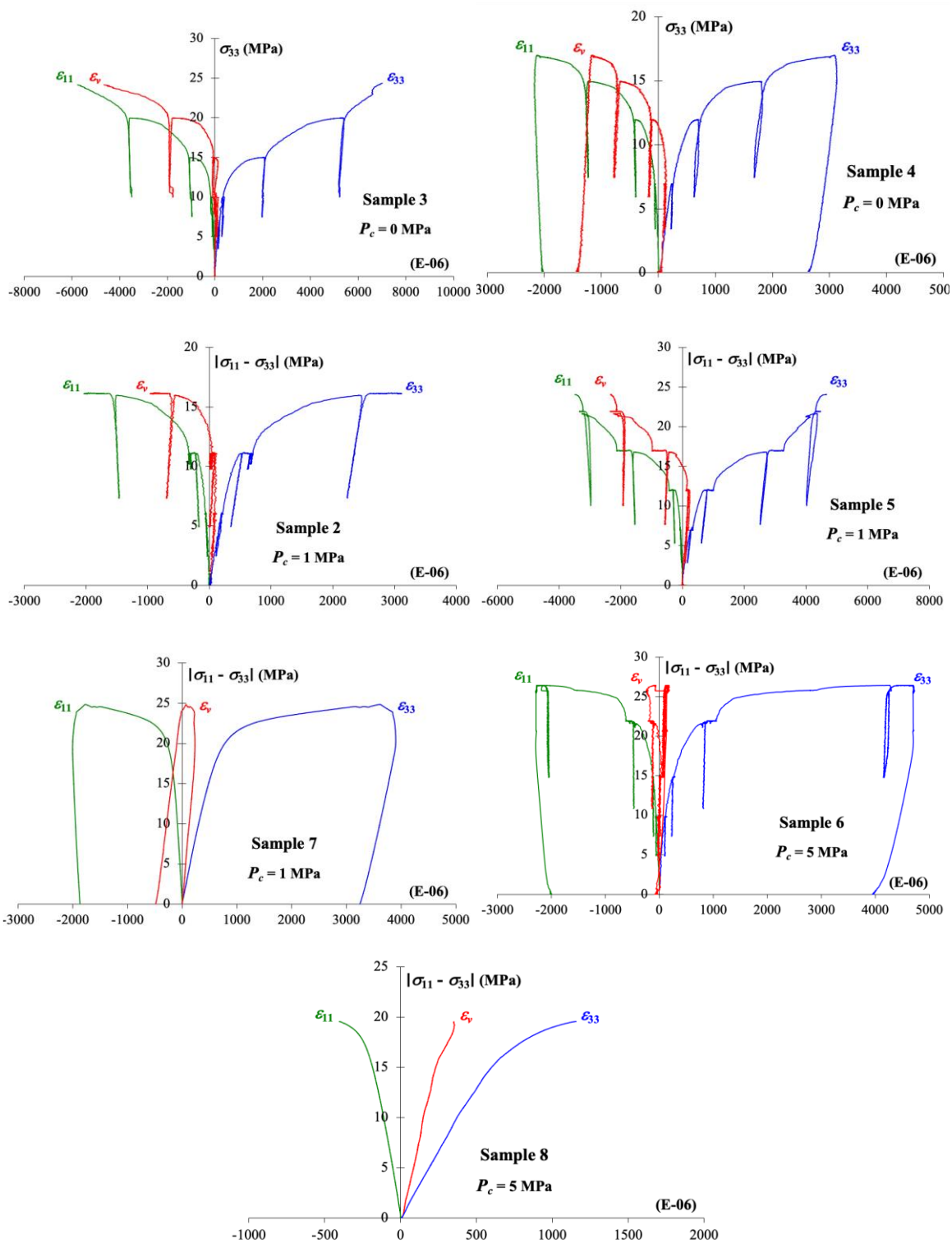

Fig.5: Courbes contrainte-déformation des essais de compression uniaxiale et triaxiale sur les échantillons de sel MDPA

Pendant le chargement déviatorique (jusqu'à 25 MPa), une augmentation modérée de la perméabilité au gaz (jusqu'à un ordre de grandeur) a été mesurée pour la plus faible pression de confinement de 1 MPa (Fig.5). La perméabilité commence à augmenter approximativement à partir du seuil de dilatance identifié à partir des essais de compression. Pour la pression de confinement plus élevée de 5 MPa, aucune augmentation de la perméabilité n'a été mesurée car le matériau devient parfaitement plastique ce qui élimine pratiquement le processus d'endommagement par microfissuration et donc la dilatance du matériau. Si la durée de l'essai est trop importante (échantillon 6 dans Fig.6), la guérison de l'endommagement restaure la perméabilité initiale. Comparativement aux autres études similaires dans la littérature (e.g., Popp et al. 2001 ; Zhang et al. 2020 ; Peach and Spiers 1996 ; Schulze et al. 2001), l'impact modéré de la contrainte déviatorique sur la perméabilité de notre spécimen de sel

peut être expliqué par sa nature très plastique, même à de faibles pressions de confinement et à faible température. Sous chargement hydrostatique, (jusqu'à 5 MPa), la perméabilité au gaz diminue (un ordre de grandeur) à cause de la fermeture des vides (pores et fissures). Cette diminution de la perméabilité est irréversible si la pression de confinement et la durée de l'expérience sont suffisamment importantes, ce qui peut permettre la restauration de la perméabilité initiale de la roche naturelle saine (non endommagée). Ceci peut être expliqué par la fermeture irréversible des microfissures initiales du au mécanisme d'auto-guérison. Nous avons montré que, même à faible pression de confinement (1 MPa) et pour une expérience de courte durée (2 jours), une diminution significative (un demi ordre de grandeur) de la perméabilité de produit grâce au mécanisme d'auto-guérison. Les essais de fatigue mécanique dynamique (cyclique) et statique avec une pression de confinement de 1 MPa ont montré que la dilatance se développe et augmente légèrement la perméabilité pendant la phase dynamique du fait de l'endommagement par microfissuration, tandis que le mécanisme d'auto-guérison réduit l'endommagement et diminue légèrement la perméabilité pendant la phase statique. Ainsi, les différents mécanismes (viscoplasticité avec durcissement, endommagement par microfissuration et auto-guérison des fissures) impliqués dans la déformation du sel gemme pendant la fatigue statique et dynamique agissent de manière compétitive pour annihiler toute évolution significative de la perméabilité. La fatigue thermique cyclique induit une légère augmentation de la perméabilité du fait de l'endommagement par microfissuration qui se développe à l'échelle microscopique. Ceci est lié à l'anisotropie de la déformation thermique des minéraux constitutifs de la roche (sel gemme) et à sa nature polycristalline, ce qui peut induire des hétérogénéités de déformation et donc des contraintes thermiques différentielles et de l'endommagement par microfissuration.

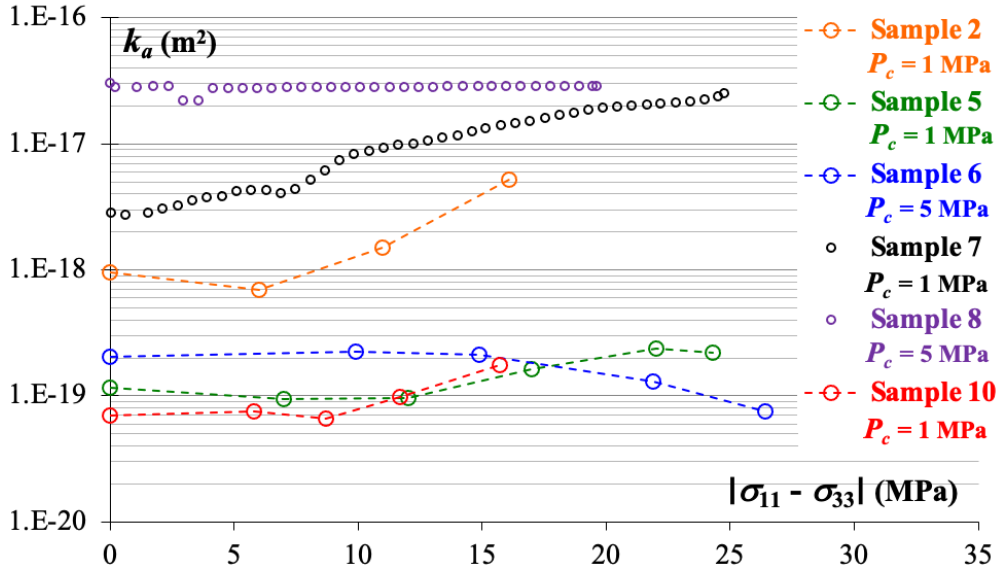

Fig.6: Evolution de la perméabilité au gaz apparente ka en fonction de la contrainte déviatorique pour différents échantillons Conclusion sur le stockage de l'hydrogène en cavités salines profondes

Dans le cadre du stockage de souterrain l'hydrogène en cavités salines profondes, les fractures et l'augmentation de perméabilité associée en champ proche (i.e., près de la paroi de la cavité) pourrait favoriser une fuite d'hydrogène à cause de l'excavation qui induit des contraintes déviatoriques élevées et à cause des cycles (haute fréquence) de pression de gaz qui induisent des variations de contraintes et température. Heureusement, l'épaisseur de cette zone endommagée (EDZ) est relativement faible et l'augmentation de l'endommagement et de la perméabilité dans cette zone devrait être modérée, spécialement pour le sel très plastique étudié ici. De plus, le mécanisme d'auto-guérison de l'endommagement et la grande capacité de fluage du sel empêche toute augmentation significative à long terme de la perméabilité. Par conséquent, la très faible perméabilité du sel gemme et l'intégrité du projet de stockage d'hydrogène ne sera pas impacté négativement. Tous nos résultats expérimentaux supportent l'idée que la fuite advective de gaz à travers les parois de la cavité devrait être négligeable et donnent plus d'informations utiles sur l'exploitation future des cavernes de sel pour le stockage de l'hydrogène. Cependant, une attention plus grande devrait être accordée à la contribution d'autres mécanismes de transport du gaz, en particulier par diffusion de l'hydrogène dissous dans la saumure interstitielle. Des recherches supplémentaires devraient également être menées pour étendre cette étude à d'autres types de sel gemme et déterminer les formations de sel gemme les plus appropriées pour le stockage de l'hydrogène.

4. Le Stockage d'Hydrogène dans les roches poreuses

4.1 Problématique

L'interaction entre l'hydrogène, le milieu et l'eau peut stimuler la dissolution et la précipitation minérales. Ceci pourrait modifier la perméabilité et la porosité du milieu. Cependant il n'a jamais été prouvé que ces réactions sont importantes et peuvent induire des grands changements. L'accent est désormais mis sur les réactions biogéochimiques qui peuvent être importantes et altérer le stock de gaz (Lassin et al., 2011; Ortiz et al., 2002a; Pichler, 2019).

Afin d'étudier ces phénomènes sur un grès analogue aux roches réservoirs poreuses, nous avons développé un nouveau dispositif expérimental pour simuler l'activité biogéochimique dans des conditions représentatives (T=35°C, P_{H2}=50bar, Pconfinement=200bar) du stockage aquifère. Cette nouvelle approche expérimentale combine des tests d'injection de gaz (hydrogène) en cellule de compression triaxiale avec des méthodes analytiques géochimiques pour tracer et quantifier les processus biologiques de conversion et d'altération de l'hydrogène. Nous avons choisi une roche analogue pour évaluer la capacité de stockage du stockage souterrain d'hydrogène : le grès des Vosges du Buntsandstein (Trias inférieur). Cette roche est formée de : 67,14 % de quartz, une faible teneur en muscovite de 10,20 % et une très faible teneur en argile d'environ 4,81 %. Sa porosité en eau est de 23.3%.

Nous utilisons comme souche bactérienne la *Shewanella Putrefaciens*, bactéries connues dans les réservoirs ultra salins et, responsables de la réduction du fer et de la fixation de l'hydrogène selon la réaction :

$$2Fe^{III} + H_2 = 2H^+ + 2Fe^{II} \qquad (01)$$

Nous devons travailler dans des conditions optimales pour la croissance bactérienne. Nous préparons donc une solution de développement bactérien similaire à celle *in situ* mais enrichie en fer. Ceci se fait en mélangeant une solution équilibrée du grès des Vosges puis centrifugée avec une deuxième solution enrichie en citrate Fe^{3+}concentré. La solution est bouillie pendant 5 min pour éliminer l'air dissout puis nous ajoutons du formiate comme source de carbone nécessaire au développement des bactéries ainsi que d'autres vitamines. Le pH est proche de la neutralité. Le milieu est stérilisé à l'autoclave et dégazé. Cette solution est utilisée comme milieu bactérien pour l'incubation des cellules.

Nous réalisons d'abord des expériences en batch pour quantifier la consommation d'hydrogène par le modèle de bactéries réductrice de fer Shewanella putrefaciens en conditions anaérobies et en présence de H_2 dans des conditions très optimales. Ceci est réalisé en autoclave dans plusieurs milieux de culture : sans formiate avec hydrogène, un milieu avec 4 mM de formiate non limitant et H_2, un milieu servant de témoin positif avec du formiate comme seule source de carbone organique et d'électrons sans ajout d'hydrogène. En batch nous avons suivi la croissance de la souche bactériennne sous les différentes conditions et contrôlé la consommation d'hydrogène en mesurant le fer dans un milieu salin et non salins.

L'évolution de la croissance cellulaire est contrôlée par le suivi de la densité optique DO. Le nombre total de cellules est déterminé par marquage au SYBR Green II. Puis le nombre de cellules est compté sous microscope d'objectif à immersion x100 et excitation par épifluorescence UV. La mesure de Fe^{2+} permet d'estimer le taux de bioréduction de Fe^{3+}. La mesure du Fe^{2+} se fait par test colorimétrique par la méthode à la phénanthroline (Fadrus & Malỳ, 1975) après digestion d'acide HCl et doser le fer réduit par son degré d'absorption d'une coloration intense.

4.2 Description du dispositif expérimental

Un échantillon cylindrique de grès est placé dans une cellule triaxiale confinée à 200 bars et chauffée dans un bac d'huile jusqu'à 35°C. Le système est ensuite purgé à l'argon et décontaminé par de l'eau distillée en augmentant la température à 100° pendant quelques heures. Puis l'eau est purgée encore par de l'argon et la température est abaissé à 35°C. Ensuite, on réalise l'ensemencement en introduisant la solution bactérienne incubée dans le milieu de culture enrichie de fer et de formiate, avec le gaz hydrogène. La solution reste en contact avec l'échantillon de grès pendant 48 h. Enfin, la solution est évacuée et récupérée pour calculer la saturation en eau résiduelle et le nombre éventuel de cellules restantes dans le système.

Finalement, le gaz H_2 est introduit dans le système est pressurisé à 50 bar afin d'établir un système d'équilibre (circuit fermé) entre amont et aval. Toutes les 72 heures, un système d'échantillonnage valve-micro-GC prélève 3 ml de gaz du système en aval. Le volume est compensé par une injection d'Argon, en amont pour maintenir la pression constante. On utilise l'argon étant un gaz inerte différent du gaz dans le circuit fermé pour pouvoir observer une variation significative de la concentration initiale du gaz sous l'influence de l'altération bactérienne. L'expérience a été réalisée sur un échantillon en présence de bactéries et un autre sans bactéries qui peut servir de test à blanc. Par cette méthode, l'évolution de la concentration du gaz de sortie peut être identifiée et donc une éventuelle altération microbienne quantifiée.

4.3 Résultats préliminaires

Les résultats sont discutés à la lumière de nos connaissances actuelles et des limites des appareils expérimentaux comparant aux résultats obtenus sur des tests blancs et sur des tests en batch. L'incubation de la souche Shewanella *Putrefaciens montre* que cette espèce peut survivre dans un milieu salin mais la salinitié ne doit pas dépasser les 300 g/L sinon elle ne peut plus survivre à cause de l'effet osmose. Les cultures de cette bactérie en différents milieux nutritifs ont montré que :

- La souche à une croissance réduite dans les milieux hypersalins et peut tolérer une salinité jusqu'à 300g/L
- en absence de toute source d'électron dans le milieu, *S. putrefaciens* est capable de réduire une partie le Fe^{3+} présent par des électrons endogènes composés des réserves accumulées durant la préculture.
- S. putrefaciens était capable d'utiliser comme donneur d'électrons et source de carbone le formiate et le lactate mais pas l'acétate et préfère consommer primordialement le carbone organique par rapport à l'hydrogène présent, que se soit sous forme dissoute ou gazeuse.
- Sa vitesse de consommation d'hydrogène en dehors de tous sortes de donneurs d'électrons endogène ou exogène est de 0.16Mm/H pour une réduction de Fe^{3+}de 0.48Mm/h en présence de 4Mm de formiate.

Les résultats du nouveau dispositif expérimental, pour une incubation de bactérie *S. putrefaciens* sur une carotte de grès solide que, pour un stockage d'hydrogène, l'activité bactérienne est inhibée. La forte concentration en hydrogène apparait limitante pour activation de la réduction de fer selon la loi de conservation de masse et la stoechiométrie de la réaction redox. Mais pourtant, pour une concentration d'hydrogène de 5% plus faible on n'a pas remarqué un effet d'altération de la cocentration du gaz. Cela peut être due :

- La pénurie en hydrogène dissout dans l'eau résiduelle préférablement consommé par les bactéries dans les aquifères et les réservoirs poreux
- La limitation de la surface d'échange sur une carotte solide pour réaliser des réactions biogéochimiques, et les incertitudes et variabilité entre les échantillons liés à la répartition des pores et les différences alors du comportement hydraulique du gaz
- La limitation de la cinétique de la réaction bactérienne dans les conditions proches de l'in-situ. La bactérie a préféré utiliser le formiate et ses réserves endogènes comme source de carbone sur l'hydrogènne présent dans le milieu
- L'augmentation des incertitudes de mesures, comparant aux tests réalisés en batch dans des conditions optimales.

Ces hypothèses nécessitent d'être valider par des analyses post-mortem, qui comptent les cellules restantes sur la carotte de grès après l'essai et quantification du fer réduit aussi.
Mais cela n'empêche de tester d'autres souches bactériennes comme les sulfato-réductrices ou méthanogène ayant une cinétique plus importante en terme de consommation de l'hydrogène. Mais cela ne peut être fait, qu'en adaptant le dispositif aux conditions de culture de ces bactéries et amélioration de la méthode expérimentale.

4.4 Conclusion

L'objectif principal de cette étude est de contribuer au suivi de la concentration en hydrogène du stockage d'hydrogène dans les aquifères salins profonds ou les réservoirs épuisés du pétrole et gaz considérées comme des roches poreuses. Ces roches habitent plusieurs phases fluides (pétrole, eau, gaz) en même temps et ont une perméabilité considérablement élevée. Ceci permet l'établissement d'un écoulement multiphasique avec des comportements particuliers selon la spécificité de chaque phase. Ces interactions aussi permettent de modifier le pH des eaux souterraines et résiduelles présentes dans le sous-sol et augmenter les réactions géochimiques entre

les fluides et les minéraux. Ceci permet la dissolution de certains minéraux et la précipitation d'autres, changeant ainsi la structure du réseau poreux et augmenter la perméabilité et les risques de fuite. Cependant, il est presque valide que ces réactions sont assez minimes ou négligeable souvent sans la présence d'un catalyseur biologique. La communauté bactérienne peut fortement proliférer dans de tels environnements en conditions anaérobiques extrême en consommant le H_2, donneur d'électrons et en fixant d'autres substrats comme le fer, le sulfate ou l'acétate. De nombreux modèles prouvent l'existence de ces communautés et aussi certains tests in-situ. Pourtant, l'importance de cette nouvelle méthode expérimentale est la simulation globale des conditions in-situ de stockage aquifère en termes de température, de confinement et de pression d'hydrogène, mais aussi de nutriments, de substrat et de bactéries en système de circuit fermé représentant la caverne de stockage en régime permanent. Le concept est d'incuber une souche bactérienne hydrogénotrophe (ici, la *Shewanella Putrefaciens*), sur une carotte de grès solide (ici le grès de Vosges) dans une cellule triaxiale permettant l'entrée et la sortie des gaz comme l'hydrogène et des fluides dans des conditions de température et pression proche de l'in-situ dans un circuit fermé. L'échantillonnage se fait périodiquement pour voir l'évolution de la concentration du gaz par un système-valve micro chromatographe à phase gazeuse lié au système. La pression est équilibrée à chaque échantillonnage par une réinjection en amont de gaz. Nos résultats n'ont pas montré une altération de l'hydrogène dans par la *S. Putrefaciens* comparant aux résultats en batch et les résultats sur le un échantillon blanc. Ceci montre que les conditions proches in-situ ne sont pas favorable à la croissance de tels bactéries et l'altérations importantes de gaz. Donc, le stockage peut être considéré fiable. Cependant, des preuves par des analyses post-mortem (comme comptage des cellules bactériennes restantes sur l'échantillon, évaluation de la quantité de fer réduite etc.) sont nécessaires pour valider nos résultats. Egalement une amélioration des conditions de l'expérience est proposé en réduisant la concentration en source de carbone pour accélere la consommation de l'hydrogène gazeux, augmenter la durée de suivi de l'expérience, travailler dans des conditions saturée, conditions standards plus favorables à la croissance des bactéries. Mais aussi, en perpective, Utiliser un différent substrat d'électron et tester une différente souche hydrophile ou même plusieurs souches pour évaluer les effets de la compétition bactérienne.

I – General Context

1. General Context

1.1. Environmental and economic problems of energy today

The question of energy transition today is closely associated with the environmental problem of global warming. The greenhouse effect is defined as an upsurge in the temperature of the Earth. It is caused by the ability of carbon dioxide, methane, nitrous oxide, and fluorinated gases (Greenhouse gases GHG) to capture and store energy from the sun. The excessive burning of fossil fuels (oil and gas and coal) results in the accumulation of CO_2 and other GHG in the atmosphere. Adversely, global warming potential increases (Marbán & Valdés-Solís, 2007; International energy agency, 2020; US EPA, 2020). Climate scenarios deduced from General Circulation Models (GCMs) show that this phenomenon stimulates the risk of extreme events such as droughts, heavy rains, fires, cyclone, melting icebergs, etc. These scenarios highlight the vulnerability of social and economic systems to climate change in the long term (Schelling, 1992; Tol, 2009; Meyers, 2010).

According to the 2020 International Energy Agency report, 2020 was marked by a 5% drop in energy demand simultaneously with a 7% drop in CO2 emissions. It coincided with the Covid-19 health crisis and the global financial recession. Based on these numbers, the expert groups proposed a proactive scenario for net zero emissions in 2050: a 60% reduction in carbon dioxide emissions between 2019 and 2030 with a 17% reduction in energy demand (twice the number projected in 2006). However, the projected numbers rebounded in 2021 in conjunction with the economic recovery and the market growth of 6%. The demands of emerging markets and developing economies now account for more than two-thirds of global CO_2 emissions. Hence, while emissions in advanced economies are in a state of structural deterioration, a 4.6% increase in global warming emissions is expected by 2021 (International energy agency, 2021). It witnesses the tight relationship between the energy consumption for industrial development and the anthropic climatic change. The planet has already warmed by more than one degree since the start of the industrial age. Therefore, based on the Paris Agreement (2015), the 195 participating countries have agreed on a global objective, to reduce global warming to less than 2 ° C-1.5 ° C, by carbon neutrality politics by the end of the century. Energy transition toward renewables sources (sun, wind, water, biomass etc.) is the key future to reduce CO2. Oil burning is the main reason of climate change. Fossil fuel constitutes 33% of global primary consumption. Parallel to that, the incorporation of emerging countries evidencing a population booming, increase the rate of oil consumption. Global energy markets are becoming tighter. It affects the oil stock market, and elevate prices (Marbán & Valdés-Solís, 2007). Some countries, such as those of the European Union, rely heavily on importing primary energy, with production declining over the past decade. The quantity of imported natural gas more than doubled over the period 1990-2019, reaching 360 Mtoe. Crude oil maintained the first place in imported quantities, with 513 Mtoe in 2019, only 1.2 % less than 10 years ago. Oil continued to be the most significant energy source imported by the EU (26% share) in 2019 (EU_Eurostat, 2021).This can threaten the countries economical and security stability. Hence the importance of diversification in the energy mix (Weisz, 2004; Smil, 2010). Since the Industrial Revolution, electricity has driven the industrial and technological activities. Electricity grid is in a perpetual upgrading because of the increase of demand in industry, mobility, urban heating and other. Electricity production still highly dependent on fossil fuel burning. In the European Union, by 2010, only forty-five percent of the power depends on low carbon energy sources (nuclear and Hydropower), all of the rest in the energy mix depends on fossil fuel (European commision-Directorate General for Energy, 2011). European governments set an energy policy called “the EU green deal initiative” to invest in renewable energy infrastructure in the frame of the energy roadmap to 2050, based on energy saving strategies and improved management of energy demand. The main goals set in the energy model:

- reducing GHG emissions by 40% considering today's emissions as baseline and considering that EU emissions already dropped by 25% at 2019
- integration of renewable energy (sun, water, and wind) in the process is a priority to decarbonize electricity system,
- implement a 20% improvement in energy efficiency.

By 2030 Europe could be generating more than 40% of its energy from renewables. Europe could be on track to deliver a 100% renewably powered energy system by 2050. Many of the green-energy and low-emission technologies exist today but need to be developed and expanded further. Besides cutting the vast majority of its emissions, Europe could also reduce its use of key resources like oil and gas, raw materials, land and water. The challenge with the emergence of renewables is their intermittency, uncertainty and the inability to secure a stable production. In spite of their importance in the energy transition process, the variability of these sources reveals high concerns on their reliability and the cost of their implementation in the system which emphasize the importance of the energy storage (European Commission. Directorate-General for Energy, 2012; 2013).

1.2. Assessment of underground energy storage

The supply of electricity must always reconcile with changes in demand. Seasonal and daily fluctuation patterns in the market are driven by many factors such as the need for heating, cooling, lighting, etc. Low production seasons of renewable energy sources exacerbate the issue. Therefore, flexible measures are taken on the electricity grid-like reducing electrical power losses in the distribution system, expanding transmission, flexible production, increasing subsidies, and most importantly energy storage. It can be an important option to bridge the temporal gap of the low production seasons of the renewables and market fluctuations in the short and long term. Also, it increases the electricity grid stability and allows security in case of any emergency (Denholm et al., 2010).Investment in these techniques is a pillar in the 2050 European Energy roadmap for energy transition, especially for energy produced from green sources like the renewables (Kruck et al., 2013).

Several technical and economic criteria play on the classification and the assessment of underground energy storage technologies for a certain region. Technical criteria are efficiency or the ratio between released energy and stored energy, the maturity of the energy technology such as idea verification, prototype, demonstration, and commercialization, storage capacity of the geological storage sites, the lifetime and durability, the interval time a storage unit takes to react to a given input, and the power density or the output of the storage. While economic criteria are capital costs, operational and maintenance cost, fuel cost, end-life cost, the security cost and the recurrent cost or the cost per unit of energy divided by the life-cycle. Some other criteria are related to social acceptance, health and safety of the population, security of the facility, but also , to environmental criteria of water and air pollution , impact on land, wildlife and other resources (Daim et al., 2012).

Some common examples of energy storage are rechargeable batteries which store chemical energy convertible into electricity, hydroelectric dams, which store energy in a reservoir as gravitational potential energy (Underground Pumped Hydro-Storage), thermal Energy Storage (ATES) by steam accumulations in rocks or hot water in aquifers, famous especially in Finland. For fluids, the first successful storage of natural gas was accomplished in 1915, in a partially depleted gas field, in Ontario, Canada. Since then, the gained knowledge was transferred to store other fluids. Liquefied gases have been stored in excavated caves since 1951. The underground storage of compressed air (CAES) originated in 1910 in the Striberg Mine, Sweden. Hydrogen conventionally has been stored above ground in small quantities at industrial plants, where it is used in the manufacturing of petroleum products, like ammonia, petrochemicals, etc. Hydrogen has been successfully stored the first time in solution-mined salt caverns in England, by Imperial Chemical Industries at Teesside. In a reservoir near Beynes, France, Gaz de France operated an aquifer storage for hydrogen-rich (50% to 60 %) manufactured gas from 1950 to 1972, the field was successful y converted to natural gas storage in 1973 (Foh et al., 1979). The next sections will give an overview of the most relevant of these techniques (Fig 1.1).

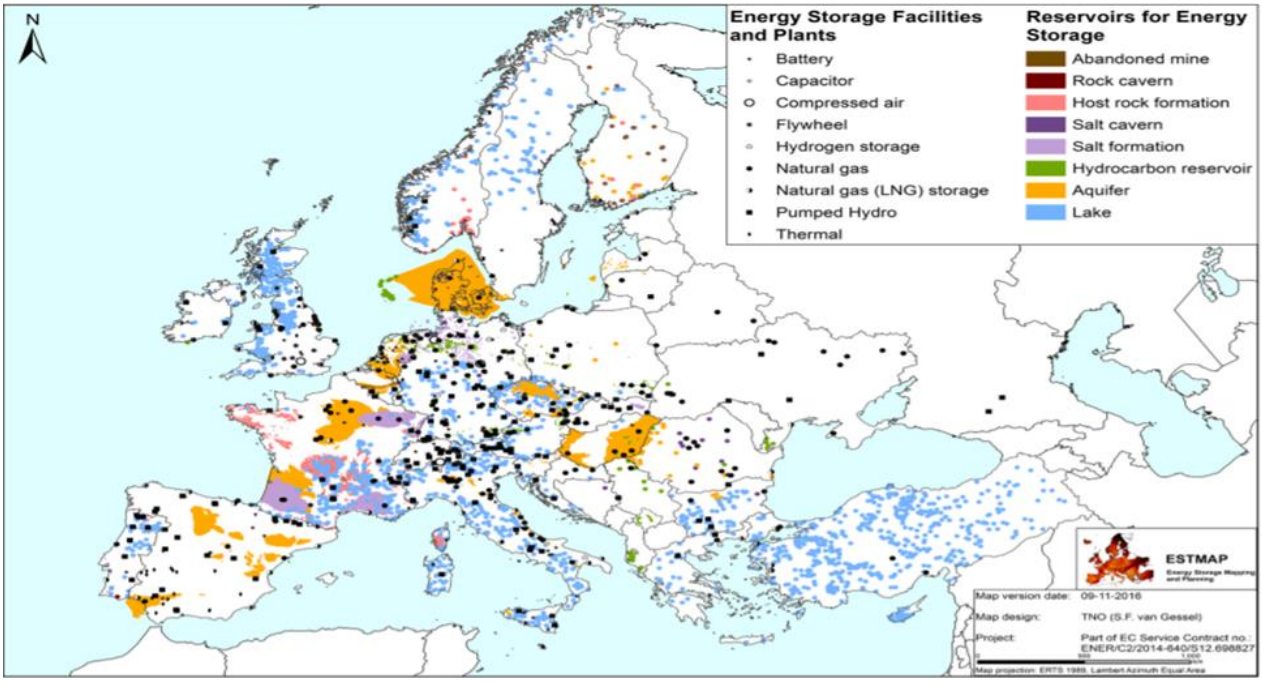

Fig 1.1: Geographical distribution of energy storage techniques and facilities in the EU and it neighborhood (edited:www.estmap.eu)

1.2.1. Pumped Hydro Energy Storage

The principle of Pumped Hydro Storage (PHS) is to store electrical energy produced by renewables by using potential energy of water. During low demand cycle and high availability of power, plant pump water from the lower reservoir to the upper reservoir using electricity. In times when demand is high and electricity is more expensive, this stored potential energy is converted back into electrical energy: water from the upper reservoir is released back into the lower reservoir. This mechanical action rotates the turbine to produce electricity (Fig 1.2) The installed power range from 10 MW – 3.0 GW when there is no limitation factor. It efficiency is about 70% to 80%. The quick response for energy demands (few seconds to minutes) is an important advantage when using this technique. PHS is currently the electricity storage technology providing the largest storage capacities. There are over 170 GW of pumped storage capacity in operation worldwide. Europe the second biggest zone, with 57GW, accounting for approximately 33% of the market (Kruck et al., 2013; European Association for the storage of energy, 2016).

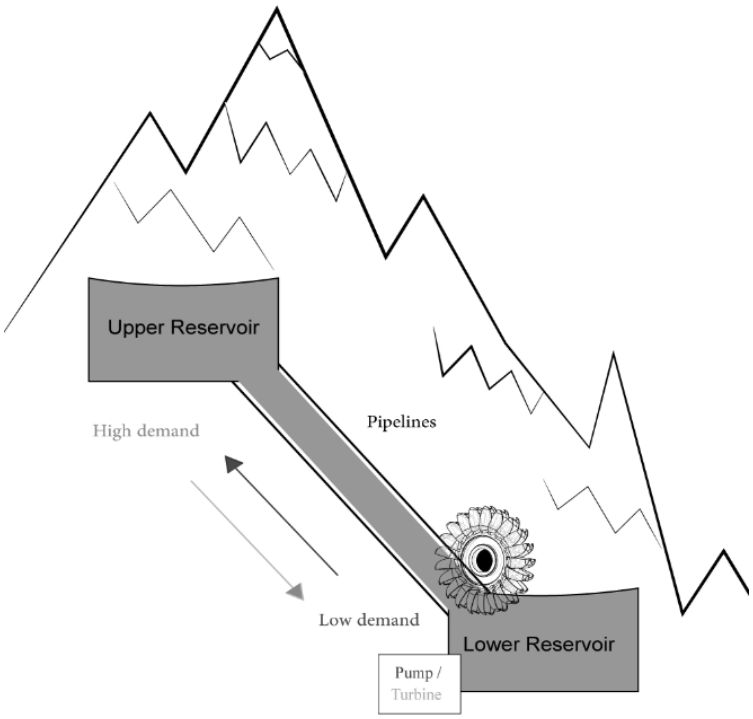

Fig 1.2 :A schematic of pumping hydro-electrical plant

1.2.2. Compressed air storage (CAES)

The CAES basic operation is very simple. CAES pre-compresses the air during low demand season using electrical power from the gridline and stores it in large rock reservoirs. When demand exceeds supply, the compressed air is mixed with natural gas, burned and expanded in a gas turbine. CAES plants can be classified as storage systems for short to medium term (minutes to hours to a day) storage times (Mahlia et al., 2014).

1.2.3. Geothermal energy storage

Geothermal underground resources range from shallow resources, through deep permeable aquifers, hot springs, fumaroles, geysers, travertine deposits, chemically altered rocks to hot dry rocks. It integrates into various usage like heating, cooling, and electricity production options, depending on the local needs, possibilities, and geological conditions. Despite the good overall understanding of the subsurface, several unknown factors remain vicious for successful geothermal exploitation due to geological heterogeneity, anisotropy, faults, diagenesis reducing porosity and permeability, scaling, and corrosion. Until recently, geothermal power systems have exploited only resources where naturally occurring heat, water, and rock permeability are sufficient to allow energy extraction. Enhanced Geothermal System technologies have allowed to exploit new geothermal resources in hot dry rocks (Kruck et al., 2013).

1.2.4. Hydrogen gas storage

Hydrogen could account for almost one-fifth of total final energy consumed by 2050. A prospective Mackenzi study showed that by 2050, hydrogen in France will represent: 20% of the energy demand, 18% of the vehicles market, and a 55 millions of tons reduction of CO_2 emissions. By this time, this industry would represent a turnover of 40 billion euros and more than 150,000 jobs (Air Liquide, 2018). On the European side, Hydrogen usage will reduce annual CO_2 emissions by roughly 6 gigatons compared to today's levels, and contribute roughly, up to 20% of the abatement required to limit global warming to 2°C (Air Liquide, 2017). Hydrogen gas is considered green; it combustion produces only water. Hydrogen exists as natural ressources. The first prospects were discovered at the bottom of the sea in the 1970s and more recently on land. Also, it can be produced by steam methane reforming. Although this process emits CO2, the gas could possibly be captured and stored to produce carbon-free hydrogen. Instead of natural gas, the use of biomethane (methane from the fermentation of biomass) is also a solution. other known techniques to produce hydrogen is coal gasification or combustion but this process emits a lot of CO2 and CO, and considered as very pollutant. Thus, the most efficient technique is the electrolysis of water by the electricity generated by renewable energy like windmills. The electrolysor separates a water molecule into hydrogen and oxygen. Hydrogen produced is considered green. A wind turbine can produce a maximum of 12 MW of electricity and an efficient electrolysor needs 0.04 MWh in average (Bertuccioli et al., 2014).

Hydrogen fuel will lift-off as a new vector of transition in the world of energy. The next chapters, will discuss the importance of hydrogen storage in energy transition process.

1.3. The aspects of underground hydrogen storage

The production of electricity from renewable energies is green and sustainable but intermittent and does not always succeed in meeting unpredictable market needs. Power-to-X models are business models based on the transfer of energy from the electricity grid to the gas storage grid. The main objective is to store electricity during the season of high production - low demand and to reuse it during the season of scarcity. One promising response is the conversion of electricity into hydrogen, a green and versatile energy carrier gas. This is done by electrolysis technology that decomposes water into oxygen and hydrogen gas using the electricity produced from renewables. Hydrogen gas can be used as energy carrier for combustion and power production. Hydrogen fuel cells are not new to utilities. It started in 1997 to power the forklifts batteries for industrial usage. Now upscaling this technology is a must because of it multiple advantage over electricity storage. Like for example, transportation loss is much lesser if using a gaseous carrier (<0.1%) compared to using the power network (8%) on the grid (Davison et al., 2010; Michalski et al., 2017; Zivar et al., 2021).

Hydrogen storage can be physically as either a gas or a liquid. Hydrogen gas can be stored above or underground in high-pressure tanks (350–700 bar). It storage as a liquid requires gas cooling at very low cryogenic temperatures

considering that it boiling point is −252.8°C at atmospheric pressure (Energy.gov blog, 2021). Hydrogen in light weight solids is also a new storage technique, especially for mobile and rapid usage. The molecule can combine with solids like coal either physically or chemically by adsorption and absorption. It density is preserved and the volumetric losses of liquefaction and compression are avoided by this method (Prachi et al., 2016).
For long term storage, deep ground geological formation enables large volumes of gas stocking at an adequate pressure in a small land parcels (Davison et al., 2010; Michalski et al., 2017; Zivar et al., 2021). Depending upon the way it is produced but also its final usage, hydrogen can be stored in a mixture with other different gases (such as carbon dioxide, carbon monoxide, methane, and nitrogen) or as a pure hydrogen (Zivar et al., 2021). According to its application, hydrogen is stored according to power-to-mobility model for automation ; fuel cell electric vehicles (FCEVs), power-to-industry model for industrial feedstock, power-to-power model to feed fuel cells for electricity generation and compensate shortage during low generation periods and can be also used for urban heating (Robinius et al., 2017). In addition, there is the power-to-gas model, which consists in injecting directly the produced renewable hydrogen into the city gas network in a small proportion to enhance the energetic mix. An alternative is based on the conversion of hydrogen in the storage by a reaction with the CO_2 into renewable methane and water, under the influence of microbial activity or in presence of other catalyzers. Renewable methane can be then injected in the natural gas network without limitations to enhance the calorific value (Haeseldonckx & D'haeseleer, 2011; Gahleitner, 2013). There are two storage types of facilities for geological hydrogen storage:

- Cavern storage, in which the gas is contained in excavated or solution-mined cavities of dense rock like salt rock. Those salt rocks can be dome salt or thick beds of salt;
- Porous media storage, in which the gas occupies the naturally occurring pore space between mineral grains or crystals in sandstones or carbonate formation.

1.3.1. Hydrogen storage in salt caverns

Storage options are dictated by the regional geology and operational needs. Salt caverns storage is considered very practical because of salt tightness, favorable mechanical properties of salt and resistance to chemical reactions. Also the high saline condition restricts the hydrogen stock losses by microbial consumption. A prerequisite for the construction is a suitable geological salt deposits in the form of salt domes or bedded salt with a sufficient thickness and extent at a favorable depth. Mining technique for salt cavern is leaching, also called solution mining. It consists of injecting into a saline cavern freshwater through the string to the well bottom. Freshwater having a lower density than the brine flows out of the string to the cavern roof and saturates gradually with salt within the process. Brine is discharged out of the cavern via the leaching string. After this process, the salt cavern is finished when its shape and volume meet the requirements for storage. Most of the caverns are cylindrical. Eventually, the leaching string is replaced by a gas withdrawal tube above the cavern and the brine string is placed on the sump to empty the cavern while the first filling of gas is done (Kuntsman, 2007). The physical characteristics of the storage type must meet its economical capacities and containment for a suitable application. Two of the most important characteristics of a ground facility are the gas storage capacity and the rate at which gas can be withdrawn known as deliverability rate. Therefore, we define cushion gas as the unrecovered gas volume required in a reservoir for management purposes and to maintain minimum pressure for gas delivery. It is important for the stability of the reservoirs. Also, we can define the working gas volume as the gas in the storage plant above the cushion gas volume, withdrawn or injected compatibly to legal and technical limitations. In salt caverns, capacity is given by the chamber volume and sealing is provided by the impermeable host rock surrounding the cavern. Because most rock lithology cannot be considered to be absolutely impermeable, the limiting pressure for almost all forms of underground storage is related to the hydrostatic pressure gradient of 0.1 bar/m below the water table. While the overburden pressure or the confinement pressure is between 350-450 bar, every storage facility operates below those limits or slightly above, stays in safety range of 0.16 bar/m to avoid hydraulic fracking. As the storage pressure increases, less void volume is required for a given quantity of stored gas. Therefore, salt caverns provide very high deliverability rate considering their working gas volume. They have relatively low cushion gas requirements (about 25%), compared to gas-oil depleted reservoirs and aquifers characterized by their large storage capacities (Ozarslan, 2012).However, hydrogen density is nearly one-third of natural gas. Thus, for storage it needs to be compressed to 20 MPa and above for and efficient stock of gas. For example, taking a salt cavern at around 1000m of depth having a geometrical volume of 700,000 m^3, the gas storage capacity would be at around 6 million kg of hydrogen, at a maximum operating gas pressure level while the cushion gas remaining after the operational pressure reaches its minimum is 3 million kg of hydrogen. So, based on construction conditions, salt

caverns for a sufficient storage of gaseous hydrogen can be built up to 2000 m deep, 1,000,000 m3 volume, 300-500 m height, and 50-100 m diameter (Michalski et al., 2017; Zivar et al., 2021).

1.3.2. Aquifers

Considering the storage in porous media, generally it's done in aquifers or depleted reservoirs of oil and gas. Pore space of aquifers is generally filled with fresh or saline water. Overlying rock beds or trap head guarantee the sealing (Ozarslan, 2012). Aquifers are geographically widespread making them an easy and fast option for hydrogen storage.

The injection pressure of hydrogen should be higher than reservoir natural pressure. As the hydrogen is injected into the aquifer the present liquid moves downward or aside leaving the place to the gas in the porous network creating a gas-liquid interface and increases porous pressure. However due to the low viscosity of hydrogen, fingering and overriding is evidenced. Safety challenges may arise but also a risk of producing two liquid phases from the storage site. Storage practices show that reservoir pressure remains constant while volume varies over the period of months. But, over a period of days, volume remains constant while pressure varies. This variation is related to geometrical and petrophysics of the aquifer controlling flow behavior by permeability, porosity, fluid saturation, location and geometry. It also depends on the fluid mobility ratio and the multiphasic flow due to the presence of gas and water (Carden & Paterson, 1979). Another challenges faced in aquifers storage is related to leakage if the sealing rock isn't efficient, or mechanical stresses and undetected active fault leads to fracturing. Not to forget the high risk of stock losses by microbial consumption or gas conversion because of the reservoir favorable conditions such as temperature, pressure, and salinity. Therefore, most of the hydrogen storage projects in aquifers present around the world are still under research and pilot projects or the stored resource is a gas mixture including hydrogen but no pure hydrogen gas (Zivar et al., 2021).

1.3.3. Depleted oil and gas reservoirs

A depleted oil and gas reservoir is a naturally ready-to-use reservoir for hydrogen storage. It consists of a porous reservoir capped with an impermeable layer in a bearing geological trap. The depleted reservoirs are well-identified geological structures with enough tightness, integrity and the necessary pre-existing surface and requirements to make them appropriate sites for hydrogen storage. Furthermore, the sufficient information and knowledge already proves their characteristics. The existing of a remaining gas, for instance, is considered an advantage because it establishes the cushion gas, and the risk of hydrogen loss in the cushion due to mixing is very low (1-3%,Srinivasan, 2006). Also, the risk of dissolution in oil phase if it's an oil reservoir, is also low (1.5 mol. % at 100°C at150 bar in heavy oil, Torres et al., 2013). But, it's important to cease oil or gas extraction from the site way long before planning the hydrogen storage. This allows the storage to be created in a shorter time and at a low cost. During hydrogen storage, the maximum pressure in the site often exceeds the original reservoir pressure. This makes it possible to expand the volumetric capacity of the storage. Nevertheless, the presence of another gas or oil may be a repulsive factor for choosing such site. The other fluid may reduce the purity of hydrogen that needs to be extracted. Also, the interactions between fluids can lead to a chemical conversion and mutation or losses in the hydrogen gas stock. Not to forget also, the microbial factor present in the site that might contribute to this alteration (Zivar et al., 2021).

1.4. Hydrogen gas fundamentals

1.4.1. Hydrogen gas chemical aspect

Hydrogen having low density, viscosity and small molecular size, risks of leakage need to be tackled. The previous experiment of helium storage, having similar atomic property like hydrogen revealed similar leakage issues. Therefore, the gas chemical and physical characteristics should be very well understood before geological storage in order to ensure safety and success (Carden & Paterson, 1979). Hydrogen is the lightest of all elements with an atomic weight A=1.00794 a.m.u, and atomic number Z=1. At Standard Conditions of Temperature and Pressure (STP), hydrogen is colorless, tasteless, noncorrosive, nonmetallic, and nonpoisonous physiologically (Lide, 1994).

The molecule H_2 consists of two atoms of Hydrogen "H" and appears at STP, in two forms Para-Hydrogen (and Ortho-Hydrogen, based on the orientation of the nuclear spin). Under STP conditions, the equilibrium composition of the normal hydrogen states is 25% of para-hydrogen and 75 of ortho-hydrogen. However, this equilibrium varies

with temperature and pressure. As temperature decreases, ortho-hydrogen transforms into para-hydrogen-the exclusive form of hydrogen at liquid state. This transformation is accompanied by heat release. This energy is higher than the evaporation heat (445.6 J/g or 191.7 BTU/lb (british thermal unit per pound) causing eventually quantity losses by boil (Ordin, 1997). This thermophysical property is a challenge for liquefaction process and hydrogen storage at liquid state (Fig 1.3).

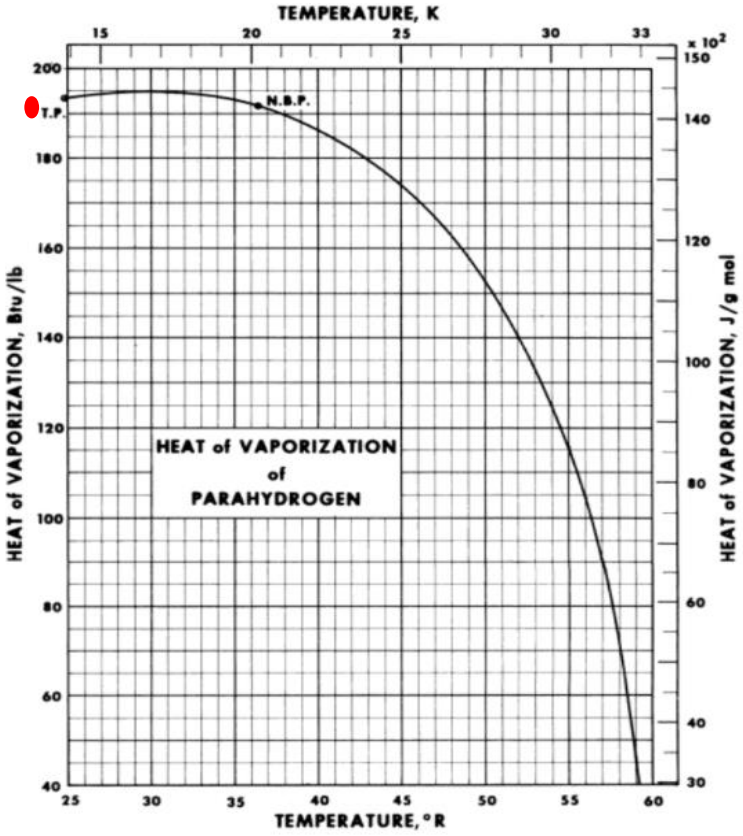

Fig 1.3: Hydrogen phase diagram (McCarty et al., 1981; Ebrahimiyekta, 2017)

1.4.2. Thermophysical properties

At STP conditions, hydrogen is in a gaseous state. At atmosphere pressure, hydrogen can liquefy at -252.87°C, the second-lowest boiling point among all elements after helium. Its solidification temperature is –259.34°C. That is why hydrogen is not used as primary fuel and why it is hard to store it under STP conditions compared to other liquefied gases. When pressure increases, the boiling point increases up to –253.15°C at 13 atmospheres and stops at this value even if pressure increases (Ebrahimiyekta, 2017).

Hydrogen has a very low density in the gaseous state and the liquid, ie. about 7% of the air density and 8 times denser than natural gas at room temperature. It is a challenging property for storage that requires compressing the hydrogen before any use. Its density is 0.08988 g / l in the gaseous state and 70.8 g / l in the liquid state (Züttel, 2003).

The model of ideal gas is generally used to estimate gas density. However, the behavior of hydrogen deviates significantly from the thermophysical principles of gas at high pressure (above 100 atm). It is mainly because hydrogen molecule is highly polarised.The attraction forces between molecules slightly change the gas partial pressure resulting in gas compression at higher pressure. Ideal gas overestimates gas density at a presure higher than 400 bars (Fig 1. 4) . So, other models are used like Van der Waals, Virial function, Berthelot equation to predict accurately the hydrogen behavior. Integrating the energy content in those models and the calorific factors can somehow overcome the inacuracy at high pressure (Klotz & Young, 1964; Tzimas et al., 2003) (Fig 1.4).

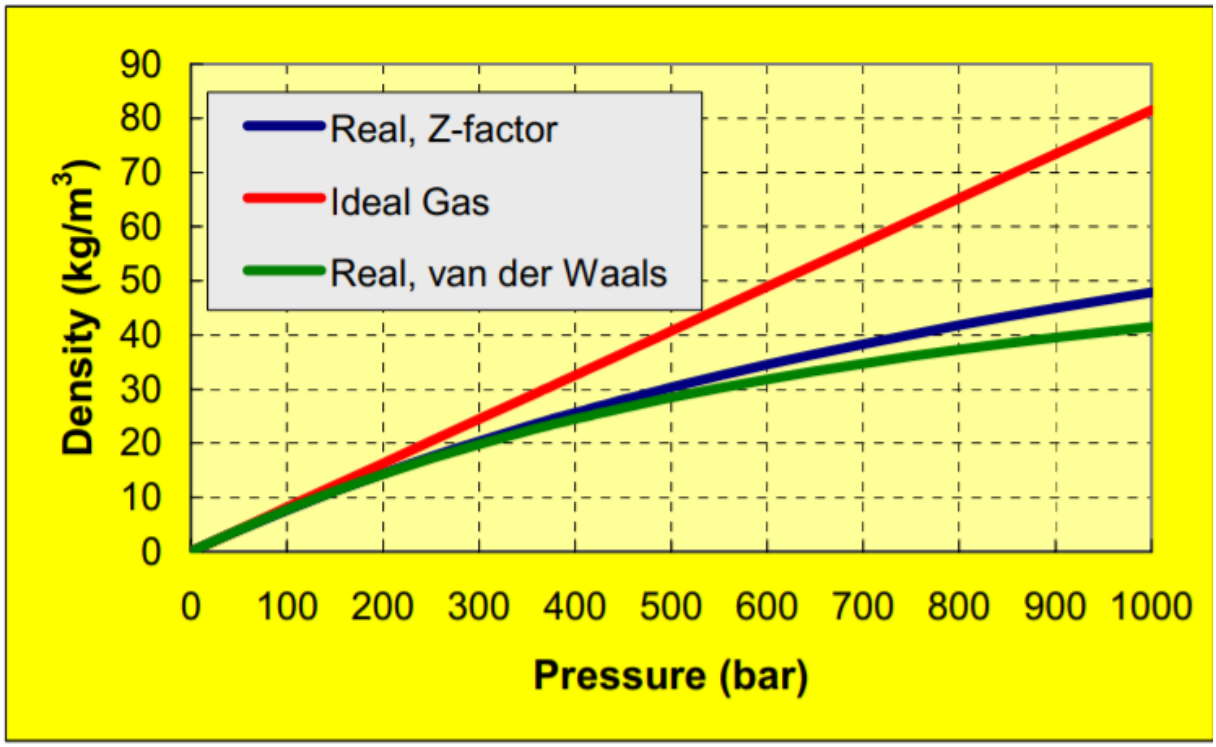

Fig 1.4: Hydrogen density diagram (McCarty et al., 1981; Ebrahimiyekta, 2017)

Hyrogen also has a low viscosity compared to methane for example. So, it shows higher mobility leading to a very low residual gas in the porous network. It withdrawal is so easy and efficient with low chances of coning during pumping procedure (Thakur & Flores, 1974; Zivar, et al., 2020).

1.4.3. Energy Content

Hydrogen reacts with oxygen during combustion, gives water (H_2O) and releases energy. This makes the hydrogen as a green fuel with minimum releases of greenhouse gases. However, it's also important to look to it energy density to study it capacity. The energy density is the heat released during combustion normalized to the amount of reacted hydrogen. It ranges from the low Heat values (LHV) to the high Heat Values (HHV). Those two boundaries are distinguished by the type of H_2O released used in the calculations by the exothermal equations. Hence, if H_2O is in the vapor phase the normalized energy released is called the LHV (or net calorific value). And, if H_2O is in a liquid state then the normalized energy released is called HHV (or gross calorific value), that is higher than the LHV by about 10% accounting also for the heat of condensation of water vapor into liquid. Thus, the energy density of hydrogen can be expressed either on a weight basis (mass-energy density) or on a volume basis (volumetric energy density).

It can be easily calculated based on basic thermodynamic principles, with respect to the equations of hydrogen combustion.

$H_{2(g)} + ½O_{2(g)} \rightarrow H_2O_{(g)}$ $\quad \Delta H_{298.15\,K} = -241.826$ kJ/mol (1.1)

$H2(g) + ½O2(g) \leftrightarrow H2O(l)$ $\quad \Delta H_{298.15\,K} = -285.830$ kJ/mol (1.2)

First equation above is used to calculate LHV of hydrogen when water is in form of vapor while, the second one is for the calculations of HHV of hydrogen. So, the mass energy density of hydrogen is the ratio of the heat of formation mentioned above over the molecular weight of hydrogen (i.e. 2.02×10^{-3} kg). Therefore, the mass-energy densities of hydrogen at 25°C are 119.716 MJ/kg (LHV) and 141.500 MJ/kg (HHV). Compared to other conventional fuels, hydrogen has the highest mass-energy density, almost 2.5 times the energy released during the combustion of conventional hydrocarbon fuels (Fig 1. 5, Tzimas, et al., 2003).

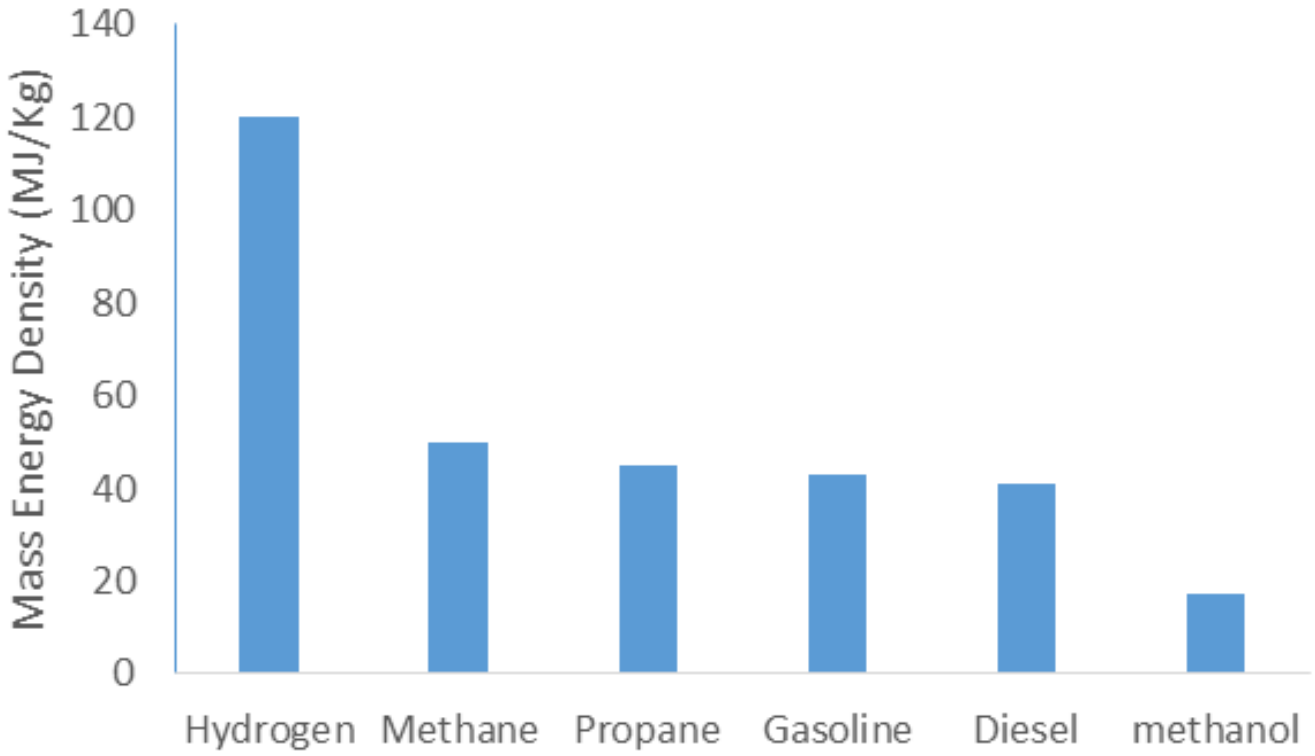

Fig 1. 5: Mass energy density of fuels (LHV) (Tzimas et al., 2003)

However, hydrogen is a flammable gas. In underground storage conditions, it is evident that hydrogen is not incendiary, due to the lack of oxygen and required temperature and pressure conditions. The gas only becomes dangerous if it leaks and mixes with air within the flammable range. Flammability is the range of concentration in which hydrogen sets off a self-propagating flame when ignited. The range is very broad between 4% and 75% under STP conditions. On the other hand, in a narrower range (15 to 59%), hydrogen can become explosive. Since hydrogen diffuses very quickly, increased fire and explosion hazards in case of leakage (College of the Desert, 2001).

In addition, the auto-ignition temperature, i.e. the minimum temperature required to initiate self-sustained combustion in a fuel mixture, without source is 585°C for hydrogen. This temperature is considerably higher than for any other conventional fuel such as methane (540°C) and gasoline (230-480°C). However, the minimum energy required for hydrogen ignition is 0.03 mJ, almost an order of magnitude lower than that of conventional fuels. Therefore, hydrogen can ignite more easily than other fuels (College of the Desert, 2001).

1.4.4. Hydrogen reactivity and solubility

Hydrogen can chemically deteriorate the metal or alloy material used (pipelines, metals, tanks, etc.). Gas atoms dissolved in metals tend to concentrate at the grain boundaries of crystals, which increasing the potential of metal embrittlement. Furthermore, their saturation in metal pores resulting in hydrates formation and the chemical interaction of hydrogen with the metal are additional mechanisms causing material corrosion (ASM International, 1978).

On the other hand, the solubility of hydrogen in the site's storage water is important because it affects the pH of the medium and modifies the redox potential of the system especially in case of storage in aquifers. Like other gases, it increases with increasing pressure, temperature and salinity. However, the non-polar nature of hydrogen limits its dissolution in water. In pure water, it is about 0.14 mol. L^{-1} (at 65 ° C and 20 MPa), similar to that of CH_4 solubility. For solubility in NaCl-brine it's between 0 and 5 for a temperature range between 49.85°C and 99,85°C and a pressure between 10 and 230 bar for a molality less than 5 (mol/kgw) (Chabab, Theveneau, et al., 2020). So risks of pH changing and the loss of hydrogen gas by dissolution are minimal (Carden & Paterson, 1979; Hassanpouryouzband et al., 2020). It should be noted that the presence of other dissolved substance in the water reduces hydrogen solubility (Lassin et al., 2011).

1.5. Worldwide hydrogen storage examples in geological structures

Up to now, hydrogen storage attempts around the world are still limited. Currently, four large working hydrogen caverns in pure salt (95%) operates successfully; Teesside in the United Kingdom is site of three elliptically-shaped salt caverns at a depth of 350-450 m and with a total volume of 210000 m^3, has been operating since the 1970s (Caglayan et al., 2020). The three others are located in the United States (Texas) built in pure salt domes (Clemens Dome, Moss Bluff, Spindletop). The salt caverns at Clemens Dome and Moss Bluff are built at a depth of 800m (top of the cavern) with volumes of approximately 580000 m^3. The caverns have operated since 1983 and 2007, respectively (Tarkowski, 2019; Caglayan et al., 2020). Spindletop is the world largest underground hydrogen storage facility in a salt cavern operated by Air Liquide. The cavern is 1500 meters deep and about 700 meters in diameter. Its function is to store hydrogen to meet large-scale methane vapor needs and to cover daily fluctuations, up to 30 days. It is located in Spindletop, Beaumont, in the Gulf Coast region of the United States, in a salt dome that is part of the Texas salt belt known as the middle Jurassic Louann evaporites layer (Hyne, 2019; Air Liquide, 2017).The cavern is a diapiric pure salt covered by a cap rock of anhydrite bed overlying the halite stock, over this layer, a zone of gypsum, calcite, and sulfur separating the Anhydrite from the limestone (Murray, 1966; Kyle et al., 1987). These projects demonstrated the technical feasibility of underground gaseous storage of hydrogen and opened the doors for many small and pilots' projects around the world.

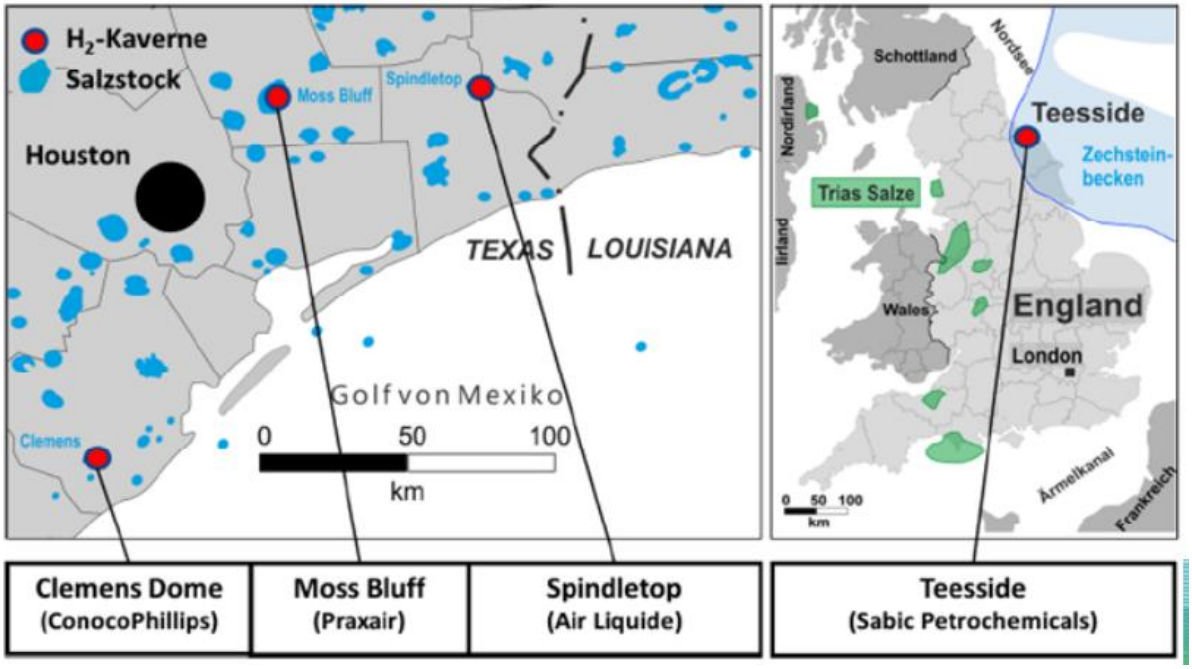

Fig 1.6: Geographical repartition of the four main sites for hydrogen storage in salt caverns (Storengy)

Henceforth, the capacity and number of hydrogen underground storage facilities have considerably grown in the last decades especially in the northern hemisphere. The number of facilities reached 642 by January 2010 where mostly situated in depleted reservoirs of oil and gas (476), then in aquifers (82) and in salt caverns (76) (Tarkowski, 2019).

In north America, there is 399 facilities in USA and 50 in Canada. Europe is considered the second place with 130 facilities. The common Commonwealth of Independent States 50 facility , Asia and Oceania 12 and one in Argentina (Tarkowski, 2019).

In Poland, the storage potential in salt caverns is evaluated up to 7 of 27 analyzed salt domes were found to be favorable (Tarkowski, 2019). In Germany, estimated hydrogen storage capacity in three regions (northern North-Rhine Westphalia, northwestern Germany and central Germany) is 26.5 TWh H_2 in total. At Kiel, town gas with up to 60% hydrogen has been stored in a salt cavern with the volume of 32 000 m^3 (Schiebahn et al., 2015). For storage in depleted oil and gas reservoirs or in aquifers, the examples are few. Many of the projects are still under experiment or pilot projects. Others are small size projects for industrial purposes. Several examples of underground storage of hydrogen in the world are given in Tab 1.1.

Tab 1. 1: Examples of underground storage of hydrogen worldwide in aquifers or depleted oil and gas reservoirs

Storage	Type of storage	Rock Geology	Depth	Date	Usage	Hydrogen purity	Pressure	Capacity
Kiel Germany Hypothetical site (pilot)	Aquifer	Rhaetian deposits of the upper Triassic: Sandstone layers with intermediate shale layers	1335 m	Since 1971	92 Gwh for electricity	62%	80-100w bar	32000 m3
Ketzin Germany (pilot)	Saline Aquifer	Triassic Stuttgart Formation Sandy channel facies	200-250m	Since 1964	NA	62%	NA	NA
Beynes (GDF) France (successful)	Aquifer	Lower Cretacious/Upper Jurassic layers of sandstone (anticline trap)	430 m	nearly 20 years	for refinery needs	50_60% the rest is Natgas	NA	1.185 millions sm3
Lobodice Czech (local)	Aquifer	Lower Miocene (Carpathian) heterogeneous gravels and sandstone	400-500 m	Since 1960	for surplus coke gas from Ostrava area	15-50% (15-50% of CH4 and other traces of CO,C,N)	45-59 bar	400 millions sm3
Kasimovskoi Russia	Aquifer	Na	NA	NA	NA	NA	NA	18000 million sm3
Hychico Argentina (successful)	Depleted gas reservoirs	sandstone	600–800 m	2015	24.6 Gwh for electricity	pure Hydrogen	10 bar	NA
Sun Storage Austria	Depleted gas reservoirs	upper Austrian Molasse basin, Hall formation, sandstone with conglomerates intercalations	1022m	since 2013-2017	power to gas seasonal storage by sun/wind electrolysis 92,000 GWh for urban heating facilities	mixture of Hydrogen and Methane	100 bar	> 8 billion m^3

1.6. Objectives of the thesis

This thesis focuses on the evaluation of the thermo-hydro–chemo–mechanical behavior of underground hydrogen storage in salt caverns and aquifers rocks and risk assessment of gas leakage and alteration. Part of this research was carried out within the Rostock-H project which aim is to analyze the techno-economic, regulatory and social conditions for the deployment of hydrogen underground storage technology (UHS) in salt cavities in France and Europe. The project is funded by ANR (Agence Nationale de Recherche, France) through the scientific Interest Group Géodenergies (Géodénergies, 2016). Additional PhD funding was provided by the regional council of Lorraine.

First part of our mission is to characterize the complex relation between permeability and damage evolution during mechanical loading of rock salt. For this purpose, we will perform a complete set of laboratory experiments on a rock salt specimen to study the permeability evolution under different kind of loading conditions. First, the initial microstructure of rock salt will be identified with different porosity methods and with X-ray 3D tomography, thus allowing the determination of voids (pores and cracks) proportion at different scales. Then, different short-term mechanical tests (hydrostatic compression tests, uniaxial and triaxial compression tests, uniaxial compression test with ultrasonic P and S-wave velocities measurement) will be performed on large core samples to characterize the poromechanical behaviour (deformation mechanisms, elastic properties, Biot's coefficient) of our rock salt specimen. Gas (helium) permeability measurements will be carried out at different stress levels to analyse the impact of the deformation mechanisms on the permeability evolution, and at different gas pressure to characterize the slippage effect and obtain the real intrinsic permeability of rock salt at low gas pressures. The impact of mechanical fatigue, under dynamic/cyclic triaxial loading and static triaxial loading (creep test), and cyclic thermal fatigue on rock salt permeability will be also analysed. Experiments will be conducted on analog sample: the MDPA salt. Salt specimens were taken at 530 m depth in the salt bed of the Alsace potash mines in the East region of France (Stocamine site for ultimate waste storage). It belongs to the Sannoisian-Oligocene (Cenozoic) geological stage. This layer is a powerful saline series located under a collapsed potash bed. This salt rock is considered as a natural analogue of salt caverns used for in situ H_2 storage.

The second part concerns the storage in aquifers or depleted oil and gas reservoirs. The aim is to identify the main microbial phenomena able to alter the stored H_2 resource and quantify this mechanism. Indeed, bacterial activity is susceptible to produce other gases (e.g., H_2S) by consuming H_2. This will be performed by percolation tests (i.e., flow-through tests in a triaxial mechanical cell) on partially saturated cylindrical samples with the presence of hydrogenotrophic bacteria in order to evaluate the bacterial processes likely to promote the degradation of H_2. An experimental apparatus will be built up to serve as proof of concept of the significance of biological activity in pressure and temperature conditions of aquifer storage. Experiments will be conducted on samples of Vosges sandstone, selected as representative reservoir rock.

Thus, after this first introductive chapter about the general context of PhD thesis, the manuscript is organized as follows:

- **Part 1** is devoted to the study of UHS in salt caverns. We start in ***Chapter 2*** with a general review about the nature of rock salt as a polycrystalline mixture and its rheological behavior as visco-elastoplastic material. This review details the mechanical properties of salt including healing and the creep deformation. It also presents the experimental works achieved in the literature to follow the evolution of permeability with respect to the damage of rock salt induced by short-term, long-term and cyclic thermo-mechanical loading. The properties of rock salt as a porous medium (gas flow and poromechanical properties) are also discussed. Then, the experimental methodology proposed in this thesis and obtained results on the evolution of gas permeability of rock salt under different loading conditions are presented in ***Chapter 3*** in the form of a scientific paper (*D. Grgic, F. Al Sahyouni, F. Golfier, M. Moumni, L. Schoumacker, 2021. Evolution of gas permeability of rock salt under different loading conditions and implications on the underground hydrogen storage in salt caverns. Rock Mechanics and Rock Engineering, submitted July 2021*). A preliminary conclusion and the implications of this work for storage in salt cavern is given in ***Chapter 4***.
- **Part 2** focuses on the underground hydrogen in porous rock of aquifers and depleted oil and gas reservoirs. First, I give in ***Chapter 5*** a general review about the geochemical reactivity of gas and fluids in reservoir pore space and the multiphase behavior and fluid flow in such porous network. Basic concepts are reminded such as solubility, diffusivity, thermodynamical and redox-potential of hydrogen influencing the behavior of hydrogen in the subsurface and biogeochemical reactions. An emphasis is given to biotic interactions of the microorganism's communities in the subsurface responsible for hydrogen alteration or conversion influencing the stock of gas at the field scale. Then, **Chapter 6** presents the experimental

methods and material used to conceive a new experimental setup in order to simulate the biogeochemical activity in representative conditions (P, T) of aquifer storage. This new experimental approach combines flow-through tests in triaxial compression cell with geochemical analytical methods to trace and quantify the biological processes of hydrogen conversion and alteration. Results are discussed in the light of our current knowledge and experimental apparatus limitations. A preliminary conclusion on the significance of this work for aquifer storage of hydrogen is discussed in ***Chapter 7***.

- Finally, ***Chapter 8*** gives a general conclusion and the perspectives of this work with the implications in terms of risk assessment for hydrogen storage in salt cavern and porous rock.

-
-

-

II – Hydrogen storage in salt caverns

2. State-of-art

2.1. Rock salt a polycrystalline material

2.1.1. Salt rock structure and mineralogy

Rock salt or halite belongs to the sedimentary family of evaporites. In general, evaporites are composed of minerals deposited by solar evaporation of saline solutions. Those deposits can be either marine or continental. Structurally, rock salt is found as bedded salt layers due to cyclic sedimentary deposits of evaporites. This might be due to eustatic sea level variation, or basin tectonic events. Under high temperature and pressure of burial, salt layers structurally deform into salt domes by holokinesiss process. They present more fractures than the bedded salt because of the mechanical stresses. Salt domes are thicker but less extent than the bedded salt (Gloyna & Reynolds, 1961). Halite is the next mineral in abundance in the evaporite deposits, after the gypsum and anhydrite (the calcium sulfate rock), followed by the potash salts, sylvite, satellite, langbeinite, polyhalite, and kainite, and the magnesium sulfate, and kieserite (Boggs Jr, 2014). Rock salt is dominantly composed of halite crystals (NaCl) henceforth the name. The mineral is formed, presumably, in shallow isolated water. Deposits can reach 1000m of thickness (Boggs Jr, 2014). They are often constituted of pure homogeneous salt and protected by a sealing cap, made of different layers of evaporites, calcite and anhydrite. However, bedded salt can present salt heterogeneity and interlayers of different lithology. It might contain fluid intrusions in grain boundaries (GBS) that has a major role in permeability and the recrystallization (Roedder, 1984; Urai et al., 1987; Cosenza et al., 1999; Schoenherr et al., 2007).

The salt has visco-elasto-plastic properties mainly influenced by its polycrystalline composition (for example in Fig 2. 1). Some of the minerals are:

- ***Halite (NaCl):*** presents in two forms in the halitic dominant lithofacies: a milky form and a clear form. Milky halite is a crystal of a diameter going from millimeter to centimeter, xenomorph to subautomorphic. Anhydrite and calcite microcrystals are sometimes embedded inside. The milky appearance is due to the light scattering by fluid inclusions concentrated in large numbers in this crystal in the growth bands. On the other hand, the limpid clear halite is present as pure transparent crystals of centimeter size in the phenoblastic salt lithofacies and millimeters in other facies. Fluid inclusions in this crystal are scarce and most of the time absent.

- ***Calcium sulphate:*** or also called anhydrite or gypsum, occurs mainly as isolated nodules dispersed between halite crystals or in clay–carbonate matrix. The texture of these nodules is enterolihitic or mosaic. Another form of anhydrite is also found as inclusions in halite crystals and at grain boundaries (GBS) as a major constituent of the matrix in phenoblastic salt. In addition, celestine (strontium sulfate) crystals are present at some levels.

- ***Carbonates (calcite, dolomite)*** are generally isolated in the micritic matrix of clay-carbonate passages. The various forms in which calcite occurs are:
    - automorphic phenocrysts on the edge of halite crystals or in the halite inclusion
    - sparitis in gypsum pseudomorphosis,
    - micrite, the carbonate lime mud

- ***Clay phase and silica:*** different varieties of silica (chalcedony, quartz) were observed in clay-carbonate passages. Silica occurs mainly in fibrous forms (quartzine and lutecite) or other forms: petaloid, palisade, or pseudocubic quartz. The clay phase includes mainly illite, kaolinite, chlorite, chlorite, illite - smectite interlayers.

The assembly of these minerals and their presence in different habits leads to many halitic lithofacies (e.g., lithofacies of phenoblastic salt) of different texture and composition. They also influence the rheological behavior of salt under stress or any damage process (Van Hasselt, 1991; Pouya, 1991; Cosenza, 1996).

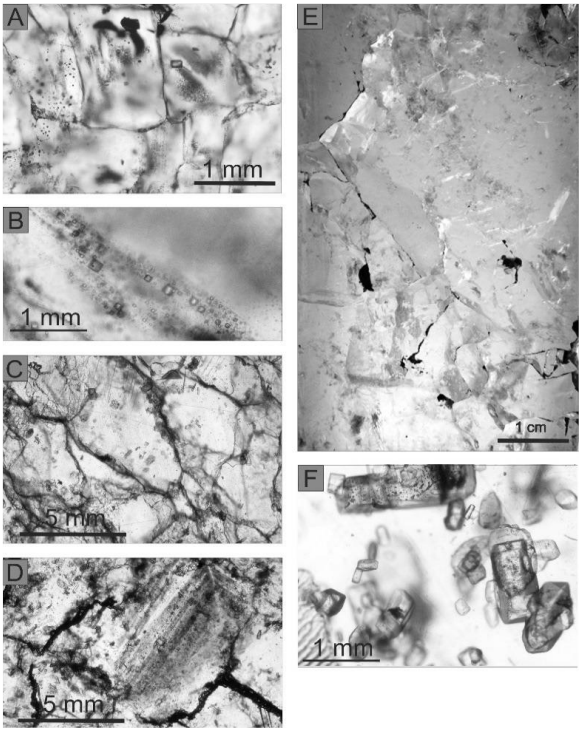

Fig 2. 1: Petrography of polish Zeichstein rock salt samples Fine-grained rock salt from the MSD. Different shapes and size of halite grains with dark shades and spots related to inclusion and impurities of carbonates, anhydrite and clay. Available from: https://www.researchgate.net/publication/283018575_Laboratory_investigations_of_geotechnical_properties_of_rock_salt_in_Polish_salt_deposits [accessed Jan 03 2022].

2.1.2. Structure and mechanical properties of halite mineral

2.1.2.1. The halite NaCl crystal

Halite (NaCl) crystal is an ionic structure that crystallizes in a face-centered cubic-type network. The NaCl lattice consists of two cubic sub-lattices, one formed by positive Na^+ ions and the other by opposing Cl^- ions; the existence of sub-networks defines the preferred orientation of sliding planes in case of deformation (Thorel, 1994). In monoatomic crystals, dislocations occur in lattice cleavages planes of low energy, depending only on the interatomic distance. For the ionic single crystal of halite (NaCl) the dislocation movement in a given direction depends on the nature of the ion they might encounter and the energy emitted. At higher temperature other sliding systems activate the dislocations (Pouya, 1991).

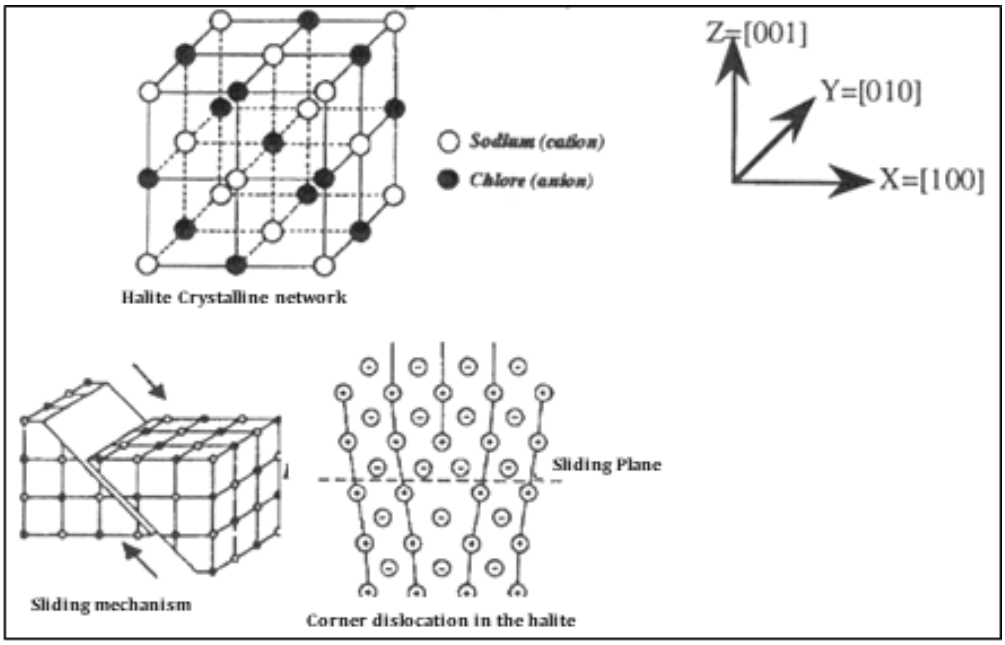

Fig 2. 2: NaCl crystal lattice and preferential sliding plane (after Horseman and Passaris, 1984 cited by Thorel, 1994).

The main sliding systems or mechanisms of deformation defined for the NaCl crystal are dodecahedral, octahedral and cubic, characterized by their normal planes and the sliding direction (Fig 2.2). These deformations are activated by deviatoric stress changing the elastic properties of the monocrystal (Fig 2.3). Temperature effect and confinement pressure also influence the stress-stain curve (Thorel, 1994).

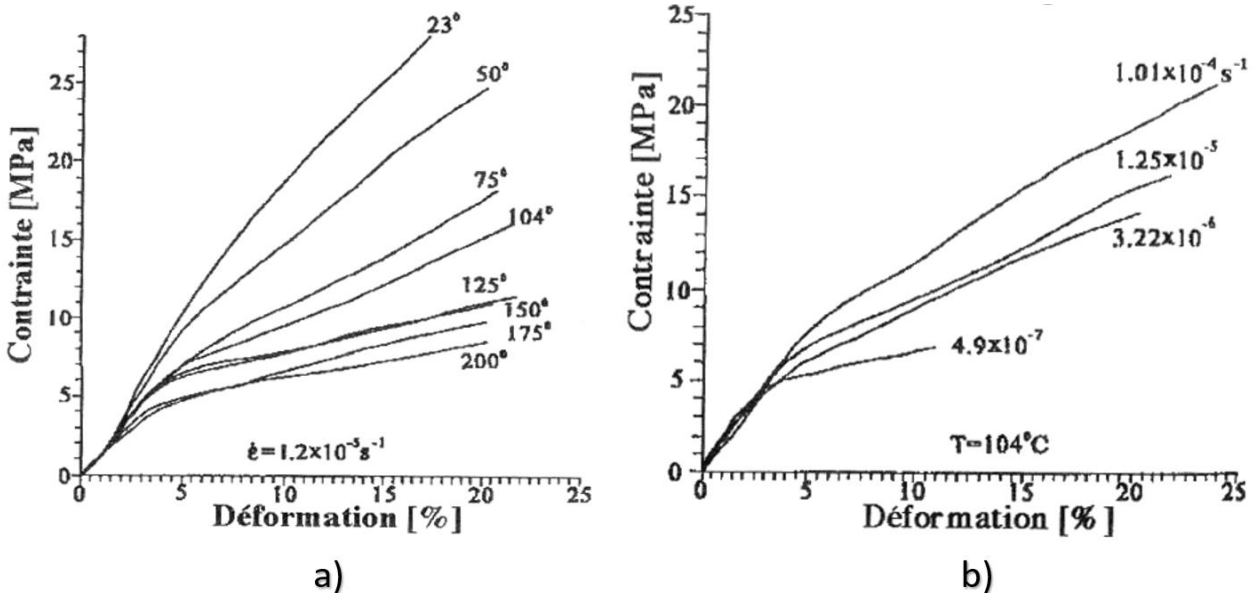

Fig 2. 3: Influence of the loading rate (a) and the temperature (b) on the behavior in uniaxial compression of the NaCl monocrystal (after Wanten et al., 1993, cited by Thorel, 1994).

There are four textural elements characterizing the halite crystal and so the rheological behavior: fluid inclusion, beds and chevrons, granularity and crystal joints (Thorel, 1994).

2.1.2.2. Inclusions

Inclusions can be of two types: fluid or rigid. Fluid inclusions, of primary or secondary diagenesis are located inside the halite crystals (intragranular) or at grain boundaries (Intergranular, Roedder, 1984). Fluid intergranular halite inclusions (Fig 2.4) are of three forms (Schoenherr et al., 2007):

- very irregular with elongated bands, often limited by curved faces (convex/concave);
- cubic shape, most of it edges slightly rounded resulting from the recovery process of cracks, present mainly in partly healed boundaries.
- rounded of small size or slightly curved surface distributed in the same planes mainly resulting from the healing process of the cleavage plane present in certain grain boundaries in droplet shape or small interconnected channels or tubes.

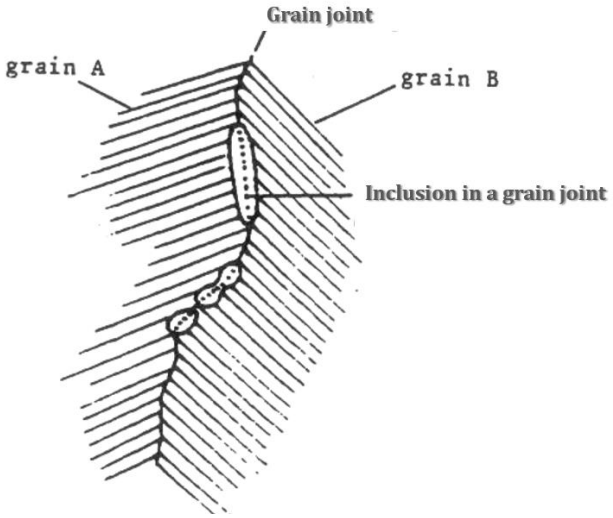

Fig 2. 4:Chematic representation of the morphology of intergranular inclusions (after van Hasselt, 1991, Thorel 1994).

The rigid inclusions found in halite are anhydrites with often millimetric size. More complex rigid inclusions are formed by aggregates of particles of a carbonate or clay - carbonate nature with anhydrite particles. The presence of these inhomogeneity affects the salt rheology but are considered as secondary inclusions (Thorel, 1994b).

2.1.2.3. Chevrons and beds

Beds and chevrons are textural elements in sections of "fish scales" arrangement presenting rhythmic alternations of successive layers with and without fluid inclusions. The presence of chevrons gives anisotropy to the milky salt (Thorel, 1994b).

2.1.2.4. Granularity

The granularity obtained from grinding the rock to it finest grains does not vary from one sample to another for the same facies. But because of excavation, some grains may present cleavage planes but cannot be considered as effective artefacts (Van Hasselt, 1991).

2.1.2.5. Crystal joints

Grain joints or grain boundaries (GBS) are multicrystalline scale textural elements, characterized by their content or the nature of neighboring grains. They may contain impurities, fluid inclusions or a continuous fluid film. Their appearance depends on the grains dispersion in crystalline network. GBS that limit the milky halite are often irregular due to crystal growth and dissolution. The clear halite which is cemented between the grains follows the pre-existing contours, the cementing ranges often being of limited extension with regular and clear contacts. The clear halite crystal patches located in the milky halite can also result from recrystallization after local dissolution in this case the contours are much smoother. The phenocrystal halite present generally very clear and flatten contours (Thorel, 1994b).

2.2. Rock salt mechanical properties and behavior

2.2.1. Salt crystal deformation types

The deformation of rock salt is governed by several mechanisms based on the temperature, the hydrostatic pressure, the deviatoric stress and the presence of brine (Langer, 1991; Munson & Dawson, 1981; Spiers et al., 1986). There are three types of salt strain deformations:

- intracrystalline deformations;
- intercrystalline deformations by dissolution - crystallization;
- brittle or cataclastic deformations

2.2.1.1. *Intracrystalline deformations*

Intracrystalline deformations are characterized by crystal distortion changing slightly the rock volume. These deformations are very sensitive to temperature. Distortions follow three stages according to creep experiments on salt of (Van Hasselt, 1991):

- sliding of a crystalline plane over one another. Simultaneously, the present fluid or solid inclusion of the mineral deforms.
- creation of new sliding planes
- migration of dislocations

The importance of these deformations is influenced by salt texture and mineralogy (Pouya, 1991; Van Hasselt, 1991). Previous work on Bresse salt showed that samples exhibiting a milky pure facies had a higher straining ability (up to 99%) than samples showing a phenoblastic heterogeneous facies embedding impurities. Fluid inclusions of brine (NaCl) generate wider and free dislocation mobility, increasing the plasticity of the crystal and the creep ability of salt. On the contrary, solid inclusions, usually, anhydrite, are less deformable than the halite phase and, unlike fluid inclusions, will make the rock salt less ductile and more brittle. However, this property of inclusions

depends on the crystal size: if size increases, the resistance of the salt to deformation decreases (Van Hasselt, 1991).

2.2.1.2. Intercrystalline deformations by dissolution-recrystallization

These types of deformations take place by transfer of brine solution, generally from areas of high stress to areas of low stress (Cosenza, 1996). It happens in three stages: dissolution of salt, transportation of brine through crystal joints and finally the solution deposition and recrystallization. This deformation is very common in rock salt, but it happens to be more controlled by brine diffusion than the kinetics of the chemical reaction of salt dissolution at the grain-brine interface (Spiers et al., 1986). At microscopic sale, the observation of stylolitization at the grain boundaries containing fluid inclusion is an evidence of this phenomenon. It is mostly observed during creep tests, so time effect is an important factor to its occurrence (Chemin, 1990; Ghazali, 1995). In MDPA salt, recrystallization features were not observed maybe due to the rarity of fluid diffusion and inclusion between joints (Thorel, 1994b).

2.2.1.3. Brittle or cataclastic deformations

It corresponds to the damage mechanism defined as "the action to degrade the material from its cohesive initial state, by a stress exerted in a certain monotony over the matter, leading to a volumetric crack or rupture" (Lemaitre & Chaboche, 1978). Cataclastic or brittle deformation is the progressive deterioration generating fractures. This type is frequent in presence of anhidritic impurities. Cracks observed during damage are more abundant at heterogeneous phase joints (Van Hasselt, 1991). They appear under high loading stress in a very short-time.

2.2.2. Salt mechanical properties evolution under instantaneous loading

2.2.2.1. General description

The rock salt mechanics is studied along two axes: instantaneous loading and time dependent loading. This part will focus on the mechanism of the instantaneous damage by compression tests with the evolution of microckracks until failure, i.e, the occurrence of a macroscopic fracture (Thorel, 1994). All elasto-plastic material under instantaneous deviatoric stress compacts then dilates. The two domains are separated by the contractance-dilatancy boundary at which point there is a minimum or zero volumetric straining (Cristescu & Hunsche, 1998). Dilatancy corresponds to cracks nucleation prior to their development into a fracture. The synthesis of the results of the experimental tests in uniaxial and triaxial compression shows a similar mechanical behavior for different salts with some exceptions related to the rock composition and damage state. Hereafter, when possible, we will focus more specifically on behavior of MDPA salt which is the rock salt material used in our experiments.

According to Thorel (1994), uniaxial compressive strength of salt varies between 18 MPa and 30 MPa depending on its purity and the sample state of damage. Strength is defined as the ability of the material to endure maximum load without cracking or excessive strain in a short term. For triaxial tests, in presence of confinement pressure, the compressive strength strongly depends on the hydrostatic pressure level. For confinement pressures up to 60 MPa, Thorel observed an increase in samples ductility. The stress–strain curves exhibited during the first deviatoric phase a short linear phase where a reversible elastic straining occurs. At a certain level of stress, a beginning of a volumetric expansion is detected due to microcraking. Cracks are parallel to the axis of the sample. In the case of MDPA salt, it is difficult to identify the threshold of contractance– dilatancy. However, the acceleration of dilatancy straining corresponding to the development of irreversible cracks is considered as the threshold. The presence of confinement pressure slows down the reaching of the dilatancy phase. The final shape of the cylindrical sample showed an evolution of quasi-vertical cracks parallel to the axial load, and a deformation in a barrel shape (Fig 2. 5 , Thorel, 1994). The loading stress rate also influences the dilatancy boundary. When rate increases the threshold increases manifested by a clear volume variation (Alkan et al., 2007).

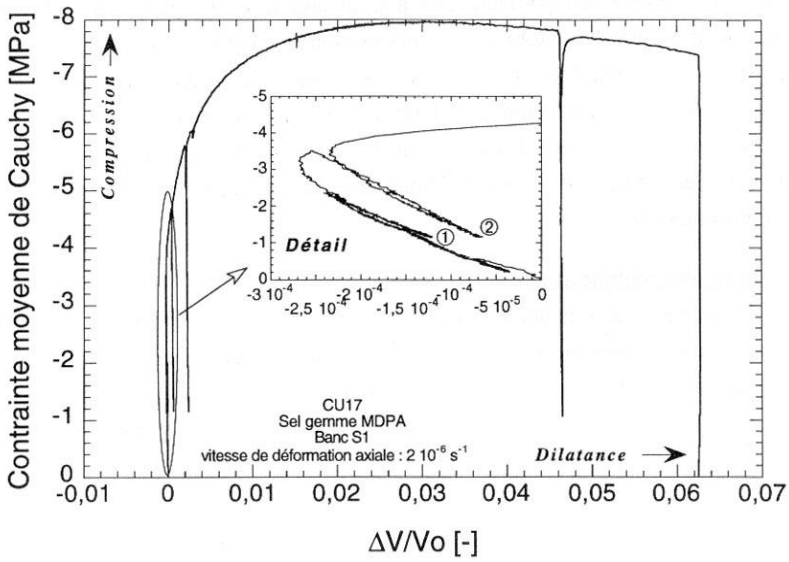

Fig 2. 5:Evolution of deviatoric stress and local volumetric strain with respect to local axial strain on MDPA salt (Thorel, 1994)

Previously to the compression tests, a brazilian tensile test was done also on some MDPA salt samples by Thorel (1994). The value of the tensile strength obtained varies between 0.26 MPa - 1.65 MPa. Also, several axial extension tests were done. Tests show that the response of the deviatoric stress as a function of the strain is monotonic. For confinement pressures up to 60 MPa, strain continues to harden and dilates with no softening at a certain stress peak. The concept of strength used in compression cannot be retained in extension (Thorel, 1994).

2.2.2.2. Elastic properties of rock salt

The dynamic elastic parameters can be determined from acoustic methods; piezoelectric transducers are used to emit compression and shear waves. The velocities of each wave type is related to the properties of the material (Young's modulus E; shear modulus G; Poisson's ratio; Lamé coefficient λ; density ρ Thorel, 1994). The dynamic elastic parameters for the MDPA rock salt are presented in Tab 2. 1.

Tab 2. 1: The mean values of the dynamic elastic parameters of rock salt MPDA (Thorel, 1994)

Material	Young Modulus E_d [GPa]	Shear Modulus G_d [GPa]	Compressibility modulus K_d [GPa]	Poisson Coefficient ν_d
Intact MDPA salt	31.6	12.1	26.3	0.30

For the same rock salt of the MPDAs, the elastic parameters were determined during the deviatoric loading from the tangent of the loading-unloading cycle executed during the test. The Young modulus E is considered as static modulus calculated by assuming the isotropy of the polycrystalline structure (Gevantman & Lorenz, 1981; Thorel, 1994). The static elastic parameters for the rock salt MPDA are presented in Tab 2. 2.

Tab 2. 2: Mean values of the static elastic parameters of MPDA salt obtained during triaxial compression tests (Thorel, 1994)

Material	Young static modulus E [GPa]	Shear modulus G [GPa]	Compressibility modulus K [GPa]	Poisson Coefficient ν
Damaged MDPA salt	14.8	6.3	7.5	0.17

2.2.2.3. Damage evolution under deviatoric stress: dilatancy boundary

Initially, rock salt deforms elastically in the non-dilatant compaction domain. After a short region of pre-existent cracks compaction, grains start to distort elastically, then, shift slightly and slip relative to one another without any accumulation of volumetric straining. No hysteresis is observed on the stress-strain curve if stress is cycled. So dynamic elastic modulus is not yet deteriorated by irreversible straining (Walsh, 1965; W. F. Brace et al., 1966) .
The inelastic increase of the rock salt volume corresponds to the crossing of the dilatancy boundary. It's represented on the stress-volumetric strain curve by the inflexion point from the linear elastic behavior. Elastic modulus starts to decrease with damage. It is characterized by a domination of brittle behavior (W. F. Brace et al.,

1966; Schofield & Wroth, 1968; Schulze et al., 2001; Popp et al., 2001). In the dilatant domain, under deviatoric stress, the development of cracks occurs slowly and progressively. This is what we call the damage mechanism. The differential stress generates a very small volumetric deformation on the scale of a halite monocrystal (dislocations, diffusion, dissolution and recrystallization). However, at the scale of a polycristal, stress activates the sliding mechanisms at the grain interfaces. Energy is concentrated at the cracks boundaries. It allows the widening and growth of microscopic cracks or pre-existing cracks, and the relative displacements of grains and fragments. Dislocations continue to slide under stress until coalescence into a volumetric fracture. The reconnection of cracks is irreversible but not sudden. Consequently, damage profoundly modifies certain properties of the rock (acoustic waves propagation, volume). This can lead to a significant increase in the permeability and as a result, the initial seal of undamaged rock decreases (Thorel & Ghoreychi, 1996). Hence, salt permeability is function of the applied deviatoric stress. In the compaction domain, micro-cracks are closed or even suppressed. Hence, permeability decreases and no failures occur. Also with time, under a high deviatoric stress, microcracks tend to heal because of the domination of compaction regime, due to the ductility property of salt (Spiers et al., 1986; Urai et al., 1987; Looff & Rautman, 2010).

Note that the dilatancy boundary depends only on stress and slightly of loading geometry or rock salt lithology (Schulze et al., 2001). Damage mechanism of salt is highly sensitive to confinement pressure, temperature and loading rate (Thorel & Ghoreychi, 1996). However, in multiple types of salt because of the plasticity, failure is never reached. Cracks instead reach a certain stability with the increase of stress, this is called cracks hardening (W. F. Brace et al., 1966).

2.2.2.4. Plastic evolution under compressive deviatoric stress: the hardening effect

From an energy point of view, strain enters plastic domain whenever the stress exceeds the elastic limit of the irreversible strain. Plasticity is the property of solid bodies to endure irreversible deformations without failure. It happens without loss of pore network cohesion when external forces are canceled. Permanent deformations occur for a stress threshold called plasticity threshold or plastic limit. Plasticity depends on the loading velocity or the strain rate. An increase in the stress rate leads to a decrease in elastic modulus and tensile strength. Consequently, ductility decreases (Thorel, 1994). Different types of strain can be observed (Gramberg & Roest, 1984; Thorel, 1994):

- Pure or perfect plasticity: a permanent plastic deformation “flow” without any fractures or cracks, nor any further increase of volumetric strain.
- Crystalline plasticity: irreversible strain is due to dislocations (atomic shearing in the same crystallographic directions). The local concentration of stress allows the formation of microcracks and volume enhancing (plasto- micro-cataclastic structure), this deformation is very common in pure salt.
- Granular plasticity: A plasticity due to possible irreversible deformations of the granular mass: shear and rotation of some grains in contact with each other might lead to a change in grains disposition and slightly change the volume.
- Cataclastic plasticity: irreversible strain due to internal deformation of the crystal structure; Resulting microcracks and fractures can enhance the volume of the material considerably. The cataclasis is a phenomenon of rock grinding into small angular twisted and dilated particles. An example on a macro-stage is the particular shapes observed in Varangeville salt mine in France for instance. This phenomenon results of severe stress concentration on the rectangular corners of a cavern creating parallel curvy scales.

Hardening is a phenomenon whereby a rock is subjected to plastic deformation at a constant rate and at a given temperature as function of time. Pouya (1991) studied numerically the hardening using two micro-macro approaches: the Kröner model and the Berveiller and Zaoui models. The models show that the simple structure of an orthogonal crystal like halite is highly responsible of the perfect plasticity of a polycrystal system. The behavior is given by their analytical solution under a random radial loading. In the case of NaCl salt, the state of perfect plasticity will never be reached. The energy stored during loading increases indefinitely and therefore the hardening curve will have a positively increasing slope. Permanent strain is due to dislocations shearing (atomic friction in the same crystallographic directions) when external applied stress exceeds the internal resistance stress of the dislocation. The local concentrations of shear stress allow microcracks nucleation and volume variation (plasto-cataclastic structure). So salt responds at a high deviatoric stress in a perfect plastic positive hardening (up to 10% of the strain) which increases with the confinement (Stormont, 1990; Peach, 1991). The hardening curves obtained by (Pouya, 1991) for a salt considering its Poisson's ratio ν_d = 0.25 is represented in (Fig 2. 6).

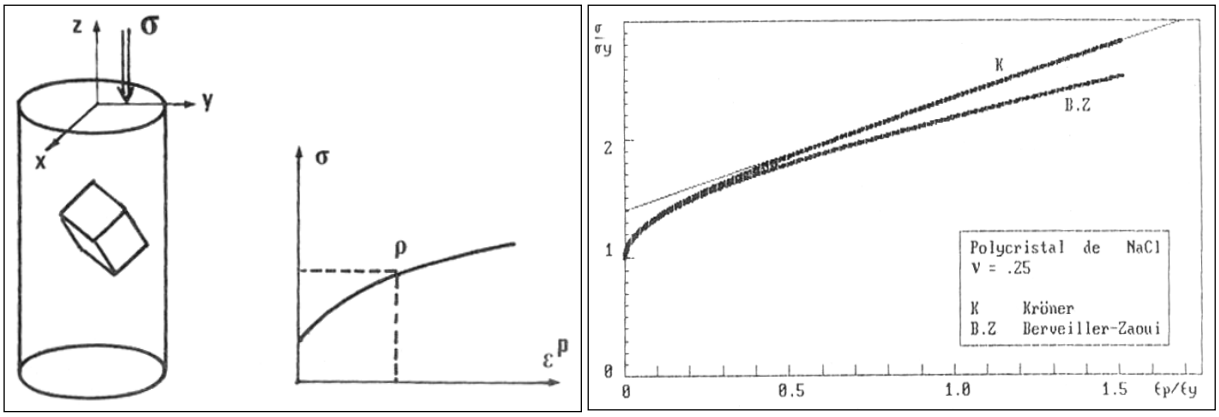

Fig 2. 6:Work hardening curves: a) NaCl polycrystal work hardening curve under monotonic radial loading; b) compression strain hardening curve of the NaCl polycrystal according to the models of Kröner and Berveiller and Zaoui (Pouya, 1991).

Thorel (1994) compared the curve of hardening of the MDPA sal under a confining pressure of 20 MPa to the models of Pouya (1991). The curves obtained were plotted assuming the modulus E = 28008 MPa. Confinement pressure does not change from the curves of theoretical models. The value of the hardening modulus is 13400 MPa for Krôner and 9600 MPa for Berveiller and Zaoui (Pouya, 1991). The test was extended over a longer strain period. The curve reaches an almost linear hardening phase with a very low slope (Fig 2. 7).

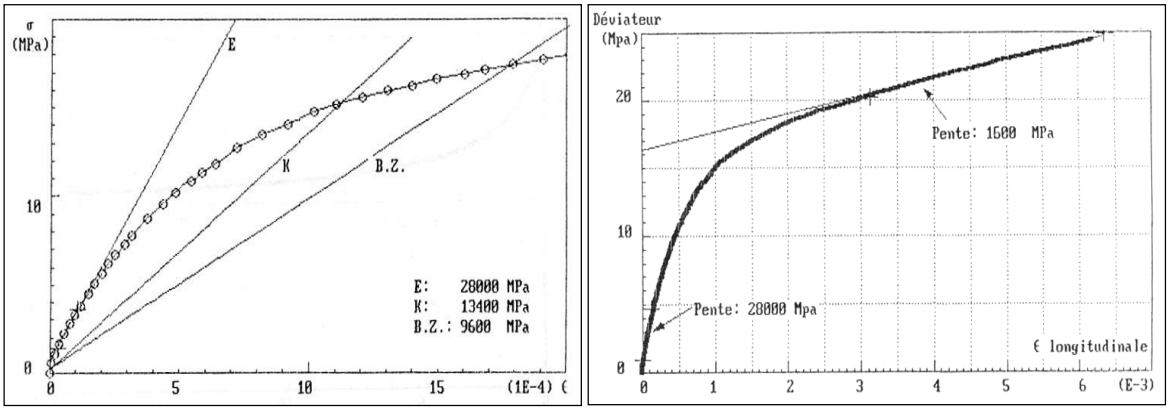

Fig 2. 7: Work hardening curve for salt from MDPA: a) comparison with the asymptotic behaviors of the models: E: elastic; K: Kroner; B.Z. : Berveiller and Zaoui; b) strain hardening curve for a longer strain interval (confining pressure of 20MPa and strain rate 10-5/s) (Pouya, 1991).

By analyzing the resulting curves obtained by (Pouya, 1991, Fig 2. 7), it can be seen that under high confinement pressure, the strain curve shows a peak at a stress of 30 MPa and a strain of 3%. Consequently, cracking is not observed and the only phenomena involved are inter and intragranular hardening of the polycrystalline medium (Pouya, 1991).

Salt damage behavior under compression loading is visco-elastoplastic. The theory of plastic deformation of crystals implies the presence of sliding movements and dislocations along grain contacts. These dislocations are the results of shear stress accumulation at grain boundaries (GBS) between crystals. One of the weak points of the theory of plasticity is the poor knowledge of the lattice structure of undamaged crystals. In fact, higher stress enhances the sliding phenomenon and shear stress accumulation. Taylor (1934) clarifies that strain hardening is an impediment to movement due to the accumulation of shear stresses at new dislocation interaction points at very high deviatoric stress. Dislocations piles up and develop slip planes allowing frictional motion. Creep rate decreases when dislocation increases. Thus, further deformation by creep straining becomes more difficult.

It's important to distinguish between two sliding phenomena: the slip within a planar network of multiple dislocations and a single dislocation. In the first case, slip happens simultaneously among planes on a macroscopic level, while in the latter case slip extends gradually above the sliding line. This linear dislocation constitutes the boundary between two different regions where slip is accelerated or inhibited. It gradually appears within the crystal with stress accumulation. Based on that, Orowan (1940) suggested another hypothesis that relates dislocation activity to the kinetics of the deformation. The concept explains that, in the first stage of the viscoplasticity, when stress increases, sliding motion increases leading to the gradual piling up into saturated bloc

of sliding planes. Straining reaches the yield point despite the continuous increase of the applied stress. Deformed crystals release their internal energy accumulated by the activation of dislocation points. This process is called the recovery. Dislocations slip and climb to reduce their density. This motion increases the friction instead of the shearing and increases the material resistance to strain by hardening. The main difference between slip and climb is that slip depends less on temperature than climb but both result from shear stress accumulation (Grgic, 2016). Those dislocation motions increase the friction and the material resistance to strain (material plasticity, Orowan, 1940).

For moderate stress levels or low confinement stress, the strain is totally reversible when stress is removed. However, after a hardening period, the interaction forces between the piled-up dislocation are sufficient to keep strain permanent. The local stress concentrated in specific region of the rock is larger than the applied stress. So the dislocations resistance to glide is important increasing the plastic strain even at low temperature (Boyko et al., 1997; Grgic, 2016).

2.2.3. Salt mechanical properties under long-term loading

2.2.3.1. General description

The phenomenon of deformation under a constant stress over time is called creep deformation. Creep leads to cavern shrinkage and brine pressure increase in closed space (Wallner et al., 1998).
When a constant axial load, during a uniaxial test or with the presence of confining pressure (triaxial test) is applied to a cylindrical specimen, an instantaneous elastic response is observed followed by a persistent axial strain. Creep curves show three steps of strain with respect to time: transient, steady-state and tertiary phase. The strain rate first decreases (primary or transient creep) and leans to an approximately constant value (secondary or established creep, Fig 2. 8). The rate of straining can remain constant or slow down because of entering into the hardening phase. Steady-state creep refers to constant deformation rate with time under a constant load. Sometimes the accumulation of deformation leads to failure and so a tertiary creep stage occurs where we observe a fracture opening (Duffaut, 2004). These observations were made based on creep models of salt accounting especially, transient and steady-state creep. Models are used to predict the behavior of salt over many years. However, models ignore the fact that geomaterials also dilate and yield plastically (the instantaneous rheological behavior). Therefore, microscopic observations especially at steady-state phase enhance model accuracy. Images show dislocation glide and slide and other structural mechanisms at grain boundaries expected to be dominant during creep (Fuenkajom & Daemen, 1988).

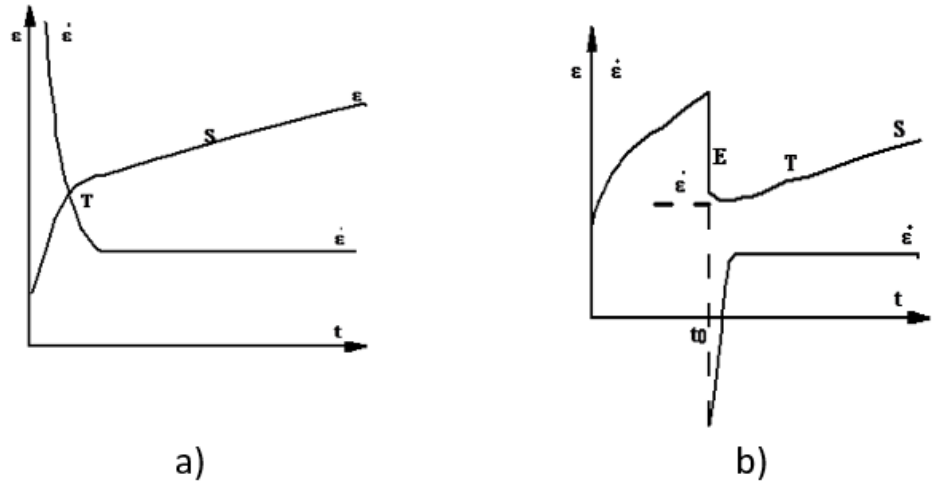

Fig 2. 8: Creep deformation ε and creep deformation rate ε̇ curves: a) Constant loading ; b) Partial unloading at time t0; (E) elastic responses; (T) transient responses and (S) established (Duffaut, 2004).

Measurements of pillar deformation in a cavern for a period of thirty years after the end of operation, have shown a transient deformation characterized by a decrease of damage rate. Slowly, the straining rate reaches a constant value, the secondary creep (Duffaut, 2004). So creep has been the subject of study by many researchers because of its practical importance for structures of cavern construction (Bérest et al., 2005; Duffaut, 2004). The following conclusions can be drawn:

- Over a long term, salt creeps even under a very low deviatoric stress of 0.1 MPa. Without this viscoplastic criterion, that salt behavior is similar to fluid. This explains the frequent existence of geological structural phenomena in salt characterized by very large deformations, such as domes or diapirs.
- The strain rate during secondary creep is a nonlinear function with respect to deviatoric stress, temperature and water content (can remain constant or decrease).
- The stationary or the secondary creep is reached during several weeks or months of constant load application.
- The primary creep or the transitory is associated to a rapid change of the stress. It displays high strain rate at the beginning of load increasing, and decrease progressively to reach the equilibrium state.

Pouya, (1991) studied the creep on large cylindrical samples of Etrez salt (phenoblastic, milky salt). Creep tests were carried out in uniaxial compression, the applied deviatoric stress is between 2.5 - 20 MPa and the temperature between 20 and 200 ° C. Few tests only reached the tertiary creep stage where failure occurs, like the one in Fig 2. 9: a single step test corresponding to a temperature of T = 100 ° C - 200 ° C and σ_3 = 15.3 MPa; we distinguish on the curve the tertiary phase after 1250 hours (Pouya, 1991).

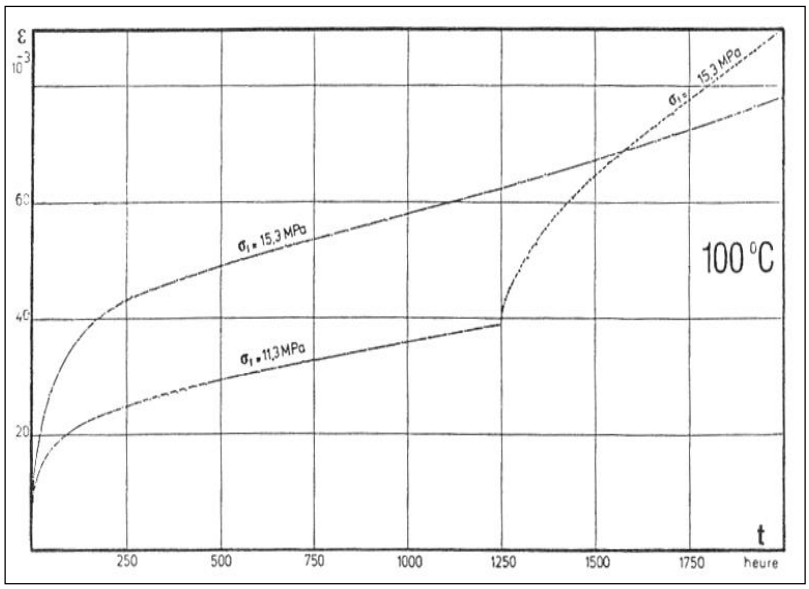

Fig 2. 9:Creep of Bresse salt at 100 -200 ° C (Pouya, 1991)

Rock salt exhibits a complete creep curve during compression tests. However, for extension creep tests on rock salt, the tertiary creep phase is more important due to the low tensile strength of salt inducing fractures at low deviatoric stress (Fig 2. 10).

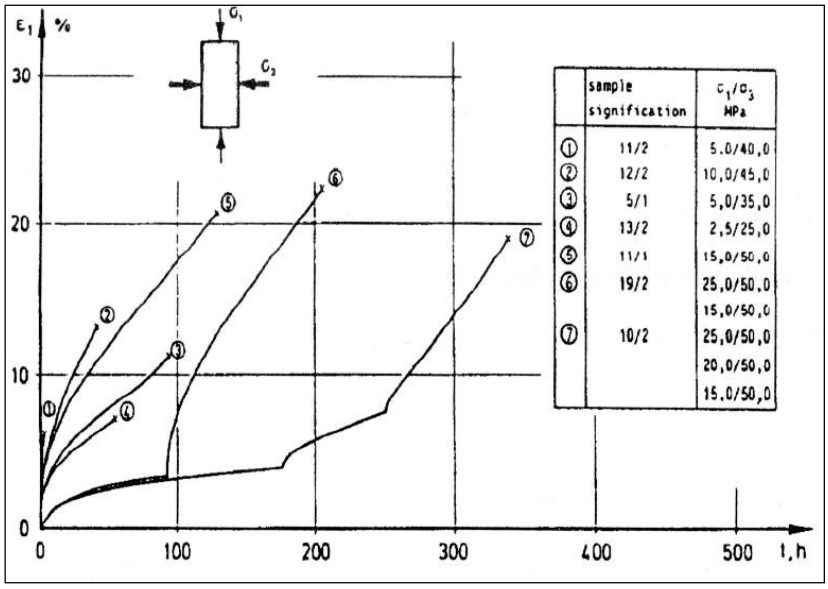

Fig 2. 10:Creep tests on salt sample in extension (Erslev salt - Germany) (Thorel, 1994).

2.2.3.2. Micromechanisms of salt creep

Creep studies carried especially on crystals and on rock salt have shown the process dependence on temperature. For a rock with a given structure (*g*), under conditions of applied stress (σ) and temperature *T*, the creep rate can be expressed by the Arrhenius equation using Δu as the activation energy of the process and *K* the Boltzmann constant:

$$\varepsilon = f(\sigma, T, g) \times e^{-\frac{\Delta u(\sigma, T.g)}{KT}} \qquad (2.\ 1)$$

Generally, during creep σ and *T* are constant, but the structure of grains and also the internal state of the stresses can be modified with strain accumulation and therefore with the creep rate. Different mechanisms integrate to determine the final grains matrix at the end of the creep test: dislocation slip, displacement of a part of the network in a symmetrical position with respect to the mean plane, dislocation, grains rotation, crystallization at the grain boundary (Thorel, 1994).

During the dislocations sliding, crystal lattice remains intact, so the structure does not change. However, under the influence of high strain, a reorganization takes place in the polycrystal structure (Kern, 1977). The dislocation creep can be mathematically analyzed and explained using dislocation theory. Migration and stacking, dislocation rotation, polygonization, subgrain formation, fine grain boundaries migration, void network diffusion, recrystallization are the processes that integrates in the dislocation sliding (Todorescu, 1986).

2.2.3.3. Salt creep characteristics

The differential behavior of rock salt has been studied heavily by numerous authors (Berest et al., 1979; Da Gama, 1979; Fairhurst et al., 1979; Wallner et al., 1998; Langer, 1982; Munson & Dawson, 1981; Cosenza et al., 1999; Schulze et al., 2001a; Mansouri & Ajalloeian, 2018; Bérest et al., 2019).

The micromechanism of creep salt follows three stages: the transient (primary creep), stationary (secondary or constant) and tertiary creep. These laws determine grains deformation (Langer, 1991). At low deviatoric stress and temperature, at the microstructural level, dislocations do not assist in the creep recovery. The creep law follows the logarithmic trend. At high stresses and temperature, the creep mechanism and recovery becomes more apparent in the first stage. At secondary creep (stationary or constant), the rate become constant because the strain hardening process occurs at the same rate as the recovery creep process. The creep movements observed can be grains polygonization, fine grain migration and recrystallization type. Tertiary creep is characterized by the activation of an additional grain deformation by sliding mechanism. This mechanism creates a gradual discord disturbance at the grain boundaries and allows grains separation. Strong creep strains accumulation at GBS leads to fracturing when stress become very close to the strength threshold. The three stages under compression stress are represented in Fig 2. 11.

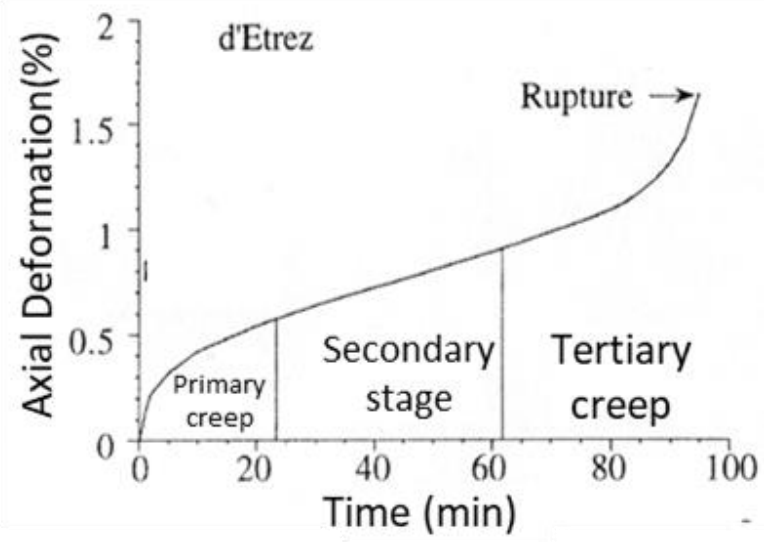

Fig 2. 11:Creep tests on salt samples under compression deviatoric stress

At higher strain rate and high temperature, for a maximum stress σ = 4.5 bar, diffusion creep dominates (Heard, 1972). Two types of diffusion creep are possible: Nabarro - Herring type creep and Coble type creep. Nabarro-Herring diffusion occurs by transporting atoms from crystals to crystal boundaries. Creep strain rate characteristics in this case strongly depend on grains diameter, viscous behavior, temperature, and the absence of transient creep. In Coble-type creep, the scattering movement of voids happens along grain boundaries (Coble, 1963).

Salt creep test under low confinement pressure is described by the Burger viscoelastoplastic model for soft rocks deformation mechanisms especially in the first transient stage and the constant creep (Mansouri et al., 2018). The most important creep deformation mechanisms are dislocation slip, polygonization, diffusion and GBS slip, observed during laboratory experiments. The dislocation slip prevails at high stress and low temperature (relative to the melting temperature of halite Tm = 1074 K = 801 ° C). The deformation increases sharply and enhance dislocations density until the steady-state creep stage is reached (Heard, 1972). Strain rate decreases and enter into a time hardening domain (Haupt, 1991). At moderate deviatoric stress (σ), the steady-state creep rate for salt is typically of order of magnitude $\dot{\varepsilon} = 10^{-10}\ s^{-1}$ (results based on experiments on Varangéville salt in France and Rapid city South Dakota; Bérest et al., 2019) . This type of creep can exhibit an immediate dilation when loading but in some cases, damage is delayed and salt is considered non-dilatant (Spiers et al., 1986; Thorel & Ghoreychi, 1996; Cristescu & Hunsche, 1998; Peach, 1991; Popp et al., 2001; Schultze, 2007). It depends on the salt rheological properties, but also on the magnitude of the deviatoric stress applied during the first stage and the time needed for strain accumulation. Transient stage at low deviatoric stress is longer than perceived and steady-state strain rates for low-stress tests is than reached at higher stress (Bérest et al., 2019).

Due to the limited time of laboratory experiments, grain size and sample machining, diffusion creep is not often identified in experimental results (Hansen et al., 1984; Heard, 1972; Wawersik & Hannum, 1980; Hunsche & Hampel, 1999; Li & Urai, 2016). However, this type of creep mechanism is observed during long term in situ experiments, at low deviatoric stress, especially on coarse grain rocks. Conditions are suitable for fluid-assisted creep and dynamic recrystallization (Bérest et al., 2005, 2019). On the other hand, at high creep stress and due to strain build-up, dislocations in the crystal lattice intensify. Salt shows progressive damage and the development of wings-microcracks. Creep damage reaches the third stage characterized by rapid volume expansion and permeability increase (Munson & Dawson, 1981; Schulze et al., 2001; Berest et al., 1979). For extension creep tests on rock salt, the tertiary creep phase is not always reached. It depends on salt inhomogeneity and the very low tensile strength that leads directly to failure (Thorel, 1994).

Daily room temperature fluctuations can generate thermoelastic strains. Thus, straining is the sum of three components: the thermoelastic strain (ε_{el}), the transient viscoplastic strain (ε_t), and the steady-state viscoplastic strain (ε_s), expressed in one dimensional equation:

$$\dot{\varepsilon} = \frac{\dot{\sigma}}{E} - \alpha_{th}\dot{T} + \dot{\varepsilon}_s + \dot{\varepsilon}_t \qquad (2.2)$$

where contractive strains and compressive stresses are positive, σ is the applied stress, E is Young's modulus, T is the absolute temperature, and α_{th} is the thermal expansion coefficient of salt (Bérest et al., 2019). The increase in temperature triggers a reduction in material strength and an increase in straining but it depends on the mineralogical structure of the rock. Higher temperature leads to higher strain rate. For every 50°C increase in temperature, the strain rate increases up to 1.5–2 orders of magnitude for a certain differential stress level (Li & Urai, 2016). Some authors even believe that the transition from transient creep to secondary creep depends on the temperature according to the logarithmic law of creep with respect to temperature (Thorel, 1994).

2.2.3.4. Salt relaxation processes

Relaxation is the dual property of creep. It also makes possible to follow the evolution of the mechanical properties of material over time. Relaxation is defined as the decrease in deviatoric stress over time under constant deformation. During the relaxation tests the deviatoric stress is released at a certain level, strained material relaxes and reaches a new state of deformation of long-term equilibrium state (Fig 2. 12).

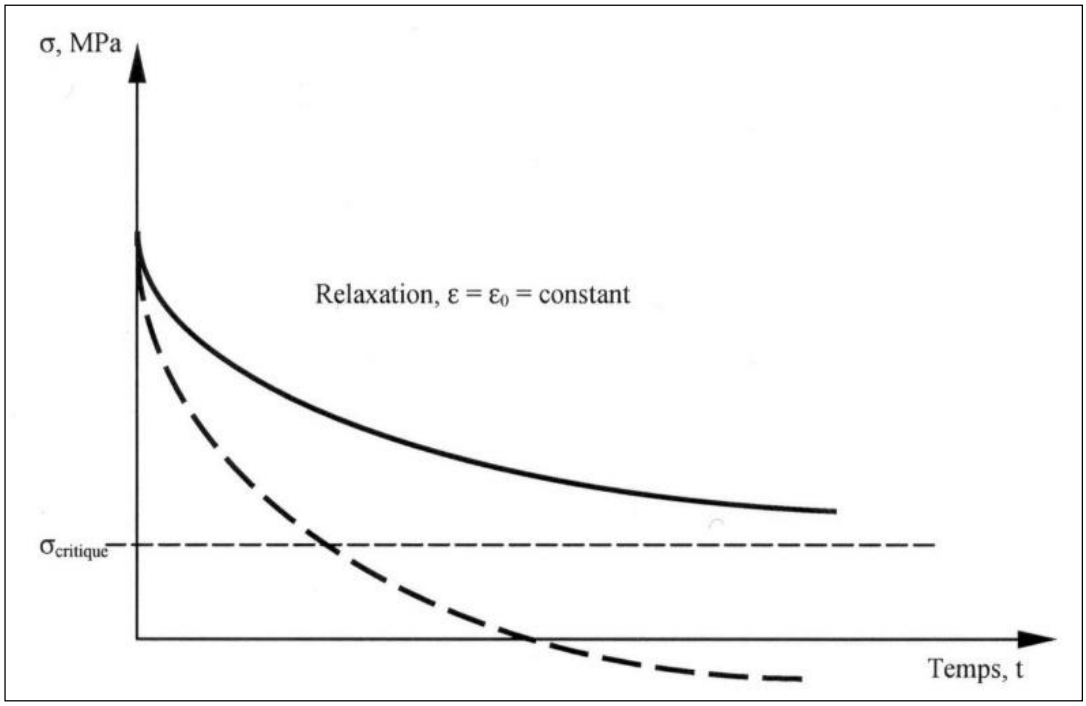

Fig 2. 12:Relaxation phenomenon definition (Maxwell, 1868)

This stress threshold or the critical point of the relaxation curve is considered as the strain rate limit characterizing the relaxation test (Fig 2. 13). For a creep test, under low deviatoric stress, the asymptotic curve tendency is difficult to be determined. Also, if the imposed deviatoric stress exceeds the maximum deviator of the possible quasi - static regime, then the equilibrium is not reached at a long term. So, we will always have an indeterminacy to predict material behavior over a long period. However, in relaxation the long-term asymptotic equilibrium can still be determined in theory and makes it possible to demonstrate the viscosity and hardening of a rock by studying the history of the damage.

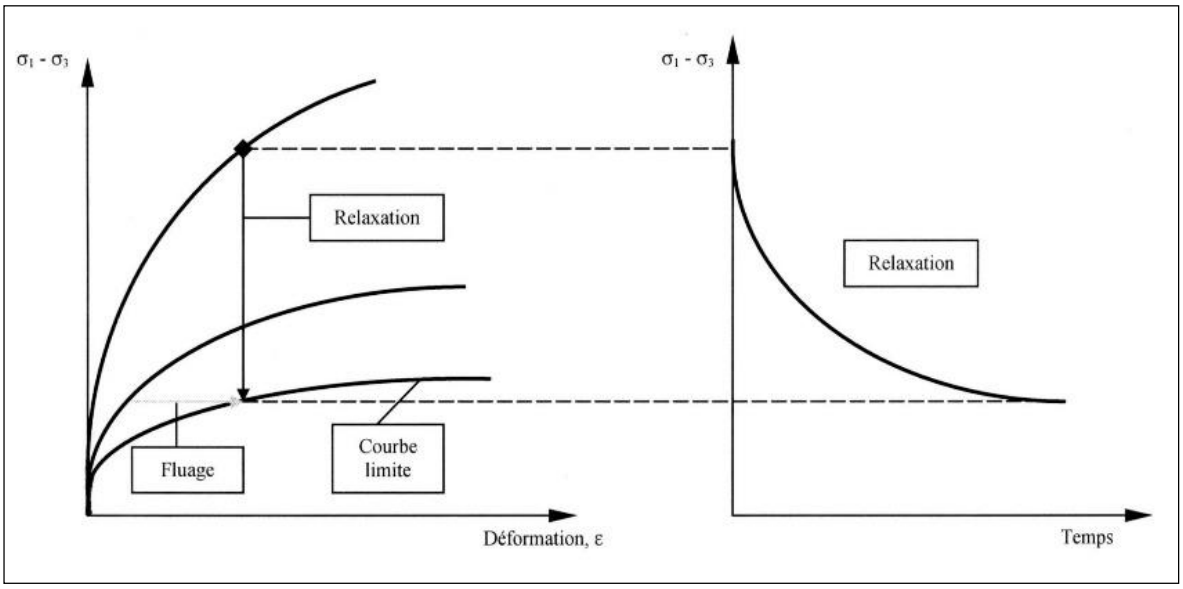

Fig 2. 13:Creep and relaxation schematic representation

Some relaxation tests were executing on salt cylindrical samples of Etrez site and Varangéville salt of France. A triaxial test in extension was executed on the specimen, then, axial pressure was abruptly dropped (Merar, 1999, Fig 2.14 (a)). The obtained relaxation response of the salt was compared according to Lemaître model corresponding to a compression creep test (Fig 2. 14, (b)).

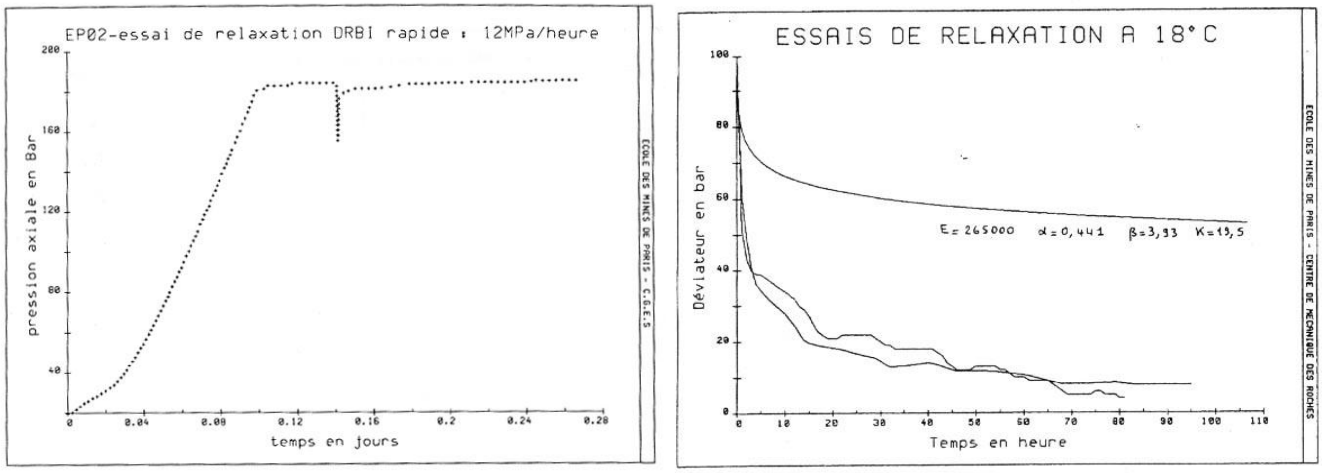

a) b)

Fig 2. 14:Salt under a relaxation test: a) rapid relaxation; b) relaxation in extension by a Lemaître model deduced from a compression creep test (after Merar, 1999).

The evolution of the elastic modulus observed during relaxation test is much lower than during hardening test (instantaneous test under incremental deviatoric stress). So rock salt exhibits a straining over time at various stress level. Deformation considered during instantaneous tests is probably the sum of strain due to instantaneous load and a differential strain (elastic or plastic) (Merar, 1999). So, parameters of the deformation highly depend on test duration in case of salt.

2.3. Salt poromechanical properties

2.3.1. General theory of poroelasticity

Salt caverns stability used for underground storage is highly dependent on the salt permeability to gas and brine. This parameter is coupled with other thermal, mechanical and chemical properties of salt influencing the sealing integrity of cavern (Spiers et al., 1986; Cosenza & Ghoreychi, 1999). Poroelasticity studies the interaction between fluid flow and solids deformation within a linear porous medium. It allows to understand the solid skeleton reaction when introducing a fluid by extending the fundamental concepts of continuum mechanics (elasticity behavior) to continuum poromechanics.

Thus, Biot (1941) worked on the constitutive equations to estimate deformations in porous media structure and in fluid pressure with respect to applied forces and field pressure. Empirical equations were constituted describing in a phenomenological approach the change in total stress, pore pressure, porous structure and fluid volume due to hydrogeomechanical interactions. The medium is assumed to be homogeneous and isotropic. In general, the hydrostatic stress system is the average of three normal stress component of any stress tensor. The mean stress σ is radially constant on hydrostatic conditions following the equation below :

$$\sigma = \sigma_1 + \sigma_2 + \sigma_3 = \frac{1}{3}\sigma_{ii} \qquad (2.3)$$

Biot coefficient "*b*" quantifies the part of the bulk volumetric strain caused by the change in porosity at constant pressure and temperature. It's the fluid volume change induced by the bulk volume deformation of the porous media in drained conditions.

The effective stress law decomposes the mean stress tensor of an elastic porous media into an effective stress tensor and a fluid stress tensor. Fluid introduction into a porous media provoke a body distortion and strength reduction (Jockwer et al., 1992; Schulze et al., 2001).

Biot parameter *b* takes into count this disturbance affecting the mean pressure holding the whole body and creating effective stress σ':

$$\sigma' = \sigma - bp \qquad (2.4)$$

So, pore pressure or fluid pressure reduces the effective mean pressure:

$$\sigma' = \frac{1}{3}\left[(\sigma_1 - p) + (\sigma_2 - p) + (\sigma_3 - p)\right] \qquad (2.5)$$

The first state equation of poroelasticity describing the mean stress state σ disturbance and the volumetric strain ε_v (and it stress tensor ε_{ij}) by fluid introduction is :

$$\sigma = K\varepsilon_v - bp \qquad (2.6)$$

K the skeleton bulk modulus, measures the change in volume with the pressure change. Biot coefficient *b* is so the compatible relationship between skeleton compressibility *K* and solid matrix compressibility expressed by the modulus K_s according to the relation:

$$b = 1 - \frac{K}{K_s} \qquad (2.7)$$

This relationship involves the fluid mass content and the pore pressure in conditions of a fully saturated medium. Under a drained regime, we assume that there is no fluid pressure variation within the rock. Any mechanical disturbance is only provoked by an external stress allowing fluid flow without any change in fluid pressure (Δp=0) but only a change in pores connectivity. So, the stiffness of the porous material is determined by drained bulk modulus of the matrix *K* according to the ratio between the changes in confining pressure ΔPc and the resultant volumetric strain $\Delta\varepsilon_v$ (solid + voids/pores):

$$K = \frac{\Delta Pc}{\Delta\varepsilon_v} \qquad (2.7)$$

In undrained conditions, pore pressure increases without any fluid transfer between pores. So fluid pressure variation can disturb the mean stress state holding the porous network and reduces the hydrostatic pressure (effective pressure). The resultant volumetric strain corresponds to solid matrix deformation and the fluid pressure. So the skeleton modulus K_u can be inferred by the ratio below:

$$K_u = \frac{\Delta P_c}{\Delta\varepsilon_v} \qquad (2.8)$$

Biot coefficient is given by the ratio between the two coefficient according to the equation:

$$b = 1 - \frac{K}{K_s} \qquad (2.9)$$

Or else, based on the poroelasticity theory (equation 2.4), any disturbance of the mean stress induces a change in the volumetric strain. *b* can be also directly calculated as the ratio between volumetric strain induced by pore pressure variation and the one induced by mean stress variation, if a rock was tested under a 2 steps successive incremental pressure:

$$b = \frac{\Delta\varepsilon_v\left[\Delta P = \Delta Pc\right]}{\Delta\varepsilon_v\left[\Delta P\right]} \qquad (2.10)$$

So, Biot's effectives stress coefficient weights the contribution of pore pressure to the load reduction, but it's also a property of the solid and the porous frame only independent of the fluid properties. If the solid matrix is incompressible compared to the skeleton, like in soils, *b* is equal to 1. In the case of rocks, *b* is less than 1. *b* decreases with the decrease of connected porosity and the increase of occluded porosity and small isolated pores

inside the matrix. If *b* tends to 0 this means that coupling between fluid flow properties and the mechanical aspects of the porous media is very small to negligible. The material behaves as non-porous material.

2.3.2. Effective mean stress influence on salt rock mechanical behavior

The influence of effective pressure on the permeability of rock salt has been little treated in the literature. Peach (1991) has shown that the permeability measurements carried out on the Asse salt, under different confinement pressures, can be reproduced with the Walsh model. He observed that any variation in permeability results essentially from a change in the opening of cracks. The author assumed an elastic matrix and a random topography of cracks involved in the flow. He calculated the variation in hydraulic conductivity of a crack under mean stress. This allows him to obtain the evolution of rock permeability induced by cracks connection uniformly distributed in the porous network. The relationship obtained between the permeability k and the mean effective stress σ' can be expressed as:

$$\frac{k}{k_0} = \left[1 - \sqrt{2}\left(\frac{h}{a_0}\right)\ln\left(\frac{\sigma'}{\sigma'_0}\right)\right]^3 \qquad (2.11)$$

where k_0 is cracks permeability, and a_0 mean half-opening diameter of cracks (with respect to the reference effective stress state σ_0'); *h* the square root of the mean of the squares of the distribution of the heights of the indentations on cracks surface. So, the effective mean stress verifies the condition of poroelastic coupling according to Biot coefficient (Eqs. 2.11 and 2.12). During slow hydraulic loading of a sample, the progressive closure of cracks causes a progressive increase in the drained compressibility modulus K_S, inducing a decrease in the Biot coefficient, as shown by the theoretical expression (Equation 2.12). Salt effective compressibility K_S decreases with hydrostatic pressure and reaches a constant value attributable to the residual porosity which remains after the sample was healed (Sutherland & Cave, 1980; Stormont & Daemen, 1992b). So, permeability (*k*) recovery is related to porosity reduction due to cracks closure and both are related to the effective hydrostatic stress by the proportional relationship explicitly explained below:

$$k^y \propto \log \sigma' \qquad (2.12)$$

where y is a constant (y = 1 fitting the salt data) (Walsh, 1965; Stormont & Daemen, 1992). Hence, a risk of enhancing stably the volumetric creep rises at small stress when dilatancy boundary is crossed and stiffness stability of the material is lost. So, this might increase permeability and dilated salt grains will act as flow path for gas (Schulze et al., 2001; Cosenza et al., 1999).

For most of the rock salt , this effect is small or neglected .For example, Biot coefficient for MDPA salt is around 0.1 (relatively small) according to (McTigue, 1986; Cosenza et al., 1999). The coupled effect of pore pressure and mechanical deformation is so insignificant. Nevertheless, sometimes, the fluid presence in pore creates an effective pressure which may affect the cracks interconnection, opening and growth before any external dilatant stress in salt. Alkan et al. (2007) showed from two triaxial tests conducted at different pore pressure that higher pore pressure lowers the dilatancy boundary and speed up the damage initiation and development. He then determined Biot coefficient from triaxial test at different pore pressure and different stress levels. The dilatancy boundary values obtained were used to calculate the averaged normal and octahedral shear stress for Biot coefficient from 0 to 0.5. The value of dilatancy boundary that corresponds to the minimum average standard deviation corresponds to the actual Biot coefficient. It is around 0.25 for Asse rock salt still very low unlike other sedimentary rocks like shale or sandstone (Alkan et al., 2007). Zhang et al. (2020), on a heterogeneous salt sampled in the East of France, measured the volumetric expansion induced by the fluid introduction into the salt at different confinement pressure and different state of damage. Although the values of the coefficients are low and vary from 0.37 to 0.04, they are sensitive to hydrostatic pressure and material damage. This proves that fluid flow only occurs through cracks in salt and so affects the permeability measurements in salt.

On the other hand, poromechanical coupling in salt can be studied over time. Due to salt visco-plastic behavior, Biot and compressibility coefficients may also decrease with creep damage (Zhang et al., 2020). And, in general, poromechanical coupling in salt is tenuous when using gas instead of brine.

2.3.3. Anisotropy/isotropy of rock salt

In general, crystals of salt rocks behave isotropically on large scale because of the large grain size of the halite single crystal and the polyhalite (Gevantman & Lorenz, 1981; Schulze et al., 2001). Overall, phenoblastic salt is isotropic but heterogeneous. Milky salt is characterized by an anisotropy induced by the presence of chevrons. For the mixed milky / limpid salt, a slight anisotropy is noticed due to the mix of both components and also the chevrons presence. The anisotropy is more pronounced in zones of solution-filled with clear halite that have the appearance of " fingers" perpendicular to beds (Thorel, 1994).

Unlike domal salt, salt in beds is characterized by original sedimentary layering which forming interfaces between various evaporitic minerals. Flow in bedded salt occurs mainly in fractures, intercrystalline planes and interfaces. They can have different orientations with respect to the differential stress direction. Various factors such as bonding strength at the interface, flexure caused by differential strength at of the beds interface determine the anisotropic behavior of the various layers under shear stress, and finally the bedding orientation (vertical, horizontal and oblique) to the loading axis. On the other hand, bedding anisotropy can affect also the poromechanical coupling but also on the permeability through boundaries, cracks and space expansion of the interlayers (Gloyna & Reynolds, 1961; Hatzor & Heyman, 1997; Liang et al., 2007, 2012; Muhammad, 2015).On microscale, the secondary mineral deposition of anhydrite, potash, polyhalite and many other present especially in bedded salt behave anisotropically when mechanically loaded (Schulze et al., 2001).

On the other hand, damaged samples are highly anisotropic due to orientation of microfractures (Gloyna & Reynolds, 1961; Jockwer & Wieczorek, 2008; Muhammad, 2015).

2.4. Salt as a tight porous media

2.4.1. Definition of a porous media

A porous material is a persistent solid medium presenting pores (voids) in its structure. Fluids like gas, water or oil can occupy these pores in one sole phase, different separated phases or miscible phases. Some materials are considered porous like sand, others tight like clay or even rock salt (Bear & Bachmat, 2012; Bear, 2013). However, porous medium should be permeable to a certain level and allow fluid to pass by interconnected network. The closed and the internal pores are integrated into the solid matrix (Boulin, 2008; Dullien, 2012). Hydrodynamics in porous media is characterized by the pore space structure, called porosity, and the ease at which fluids between those pores can flow, called permeability. Thus, it's essential to know the petrophysical properties of a rock before studying the fluids residing in the porous space (De Marsily, 2004).

- ***Porosity:*** The shape irregularity of rock minerals doesn't allow a good and solid packing, but permit the display of porous spaces (voids) in the solid matrix of the rock. This void called pores can be occupied by liquids or gases. Thus, the porosity of a reservoir that will be used in this work, is defined as the total volume of void space of the reservoir not occupied by solid components (Donaldson & Tiab, 2004; Boulin, 2008).The equation below explicit this definition:

$$\Phi = \frac{\Omega_e}{\Omega} \qquad (2.13)$$

  where Φ is the porosity, Ω_e the volume of void space present in the rock and Ω the bulk volume of the whole specimen. Two types of porosity exist: the porosity between the granular particles and fissures, and cracks porosity due to tectonic and mechanical damage (Morton-Thompson & Woods, 1993; De Marsily, 2004). Pores are affected by granularity, the shape of grains and the packing (Houpert, 1959; De Marsily, 2004).

- ***Permeability:*** is defined as the ease at which fluid can be transmitted through interconnected pores. So, the permeability of a rock is tightly related to effective porosity or the connectivity of pores. It represents the advective flow of the porous fluids depending only on pressure gradient between the upstream and downstream. In addition, it's also related to the fluid properties and flux properties. Thus, according to (Darcy, 1856), Volumetric flow Q (m^3/s) is expressed in function of dynamic fluid viscosity μ (Pa.s), pressure

gradient ∇p, and intrinsic permeability k (m^2) which is a geometrical value independent from the fluid nature, but related only to pores interconnection, granulometry and lithology of the rock. *k* can be calculated when the pores are only filled with one phase solely:

$$Q = -\frac{k}{\mu}\nabla p \qquad (2.14)$$

2.4.2. Fluid flow dynamics and laws in porous media

2.4.2.1. Advection or permeation concept

Advection is a macroscopic phenomenon of general fluid transport in porous media under the influence of a pressure gradient effect. The fluid viscosity is inversely proportional to pressure. Fluid flow follows the Darcy's law 2.14. The equation relates the fluid flow rate and the pressure gradient (Lefebvre, 2006; Boulin, 2008; De Marsily, 2004; Bear, 2013).

Note that gas viscosity is dependent of the square root of the temperature variation, and less dependent on the pressure variation. In hydrogen case, it varies only by 2% between 1 and 5 bar (Bear, 2013; Loeb, 2004; Boulin, 2008; Didier et al., 2012).

2.4.2.2. Difference between diffusion and dispersion

Diffusion and dispersion are different modes of mass transfer. At microscopic scale, an element of a mixture is transported by convection or diffusion either in liquid phase or gaseous phase. Diffusion is a net movement of each molecule from areas of high partial pressure to areas of low partial pressure. It results in a random motion of elements within the fluid during transportation, while convection motion is driven by flow direction. In the gaseous phase, the total flow of an element is the sum of convective flow and diffusive flow.
If a difference of concentration occurs in the stagnant gas phase mixture, it results into a random dispersive movement of suspended particles due to their collision with the fast-moving molecules in the fluid (friction): Brownian movement. This movement aiming to reduce the concentration gap is called diffusion. Hence, diffusion phenomena are represented by Fick's Law:

$$\vec{N}_i = -D_{i,j}\nabla\left(\frac{\vec{P}_{X_i}}{RT}\right) \qquad (2.15)$$

Where $\vec{N}_i^{\,D}$ the flow vector, $\frac{P_{X_i}}{RT}$ represents the molar concentration of an ideal gas and $D_{i,j}$ the diffusion constant in a binary gaseous mixture in m^2/s controlling the diffusion velocity (Loeb, 2004; Boulin, 2008; Didier et al., 2012). The diffusion coefficient is closely dependent of molarity *M* of the mixture components, inversely proportional to pressure P but directly proportional to temperature T. It's expressed by the equation below, where $\sum \upsilon$ the volume of atomic diffusion (Bird & Stewart, 1960; Fuller et al., 1966; Karaiskakis & Gavril, 2004; Didier et al., 2012):

$$D_{1,2} = \frac{0.00143T^{1.75}\sqrt{\left(1/M_1 + 1/M_2\right)}}{P\left[\left(\Sigma\nu\right)_1^{1/3} + \left(\Sigma\nu\right)_2^{1/3}\right]^2} \qquad (2.16)$$

In porous media, at the macroscopic scale, local changes in velocity within pores and pore to pore generates macroscopic spreading of concentration. This is the so-called dispersion mechanism. Dispersion can be differentiated from diffusion in the sense that it is caused by deviation from pure plug flow.

2.4.2.3. Pore-walls and gas interactions: impact on gas transport and Klinkenberg effect

The ideal gas model of Maxwell assumes that gas molecules are so far apart, that they have collisions with each other creating gas pressure. Reality shows molecules do collide with pore walls too, influencing the velocity of the

flow. Therefore, the mean free path λ is defined as the average distance a gas molecule travels between two successive collisions with other gas during flow expressed by the equation below:

$$\lambda = 3/2 \times \frac{\mu \times \sqrt{\pi RT / 2M}}{p} \qquad (2.17)$$

λ is directly proportional to fluid viscosity and so inversely proportional to mean pore pressure. But, it also depends on gas physical properties such as gas radius R and the average molecular weight M (Present, 1958; Loeb, 2004a; Letham & Bustin, 2016).
The effect of collision with pore walls and molecules with each other's, appears to be very important in nanometric (tight) porous media like in salt and clay. The classical approaches of Darcean gas transport reach their limits. Knudsen, defined a number "*Kn*", describing the diffusion of gas molecules and their collision to pore walls. This number is the ratio of the molecular mean free path *"λ"* to the pore size radius "*r*":

$$K_n = \frac{\lambda}{r} \qquad (2.18)$$

So when Knudsen number is less than 0.01, the flow is considered as continuum conventional to Darcy fluid dynamics. When Knudsen number approaches to 1, the mean free path of gas molecules approaches to pore diameter, and so the continuum Darcy's law of fluid mechanics is no longer a good approximation (Knudsen, 1995). Between these two limit cases, intermediate regimes can be defined. Hence, measured permeability and diffusion type varies with pore size (Freeman, et al., 2011; Li & Sultan , 2016):

Tab 2.3: Flow regimes with respect to Knudsen number range

Kn	0-0.001	0.001-0.1	0.1-3	3-10
Flow regime	Darcy/non-darcy	Slippage	Transition	Free molecular flow

As as example, during slippage regime, the classical Darcy law needs to be modified since the boundary conditions of total adherence of fluids on the pore walls is not verified anymore. Hence, an apparent increase of permeability at macrosopic scale is observed, also known as Klinkenberg effect (Boulin, 2008).

At low pore pressure, indeed, gas permeability calculated according to Darcy's Law in a tight porous media is higher than the water permeability. So, in 1941, Klinkenberg noted a relationship between this pore pressure-dependent permeability, and mean free path of the flowing gas molecules. This relationship represents a process called gas slippage, whereby the interaction of the gas having a non-zero velocity with the pore walls, in the same direction of the flow, contribute apparently to a higher quantity of gas flowing through the pore (Letham & Bustin, 2016). Thus, the more the pores are small, the more the interactions between the molecules and the walls increase while the molecules-molecules interactions decrease. Molecules flow faster by a non-Darcian velocity due to the shocks (Didier et al., 2012). The mean free path of a gas controls slippage effect by the average velocity of gas flow at the pore walls. Slippage effect takes place when a gas with small molecular size and therefore a higher mean free path, flows at low pressure.

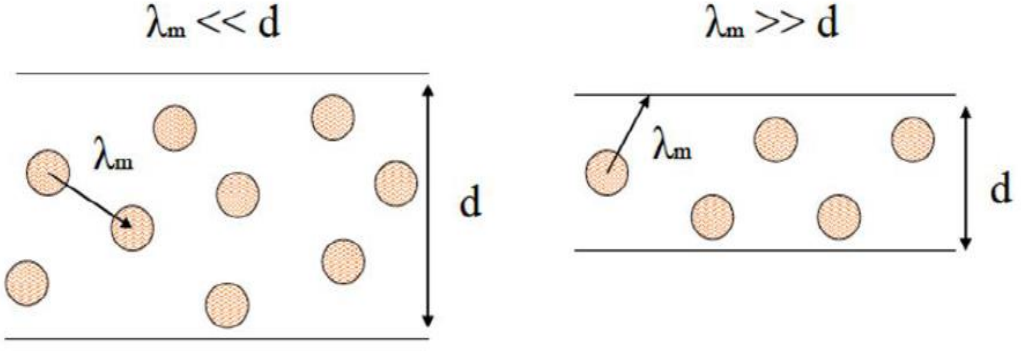

Fig 2. 15:Klinkenberg Effect with respect to the mean free path λ and pore size diameter d (Boulin, 2008)

Darcian law overestimates intrinsic permeability *K* because of the apparent velocity of the flowing gas. Nevertheless, this is less important when the pressure increases because of the average mean free path which decreases with pressure. Then, at infinite pressure, gas behaves as a classic fluid-water for instance- and Klinkenberg effect is negligible. Klinkenberg found the following relationship between the apparent and the intrinsic permeability:

$$K_g = \beta \times K_l \times \frac{1}{P_m} + K_l \qquad (2.19)$$

Where *k* the intrinsic permeability, K_g the apparent gas permeability and β is the Klinkenberg's slippage parameter which quantifies the variation due to slippage. β is related to pore size diameter *d* and gas compressibility by λ (Boulin, 2008):

$$\beta = \frac{\lambda(p = 1Pa)}{d} \qquad (2.20)$$

In practice, in order to find graphically the accurate value of intrinsic permeability, first, apparent permeability is plotted on the y-axis, against the inverse of mean pressure for each pressure gradient on the axis. Then, a linear fit is applied to the data. The intercept of the linear fit with the permeability axis gives the value of the real intrinsic permeability K_l ,where no slippage takes place (Klinkenberg, 1941).

2.4.2.4. Fracture permeability

Fractures are openings in the porous media, created by tectonic movement or mechanical stress causing a failure in the structure. Fractures can enhance permeability in tight rocks like dry clay and salt, if an interconnected network large enough for hydraulic transport. Such a sudden change in the hydraulic behavior would distort the predictions made for intergranular permeability estimations and increases uncertainities.

Fractures can be created by the breakthrough of the fluid transported via an intergranular flow. The flow can increase the stress of the whole sample, reduces surface energy and permits the fissures and cracks creation and evolution. Some materials can easily form fractures by a pressure increase in the rock specimen like in carbonates and evaporites. Other due to chemical dissolution due to water introduction or thermal induced fracturing. However, cracks generation solely, isn't sufficient to maintain a high permeability. It could be sealed with impervious material by a secondary sedimentation. On the other hand, high temperature, moisture and constant pressure overtime can also fracture the rock and change the flow dynamics.

2.4.3. Fluid flow in rock salt reservoir: Gas permeability measurement methods

Salt is considered an unconventional reservoir of gas-tight due to its very low porosity and permeability. This is based on the results of permeability tests executed in situ (Stormont, 1997) or in laboratories (Sutherland & Cave, 1980; Stormont & Daemen, 1992b). As a consequence, salt is a geological seal and a good host for cavernous storage of energy vectors (gas, oil, nuclear waste etc.) (Bredehoeft, 1978; Sutherland & Cave, 1980; Stormont & Daemen, 1992; Stormont, 1997).

Permeability measurement methods are of two types: stationary and non-stationary (Loosveldt, 2002). Usually, for very low permeability medium, the stationary method also called "steady-state method" is widely used but time consuming. It consists of imposing a constant pressure upstream and constant pressure at downstream of a cylindrical core sample under a confining pressure and measuring the flow rate out of the sample in constant conditions in order to determine permeability according to Darcy's law equation (2.14) adequate to a gas in single phase flow (Escoffier et al., 2005; Boulin, 2008).

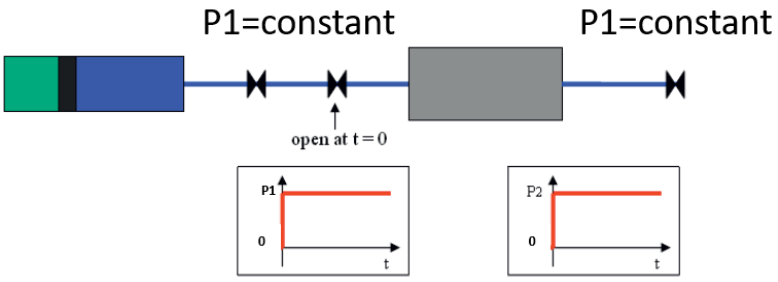

Fig 2. 16: Steady-State Method (edited from (Boulin et al., 2012)

On the other hand, the transient method consists of imposing a sudden rise in pressure in the upstream reservoirs and then recording the pressure evolution at the downstream compartment, to the moment when both reach the equilibrium pressure due to reservoir compressibility. Results interpretation is based on the exponential decrease of pressure from upstream to downstream with time or the kinetics of pressure change (Fig 2. 16, W. Brace et al., 1968; Escoffier et al., 2005; Boulin, 2008).

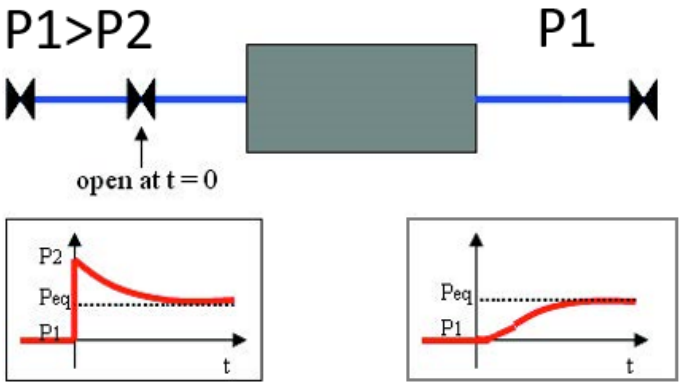

Fig 2. 17:Pulse test concept (cited by (Boulin et al., 2012)

A similar method measures in downstream, the shifting or the decrease in sinusoidal amplitude of imposed (water or gas) pressure (Suri et al., 1997). This method can be used when working around 70 bar of pore pressure and a change of 7 bar during the pulse test. This high pressure minimizes the effect of variations of certain parameters like viscosity and permeability (W. Brace et al., 1968; Boulin, 2008).

Several factors may impact the accuracy of permeability measurements in rock salt. First, in rock salt, especially in bedded salt, we distinguish two zones: the undisturbed zone and the damaged zone. Permeability values delineate the boundaries between both in order to estimate the vulnerable regions for leakage risk. At the large scale of the field, the salt inhomogeneity and texture variability might be also responsible of local disturbances in hydrogeomechanical properties. The change in permeability indicates a deformation in pore structure due to any mechanical or hydraulic stress (Stormont & Daemen, 1992; Stormont, 1997). In general, permeability of undisturbed samples is less than 10^{-20} m^2 (low values). On the microscopic scale, pore structure in this region is basically disconnected voids or some others connected refilled with crystallized brine functioning as sealing for fluid transportation (Stormont, 1990). The minimum measured permeability at low pore pressure is governed by slippage laws because of the small pore size. On the other hand, the disturbed rock zone (DRZ) is adjacent to excavations especially. This zone is subject to dilatancy (volume expansion) of the surrounding rock mass and discontinuous deformations of crystals (separations, fractures, and shear slip , Stormont & Daemen, 1992). Excavation zone disturbs the stress state of the rock media resulting in changing the pore structure. Pores straining and dilation allows gas to come out as the pore pressure decreases more than brine can expand (Borns & Stormont, 1989; Stormont & Daemen, 1992b; Beauheim & Roberts, 2002). DRZ permeability becomes around 10^{-18} $m^{2.}$ Thus, the gas transport mostly occurs in fractures and not between particles in no-slip conditions (Berést et al., 1996; Stormont, 1997; Cosenza et al., 1999; Schulze et al., 2001a). The sample preparation procedures may also be a source of disturbance. The fact of coring samples and rectify their face using rock saw is called “machining” and it is similar to the disturbance by excavations and might disturb the integrity of intrinsic permeability measurements (Sutherland & Cave, 1980). The most important reason for the imperviousness of the salt is the rheological properties, especially the stiffness and ductility related to its texture, structure and mineralogical composition (Wallner et al., 1998; Schulze et al., 2001). For that, two processes are known to increase permeability. The first is micro cracking, related to salt geomechanical properties or the damage disturbance factors (Peach & Spiers, 1996;

Stormont, 1997; Cosenza et al., 1999; Popp et al., 2001). The second process is the formation of connected brine-filled pores and triple-junction tubes in halite grain aggregates at a pressure and temperature corresponding to depths > 3 km (Lewis & Holness, 1996). Because of the importance of this property, the study of the permeability and porosity changes with respect to damage was largely discussed in literature based on experimental and numerical studies. In the table below (Tab 2. 4) we cite some examples:

Tab 2.4: Summary table of some permeability measurements to test salt transport properties in the laboratory and in situ

Transport properties	**Permeability methods**	**Salt origin**	**Reference**
Permeability values: $5{\cdot}10^{-19}$ à $2.3{\cdot}10^{-17}$ m^2 Mean porosity :1.7 %	Steady-state permeability under constant load (17 MPa maximum) (Oil and gas/brine)	Salt dome (depth=213 m) beds (depth=196 m)	(Gloyna & Reynolds, 1961)
Permeability : $8{\cdot}10^{-19}$ à $6{\cdot}10^{-13}$ m^2 Mean porosity : 0.8 à 6 %	Steady-state permeability (5.5 MPa maximum) (oil/gas brine) under confinement	Bedded salt samples extracted from different mines in Canada and the US	(Aufricht & Howard, 1961)
Permeability: $7{\cdot}10^{-18}$ à $3{\cdot}10^{-19}$ m^2 Average porosity : 0.6%	Pulse test under confinement (Pconf= 35 MPa maximum)	Salt beds of WIPP nuclear waste site in the USA of 92% purity (depth=640 m-792 m)	(Sutherland & Cave, 1980)
Permeability of phenoblastic salt $5{\cdot}10^{-19}$ à $5{\cdot}10^{-21}$ m^2 Permeability of milky salt: 10^{-15} – 10^{-18} m^2 Average porosity : 0.5 %	Gas permeability using Argon gas under a confinement pressure of 24 MPa	Bedded salt from the Bresse Basin in France (depth=500m)	(Le Guen, 1991)
Permeability 10^{-21} - $4{\cdot}10^{-18}$ m^2	Argon Pulse Test method under confinement of 20 MPa	Salt dome of 98% purity Asse mine in Germany (Depth=800m)	(Peach, 1991)
Permeability $8{\cdot}10^{-19}$ - $6{\cdot}10^{-13}$ m^2 Average porosity : 0.8 à 6 %	Argon Pulse Test method under confinement of 7.6 MPa	Salt dome of 98% purity Asse mine in Germany (Depth=650 m)	(Stormont & Daemen, 1992b)
Permeability :8.8 10^{-21} m^2 Average porosity : 0.6 %	Argon Pulse Test method under confinement of 21 MPa	MDPA salt at 500m of depth	(Lebrun, 1993)
Permeability :2.10^{-21} m^2	In situ , Brine steady-state method (continuous injection)	MDPA salt at 500m of depth	(Cosenza, 1996)
Permeability: K <10-22 m2	In situ , leakage test , multiple injection of Nitrogen gas at different pressure	Tersanne-France and Etrez (1000m of depth)	(Brouard et al., 2001a)
Permeability 10^{-17} - $4{\cdot}10^{-19}$ m^2	Nitrogen , pulse Transient in lab	Groleben salt dome Zeichstein Germany (depth=200-800m)	(Popp et al., 2001)
Permeability 60.4nD for Helium 50 nD for Nitrogen	Nitrogen, Helium, pulse Transient in lab	salt bed of the first Zechstein cycle (PZ1),Poland (depth=900m)	(Ślizowski et al., 2017)

2.4.4. Mechanical influence on petrophysical properties of salt

2.4.4.1. Hydrostatic effect on permeability: the healing process

Permeability of rock salt is highly dependent of mechanical behavior changes. Confinement is a parameter of strong influence on the macroscopic behavior of the rocks in general. In situ, a buried rock is subjected to the stress exerted by all surroundings in the horizontal plane. The lithostatic gradient is estimated at 22 MPa/Km, so the stress magnitude is related to the rock burial depth. If the pressure is isotropic, it is called the confinement or the hydrostatic pressure (Thorel, 1994). Experiments have shown that when increasing hydrostatic pressure, salt permeability decreases quickly both instantaneously and with time (Peach, 1991; Le Guen, 1991). This irreversible reduction is due to recoverable changes in the pore structure and suture cracks (Gloyna & Reynolds, 1961; Sutherland & Cave, 1980; Le Guen, 1991; Cosenza, 1996). This phenomenon is called the healing process and can occur by three different stages: mechanical, surface energy reduction and recrystallization (Koelemeijer et al., 2012).

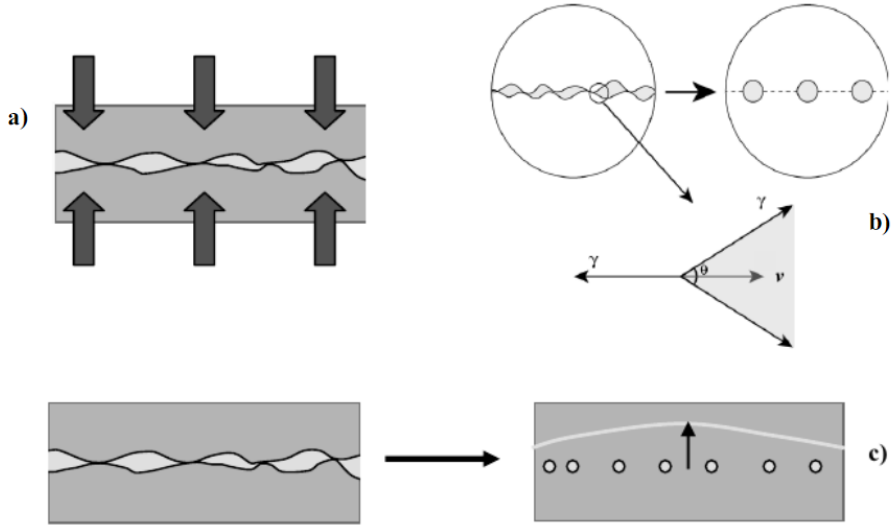

Fig 2. 18:Physical mechanisms of crack healing/sealing and permeability reduction can occur (a) Mechanical closure of cracks by compaction. (b) Necking down of cracks and pores to form arrays of disconnected tubular and spherical inclusions (the surface energy vectors, q the dihedral angle of the crack and v the crack migration velocity) (c) Crack closure by recrystallization (Koelemeijer et al., 2012).

When increasing confinement, the salt behavior becomes perfectly plastic. This is what strengthen the material's structure and allows voids closure and reduction despite the influence of deviatoric stress. The existent cracks tend to heal and stop their propagation so dilatancy is like inhibited. This process is used in some experiments to restore permeability under high confinement pressure for DRZ samples to determine the real undisturbed intrinsic permeability of salt formation. But below a certain threshold, this effect decays and the material can lose its cohesion under any deviatoric stress. The rock reenters into the dilatancy domain and stress provokes damage. It indicates that the mechanical healing is plastic and some is reversible and elastic (Fig 2. 18, a). if exposed to high confinement for a long period, healing is fast during initial stage (200 hours) and then proceeds slowly and stabilizes gradually (Chen et al., 2013).

Sutherland & Cave, 1980 has carried out permeability measurements on salt core samples (New Mexico, USA, a bedded salt with impurities at 700m of depth) subjected to different confinement pressure, so the evolution of intrinsic permeability can be studied with respect to hydrostatic compression. Although samples from the same formation are exposed to the same stress field, permeability of samples is highly variables between cores. That iss due to the inhomogeneity and the plasticity of salt increasing uncertainties (Sutherland & Cave, 1980). Results shows that permeability curves with respect to confining pressure have a decreasing trend with asymptotic tendency. Permeability reaches a very low plateau at high confinement stress. Initial value of permeability is recovered by the occurrence of healing phenomenon. A slight impact of the pore pressure is also noticed: the percolation of gas might reduce the healing process and the rate at which permeability decreases at a certain confinement pressure (Sutherland & Cave, 1980). A similar experience studying the hydrostatic effect on damage was executed by (Perami et al., 1993) and cited by (Thorel, 1994), on samples from Tersanne -France, a pure bedded salt at 1000m of depth. Samples were damaged by thermal expansion. Then, permeability was measured

using air pulse transient method during hydrostatic loading and unloading cycles. During charge phase, permeability decreases steeply at the beginning then softly after 4MPa of confinement. It attends 1% of its initial value of 10^{-16} m^2 at a confinement of 10MPa. During discharge, the permeability doesn't regain its initial state indicating an irreversible recovery.

On the microstructural scale, the recovery of permeability when increasing the mean normal stress is attributed to microcracks closure and interconnected pores by a mechanical clamping and suturing. Under high confinement pressure, the viscoplastic straining of salt by dislocations gliding and sliding along boundaries are activated due to surface energy reduction (Fig 2. 18,b).The movement involves contraction and/or necking down of cracks, forming tubes and eventually isolated fluid inclusions conducting to the third stage of healing –the recrystallization (Cinar et al., 2006; Koelemeijer et al., 2012).

In general, healing occurs at high temperature at very high rate. Temperature accelerates particles movement during diffusional transport but also catalyzes the recrystallization of dissolved particles and grains growth in GBS (J. Chen et al., 2013). Damaged samples exposed to heating recrystallization keep the basic deformation properties of intact samples (Weiguo et al., 2004; J. Chen et al., 2013). Nevertheless, crack closure in salt can occur at room temperature if confinement is high enough and at high strain stage because of the plastic properties of salt. Highly disturbed samples tend to heal at slower rate than undisturbed samples because their cracks went under severe hardening. Observed recrystallization grains are coarser at high strain stage than those at lower strain. This relationship describes the effect of water content in the polycrystal on dynamic recrystallization based on strain energy accumulation and average grain size. Rock salt with low water content hardens with increasing strain at lower yield, recrystallizes and become much stronger than wet rock (Takeuchi & Argon, 1976; Ter Heege et al., 2005; J. Chen et al., 2013).

The reduction of salt compressibility may also be attributed to this healing process. At high hydrostatic pressure, cracks close and salt compressibility also decreases. For rock salt, the number and extent of cracks decreases to become residual as it heals under hydrostatic pressure. Healed cracks do not re-open when the sample is unloaded. We conclude that rock salt compressibility is dependent on the "state" of healing, or conversely damage, as well as the magnitude of the hydrostatic stress (Zimmerman et al., 1985). This suggests that other effective elastic moduli will also be some function of the "state" of healing or damage. A constant elastic modulus may not be appropriate for salt whose behavior depends on the pore structure cohesion (Stormont, 1990).

The effect of hydrostatic effect on permeability was studied experimentally by Popp et al., (2001) on samples from Groleben salt dome taken from EDZ at 296.72-603.6m of depth. This salt is heterogeneous with impurities and grains are coarse to medium (<500um) and fine to large (1-10mm). The cored samples of D=98mm and L=200mm were healed under incremental confinement stress from 3MPa up to 30MPa. At almost each step Nitrogen N_2 gas, was injected at P_{inj}= 1 MPa and P_{out}=Patm. Slippage effect of the gas (Klinkenberg) was not taken into consideration because it's found negligible at the injection pressure of 1MPa according to Peach (1991). Permeability measurement ranged from 10^{-16} m^2 to 10^{-20} m^2. The evolution of permeability was described by the equation:

$$k = k_0 e\left(-X \times \sigma'\right) \qquad (2.21)$$

Where *k* the permeability, k_0 is the initial permeability and σ' the effective stress known. The values of *X* parameter were found to be within the range of 0.074 to 0.22 MPa. An exponential trend with respect to confinement pressure indicating the healing irreversibility. Ultrasonic waves velocity method was also used to determine dynamic elastic modulus in order to monitor the straining and the evolution of elastic properties. So, at low confinement the velocity of S and P wave velocities increased steeply and then softly at higher pressure indicating a healing process by progressive cracks closure. Permeability plotted with respect to P and S waves' velocity shows a funnel-shaped trend that becomes narrower with compaction reaching k< 10^{-20} m^2. This value was close to undisturbed rock in situ. Thus, the confining pressure led to recover the initial permeability and porosity values of undisturbed rock at 30MPa of pressure.

2.4.4.2. Deviatoric stress effect on permeability

The most important reason for the imperviousness of the salt is its rheological properties related to its tight crystalline structure, giving the salt a very low-permeability, high-ductility, low-creep strength and capacity for self-healing by plastic flow and diffusive mass transfer increasing (Langer, 1991; Wallner et al., 1998; Cosenza & Ghoreychi, 1999; Schulze et al., 2001). The main process known to increase permeability is microcracking caused by tectonic events or mechanical damage. As long as the external stress is in the non-dilatant domain, rock salt deformation is reversible and elastic, neither crack nor volumetric strain is detected instantaneously. Salt poromechanical structure is held stiff and coherent under the reigning hydrostatic stress. If differential deviatoric stress increases, strain reaches the dilatant domain inducing cracks nucleation and leakage risk. Many authors studied this relationship in order to ensure the integrity of the sealing of the rock salt especially near pore walls and excavation zones (Peach & Spiers, 1996; Stormont, 1997; Cosenza et al., 1999; Popp et al., 2001).

A notable experimental study on damage of rock salt samples (taken from a waste isolation pilot plant WIPP at 650 m depth in Southeast New Mexico, USA) and its influence on permeability and porosity was carried out by Stormont & Daemen (1992). Samples were extracted from the EDZ and the undamaged zone of the cavern and previously healed for 10 hours under 14.5 MPa of hydrostatic pressure. Permeability was continuously measured simultaneously with a triaxial compression test. Permeability values varied between 5×10^{-22} m^2 and 10^{-17} m^2. Gas accessible porosity was also calculated. At the end, a flow model of porosity-permeability change based on an equivalent channel model was established in order to describe crack initiation and growth during damage. When stress enters dilatant domain, salt behavior became plastic to brittle. Volumetric strain increase was used to determine the dilatancy threshold. Permeability increased rapidly with the dilation. The increase of deviatoric stress allowed sliding along grain boundaries along the directional orientation of the stress. Strain departed from linearity and became irreversible. They observed the phenomenon of cracks nucleation and growth. At a certain level of stress, enough cracks became activated, crack propagation became unstable. A connected tortuous network of fracture was established with randomly oriented wing cracks that continue to dilate plastically under loading stress. Permeability increased of several orders and salt sealing integrity was disturbed. At 4% of the axial strain, the permeability enhancement reached a limit of 10^{-14} $m^{2.}$ A transition in porosity growth occured. Cracks became strongly aligned in the same direction of the tensile stress, and their development rate get more stable and constant. Salt reached the strength peak, strain hardened and dilated. After that, a modest to none increase in permeability was observed (Stormont & Daemen, 1992).

The evolution of permeability with respect to connected porosity was evaluated based on pore structure and cracks linkage incorporating percolation theory. The model developed by Peach & Spiers, (1996) suggests that flow paths in salt initially develop along GBS and then along axial intergranular tensile cracks. Equivalent flow channels were described as narrow microcracks, penny shaped, with small opening considered as a particular hydraulic radius. Their irreversible growth under deviatoric stress allows their intersection and the establishment of a fluid flow network. Visual observations of cracks within the sample support the model results (Paterson, 1983; Gueguen & Dienes, 1989; Stormont & Daemen, 1992; Peach & Spiers, 1996).

Elastic models of cracks development are not suitable to describe salt permeability changes because poroelasticity coupling is negligible most of the time and inelastic processes are dominant on the rock salt scale (Stormont & Daemen, 1992). Permeability changes manifests into a close relationship between porosity, straining and permeability values. Crack orientation also influences the permeability evolution and it's related to the sliding motion and nucleation.

The sliding plane activation and straining under the loading stress induce secondary crack initiation. Fig 2. 19 based on a triaxial test at 2.4 MPa of confining pressure display that when the sliding criterion is met, an extensive range of crack angles end up activated with little additional loading. At very low deviatoric, stress only frictional movement occur with no damage is also delineated. Continued loading will eventually provoke damage and formation of secondary cracks and cracks orientation changes. This model is mostly applicable at low confinement stress where salt behavior is ductile to near-brittle. It shows that sliding activates cracks displacement and sliding and this triggers the dilatancy by the secondary cracks nucleation.

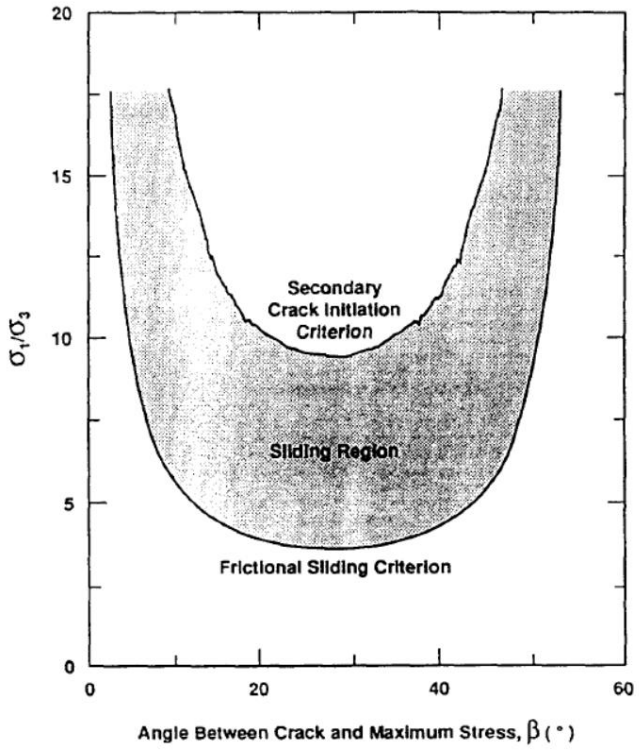

Fig 2. 19:Model using loading history of a sample tested at a 2.4 MPa confining pressure describing the frictional sliding during triaxial compression based on permeability and acccesible porosity results (Stormont & Daemen, 1992)

Popp et al., (2001) performed other experiments on healed samples of different dimensions taken from Asse bedrock in Germany from different mines and depths in range of 280 to 600m, to delineate the dilatancy boundary using permeability and straining development under damage on the salt of Stassfurt-Zeichstein in Germany.

Most of salt samples were nearly homogeneous with little amount of impurity. The triaxial tests were done under constant strain rate of 10^{-5} to 10^{-6} s^{-1}. Also other samples were used for extensional test by a creep rate of 10^{-8} to 10^{-10} s^{-1}. Tests were done at a confinement pressure between 2MPa and 30 MPa. In compressional mode, the stress-strain curve of the triaxial deformation has shown a transition from a quasi-elastic linear behavior at the beginning to a curve with a large radius at the end indicating a strain hardening. A failure was observed at almost 13% of the total strain. This transition displayed also by a decrease in the US waves velocity while permeability remained unchanged under k <10^{-18} m^2 according to results by steady-state method. When deviatoric stress reached 12 MPa, permeability jumped rapidly up to 5 orders from its initial values associated with a remarkable velocity decrease of ultrasonic waves. When entering the strain hardening, velocity became constant and decreased again with strain accumulation. Permeability, on the other side, reaches a plateau at a value of 10^{-17} m2 and $10^{-15}m^2$ at 5% and 15% of the strain for samples. For a confinement of 20 MPa, no failure occurred and dilatancy was delayed to 20% of the straining. In addition, US waves velocity decreased in the dilatant regime but less than at lower confinement because of the strength and stiffness capacity dominating the ductile behavior. In addition, permeability results reached values below the resolution of the pulse transient method (k<10^{-20} m^2). It's important to note that dilatancy threshold was found also dependent of impurity content in the rock (Popp et al., 2001). Henceforth, permeability is so well related to the change of porosity and strain evolution during a similar triaxial test described by a linkage cracks model. The damage or the dilatancy boundary is determined by an initial pore space opening, crack nucleation and gradually provokes a certain connectivity increasing porosity and permeability. This stage is characterized by a percolating regime of channels that become saturated when full connectivity is established and permeability reach a peak value. At higher confinement (>10MPa), plastic flow eliminates the interconnectivity if present between cracks leading to an ultimate percolation threshold. All, those information are validated with microstructural observation on polished sections observed by (Popp et al., 2001). This relationship of damage and permeability evolution is not simply function of stress but related also the initial state of the sample (sample machined, from excavation zones or undamaged sample) influencing the rate of straining and so the dilatancy and the percolation of fluid threshold (Peach, 1991; Stormont & Daemen, 1992; Popp et al., 2001) (Fig 2. 20).

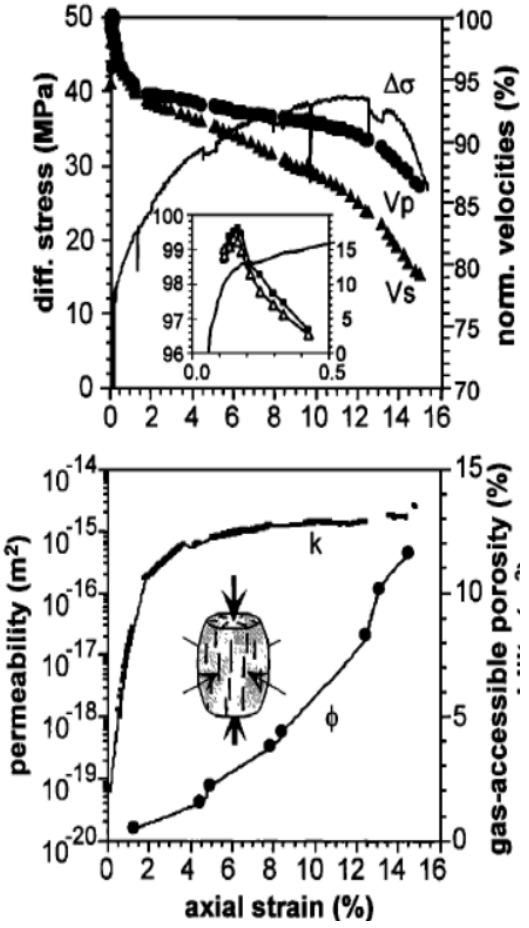

Fig 2. 20:Change of physical properties in function of strain and strength at compression controlled strain rate e=10-5s-1 m confining pressure Pc=2MPa, temperature T=30°C.Evolution of dilatancy (indicated by the decrease of Vp and Vs) as a function of compressive strain. The crack initiation stress defining the dilatancy boundary is indicated by the reversal of Vs at Δσ=10MPa. Evolution of permeability and gas accessible porosity versus strain (Popp et al., 2001).

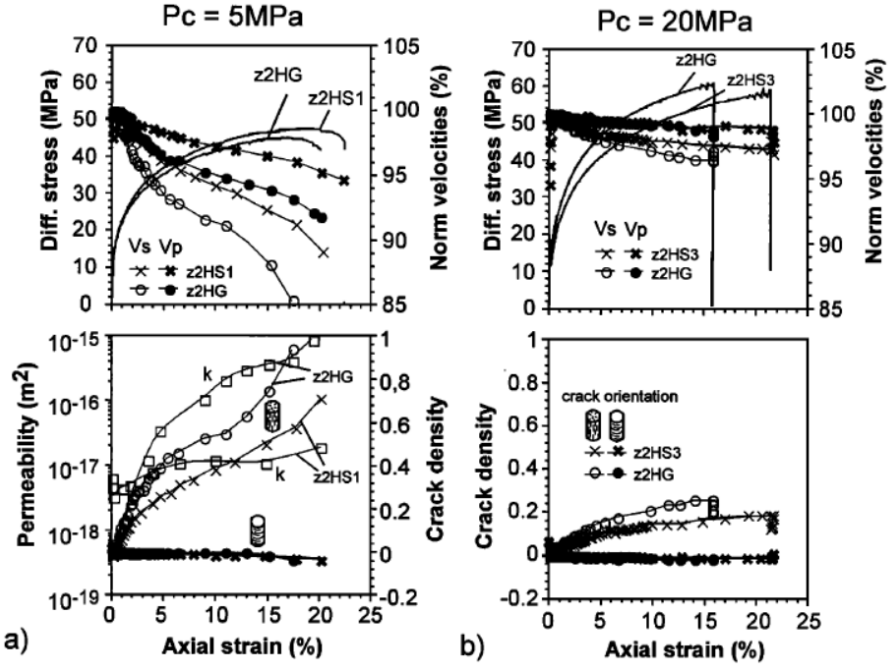

Fig 2. 21:Changes of physical properties as a function of compressive strain at 5Mpa and 20Mpa confining pressure, respectively. e=10-5s-1. (Top) Relationships between differential stress, axial strain and Vp, Vs, (normalized to Vpmax and Vmax and Pc=30MPa), and bottom relationships between axial strain, gas permeability and crack density for a- Pc=5MPa, Z2HS1 and Z2HG and b-Pc=20MPa, Z2HS3 and Z2HG.

2.4.4.3. Experimenting the sealing capacity of rock salt

Some authors reproduced those permeability tests in situ to assess cavern stability and sealing integrity. For example, permeability measurements were executed in Amelie mine of bedded salt - Mine de Potasse d'Alsace (MDPA, France) at 500-800m of depth. Nitrogen gas was injected continuously in a steady-state regime at constant temperature and pore pressure of 2 to 4.6 MPa over 75-80 days. Injection was continuous to reduce the disturbing factors of poromechanical coupling, chemical reactions, slippage and creep. Gas permeability measured by Darcy's law was $k=2\times10^{-23}$-2×10^{-21} m^2 for a salt porosity of 0.1% and penetration distance of 1.5m. When porosity increased of 1%, the penetration distance of gas decreased to 30cm in damaged zone which suggested that gas penetration cannot be solely attributed to pore creation by microcracks. Another leakage test was done by injection of brine at a pore pressure of 1MPa (very low compared to lithostatic pressure of the cavern at a depth of 536m). A leakage was detected though. It was believed that the opening of the mine has reduced pore pressure in tested zones and allowed fluid flow proving a leakage risk in excavation damaged zones (Cosenza et al., 1999).

Another permeability test was carried out in-situ, in Tersanne-France by pulse incremental pore pressure using nitrogen and brine. Gas permeability average was $k = 10^{-19}$ m^2. Realizing in situ permeability measurements requires that pore pressure should be lower than the lithostatic stress of the surrounding so we can avoid hydraulic fracturing (Cosenza & Ghoreychi, 1999). The seepage happens at low geostatic pressure when brine flow through cracks to reach the surface due to creep failure and enhanced permeability. So, it's important to measure in-situ permeability before leaching a cavern and before and abandonment strategy of a cavity in order to secure it from risks of collapse or subsidence (Berest et al., 2001; Brouard et al., 2001). A "secondary" permeability can be induced by high brine pressure in the cavern: tensile effective stresses at cavern wall may provoke rock damage and a porosity/permeability increase (Brouard et al., 2001).

At a small stress (>3 MPa), the volumetric creep rises the risk of stability loss when the dilatancy boundary is crossed. Fluid pressure at long-term storage approaches lithostatic pressure of the rock. Salt displays diffuse dilatation, allowing slow fluid escape (Fokker et al., 1995; Schoenherr et al., 2007). Studies also showed that permeability values do not differ much with respect to the nature of the gas used, hydrogen, argon, or nitrogen (Amro et al., 2012; Ślizowski et al., 2017).

2.5. Thermo-mechanical loading effect

2.5.1. Security and geomechanical stability of salt cavern

Rock salt around the cavern is subjected to cyclic stress loading due to the injection and withdraw of gas. The frequency and the rates of cycles are related to the strategic business models of markets demands and the final end use of the hydrogen and it represented in the table below (Tab 2.5):

Tab 2.5: Storage scenarios and cycles of pumping and withdraw according to business models of hydrogen storage

Storage Scenario	End use	Cycle frequency	Pressure magnitude according to depth
Power-to-power	Electricity generation	4 cycles per day	2MPa-6MPa
Power-to-mobility	Automation industry	1 cycle per day	2MPa-6MPa
Power-to-industry	Urban and chemical production	3 cycles per years	8MPa-18 MPa
Power-to-gas	Urban, electricity, industry	Seasonal	8MPa-18 MPa

The cycle corresponds of changing from maximum to minimum the gas pressure provoking also a temperature fluctuation. This stress variation can lead to a progressive accumulation and allows a thermo-mechanical damage due to long-term fatigue.

To ensure cavern stability, some design regulations are required: stress-strength ratio should be limited to less than 40% for the rocks around the cavern (risk of collapse), effective strain induced by gas withdraw should not exceed the 3% to avoid creep deformation, the stress at the middle of cavern should be smaller than the long-term strength of the surrounding rock, generally corresponding to around 25 % of the short-term strength. Those requirement avoid the creep and cavern collapse with time (Lindblom, 1997).The geomechanical aspects that might be taken into considerations for salt cavern storage safety are :

- The forecast of soil subsidence and it influence radius on cavity installation
- The variation of the storage volume in the cavity and so the variation of the internal pressure and creep rate.
- The determination of the minimum gas pressure by modelling the fast discharge of the cavity, and the optimization of the cushion gas volume.
- Determination of the minimum and maximum pressure that allows the establishment of an instability in the rooftop of the cave and so allows and excessive convergence.
- The effects of the different cycles of operational pressure on the cavity stability: seasonal variations, mixed cycles, multi-cycling, or the hydrostatic pressure
- The optimization of the geometric concept of the cavity from a geomechanical angle: height/diameter, thickness of the rooftop etc.
- Studying the effect of the presence of non-saline layers within the salt bed affecting the stability of the caverneous system.
- The long-term strain with cyclic hydrostatic pressure in the cavity.
- The effect of geomechanical properties of the interfaces between the layers.
- Rigidity effect of the layers (overburden and caprock) on the cavity stability (decreasing rigidity, rooftop stability)
- The determination of the critical parameter to improve site characterization by several laboratory/or field tests.
- The evolution of the cavity convergence until collapse or soil subsidence during dismantling phase and shut-down of the storage.

2.5.2. Mechanical cycling effect

Previous studies analyzed the halite behavior under cyclic conditions to ensure rock salt stability under fatigue. Studies investigated rheological behavior under cyclic creep until complete failure (Liang et al., 2012; Liu et al., 2014; Fan et al., 2016; Martin-Clave et al., 2021).
Cyclic compression tests were conducted in laboratories on cylindrical samples to simulate what happen in situ. Loading tests explored different characteristics of the mechanical fatigue such as (i) the magnitude of each cycle: the difference between the upper boundary limit and the lower limit of the deviatoric stress provoking the fatigue considered as the amplitude, (ii) the stress level of the loading cycle: the upper limit of cycles considered with respect to the compressive strength of the chosen salt, (iii) the cycles frequency or rate and the number of cycles and (iv) the duration of the test.

The greater the confinement is, the less the fatigue impact is detected. Therefore, it's better to perform such experiments at low confinement stresses or perform a uniaxial test in order to see greater damage. Elastic modulus is used to follow the evolution of the mechanical behavior of the salt during the mechanical fatigue experiment. It's calculated as the slope gradient of linear segment of each cycle (Liu et al., 2014). The elastic modulus of the first cycle at a low level of stress corresponds to the intact material damage state (Lemaitre, 1985; Liang et al., 2012). However, this variable conceals the internal plastic strain due to the visco-elastoplastic behavior of salt. Thus, it's better to take into consideration the loop diameter of each cycle. The area under the loading curve loop represents the work done by the external loading, while the area under the unloading curve corresponds to the released elastic deformation energy. It indicates that work during external loading is dissipated during unloading. If this area increases, it indicates the damage occurrence.

It is observed that with the increase of stress level and number of cycles, the irreversible deformation become more significant. Damage occurrence is likely to happen faster after a cyclic creep fatigue. However, stress level impact on the irreversible strain deformation is more important than the impact of the number of cycles. On the other hand, fatigue accumulation leads to dilatancy boundary and strength levels decrease (Liu, et al., 2014, fig2.22).

Fatigue activates the sliding and creep movement leading to the change in the internal structure. Shear sliding can easily take place along weak plane and leading to crack growth. Yet, strength depends on grains cohesion and size and impurity levels in the specimen. If applied stress is lower than the strength peaks and elastic limit, dilation is

not reached. For underground gas storage, rock fails at 65% -70% of the peak strength under monotonic loading (Liang et al., 2012). So dynamic fatigue induces microcracking of the rock salt, and leakage risk increases (Liu et al., 2014).

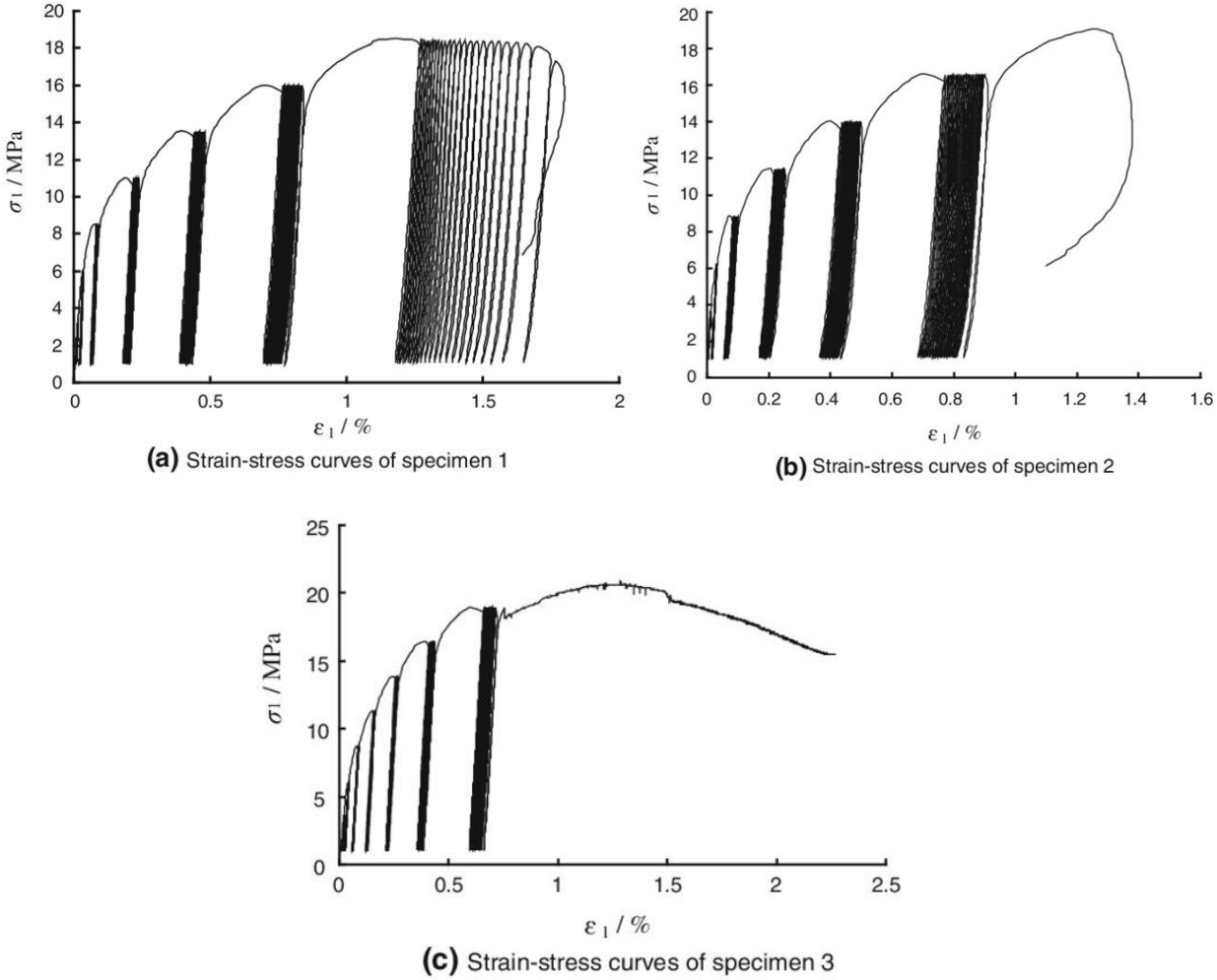

Fig 2. 22: Strain–stress curves of three samples with a cyclic loading frequency of 1Hz at different stress levels under uniaxial compression conditions (Liu et al., 2014).

In practice, gas injection and extraction operations can last for several months in each cycle. In this case, the behavior of cavern is more important, and hence attention should be paid to the stress-strain curves in the process of loading and unloading. Here, a parameter of deformation modulus is defined as an average ratio of stress difference to strain difference in each cycle during long term performance of salt cavern and loading unloading cycles. Hysteresis loops in stress-strain curves show some fundamental properties of the materials. For intact halite, almost all the hysteresis loops are tightly closed. The effect of loop hysteresis is less significant due to small crack density for few loading cycles. As the cycle number increases, the hysteresis becomes distinct indicating cracking and dilation. In that case, cavern integrity and gas leakage will be significantly affected. During the operation of gas storage, the maximum stress fluctuation could be large due to the periodicity and the adopted business model. So the cycles number and boundaries should be limited and monitored. Influenced by the difference of mechanical properties of surrounding rocks and the cyclic loading schemes of the storage, halite and other interlayers have different mechanical response. The different mechanical behaviors may cause increased damage impact to storage cavern (Liang et al., 2012; Martin-Clave et al., 2021). On higher stress level and long-term fluctuations, permeability could be recovered by the creep sliding inducing a self-healing.

2.5.3. Thermal cycling effect

The excessive frequency of cycles, might also affect the mechanical properties of surrounded rocks by the induced thermal fluctuations. Rapid gas depressurization leads to drastic cooling while loading increases temperature. Heat transfer to the surrounding rocks is limited. So, salt dilates under a tensile stress of heating and contracts under cooling inducing irreversible microcracks localized on cavern walls. Creep microcracks and irreversible damage

appears to 1 MPa/-1° C of temperature change but with a small depth of penetration due to the thickness of cavern walls made for storage. Contraction also is more significant than dilation. However, creep damage accumulation might lead to a dramatic failure of the rock mass.

Thermal fluctuations impact on rock was very few studied in the literature (Berest, et al., 2013; Khaledi, et al., 2016; Blanco-Martín, et al., 2018). Experiments were done especially in situ conditions like in Varangeville salt mine. The study focused on depressurization of (-20°C in about 8hours) by a rapid cooling chamber built in the cavern. An extensive monitoring system was set up to follow the strain to the thermo-mechanical cycling including possible damage. This amplitude of the cycle provoked a microcracking in cavern walls but with very strict extension of depth. As the cooling rate increases, energy concentrates in the cold surface and stops from dissipation in the surrounding rocks. It favors thereby the tensile fracturing. This process happens if cycling is at high rate and if the thermal contraction lasts for a long term. Although the extreme scenarios of the test, low initial stress, aggressive cooling rate, long cooling periods, the depths of penetration of the cracks remained limited (<2mm). So the thermal fracturing of salt was found to be of low impact. Most of the fractures created by the tensile strain rapidly closed, and their creation decreased with the number of cycles due to creep healing effect. It's important to notice, that the upper boundary and the lower boundary values of the cycle are of less importance on the behavior. However, strain rate decreased exponentially as temperature decreased (Blanco-Martín et al., 2018). The risk of leakage is still present because of tensile fracturing induced by the thermal fatigue.

It's also important to note that the presence of heterogeneity in salt affects directly the damage impact by thermal or mechanical creep cycling inducing heterogeneous straining from one grain to another (Martin-Clave et al., 2021).

2.6. Conclusions

As a conclusion, salt cavern walls could be damaged during hydrogen injection and withdrawal, and hence permeability could be impacted due to changes in stresses, pressure and temperature. However, this state of the art highlights that the relation between the permeability evolution and the mechanical loading is very complex because of these specific features of the mechanical behaviour (large plastic deformation, good creep properties, microcracking damage, cracks healing) of rock salt and gas flow in such unconventional reservoir (Klinkenberg effect). To the best of our knowledge, no publication in the literature has investigated all this complexity on a same rock salt specimen.

Therefore, we performed during this PhD thesis a complete set of laboratory experiments conducted on same a rock salt specimen (salt bed of the Alsace potash mines in the East region of France) to study the permeability evolution under different kind of loading conditions. Experimental methodology and results are presented in the next Chapter in the form of a research article submitted for publication in *Rock Mechanics and Rock Engineering*.

3. Evolution of gas permeability of rock salt under different loading conditions and implications on the underground hydrogen storage in salt caverns

D. Grgic, F. Al Sahyouni, F. Golfier, M. Moumni, L. Schoumacker, 2021. Evolution of gas permeability of rock salt under different loading conditions and implications on the underground hydrogen storage in salt caverns. Rock Mechanics and Rock Engineering, accepted July 2021

3.1. Abstract

We performed a complete set of laboratory experiments on a rock salt specimen to study the complex evolution of gas permeability under different loading conditions. The porosity of the studied rock salt is very low (~1%) and the initial permeability varies over 4.5 orders of magnitude. The Klinkenberg effect is only observed for the less permeable and damaged samples. The poroelastic coupling is almost negligible in our samples. Deviatoric loading under low confining pressure (1 MPa) induces a moderate increase in gas permeability from the dilatancy threshold due to microcracking. Measurement of ultrasonic wave velocities during uniaxial compression showed an almost irreversible closure of pre-existing microcracks and the opening of axial microcracks that are perpendicular and parallel, respectively, to the uniaxial stress direction and allowed a precise determination of the dilatancy threshold. Under higher confining pressure (5 MPa), no increase in permeability was measured because the material becomes fully plastic which practically eliminates microcracking and thus dilatancy. Under hydrostatic loading, gas permeability decreases because of cracks closure and this decrease is irreversible due to the time-dependent self-healing process. Permeability increases slightly during dynamic mechanical and thermal fatigue due to microcracking, while it reduces during static fatigue (creep) thanks to the self-recovery process. All these results give strong confidence in the underground hydrogen storage in salt caverns which remains by far the safest solution because the different mechanisms (viscoplasticity with strain hardening, microcracking and cracks healing) involved in material deformation act in a competitive way to annihilate any significant permeability evolution.

Keywords: rock salt; poromechanical coupling; compression tests; gas permeability; Klinkenberg effect; hydrogen storage; mechanical fatigue; thermal fatigue; ultrasonic monitoring; visco-plasticity; micro-cracking damage; self-healing.

3.2. Introduction

Hydrogen is considered as a clean and sustainable vector of renewable energy giving promising prospects, which would be able to replace fossil fuels in the near future. This promotes the development of large-scale hydrogen storage solutions to meet energy demands and mitigate the intermittency of wind and solar energy. Geological storage in salt caverns is currently the most viable option because of the ease of operation, great deliverability and, above all, sealing integrity (Zivar et al. 2020). Salt caverns are excavated in either salt beds formed by cyclic deposition of sediments or salt domes generated by halokinesis of salt layers. Storage of natural gas in salt caverns is now a relatively mature solution from an economic and technical point of view. Four hydrogen caverns are operating successfully around the world: one in the United Kingdom (Teesside) and three in the United States (Clemens Dome, Spindletop, Moss Bluff). Other pilot or research projects also exist in particular in Europe (e.g., Etrez in France). However, given the specific nature of this gas, a key point in the development of such technology is to characterize and constrain the various hydromechanical processes that could affect gas leakage and so to guarantee the storage facility safety (Tarkowski 2019).

Rock salt is a polycrystalline material made of individual grains of NaCl (halite), with crystal size varying generally from 2 to 20 mm and contains impurities in solid solution, secondary mineral phases and fluids trapped in inclusions, grain boundaries or in pores (Urai et al. 2008). In-situ intrinsic permeability of undisturbed halite is very low, around 10^{-21} m^2 (Peach and Spiers 1996; Popp et al. 2001), which imparts excellent sealing capacity. The flow

through rock salt occurs through the interconnected cracks or fractures, not through the crystals themselves (Gloyna and Reynolds 1961), which is responsible for the very low permeability of salt formations. Cracks, caused by stress relaxation and severe increase in deviatoric stresses in the excavation damaged zone of salt caverns, are responsible for a significant increase in permeability. Then, understanding the relationship between the development of cracks distributed in the rock mass and changes in petrophysical properties is of highest importance to survey any possible risk of fluid permeation or leakage through the salt formation.

The mechanical behaviour of rock salt is dominated by plastic deformation processes with a marked tendency for strain hardening and large creep ability. Creep processes in halite include glide, cross-slip, diffusion and dynamic recrystallization. At low effective mean stress, dilatancy and extensional fracture can occur in deforming salt, producing significant permeability increase by many orders of magnitude (Popp et al. 2001; Peach and Spiers 1996). The dilatancy threshold, which corresponds to the unstable micro-cracking damage, is often used as a threshold for salt cavern design (e.g., Labaune et al. 2018). However, a lot of study (e.g., Sutherland and Cave 1980; Peach 1991; Chen et al. 2013; Zhu and Arson 2015, Drury and Urai 1990) have already shown microcracks that can be self-healed under suitable temperature and pressure. From the microscopic point of view, the self-healing process is the recrystallization of rock salt crystals. The basic processes involved in recrystallization are the migration of existing grain boundaries and the formation of new high-angle grain boundaries. This process of grain boundary healing is similar to that of the healing of intragranular cracks (Smith and Evans, 1984). Cracks closure/healing process may thus contribute to mechanical stiffness and permeability recovery.

Intact rock salt is an unconventional reservoir with very low permeability and micrometric to nanometric pores. When gas flows in small size diameter pores at low pressure, the shock of molecules with walls induces slippage. The lower the pore size and gas pressure are; the larger gas slippage effect would be. Apparent permeability (k_a) measured by Darcy's law is then higher than intrinsic permeability (k_∞) related to the connected geometrical porosity. Hence, the investigation of the gas flow in such material should take into account this effect also called the Klinkenberg effect (Klinkenberg 1941; Letham and Bustin 2016). A lot of studies can be found in the literature about gas permeability measurements on rock salt under hydrostatic and triaxial loading conditions. Because of the very low permeability of rock salt, most of these gas permeability measurements were performed with the transient pulse decay method (e.g., Sutherland and Cave 1980; Cui et al. 2009; Peach and Spiers 1996; Popp et al. 2001; Zhang et al. 2020; Schulze et al. 2001). In addition, in order to avoid the slippage effect, which results in an overestimation of permeability, high gas pressures are commonly used in these experiments. The mean gas pressure of 1 MPa is high enough to eliminate this effect (Peach and Spiers 1996, Peach 1991). Very few studies using the steady-state flow method can be found in the literature. Gloyna and Reynolds (1961) used this method which allowed them the study of the Klinkenberg effect. The characterization of this effect is necessary when using low gas pressures, which is the case when low confining pressures are applied.

Whatever the method used, there are some issues with the proper measurement of gas permeability of rock salt during a mechanical loading, as already noticed by Schulze et al. (2001). Indeed, because of the long duration of this test, especially when the initial permeability is very low, it is difficult to maintain a nearly constant crack density (porosity) during measurements, especially at high differential stresses, and, importantly, non-negligible recovery of the initial damage of the samples could occur, giving rise to misleading results. Moreover, during permeability measurements, increase in pore gas pressure could induce volumetric expansion and decrease the mean stress through the effective stress concept, which complicate the analysis of the effect of pore and confining pressures on the permeability evolution. To determine if the effective stress concept applies in rock salt, which is not as obvious as for classical porous media because of its very low connected porosity, the Biot's poroelastic coupling coefficient has to be evaluated.

Storage of natural gas in salt caverns had been developed mainly for seasonal storage, resulting in only a small number of yearly gas pressure cycles with moderate gas-production rates. Nowadays, the operational modes are more aggressive (high-frequency cycling of salt caverns) to meet the needs of energy markets. This common practice fosters underground energy storage but pressure changes, and associated temperature and stresses changes, can generate fractures in the surrounding rock (Rouabhi et al. 2017). Even though the thickness of this excavation damaged zone is relatively small, the integrity of the storage project could be negatively impacted. Experimental and numerical investigations at the field scale on the impact of high-frequency cycling of storage caverns on the integrity of rock salt can be found in the literature (e.g., Blanco-Martín et al. 2018; Brouard et al. 2012). At the laboratory scale, very few studies can be found. Liu et al. (2014), for example, studied the damage evolution of rock salt under cyclic loading in unixial tests but the impact on gas permeability wasn't assessed.

Because of these specific features of the mechanical behaviour (large plastic deformation, good creep properties, microcracking damage, cracks healing) of rock salt and gas flow in such unconventional reservoir (Klinkenberg effect), the relation between the permeability evolution and the mechanical loading is very complex. There is no publication in the literature that investigated all this complexity on a same rock salt specimen. Therefore, we

present in this paper a complete set of laboratory experiments conducted on a rock salt specimen (salt bed of the Alsace potash mines in the East region of France) to study the permeability evolution under different kind of loading conditions. First, the initial microstructure of rock salt will be identified with different porosity methods and with X-ray 3D tomography, thus allowing the determination of voids (pores and cracks) proportion at different scales. Then, different short-term mechanical tests (hydrostatic compression tests, uniaxial and triaxial compression tests, uniaxial compression test with ultrasonic P and S-wave velocities measurement) will be performed on large core samples to characterize the poromechanical behaviour (deformation mechanisms, elastic properties, Biot's coefficient) of our rock salt specimen. The gas (helium) permeability will be measured with the steady-state method under hydrostatic compression and under triaxial compression with different confining pressures. Permeability measurements will be performed at different stress levels to analyse the impact of the deformation mechanisms on the permeability evolution, and at different gas pressure to characterize the slippage effect and obtain the real intrinsic permeability of rock salt at low gas pressures. Permeability measurements will also be performed continuously during some triaxial tests to limit damage recovery that could occur when the test duration is too long. The impact of mechanical fatigue, under dynamic/cyclic triaxial loading and static triaxial loading (creep test), and cyclic thermal fatigue on rock salt permeability will also be analysed.

3.3. Material and methods

3.3.1. Material description and sampling

Salt specimens were taken at 530 m depth in the salt bed of the Alsace potash mines in the East region of France (Stocamine site for ultimate waste storage). It belongs to the Sannoisian-Oligocene (Cenozoic) geological stage. This layer is a powerful saline series located under a collapsed potash bed. This rock salt is considered as a natural analogue of salt caverns used for in situ H_2 storage. For our experimental study, we took some salt blocks close to a gallery wall in which all the samples used in hydro-mechanical experiments were cored.

This salt is mainly constituted by halite crystals with heterogeneous intercalations of marls and anhydrite crystals. Crystals size ranges from few millimeters to few centimeters and their orientation is random. Mineralogical analyses (Scanning Electron Microscopy, Energy-Dispersive X-ray, Back-Scattered Electrons) have revealed (Fig 3. 1, left) limpid phenoblastic to milky xenomorphs halite crystals, some white elongated flat crystals of anhydrite and occasionally some dark crystals of clay. In addition, the microscopical images show that porosity corresponds mainly to crystal joints and isolated microcracks. The colours of the samples vary from pale yellow to brown and dark grey (Fig 3. 1, right) depending on the content of visible impurities (up to 5%).

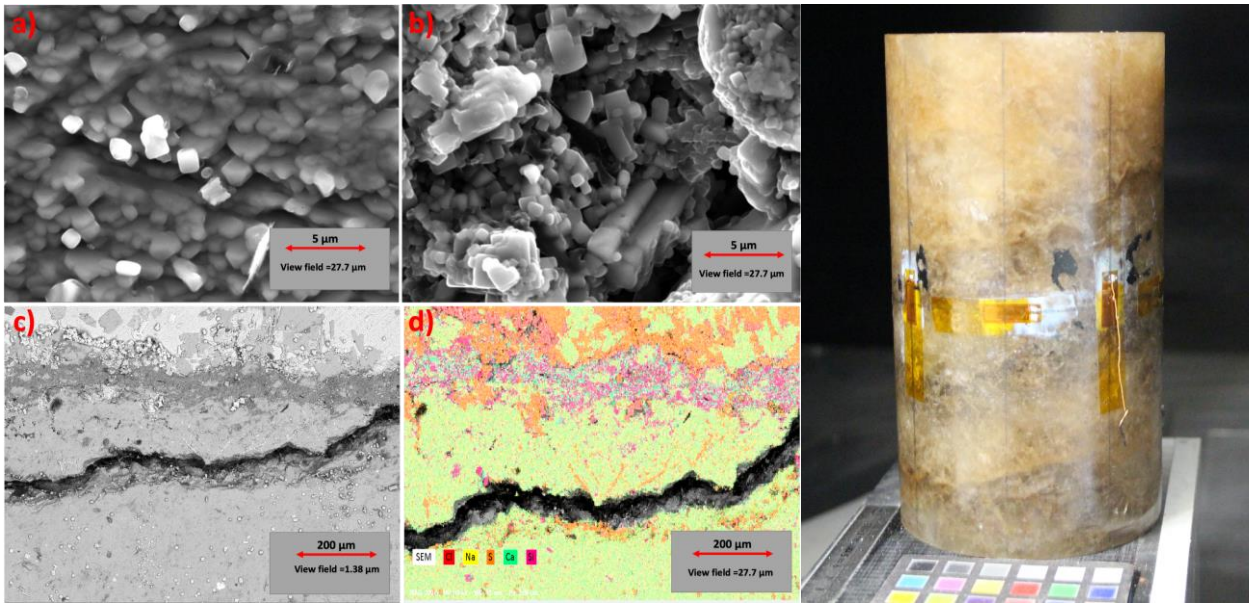

Fig 3.1: Left, SEM analyses on a rock salt sample: high magnification images (a, b), BSE map (c), EDX map (d). Right, photo of large cylindrical salt sample (diameter 100 mm, length 200mm) with strain gages for hydromechanical tests

3.3.2. Microstructural characterization of initial material

3.3.2.1. Porosity measurements

Mercury intrusion porosimetry was performed in the pressure range from 0.007 to 413 MPa, which corresponds to pore sizes from 89 μm to 1.8 nm. This technique allows the determination of the total (connected), free and trapped porosities, and the distribution of entrance radii of pores (porous spectrum). The measurements were performed on four near-cubic 2 cm rock salt samples from various parts of a sample of initial rock salt in order to take account for the mineralogical heterogeneity of the material.

The total porosity (n) is measured on 4 large cylindrical samples (three of diameter 38 mm and length 76 mm, one of diameter 100 mm and length 200 mm). It is calculated from the volumetric mass densities:

$$n = 1 - \left(\frac{\rho_d}{\rho_s} \right) \qquad (3.1)$$

Where ρ_s is the density of solid grains and ρ_d is the bulk dry density of the material.
The bulk dry density is obtained from the samples volume and mass. Then, these cylindrical samples are grinded to obtain very fine powders from which the density of solid grains is obtained with the helium pycnometer for each sample. This technique allows therefore the determination of the whole porosity (including cracks) of large samples.

3.3.2.2. X-ray 3D Computed Tomography (CT)

CT scans were performed on cylindrical samples before permeability and mechanical test to characterize the initial microstructure of the material. The tomograph used is X-Seifert cube/Baker Hughes, with a voxel size of 126 μm. After 3D reconstruction of the volume, images are analysed by VGStudio MAX Software (Volume Graphics GmbH) by colours thresholding. Then, a model quantifies the porosity according to binary grey scale segmentation. Only cracks (i.e, large voids) can be observed with this technique because of the relatively large voxel size and the very small size of pores in this material. In addition, 3D approximation of some large voids (cracks) of irregular shape by an ellipsoid will allow to assess their shape, surface, volume and orientation. This ellipsoidal approximation is based on the principal component analysis (PCA) which allows the conservation of inertial moments of initial irregular shapes.

3.3.3. Theoretical considerations

3.3.3.1. Biot's coefficient

In order to verify if the pore gas pressure influences the total mean stress and thus the mechanical behaviour of porous materials, i.e. if poromechanical coupling applies within rock salt, the value of the Biot's coefficient has to be determined. This influence of pore fluid pressure can be formulated using the effective stress concept (Biot 1941). For an elastic porous medium, the total stress tensor may be decomposed into an effective stress tensor and a fluid pressure tensor. In the case of a linear isotropic poroelastic material and under isothermal conditions, this partition can be written as follows:

$$\sigma = \sigma' - bp \qquad \sigma = \frac{1}{3}\sigma_{ii} \qquad (3.2)$$

This first state equation of poroelasticity can be written in the following form:

$$\sigma = K\varepsilon_v - bp \qquad \varepsilon_v = Tr\left[\varepsilon_{ij}\right] \qquad (3.3)$$

Where σ_{ij} is the stress tensor, ε_{ij} the strain tensor, σ the total mean stress (equal to the confining pressure P_c under triaxial conditions), σ' the effective mean stress, p the interstitial (pore) pressure, ε_v the volumetric strain of the material, K the skeleton drained bulk modulus and b the isotropic Biot's coupling coefficient.
The Biot's effective stress coefficient b can be expressed with the poroelastic material properties:

$$b = 1 - \frac{K}{K_S} \quad (3.4)$$

Where K_s is the solid matrix modulus.

The Biot's coefficient can be identified experimentally by two methods. The first one consists in determining separately K and K_s with a drained hydrostatic compression test and a hydrostatic test with the particular loading $\Delta P_c = \Delta p$ (p: pore pressure), respectively. In the former test, the resultant volumetric strain ε_v corresponds to the skeleton (solid matrix + voids) deformation. In the latter test, the resultant volumetric strain ε_v corresponds to solid matrix deformation.

$$K = \frac{\Delta P_c}{\Delta \varepsilon_V} \quad Ks = \frac{\Delta P_c = \Delta p}{\Delta \varepsilon_v} \quad (3.5)$$

The second one consists in determining the Biot's coefficient from a test with incremental loadings. According to the constitutive equation of poroelasticity (3), a variation of the mean effective stress results in the same variation of volumetric strain, whether the mean effective stress variation is achieved through a mean stress variation (confining pressure) or through a pore pressure variation. Therefore, if a test, constituted by successive 2-step incremental loadings - a confining pressure loading followed by a pore pressure loading - is performed, it is possible to identify the Biot's coefficient b, which corresponds to the ratio between the successive strain responses:

$$b = \left| \frac{\Delta \varepsilon_v (\Delta p = \Delta P_C)}{\Delta \varepsilon_v (\Delta P_C)} \right| \quad (3.6)$$

3.3.3.2. Measurement of ultrasonic P and S-wave velocities during compression test

To characterize the deformation mechanisms of rock salt, a uniaxial compression test with ultrasonic (US) P and S-wave velocities measurement is performed on a cylindrical sample. Because the sample has a cylindrical symmetry, the anisotropy due to the micro-cracks induced during uniaxial loading should be isotropic transverse. In that case, the elasticity is characterized by five independent constants and requires then the measurement of five independent US wave velocities: three compressional P-waves and two shear S-waves in three different directions ($VP_{0°}$ the horizontal-parallel P-wave velocity, $VP_{90°}$ the horizontal-perpendicular P-wave velocity, VP_θ the off-axis P-wave velocity, $VSh_{0°}$ the horizontal-parallel velocity of horizontally polarized S wave and $VSv_{0°}$ the horizontal-parallel velocity of vertically polarized S wave). Then, the 5 independent coefficients of the elastic stiffness tensor C_{ij} (in Voigt notation) are calculated using the well-known Christoffel's equations for elastic waves propagation:

$$C_{11} = \rho\, {VP_{0°}}^2 \quad C_{33} = \rho\, {VP_{90°}}^2 \quad C_{44} = \rho\, {VSv_{0°}}^2 \quad C_{66} = \rho\, {VSh_{0°}}^2$$
$$C_{13} = -C_{44} + \left[\frac{1}{\sin^2 2\theta} (2\rho\, {VP_\theta}^2 - 2C_{11}\sin^2\theta + C_{44}(\sin^2\theta - \cos^2\theta - 1)) \times (2\rho\, {VP_\theta}^2 - 2C_{33}\cos^2\theta + C_{44}(\cos^2\theta - \sin^2\theta - 1)) \right]^{1/2} \quad (3.7)$$

Where ρ is the volumetric mass density of the material (continuously corrected by taking into account the sample deformation) .

From these five independent C_{ij} coefficients, the five classical dynamic coefficients (Young's moduli E_{11} and E_{33}, Poisson's ratios ν_{12}, ν_{13} and ν_{31}) of the elastic compliance tensor S_{ij} may be calculated as follows, D being the determinant:

$$E_{11} = \frac{D}{C_{11}C_{33} - C_{13}^2} \quad E_{33} = \frac{D}{C_{11}^2 - C_{12}^2} \quad D = \begin{vmatrix} C_{11} & C_{12} & C_{13} \\ C_{12} & C_{22} & C_{13} \\ C_{13} & C_{13} & C_{33} \end{vmatrix}$$
$$\nu_{12} = \frac{C_{12}C_{33} - C_{13}^2}{C_{11}C_{33} - C_{13}^2} \quad \nu_{13} = \frac{C_{13}(C_{11} - C_{12})}{C_{11}C_{33} - C_{13}^2} \quad \nu_{31} = \frac{C_{13}}{C_{11} + C_{12}} \quad (3.8)$$

For anisotropy analysis, it is useful to calculate from elastic coefficients the dimensionless anisotropy parameters ε and γ that quantify P-wave anisotropy and S-wave anisotropy, respectively (Thomsen 1986):

$$\varepsilon = \frac{C_{11}-C_{33}}{2C_{33}} \quad \gamma = \frac{C_{66}-C_{44}}{2C_{44}} \tag{3.9}$$

3.3.3.3. Apparent and intrinsic permeability

In tight porous media, gas flow displays particular features related to gas properties but mainly to pore diameter and pore pressure. The gas flow regime is driven by Knudsen number (K_n), a dimensionless parameter defined as the ratio of the molecular mean free path (λ) to the pore diameter (d):

$$K_n = \frac{\lambda}{d} \tag{3.10}$$

λ is defined as the average distance a gas molecule travels between two successive collisions with other gas molecule. It is expressed by the following equation (Present 1958):

$$\lambda = \frac{3}{2}\frac{\sqrt{\frac{\pi RT}{2M}}}{p}\mu \tag{3.11}$$

Where M is the molar mass, R the gas constant, T the temperature, μ the dynamic viscosity of the fluid and p the mean pore pressure.

Different flow regimes are usually classified (Beskok et al. 1996; Ziarani and Aguilera 2012; Bernabé 2018; Pazdniakou et al. 2018). For Knudsen number less than 0.001 (Fig 3. 2,a), the molecular mean free path is negligible relative to the pore throat diameter and viscous flow prevails. The continuum fluid dynamics is valid and the classical Darcy's law can be applied. As the Knudsen number increases ($0.001 < K_n < 0.1$), gas molecules collide with pore walls and slip with a non-zero velocity which leads macroscopically to a departure from the linear Darcy equation (Fig 3. 2,b). A gas pressure-dependent permeability, denoted as the apparent permeability k_a, is observed. A continuum description is still possible but a correction known as Klinkenberg correction is required. The first-order correlation proposed by Klinkenberg (1941) relates the apparent permeability to the intrinsic permeability as follows:

$$k_a = k_\infty \left(1 + \frac{\beta}{p}\right) \tag{3.12}$$

Where k_∞ is the intrinsic permeability (i.e., the equivalent-liquid permeability or the gas permeability at very large pressure so that slippage effect is negligible), β is the Klinkenberg factor related to the medium properties, and p is the mean gas pressure in pores.

For higher K_n ($0.1 < K_n < 10$), the rarefaction effects become more important and the Knudsen layer dominates the flow domain (Fig 3. 2, c). In this so-called transitional flow domain, continuum description is questionable (Freeman et al. 2011; Li and Sultan 2016) but higher order slip conditions (Beskok and Karniadakis 1999; Tang et al. 2005) can still be used with Navier-Stokes equations to extend the slippage flow domain and capture the correct flow velocity. From the macroscopic point of view, empirical correlations which expand the applicability of the Klinkenberg's slippage equation have been also proposed in the literature (Beskok and Karniadakis 1999; Tang et al. 2005; Florence et al. 2007; Ziarani and Aguilera 2012; Lv et al. 2014). Tang et al. (2005) have thus suggested to use a second-order polynomial equation (Knudsen's correlation) by analogy with the higher order slip boundary condition such as:

$$k_a = k_\infty \left(1 + \frac{A}{p} + \frac{B}{p^2}\right) \tag{3.13}$$

But two empirical parameters, A and B, need to be fitted. As an alternative, easier-to-use model, we consider an exponential empirical correlation, inspired from Zhu et al. (2007), to correct the deviation from the linear model:

$$k_a = k_\infty e^{\alpha/p} \qquad (3.14)$$

where α is a constant. Note that Eq. (14) can be reformulated using a Taylor series expansion, in terms of polynomial development, similar in essence to Eq. (13):

$$k_a = k_\infty \left(1 + \frac{\alpha}{p} + \left(\frac{\alpha}{p}\right)^2 \frac{1}{2!} + \Theta\left(\frac{1}{p^2}\right)\right) \qquad (3.15)$$

Finally, for K_n > 10, we reach the free molecular flow domain where the continuum flow description fully breaks down (Fig 3.2 ,d). Boltzmann equations are required to describe the gas flow. Pore throat diameters are extremely narrow and gas molecules collide with the walls more frequently than they collide with one another.

The apparent permeability (k_a) measured in laboratory is calculated at equilibrium according to the Darcy's equation for compressible gas flow:

$$k_a = \frac{2\mu Q L p_u}{A({p_u}^2 - {p_d}^2)} \qquad (3.16)$$

Where *Q* is the volumetric flow rate, *L* the length of the sample, *The* cross-sectional area of the sample, p_u and p_d the upstream and downstream gas (pore) pressures respectively.

This apparent permeability (k_a) is then higher than intrinsic permeability (k_∞) related to the connected geometrical porosity.

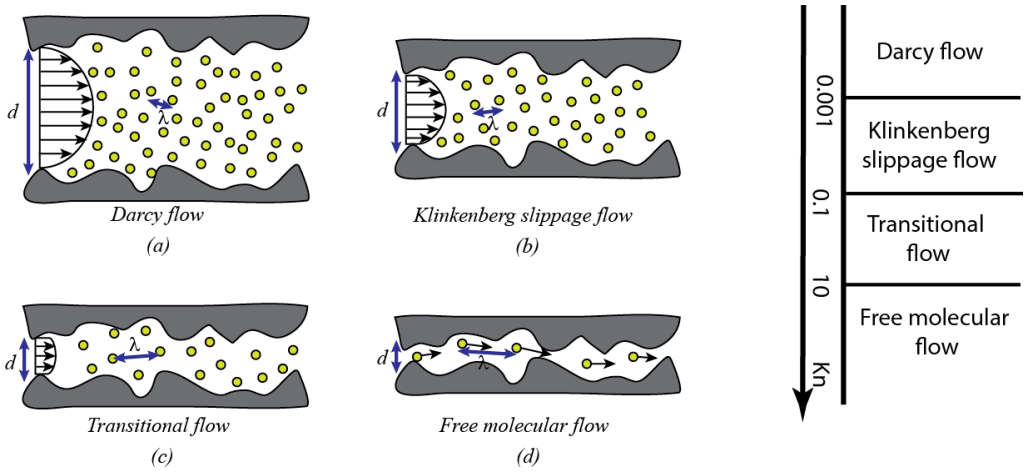

Fig 3.2: Flow regimes as a function of the Knudsen number

3.3.4. Experimental procedures for hydromechanical tests and permeability measurements

The local axial and circumferential (lateral or radial) strains were measured by strain gages (length 20-30 mm) glued at the mid-height of each specimen. Due to the material heterogeneity with crystals sizes ranging up to centimeter (Fig 3. 1, right), the size of samples and strain gages (for the measurement of deformations) has been chosen sufficiently large to respect the representative elementary volume for mechanical experiments. All tests were performed in large triaxial cells in which the tested samples are wrapped with a jacket (for the application of the confining pressure). All experimental parameters (axial stress, confining oil pressure, strains) were controlled and monitored with data acquisition software and pressures were applied with precision syringe pumps. All the tests were carried out in an air-conditioned room (20 °C). For mechanical tests, a rapid loading/unloading rate (1 MPa/min) has been chosen to avoid viscous effects and unloading-reloading cycles were performed at different stress levels on some samples in order to determine the evolution of static elastic moduli. The static elastic moduli were determined with the tangent method on the unloading curves. The convention of positive compressions for stresses and strains is used. In our reference frame (x_1, x_2, x_3), (x_1, x_2) is the horizontal plane which corresponds to the heterogeneous intercalations of marls and anhydrites. The axis x_3 corresponds therefore to the direction perpendicular to the horizontal plane.

For permeability measurements, helium gas is used as a substitute for hydrogen for safety purpose. The gas pressure *p* is applied at the bottom (upstream) and gas flows up to the top (downstream) at atmospheric pressure.

To ensure a homogeneous gas flow through the sample during mechanical tests, two metallic drainage filters are placed at both ends of the cylindrical sample. The gas (helium) permeability is measured with the steady-state method. At equilibrium, the apparent permeability (k_a) is calculated according to the Darcy's equation for compressible gas flow (Eq. 16). Gas permeability measurements were performed with two different methods:

- In the first one, the gas pressure is applied at the upstream with a bottle equipped with a manometer and a flowmeter equipped with a burette measures the gas flow rate (Q) at the downstream under atmospheric pressure. This method is used to measure the permeability at different deviatoric stress levels (just after the unloading-reloading cycles), corresponding to different damage levels, and at different gas pressures to analyze the Klinkenberg effect. For a given stress level, the permeability measurements at different gas pressures last from 0.5 to 1.5 hour. Hence, a cyclic compression test, with permeability measurements at different deviatoric stress levels and at different gas pressures, can last up to 30 hours.

- In the second one, a constant gas pressure is applied and the flow rate (Q) is measured continuously at the upstream with a precision syringe pump. To allow a continuous measurement of gas permeability during a triaxial test (with monotonous loading), a slower deviatoric loading rate (0.1 MPa/min) is applied and such a test lasts only 3-4 hours. This method is used to measure continuously the gas permeability but only the changes in apparent permeability of the sample are monitored. The description of all the experiments (and the samples dimensions) are summarized in Tab 3. 1 and described below.

Tab 3.1: Detailed description of all experiments on rock salt samples

Sample	Dimensions	Description
1	Side 50.1 mm Weight 278 g	Isotropic compression test with cyclic loading
2	Length 187 mm Diameter 99.9 mm Weight 3352 g	Hydrostatic compression test with incremental loading ($\Delta P_c = \Delta p$) for Biot's coefficient determination before and after triaxial compression test (P_c = 1 MPa) with cyclic loading. Permeability measurement during the triaxial loading at different deviatoric stress levels and gas pressures.
3	Length 201.6 mm Diameter 99.7 mm Weight 3444 g	Isotropic loading with permeability measurement at different confining pressures and different gas pressures for the lowest confining pressure (P_c = 1 MPa), then uniaxial compression test with cyclic loading.
4	Length 200.7 mm Diameter 100 mm Weight 3436 g	Isotropic loading with permeability measurement at different confining pressures and different gas pressures for the lowest confining pressure (P_c = 1 MPa), then uniaxial compression test with cyclic loading.
5	Length 187.9 mm Diameter 99.7 mm Weight 3197 g	Triaxial compression test (P_c = 1 MPa) with cyclic loading and permeability measurement at different deviatoric stress levels and gas pressures.
6	Length 189.7 mm Diameter 99.8 mm Weight 3230 g	Triaxial compression test (P_c = 5 MPa) with cyclic loading and permeability measurement at different deviatoric stress levels and gas pressures.
7	Length 199.8 mm Diameter 100.3 mm Weight 3434 g	Triaxial compression test (P_c = 1 MPa) with monotonous loading and continuous permeability measurement.
8	Length 187.3 mm Diameter 99.3 mm Weight 3172 g	Triaxial compression test (P_c = 5 MPa) with monotonous loading and continuous permeability measurement.
9	Length 103 mm Diameter 50.1 mm Weight 432.5 g	Uniaxial compression test (cyclic loading) with US wave velocities measurement.
10	Length 187 mm Diameter 99.9 mm Weight 3332 g	Long-term hydrostatic and triaxial creep test (P_c = 1 MPa) with permeability measurement at different stress levels, times and gas pressures.
11	Length 185 mm Diameter 100.4 mm Weight 3051 g	Dynamic/cyclic triaxial compression test (P_c = 1 MPa) with static stages and continuous permeability measurement.
12	Length 179.1 mm Diameter 99.6 mm Weight 3030 g	Thermal cyclic fatigue test with permeability measurement (under a confining pressure of 1 MPa) at different gas pressures before and after.

- Sample 1:

A hydrostatic cyclic compression test is performed on a cubic sample with a confining pressure ($\sigma_{11} = \sigma_{22} = \sigma_{33} = P_c$) up to 30 MPa to determine the bulk modulus K and verify if the material is initially isotropic.

- Sample 2:

The Biot's coefficient b is estimated on a large cylindrical sample before and after damage using Equation (3.6). Incremental isotropic loadings ($\Delta P_c = \Delta p$) are applied to the sample until 20 MPa. The sample is damaged with a triaxial compression test (P_c = 1 MPa) with cyclic loading until 16 MPa. Permeability measurement (1st method) is performed during the uniaxial loading at different deviatoric stress levels and gas pressures (3-9 bar) to analyse the impact of the deformation mechanisms and the Klinkenberg effect on the permeability.

- Samples 3 and 4:

The gas permeability of the initial rock is first measured (1st method) on large cylindrical samples at different confining pressures (1-5 MPa) and different gas pressures (4-8.5 bar) for the lowest confining pressure (P_c = 1 MPa). The focus is to analyse the impact of confining pressure and the Klinkenberg effect on the permeability. Then, uniaxial compression test (cyclic loading) is performed to characterize the mechanical behaviour of rock salt. Sample 3 is loaded until 25 MPa, whereas Sample 4 is loaded until 17 MPa and then completely unloaded.

- Samples 5 and 6:

A triaxial compression test (cyclic loading) is performed on large cylindrical samples to characterize the mechanical behaviour of rock salt. Sample 5 (P_c = 1 MPa) is loaded until the deviatoric stress $|\sigma_{11} - \sigma_{33}| \sim 24$ MPa, whereas Sample 6 (P_c = 5 MPa) is loaded until ~26 MPa and then completely unloaded. Permeability measurement (1st method) is performed during the triaxial loading at different deviatoric stress levels and gas pressures (3.4-11 bar) to analyse the impact of the deformation mechanisms and the Klinkenberg effect on the permeability. The focus is also on analysing the impact of the confining pressure.

- Samples 7 and 8:

A triaxial compression test (monotonous loading) with continuous measurement of gas permeability (2nd method) is performed on large cylindrical samples to analyse the impact of the deformation mechanisms on the permeability. A constant gas pressure (5 bar) is maintained during the test. Sample 7 (P_c = 1 MPa) is loaded until the deviatoric stress $|\sigma_{11} - \sigma_{33}| \sim 25$ MPa, whereas Sample 8 (P_c = 5 MPa) is loaded until ~ 20 MPa. For these samples, test duration is much shorter, which reduces significantly damage recovery during permeability measurement.

- Sample 9:

A uniaxial compression test (cyclic loading) is performed on a large cylindrical sample which is loaded with until the axial stress $\sigma_{33} \sim 30$ MPa to characterize the mechanical behaviour of rock salt. US wave velocities were measured with 0.5 inches' ultrasonic transducers (frequency: 150 kHz for P-waves and 100 kHz for S-waves) held in contact with the rock sample. The position of the piezoceramic transducers on the sample surface is shown in Fig 3. 3 with respect to our reference frame (x_1, x_2, x_3), $\vartheta = 0°$ corresponding to the horizontal plane. In our case, the off-axis angle ϑ is equal to 32°.

Sinusoidal pulses are supplied by a generator and a multiplexer allows the automatic and quasi-simultaneous (i.e., a few microseconds) measurement of velocities. Hence, ultrasonic wave velocities can be measured continuously throughout the entire duration of the uniaxial compression test. Data were recorded at a sampling rate of 100 MHz, corresponding to a precision of ±0.01µs for P-wave and S-wave arrival times.

Times of flights (TOF) of ultrasonic waves were semi-automatically picked from a threshold corresponding to 15 per cent of the first peak amplitude of the signal. Velocities are calculated from the TOF and the distance between each source and receiver transducers. Then, the dynamic coefficients of the elastic stiffness/compliance tensors and the dimensionless anisotropy parameters are calculated with Eqs. (7-9).

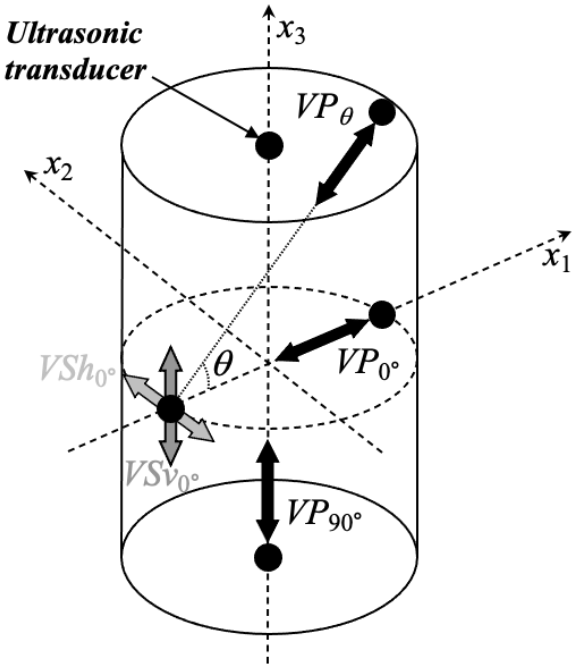

Fig 3.3: Position of ultrasonic transducers on a cylindrical sample of rock salt

- Sample 10:

A long-term hydrostatic and triaxial test is performed on a large cylindrical sample. The confining pressure (P_c = 1 MPa) is fist applied and maintained during 2 days, then a deviatoric stress $|\sigma_{11} - \sigma_{33}|$ ~ 16 MPa is applied and maintained during 10 days. The gas permeability is measured (1st method) at different gas pressures (3-9 bar) during the hydrostatic stage (at different times), the deviatoric loading (at different stress levels) and the triaxial creep stage (at different times). This test focuses on the impact of mechanical static fatigue on the permeability evolution.

- Sample 11:

A dynamic/cyclic triaxial compression test (*Pc* = 1 MPa) with static stages continuous permeability measurement (2nd method) is performed on a large cylindrical sample. A constant gas pressure (2 bar) is maintained during the test. Loading-unloading cycles (loading rate: 1-2 MPa/min) were carried out on three deviatoric stress $|\sigma_{11} - \sigma_{33}|$ ranges which are: 2-6 MPa (45 cycles), 10-15 MPa (60 cycles), 15-25 MPa (40 cycles). Between the cycle series, the deviatoric stress is maintained constant during 15 hours. The duration of the whole test is about 70 hours. The objective is to assess the impact of mechanical dynamic fatigue (with intermediate phases of static fatigue) on rock salt permeability.

- Sample 12:

The impact of thermal cyclic fatigue is studied on a large cylindrical sample of rock salt. A series of 19 thermal cycles with 6-60 °C temperature range (initial temperature is 20 °C) is imposed to the sample in a climatic chamber. This thermal amplitude corresponds to representative in-situ conditions of salt caverns during gas injection and withdrawal cycles (Rouabhi et al., 2017, AbuAisha and Rouabhi, 2019). The duration of the whole cyclic test is 14 days, and then we let the temperature equilibrate at the initial temperature (20 °C). Permeability measurement (1st method) is performed before and after thermal fatigue at different gas pressures (2-9 bar), under a confining pressure of 1 MPa. The focus here is to analyse the impact of thermal fatigue and the Klinkenberg effect on the permeability.

3.4. Microstructural characteristics of rock salt

The connected porosity of rock salt obtained from mercury intrusion porosimetry on four small samples is very low: 0.8%, 2.3%, 0.9% and 0.9% (mean value = 1.2%). The corresponding values of free porosity are 0.6%, 1.3%, 0.7% and 0.5%, respectively. The corresponding values of trapped porosity are 0.2%, 1%, 0.2% and 0.4%,

respectively. This variability is related to the mineralogical heterogeneity of the material. These values of mercury connected porosity are consistent with the values in the literature (e.g., De Las Cuevas 1997; Sutherland and Cave 1980). The distribution of entrance radii of pores (porous spectrum) and cumulative pore volume obtained by mercury intrusion porosimetry is represented in Fig 3. 4for the more porous rock salt sample (2.3%). This porous spectrum presents a polymodal distribution. Following the recommendations of Peter et al. (1970), we classified pore size distribution into three classes: macroporosity (> 7.5 μm), microporosity (between 7.5 μm and 0.1 μm) and infraporosity (< 0.1 μm). In this porous spectrum, the infrapores are the most abundant and represent 76.5% of the total pore volume. Micropores and macropores represent 11.5% and 12% respectively. The same trend is observed for the four tested samples and our data are consistent with the data obtained by De Las Cuevas (1997) with the same porosimetry technique on rock salt from the Lower Salt Unit of the Cardona Saline Fm. (Spain).

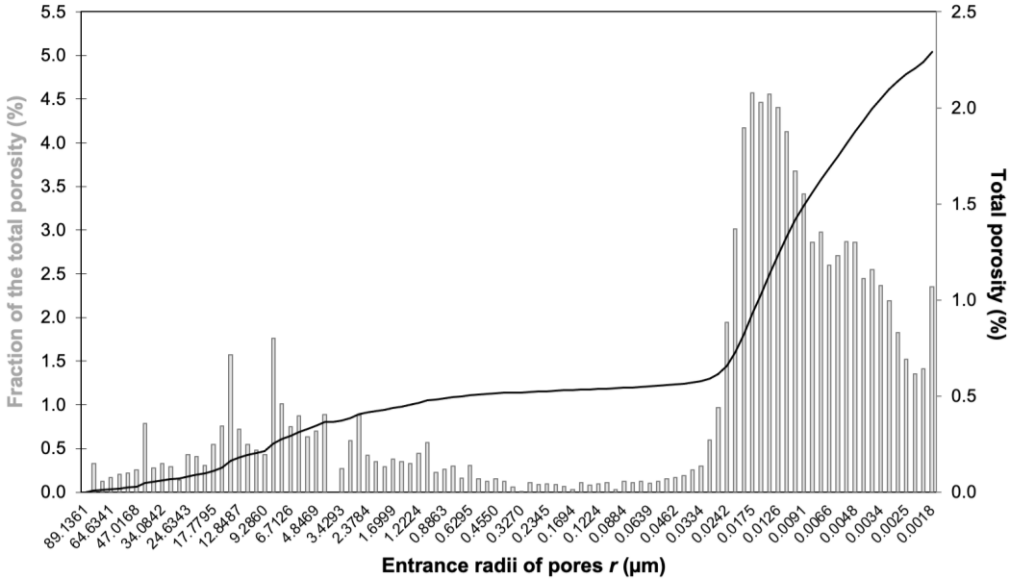

Fig 3.4: Distribution of entrance radii of pores (porous spectrum) and cumulative pore volume obtained by mercury intrusion porosimetry on a rock salt sample

Fig 3. 5 represents voids distribution in Sample 3 and Sample 4 obtained from X-ray tomography. Because of the low voxel resolution (126 μm) due to the large sample size, only large voids (much larger than the voids accessible with mercury intrusion porosimetry) can be seen. These voids are randomly oriented and localized mainly in isolated clusters. This is consistent with the results obtained by Li et al. (2019) on a similar rock (gypsum) using the same technique (CT scan) with a very similar voxel resolution (126 μm). Their analysis showed that the initial pores in gypsum rock were isolated from each other and distributed uniformly in the specimen, which did not provide a preferred flow path. The extraction from voxel data of some voids and their ellipsoidal approximation showed that pores shape in rock salt is close to sheet-like crack. An example of such ellipsoidal approximation is given in Fig 3. 5. These crack-like voids represent only 0.1% of the total volume for Sample 3. However, considering the low voxel resolution, this value is probably underestimated.

The total porosity of rock salt calculated from the volumetric mass densities (Eq. 1) on four large cylindrical samples is equal to 0.8%, 2.3%, 0.9% and 0.9% (mean value = 1.2%). With this technique, all voids (cracks and pores) are accessible. The obtained values and their variability are very close to the values obtained from mercury intrusion porosimetry on small samples.

Therefore, the total porosity of rock salt is composed predominantly of infrapores (of nanometric size) that connect dispersed cracks and macropores. This large porous spectrum with a high prevalence of infrapores suggests a multiscale porous network that could impact gas flow. As already suggested by De Las Cuevas (1997), infraporosity reflects probably the porosity inherent to the intact rock and microporosity is probably related to the presence of clay minerals. Macroporosity and cracks, which are randomly distributed, can be explained by stress relaxation and sample preparation.

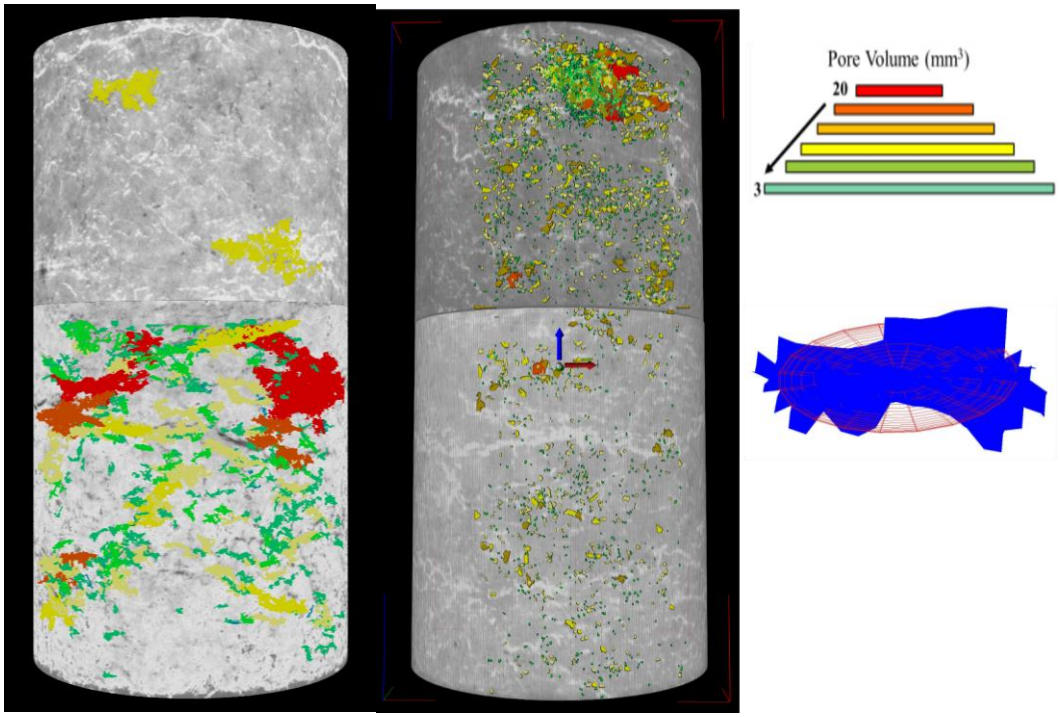

Fig 3. 5: Voids distribution in large cylindrical rock salt samples of 100 mm of diameter and 200mm of length (Sample 3 to the right, Sample 4 to the left) from X-ray tomography (126μm of resolution) and a void approximated with an ellipsoid.

3.5. Mechanical behaviour of rock salt

3.5.1. Behaviour under hydrostatic loading and poromechanical coupling

Fig 3. 6 represents the strain curves and the evolution of the bulk modulus *K* as a function of confining pressure obtained from the hydrostatic compression test on a cubic sample of rock salt (Sample 1). It results that rock salt is mechanically isotropic since deformation is almost the same in the three main directions. Besides, the behaviour is almost elastic (i.e., reversible) and linear from 0 to 30 MPa. The linearity of the volumetric strain curve at the beginning of the loading suggests the absence of large initial cracks. However, when confining pressure is completely unloaded at the end of the test, the volumetric strain curve is not completely equal to zero. This small irreversible volumetric deformation (~0.01%) that occurred during the test could be explained by the irreversible closure of initial voids. This is confirmed by the evolution of the drained bulk modulus *K* (calculated from the unloading curves) which increases from 25000 MPa to 30000 MPa; the rock salt becomes stiffer.

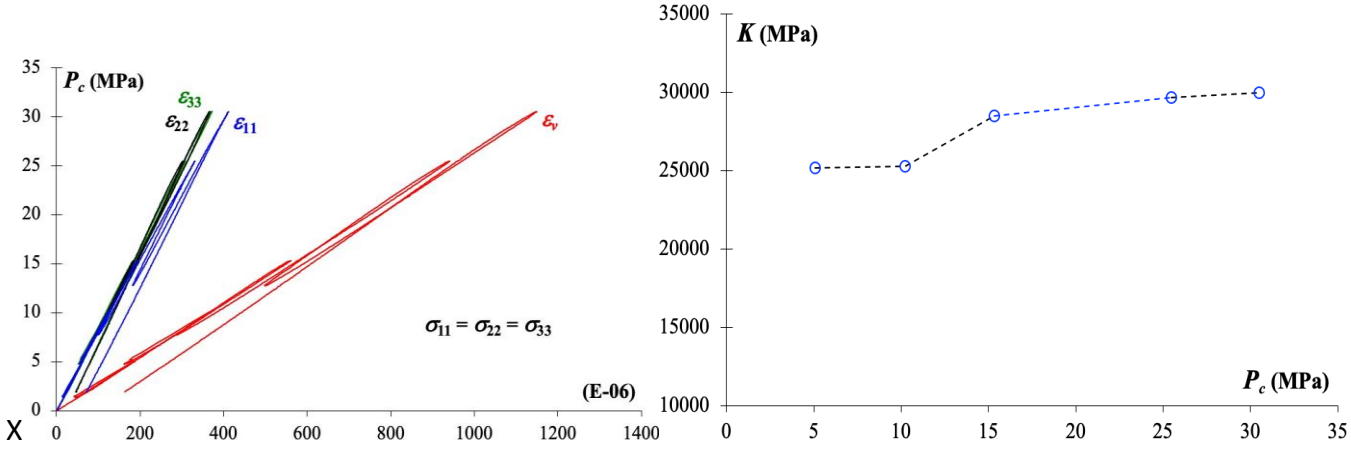

Fig 3.6: Hydrostatic compression test on a cubic sample of rock salt (Sample 1): stress-strain curves (left) and evolution of the bulk modulus K as a function of confining pressure (right).

The Biot's coefficient *b* has been identified from an isotropic test constituted by successive 2-step incremental loadings: a confining pressure loading followed by a pore pressure loading (Eq. 6). Four increments were performed: 0-5, 5-10, 10-15, 15-20 MPa. This isotropic loading has been applied on a large cylindrical sample of rock salt (Sample 2) before and after a triaxial compression test (P_c = 1 MPa) until 16 MPa (Sample 2, Fig. 7). It results that the Biot's coefficient remains equal to zero for the initial sample, i.e., no deformations induced by pore

pressure increase were observed. For soils, b is equal to 1 and for rocks it is generally less than 1. In the latter case, it means that the compressibility of the solid matrix K_s is not negligible compared to the drained compressibility of the porous material K. When b = 0, it means that the connected voids (cracks and pores) are almost negligible; then $K \sim K_s$. Therefore, this confirms that the initial connected voids volume of our salt specimens is very small. After the uniaxial compression test, the Biot's coefficient barely increases. It is equal to 0.15 at P_c = 10 MPa and decreases to zero at higher confining pressures. This small increase is therefore due to a small damage induced by the deviatoric stress. To conclude, the initial Biot's coefficient of our rock salt is equal to zero and the impact of damage is almost negligible. However, this is not the case for all rock salt specimens. For example, Zhang et al. (2020) performed the same kind of poromechanical test on rock salt cores that also come from a Cenozoic sedimentary basin in East of France. They found much higher values for b (up to 0.37) with a much greater sensitivity to the confining pressure and to the material's damage due to crack generation during triaxial test. These high b values can be explained by the initial state of their salt specimen, which probably contain more voids (pores and cracks) than our rock salt sample.

It is worth emphasizing that this Biot's theory applies for an elastic medium only but the behavior of the rock salt is unlikely to be elastic during isotropic or deviatoric loadings. Therefore, the measured Biot's coefficient is "apparent" and can mainly be used to highlight the gas-skeleton coupling intensity, as already noticed by Zhang et al. (2020). Considering the results obtained from this test, we can consider that the poroelastic coupling is almost negligible in our rock salt specimens. Indeed, increase in pore gas pressure doesn't induce significant volumetric expansion and the Biot's coefficient remains equal to zero whatever the level and the nature (isotropic or deviatoric) of the stress state. Therefore, a pore pressure increase doesn't decrease the mean stress through the effective stress concept (Eq. 3) which doesn't apply in our rock salt (i.e., effective stress = total stress). This means that during permeability measurements, the variations in gas pressure will not affect significantly the effective confining pressure which will remain almost equal to the total confining pressure.

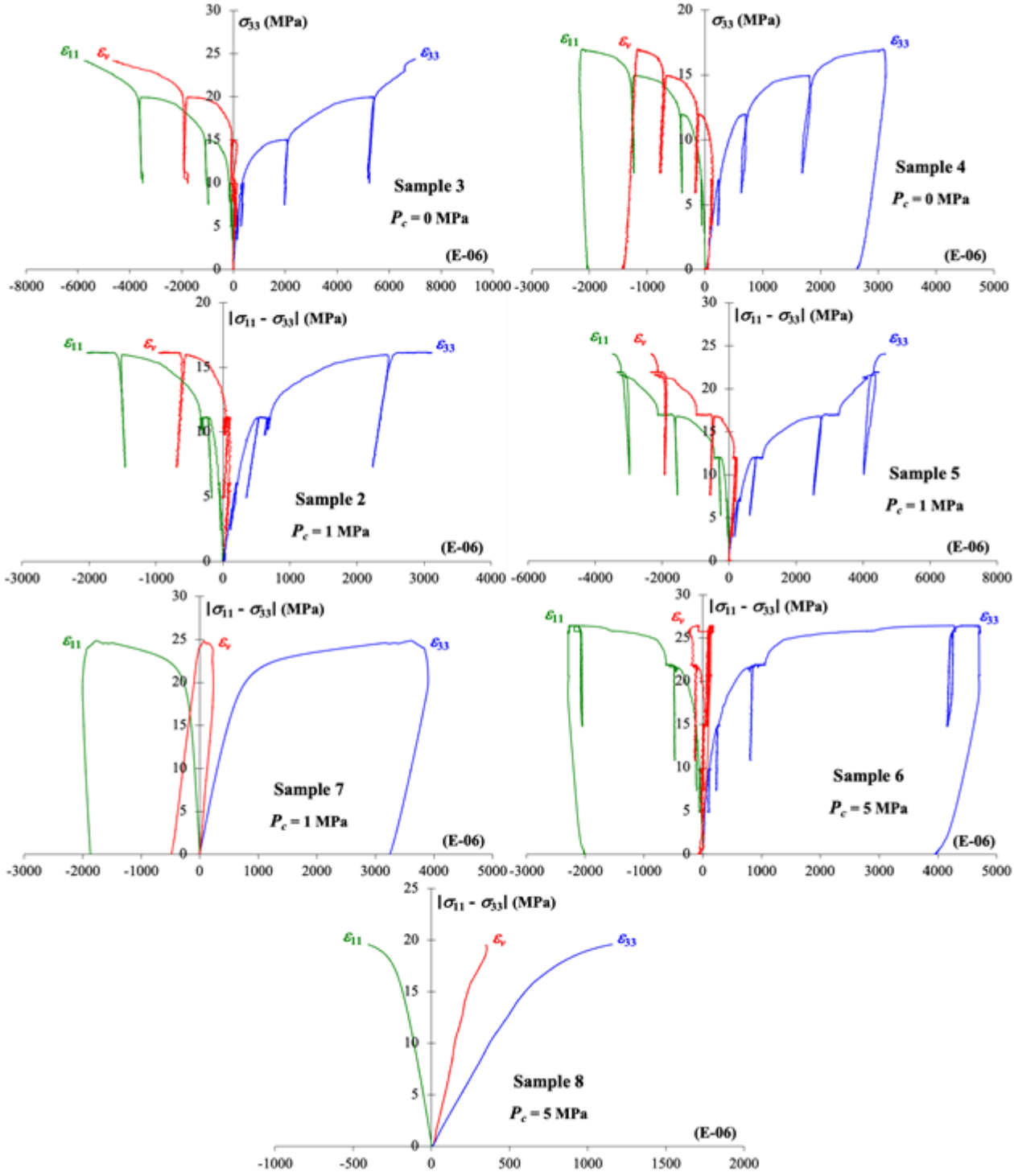

Fig 3.7: Stress-strain curves of uniaxial and triaxial compression tests on rock salt Samples 2, 3, 4, 5, 6, 7 and 8.

3.5.2. Behaviour under deviatoric loading

The progressive failure process of intact brittle rocks is generally split into different stages based on stress-strain characteristics displayed during short-term uniaxial and triaxial laboratory tests (e.g., Bieniawski 1967; Martin and Chandler 1994; Hoek and Martin 2014, Eberhardt et al. 1998). Axial and lateral deformation measurements allow the determination of the following stages limited by (deviatoric) stress thresholds.

- Crack closure threshold:

From the beginning of the loading until this threshold, the stress-axial strain response is nonlinear and exhibits an increase in axial deformation modulus. This stage corresponds to the closure of pre-existing cracks oriented at an angle to the applied main stress. From this stage, when most of pre-existing cracks have closed, stress-strain curves display a linear elastic behaviour.

- Crack initiation threshold:

At the stress where the lateral strain curve departs from linearity, micro-fracturing begins and crack growth remains stable until the next threshold. Under stable condition, crack length depends on the applied stress and crack growth can then be stopped if the applied stress doesn't increase anymore.

- Unstable cracking (or crack damage) threshold:

At the point of reversal in the volumetric strain curve, a transition from compression (cracks closure and pore volume reduction) to dilatation (cracks reopening, microcracking and pore volume expansion) occurs. From this dilatancy threshold, crack propagation becomes unstable and strain becomes localized. Under this unstable condition, the propagation process is then controlled by the crack growth velocity and crack growth would progress even if the applied stress remains constant. This threshold corresponds then to the long-term strength of the rock.

- Peak strength:

Unstable cracking continues until the coalescence of micro-cracks. At this point, the rock cannot support any additional stress increase. It is worth emphasizing that the compressive strength is not an intrinsic rock property; it depends on loading conditions (e.g., loading rate). Crack initiation and crack damage thresholds, which are independent of loading conditions, are more characteristic of the material strength.

These different stages describe the progressive failure process of intact brittle or semi-brittle rocks. However, under uniaxial or triaxial compression, the response of rock salt differs significantly because its mechanical behaviour is dominated by plastic deformation processes with a marked tendency for strain hardening Fig 3. 7. The represents the evolution of strains during the uniaxial and triaxial compression stress-cycling tests on Samples 2, 3, 4, 5, 6, 7 and 8. For triaxial compression tests with cyclic loading (Samples 2, 5 and 6), the stress plateau visible after each unloading-reloading cycle corresponds to the deformation during the permeability measurement. The Tab 3. 2 presents the characteristic thresholds (crack initiation and dilatancy) determined from the stress-strain curves.

Our experimental curves highlight the same mechanisms and present the same characteristics as those of other similar laboratory tests on rock salt in the literature, despite the heterogeneity of our rock salt samples:

- The crack closure threshold is close to 0 whatever the confining pressure (0, 1, 5 MPa), thus indicating the absence of large initial cracks as already shown from the hydrostatic compression test (Fig 3. 6).

- The elastic limit (yield strength) is very low for all tests and the axial strain curve is non-linear almost from the beginning of the loading because of the inelastic (plastic) mechanism.

- The crack initiation threshold and the unstable cracking threshold, which corresponds to dilatancy boundary, tend to increase with the confining pressure, which is a classical phenomenon for rocks (Tab 3. 2). However, this tendency is not perfect because of the material heterogeneity (mineralogical composition, initial cracks). Also, it is worth noting that strain gages do not always allow the best measurement of the material deformation, and then the best estimation of the characteristic thresholds, because they measure the deformation locally, whereas the stress and strain fields in cylindrical samples are not uniform during uniaxial/triaxial compression tests as a consequence of friction between the loading platens and the specimen ends. In addition, rock salt generally exhibits small volumetric deformation which is all the more delicate to estimate. Under the dilatancy threshold, irreversible deformations are isochoric (no volumetric deformation), as already shown by Thorel (1994) on the same rock salt specimen. Beyond the dilatancy threshold, the damage of the material is responsible for the emergence of dilatant irreversible volumetric deformations. Induced cracks are generally vertically oriented and the cylindrical symmetry is globally conserved. Under uniaxial loading condition, the dilatancy threshold of our rock salt is about 10 MPa (Tab 3. 2), as already shown by Thorel (1994). This dilatancy threshold is a turning point from which important changes in halite property are happening. In the dilatant domain, the cumulated damage caused by progressive micro-cracking during loading is responsible for the decrease in strain hardening (Schulze et al. 2001) and can induce a very significant increase (by many orders of magnitude) of permeability. Actually, permeability increases beyond the dilatancy boundary for many types of rocks because the cracks are interconnected, thus forming hydraulic pathways for fluids flow. In the non-dilatant compaction domain, micro-cracks are compacted, closed or even healed, and further micro-cracking is suppressed, thus decreasing permeability (Schulze et al. 2001).

- Micro-cracking develops mainly at low confining pressures (0 and 1 MPa). When rock salt Sample 4 (P_c = 0 MPa) and Sample 7 (P_c = 1 MPa) are completely unloaded at the end of the test, very significant permanent (irreversible) deformations are observed (Fig 3. 7), as already shown by Liu, et al. (2014) from cyclic loading uniaxial tests. These nonrecoverable inelastic deformations can result from propagation and motion of dislocations in crystals, mass diffusion, and microcracking at low confining pressure. Since the nonrecoverable volumetric strain is dilatant, the dilatant microcracking damage was the dominant mechanism during the loading.

- For higher confining pressure (P_c = 5 MPa, Samples 6 and 8), the dilatancy of the volumetric strain reduces almost to zero (Fig 3. 7), thus indicating the absence of micro-fracturing. When Sample 6 is completely unloaded at the end of the test, very significant irreversible deformations are observed. Since the nonrecoverable volumetric strain is almost equal to zero, only the isovolumetric plastic mechanism was involved during the loading. In the ductile (fully plastic) regime, the propagation and motion of dislocations in crystals leads to material strain hardening which is due, on the microscopic level, to the increasing number of dislocations and to the interactions developing between them as well as with various microstructural obstacles during straining (Yahya et al. 2000). The behaviour of halite can become fully plastic (ductile), even at room temperature, if the mean stress is high and the deviatoric stress much lower than the peak strength, which can practically eliminate micro-fracturing (Thorel 1994; Aubertin et al. 1993) and then material dilatancy. From the ductile transition, the macroscopic failure of the tested samples is not observed anymore despite very significant axial deformations. The ductile transition of halite is obtained for confining pressures about 5-10 MPa (Senseny et al. 1992; Handin et al. 1986; Liang et al. 2007). Thorel (1994) found that the ductile transition is about 10 MPa for the rock salt from the Alsace potash mines and that for higher values, the influence of confining pressure on plastic deformation decreases rapidly (stress-strain curves are barely higher).

- The unloading-reloading curves are very linear and much stiffer than the loading curve, even for the lower cycle, which means that irreversible mechanisms (plasticity, voids closure) develop from almost from the beginning of the loading. The elastic constants estimated from the unloading curves are scattered from a sample to another. There is no obvious influence of stress (confining pressure, deviatoric stress) on these elastic constants as already shown by many authors (Senseny et al. 1992; Schulze et al. 2001, Thorel 1994), even though the slopes of the unloading stress-strain curves would be expected to decrease because of the microcracking damage.

Tab 3.1: Characteristic thresholds determined from stress-strain curves of uniaxial and triaxial compression tests on rock salt samples

Sample	**3**	**4**	**9**	**2**	**5**	**7**	**6**	**8**
Pc (MPa)	0	0	0	1	1	1	5	5
Crack initiation threshold (MPa)	6.5	4.5	4.5	6	7	8	12	7
Dilatancy threshold (MPa)	12	7.5	-	10.5	11	20	15.5	19.5

The Fig 3. 8 represents the evolution of strains and static elastic moduli (E_{33}, ν_{31}) during the uniaxial compression stress-cycling test on Sample 9. There is no significant evolution of the static elastic moduli during this test. The value of crack initiation threshold is similar to those obtained on Samples 3 and 4 (Tab 3. 2). However, for this test, there is no dilatancy in the volumetric strain curve deduced from the axial and lateral strains. Indeed, as said above, strain gages do not always allow the best estimation of the volumetric deformation because they measure the deformation locally. Global measurements are more appropriate for an accurate estimation of the volumetric deformation during a uniaxial/triaxial compression test. Those can be achieved for example with LVDT sensors (for the axial displacement between the loading platens), circumferential chain extensometers (for the lateral deformation), and measurement of the volume change of the confining fluid in the triaxial cell (for the volumetric deformation). Rouabhi et al. (2019) showed, from both experimental and numerical investigations, that the strain measurements techniques (local, global or hybrid) during triaxial compression tests can provide different volumetric results with significant deviations from the idealized behaviour, and hence different dilatancy onsets. This is explained by the relatively small values of the volumetric strain of rock salt. To improve the interpretation of the dilatancy boundary during uniaxial/triaxial compression tests, measurements of acoustic emissions were performed in many studies on rock salt (Alkan et al. 2007; Schulze et al. 2001)) or on brittle and semi-brittle rocks (Grgic and Amitrano 2009; Eberhardt et al. 1999; Ohnaka and Mogi 1982; Lockner 1993). A sudden increase in the cumulative number of acoustic events is observed at the dilatancy boundary. The measurement of ultrasonic wave velocities is also a technique that allows a good global estimation of dilatancy boundary. They are very sensitive to micro-cracking, then the dilatancy onset is detected in slightly lower deviatoric stresses than from classical volume change measurements. This technique was already used for this purpose by Ayling et al. (1995) on sandstone, Popp et al. (2001) and Schulze et al. (2001) on rock salt. However, in these studies, only a limited number of compressional-wave velocity and shear-wave velocity measurements were performed and only in the direction of the maximum principal compressive loading axis. In this study on rock salt, we measured continuously 5 ultrasonic wave velocities in 3 directions, as we already did in a previous study on a limestone (Eslami et al. 2010).

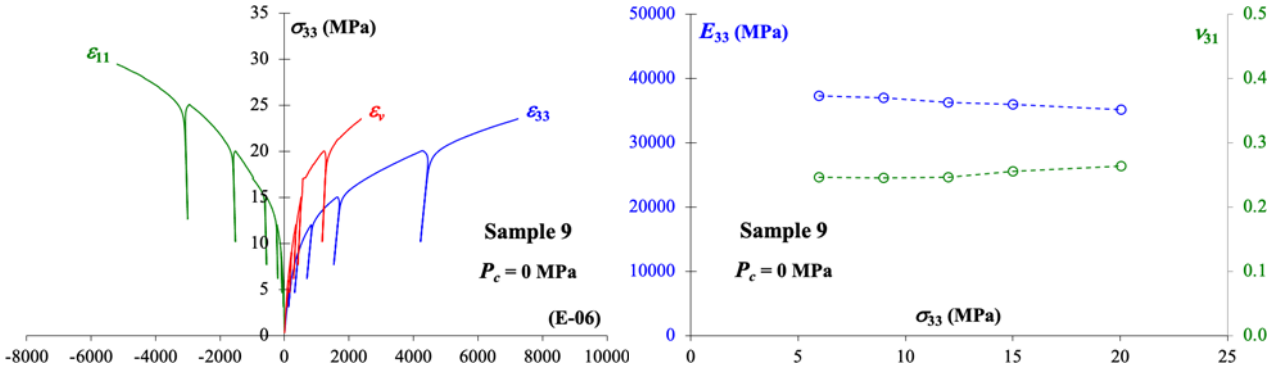

Fig 3.8: Uniaxial compression test on rock salt Sample 9: evolution of strains (left) and P- and static elastic constants (right)

The Fig 3. 9 represents the evolution of velocities during the uniaxial compression stress-cycling test on Sample 9. The evolution of P- and S-wave velocities reproduces very remarkably the shape and features of the stress–strain curves, including unloading–reloading cycles. The initial values of P-wave velocities and the initial values of S-wave velocities are identical whatever the direction of propagation and polarization. This confirms that the rock salt is initially isotropic. $VP_{90°}$ increases continuously from the beginning of the loading until 18 MPa, which indicates the preferential closure of pre-existing micro-cracks and penny-shaped pores that are perpendicular, or almost perpendicular, to the uniaxial stress direction. This increase is almost linear and not very significant (+180 m/s), which means that the initial cracks volume is very small as already shown from the hydrostatic compression test (Fig 3. 6). Besides, the unloading curves of $VP_{90°}$ are more and more stiff with stress increase and $VP_{90°}$ remains greater than its initial value, which suggests that irreversible mechanisms (closure/healing of pre-existing micro-cracks and plasticity with strain hardening) develop progressively in the direction of the uniaxial stress and increases material stiffness. The decrease of $VP_{0°}$ (and VP_{θ}) from approximately 11 MPa indicates that the opening of axial micro-cracks, whose direction is parallel or almost parallel to the axis 3 of the applied uniaxial stress, is the dominant deformation mechanism, at least for low confining pressures. This dilatancy threshold, which is a very important turning point, can be estimated very precisely with the ultrasonic method. After unloading, $VP_{0°}$ remains lower than its initial value, which confirms that the damage is irreversible, as shown by the unloading of the volumetric strain curve of Sample 4 (Fig 3. 7). $VSh_{0°}$ and $VSv_{0°}$ also decrease but in a less extent; shear waves are less sensitive to micro-cracking damage. $VP_{90°}$ starts to decrease from 18 MPa and this decrease is moderate

because this velocity can hardly record the opening of axial micro-cracks which is parallel to the lateral directions 1 and 2. The compressional P-wave velocity $VP_{0°}$ detects therefore better dilatancy threshold than the P-wave velocity $VP_{90°}$ which is parallel to the direction of the maximum principal stress. It is interesting to compare (Fig 3. 9) these US wave velocities measurements with those we already obtained (Eslami et al. 2010) on a semi-brittle isotropic rock (limestone) under the same loading conditions. The behaviour is quite similar except for $VP_{90°}$. For the limestone, $VP_{90°}$ increases much more (+500 m/s) and not linearly because the initial cracks volume is much more significant, and this increase in $VP_{90°}$ is partially reversible after unloading thus indicating that cracks closure is partially reversible. These very important differences show that irreversible mechanisms such as closure/healing of micro-cracks and plasticity with strain hardening, are very specific to soft rocks like halite.

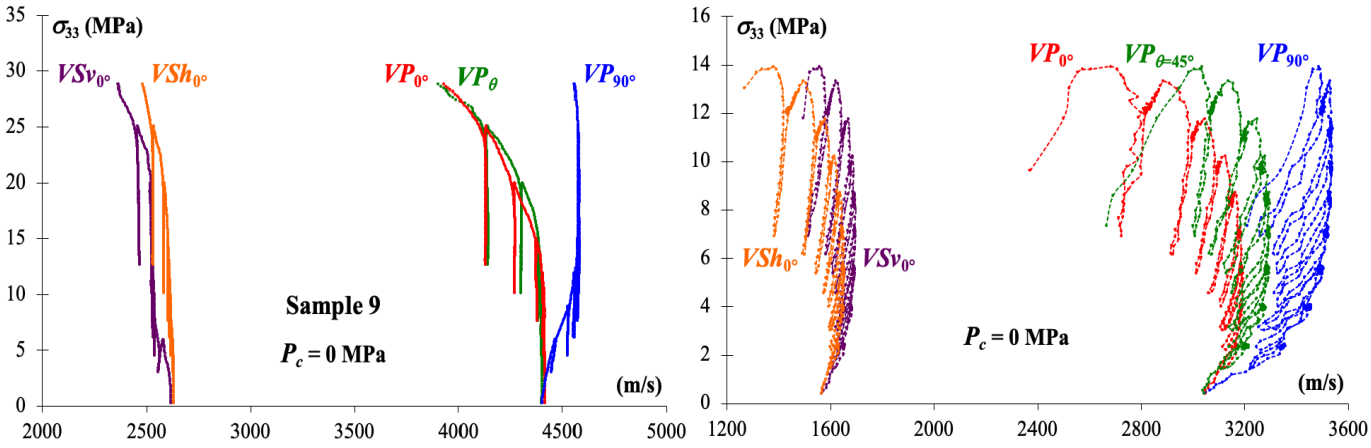

Fig 3.9: Left: evolution of P- and S-wave velocities during the uniaxial compression test on rock salt Sample 9. Right: evolution of P- and S-wave velocities during an uniaxial compression test on a limestone sample (from Eslami et al. 2010)

The Fig 3. 10 represents the evolution of the five dynamic coefficients of the elastic compliance tensor (Young's moduli E_{11} and E_{33}, Poisson's ratios ν_{12}, ν_{13} and ν_{31}) and the Thomsen's dimensionless anisotropy factors (ε and γ). The evolution of E_{11} and E_{33} confirms that the material becomes stiffer in the axial direction 3 and more compliant in the lateral direction 1. The Poisson's ratios ν_{13} and ν_{31} start to decrease from 18 MPa, thus evidencing the preferential opening of axial micro-cracks and the decrease in the material stiffness in the lateral direction. Because of these deformation mechanisms (closure/healing of pre-existing micro-cracks and plasticity with strain hardening in the axial direction, preferential opening of axially oriented micro-cracks), the P-wave anisotropy ε and S-wave anisotropy γ increase progressively during the loading. P-waves are more influenced by these mechanisms than S-waves and the anisotropy remains relatively small. The rock salt, initially isotropic, becomes therefore slightly anisotropic (transverse isotropy). It is worth emphasizing that these Thomsen's dimensionless parameters were initially introduced to interpret the wave velocities in initially transverse isotropic materials under the "weak anisotropy" hypothesis. In such materials, because of the presence of isotropic planes (e.g., bedding in shales) perpendicular to the axis 3, $C_{11} > C_{33}$ and $\varepsilon > 0$ initially and during the loading. In initially isotropic materials such as rock salt, $C_{11} = C_{33}$ before loading and, because of the anisotropy induced by loading, C_{33} becomes larger than C_{11} and $\varepsilon < 0$. Therefore, we considered the absolute value of ε for the purpose of this study.

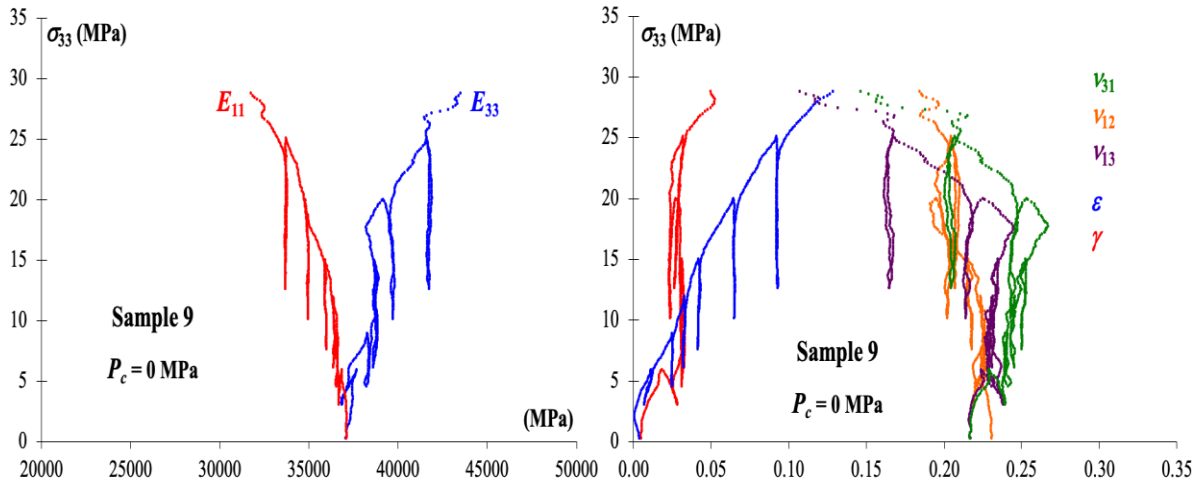

Fig 3. 10: Uniaxial compression test on rock salt Sample 9: evolution of dynamic elastic constants (E11, E33, v13, v31 and v12) and dimensionless anisotropy factors (ε and γ).

3.6. Permeability evolution during mechanical and thermal loadings

3.6.1. Intrinsic permeability and Klinkenberg effect

Fig 3. 11 represents the evolution of apparent permeability as a function of mean gas pressure for samples 2, 3, 4, 5, 6, 10 and 12. For Samples 2, 5 and 6, the gas permeability with different gas pressures was measured for different deviatoric stress levels. For Sample 3 and 4, the gas permeability with different gas pressures was measured for the lowest confining pressure (P_c = 1 MPa). For Sample 10, the gas permeability with different gas pressures was measured during the hydrostatic compression stage (2 days), then for different deviatoric stress levels during the loading and finally during the creep stage (10 days) at $|\sigma_{11} - \sigma_{33}|$ ~ 16 MPa. For Sample 12, the gas permeability with different gas pressures was measured before and after thermal fatigue. The Klinkenberg effect (i.e., decrease of permeability with the increase in gas pressure) is only observed for the less permeable (and then less initially damaged) samples, i.e. Samples 3, 5, 6 and 12. For Sample 10, the Klinkenberg effect appears at the end (2 days) of the hydrostatic compression stage because of the self-healing process that will be discussed later. In all cases where this effect appears, the exponential fit (dotted lines in Fig 3. 11) gives the best results. Hence, the exponential empirical correlation (Eq. 14) provides the better correction of the Klinkenberg effect, which is necessary to estimate the intrinsic permeability. This means that in initially intact (i.e., undamaged) rock salt samples, gas flow should fall in transitional regime (Fig 3. 12). This analysis is supported by a crude estimate of Knudsen number (Eqs. 10-11) based on the median pore diameter of intact rock salt d_{50} (~0.03 μm, Fig 3. 4), i.e., the pore diameter at which 50% of the pores are smaller than, and the physical properties of *He*, which leads to K_n values ranging from 0.15 (for the lowest mean gas pressure) to 0.05 (for the highest mean gas pressure).

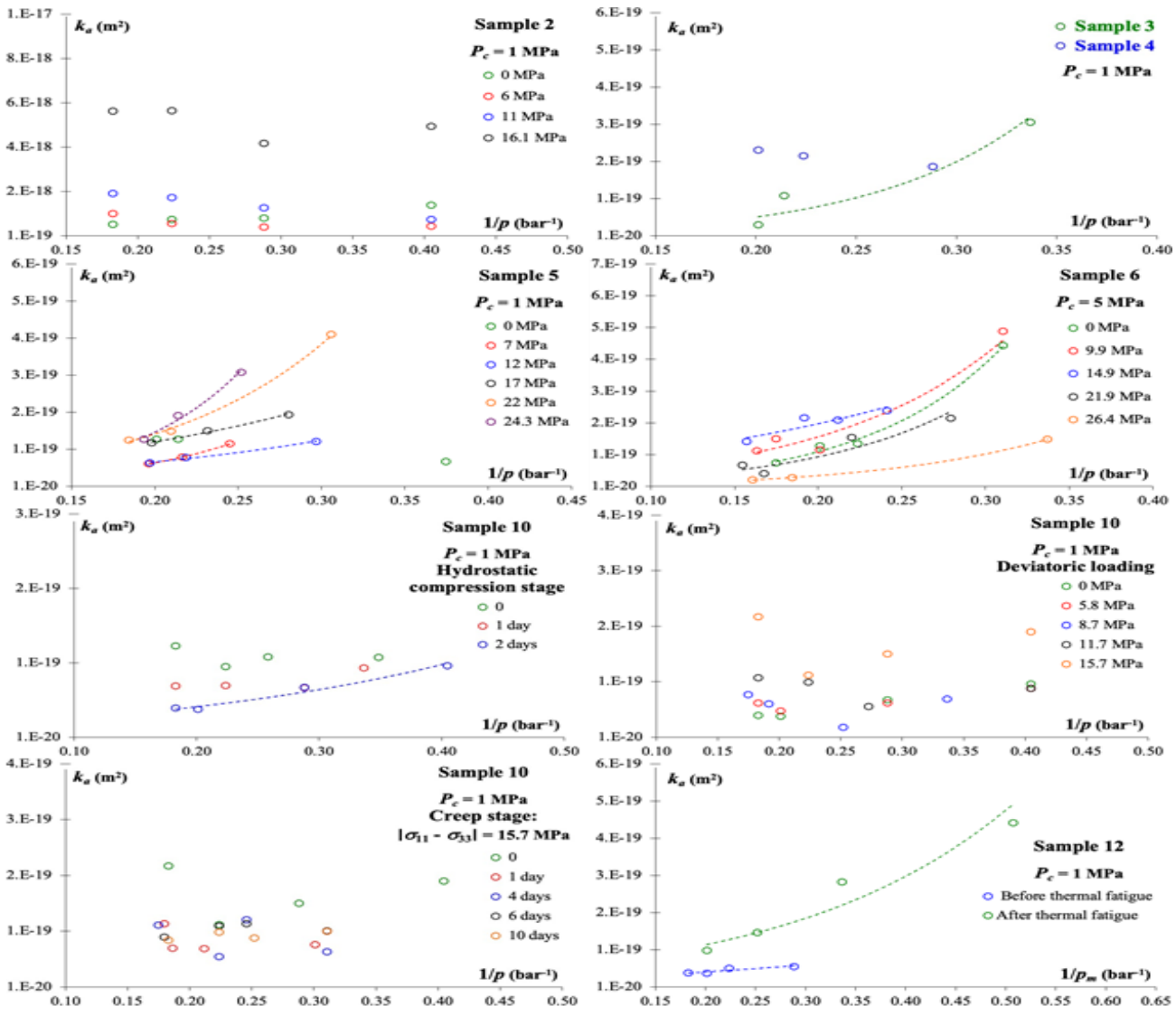

Fig 3.11: Evolution of apparent permeability ka as a function of mean gas pressure for rock salt Samples 2, 3, 4, 5, 6, 10 ,12

The values of initial intrinsic permeability k_∞ and the constant α of the slippage correction equation (3.14) for the samples with Klinkenberg effect (Samples 3, 5, 6 and 12) are given in Tab 3. 3. Intrinsic permeability was calculated at the beginning of each experiment (i.e., before any mechanical or thermal loading), except for Sample 5 for which the lowest deviatoric stress level (curve "7 MPa") was considered. Indeed, the Klinkenberg effect is visible for all deviatoric stress levels for this sample, except for the first one (0 MPa) corresponding to the unloaded state. If it is not an experimental artefact, this could be explained by an initial macroscopic crack that was closed during the deviatoric loading. α values were given at different deviatoric stress levels for Samples 5 and 6, and before and after the thermal treatment for Sample 12. The constant α seems to not be influenced by the increase in deviatoric stress for Sample 5 and 6; its variations don't show any trend. For the samples without Klinkenberg effect (Samples 2, 4 and 10), k_∞ (Tab 3. 3) is defined simply as the mean value of the apparent permeabilities corresponding to the different gas pressures. For Samples 7, 8 and 11, the permeability was measured continuously with a constant gas pressure and then Klinkenberg effect wasn't analyzed. It is reasonable to assume that there is no Klinkenberg effect for these samples because of their high initial permeability. It is worth noting that all these values were obtained under a confining pressure of 1 MPa.

The initial permeabilities of our rock salt samples are very scattered and vary over a wide range (4.5 orders of magnitude), which confirms the mechanical heterogeneity highlighted before. The highest value (1.1×10^{-16} m^2) is very important compared to that conventionally expected for a healthy (i.e., undamaged) rock salt (from 10^{-20} to 10^{-21} m^2). This large permeability range in the as-received samples, which has already been identified in previous studies (e.g., Popp et al. 2001), is a classical problem with rock salt. Large values of initial permeability are primarily due to the presence of pre-existing cracks. Cracks are caused by the stress relaxation, which induces severe deviatoric stresses in the excavation damaged zone of salt caverns or by the decompaction induced by drilling, core retrieval and sample preparation. Some authors (e.g., Schulze et al. 2001) applied an isostatic re-compaction and healing treatment (in general, high confining pressure and temperature during a few days) on rock salt samples before testing to reduce the damage produced by drilling and preparation of specimens or to restore the in-situ matrix permeability which is in general lower than 10^{-20} m^2.

Tab 3.2: Initial intrinsic permeability k∞ and constant α (if appropriate) of the slippage correction (Eq. 14) for all rock salt samples

Sample	**2**	**3**	**4**	**5**	**6**	**7**	**8**	**10**	**11**	**12**
k_∞ (m^2)	9.5×10^{-19}	5.0×10^{-21}	2.2×10^{-19}	6.9×10^{-21}	1.1×10^{-20}	2.9×10^{-18}	3.0×10^{-17}	1.2×10^{-19}	1.1×10^{-16}	2.7×10^{-20}
α		12.5		11.8 5.7 5.7 9.6 14.1	12.0 9.4 5.6 11 9.4					3.2 4.6

3.6.2. Evolution of apparent gas permeability with stress increase

Fig 3. 12 (left) represents the evolution of apparent permeability k_a as a function of deviatoric stress for Samples 2, 5, 6, 7, 8 and 10. For Samples 7 and 8, the permeability was measured continuously during the deviatoric loading with a gas pressure of 5 bar. For Samples 2, 5, 6 and 10, the permeability was measured at different deviatoric stress levels during the triaxial loading and with different gas pressures (3.4-11 bar). For comparison purpose with Samples 7 and 8, we represented for these four samples the mean value of the permeabilities corresponding to the different gas pressures for each deviatoric stress level.

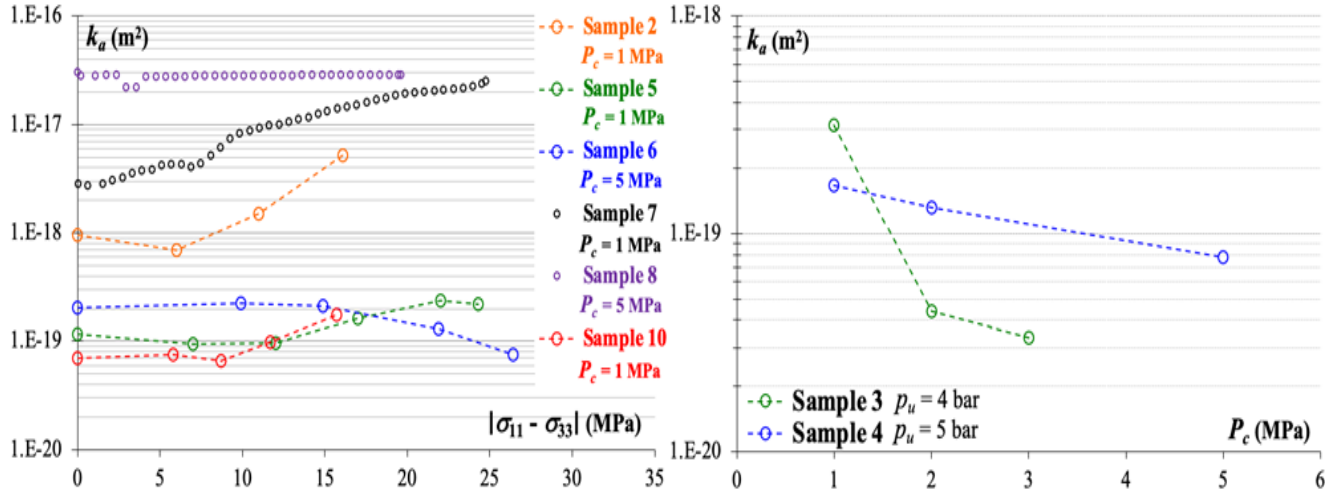

Fig 3. 12: Left, evolution of apparent permeability ka as a function of deviatoric stress for Samples 2, 5, 6, 7, 8 and 10. Right, evolution of apparent permeability ka as a function of confining pressure Pc for Samples 3 and 4.

For the lower confining pressure (1 MPa), Samples 2, 5, 7 and 10 show a moderate increase in gas permeability with deviatoric stress, whatever the value of their initial permeability. The largest increase (one order of magnitude) is observed for Sample 7, which can be explained by the shorter duration of this experiment, which limits damage recovery that could occur when the test duration is too long. The mean value of deviatoric stress threshold from which permeability starts to increase significantly is about 10 MPa even though it is difficult to determine this value for Samples 2, 5 and 10 because only a small number of permeability measurements were performed on them. This value is close to the dilatancy threshold (11 MPa) determined from US wave velocities measurements during a uniaxial compression test (Fig. 3.9). For higher confining pressure (5 MPa), Samples 6 and 8 don't show any permeability increase with deviatoric stress because rock salt becomes fully plastic which practically eliminates microcracking damage process and then material dilatancy if the deviatoric stress is much lower than the peak strength. This is the case in our experiments because the maximal deviatoric stress applied is only 26 MPa for Sample 6, whereas the peak strength of this rock salt is about 50 MPa for a confining pressure of 5 MPa (Thorel 1994). Actually, for Sample 6, permeability decreases at high deviatoric stresses (from 15 MPa), which can be explained by the damage recovery. This process is more significant during the experiment on Sample 6 because it lasted longer than experiment on Sample 8, as said previously. Indeed, for a given stress level, the permeability measurements at different gas pressures last from 0.5 to 1.5 hour and this whole experiment lasted 25 hours while the experiment on Sample 8 lasted only 2.8 hours.

In similar previous studies on natural and synthetic rock salt (e.g., Popp et al. 2001; Zhang et al. 2020; Peach and Spiers 1996; Schulze et al. 2001), a rapid and very significant permeability increase (occasionally over four orders of magnitude) with dilatancy was observed, even at high confining pressures (5-10 MPa). The reason why we observed only a moderate increase in gas permeability (maximum one order of magnitude at a low confining pressure of 1 MPa) in our experiments is first due to the very plastic nature of the mechanical behaviour of our rock salt specimen. Indeed, as shown previously, our specimen become fully plastic (ductile) with no dilatancy from a moderate confining pressure of 5 MPa. Even at lower confining pressure (0-1 MPa), we didn't observe very significant dilatant volumetric deformations (Fig 3.7). Moreover, we applied on our samples only moderate deviatoric stresses (maximum ~ 25 MPa) that are much lower than the peak strength. In these previous studies, much higher deviatoric stresses (up to 50 MPa) were applied with much larger resulting deformations (up to 20% axial strain). Actually, we limited the deviatoric stresses applied in our study to the conditions at the wall of a salt cavern at a depth of 600-700 m (considering lithostatic pressure and an isotropic initial stress state).

Fig 3.12 (right) represents the evolution of apparent permeability k_a as a function of confining pressure P_c for Samples 3 and 4. The permeability was measured with a gas pressure of 4 bar for Sample 3 and 5 bar for Sample 4. The focus herein is on the impact of confining pressure on permeability. The permeability decreases more for Sample 3 (one order of magnitude) than for Sample 4. This can be explained by the initial permeability value which is lower for Sample 3 than for Sample 4 (Tab 3. 3). Similar experiments in the literature (e.g., Sutherland and Cave 1980; Zhang et al. 2020; Popp et al. 2001) already showed a strong effect of confining pressure on the gas permeability of rock salt for values up to 35 MPa. We limited the confining pressure to 5 MPa in our compression (triaxial and hydrostatic) tests to be representative of the stress conditions at the near field of salt caverns (excavation damaged zone). Actually, an increase in confining pressure in these short-term experiments causes the

closure of voids (cracks and pores) which induces a permeability decrease. This recompaction, which is consistent with the increase in the drained bulk modulus *K* during the hydrostatic compression test on Sample 1 (Fig 3.6), is partially reversible, as already shown by Zhang et al. (2020).

However, many authors (e.g., Zhang et al. 2020; Popp et al. 2001) have shown that this decrease of permeability is irreversible, which indicates a time-dependent (irreversible) closure of pores and microcracks. The compaction of rock salt under confining pressure is partly elastic but mostly plastic and the experiment duration controls the permeability and voids reduction, in addition to pressure, temperature and intercrystalline humidity (Peach 1991; Popp et al. 2001). Hence, compaction can give rise for the restoration of the permeabilities of undisturbed natural rock salt if the confining pressure and time of run are high enough (Popp et al. 2001). To study this time-dependent effect, we applied on Sample 10 a confining pressure of 1 MPa during 2 days and we measured gas permeability each day. Fig 3. 13 (left) represents the evolution of the intrinsic permeability k_∞ as a function of time during this long-term hydrostatic compression. The permeability measurements for this test are represented in Fig 3. 13. At day 0 (beginning of the test) and day 1, permeability measurements didn't show any Klinkenberg effect, then the intrinsic permeability is the mean value of the permeabilities corresponding to the different gas pressures. From day 2, gas slippage effect occurred, then the intrinsic permeability was determined from the exponential correlation equation (3.14). The apparition of Klinkenberg effect suggests an irreversible closure of initial pores and micro-cracks of rock salt due to the healing mechanism. Many authors (e.g., Chen et al. 2013, Sutherland and Cave 1980; Zhang et al. 2020) already studied in laboratory this irreversible self-healing process under hydrostatic compression with experiments that lasted up to several weeks. Cracks healing is difficult to achieve but, despite the relative short-duration (2 days) of our long-term hydrostatic compression test and the low confining pressure applied (1 MPa), it allowed a significant decrease (half an order of magnitude, from 1.2×10^{-19} to 2.4×10^{-20} m^2) of permeability and then the relative restoration of the undamaged state of our rock salt specimen.

3.6.3. Impact of mechanical and thermal fatigue on rock salt permeability

3.6.3.1. Static (creep test) and dynamic (cyclic) mechanical fatigue

The impact of mechanical fatigue, under static triaxial loading (creep test) and dynamic/cyclic triaxial loading on rock salt permeability was studied from experiments on Samples 10 and 11. Fig 3. 13 (right) represents the strain curves and permeability measurements during the triaxial creep stage (10 days) of the long-term experiment on Sample 10. For a deviatoric stress of ~16 MPa, significant viscoplastic deformations are observed and the two first stages (primary and secondary) of creep are identifiable. During the secondary stage, the creep rate decreases slowly because of the strain hardening mechanism, which is related to immobilization and piling up of dislocations at a barrier and causes an increase in dislocation density. Moreover, the volumetric deformation is dilatant due microcracking damage mechanism that also develops during the creep because of the low confining pressure (1 MPa). Permeability measurements didn't show any Klinkenberg effect during the deviatoric loading and the creep stage (Fig 3.11), then the intrinsic permeability is the mean value of the permeabilities corresponding to the different gas pressures. The gas permeability decreases just a little at the beginning of the creep process, even though the low confining pressure favoured material dilatancy. This means that the different mechanisms involved in the sample deformation, namely viscoplasticity with strain hardening, microcracking damage and cracks healing, act in a competitive way to annihilate any significant permeability evolution. Of course, this statement needs to be confirmed with other creep tests at higher deviatoric stresses.

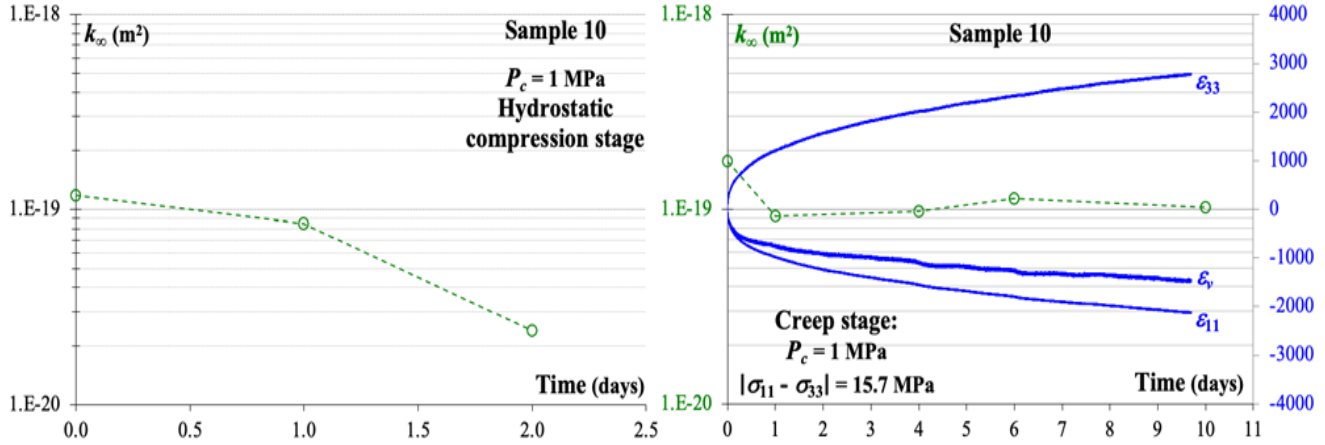

Fig 3.13: Evolution of permeability k∞ and deformations as a function of time during the long-term experiment on Sample 10 (hydrostatic compression stage followed by a triaxial creep stage).

Fig 3.14 represents the evolution of intrinsic permeability k_a and volumetric deformation as a function of time during the cyclic/dynamic triaxial compression test (with static stages) on Sample 11. A low confining pressure (1 MPa) was applied to favour microcracking damage and mimic the stress conditions at the very near field of salt caverns (excavation damaged zone). The three deviatoric stress levels, which are 6, 15 and 25 MPa, represent about 17, 43 and 71%, respectively, of the compressive strength (~35 MPa) of the rock salt for a confining pressure of 1 MPa (Thorel 1994). The volumetric deformation increases significantly during the three series of loading-unloading cycles and it is dilatant (negative), which means that dynamic fatigue induces microcracking damage in rock salt, as already shown by Liu et al. (2014) from cyclic loading uniaxial tests. During the two intermediary static stages (constant deviatoric stress), the volumetric strain evolves in the positive direction (dilatancy decreases) probably because of the self-recovery from damage of rock salt. Permeability was measured continuously during the whole test, except during the second static stage due to an experimental problem. Considering the high permeability (~10^{-16} m^2) of this rock salt sample, there is probably no Klinkenberg effect, then the measured gas permeability is the intrinsic permeability. The evolution of gas permeability is not very significant but some tendencies can be identified. The gas permeability increases a little during the dynamic fatigue (mainly visible during the first series of cycles) and decreases slowly during the static stage (creep). At the end of the third series of loading-unloading cycles, the deviatoric stress was unloaded slowly and permeability decreased also slowly during this stage. The permeability evolution is then consistent with the evolution of the volumetric deformation:

- Dynamic fatigue induces material damage and dilatancy and then a small permeability increase.
- During the static stage, self-recovery reduces damage and then decreases dilatancy and slightly the permeability, which is consistent with the experiment (creep test) on Sample 10 (Fig 3. 13).

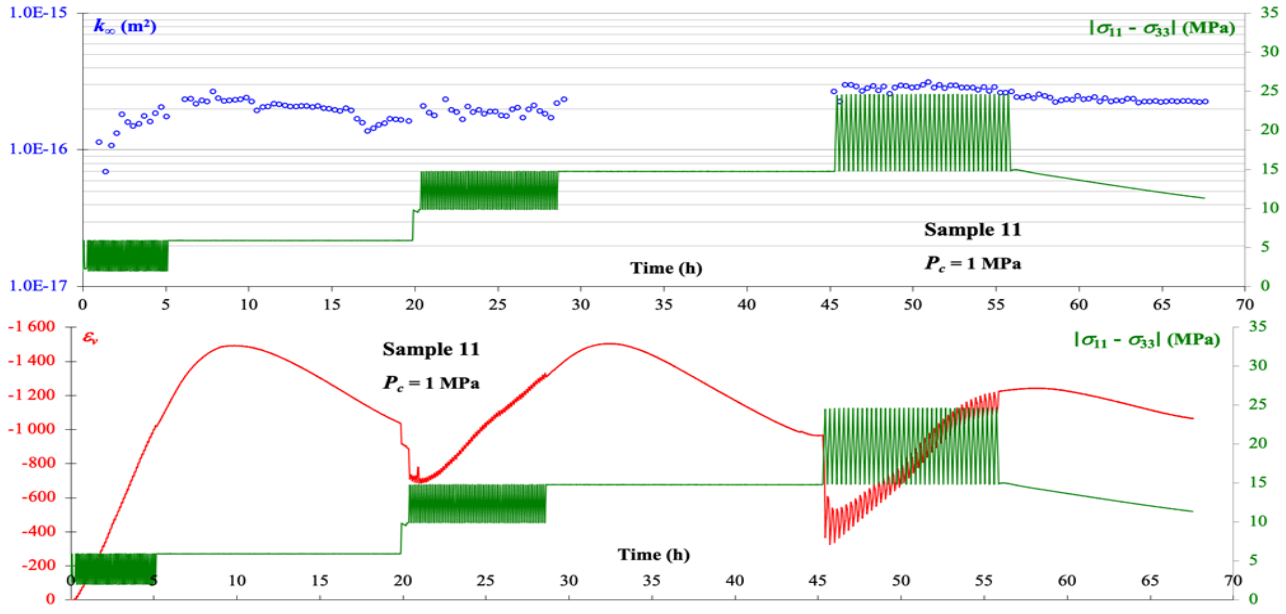

Fig 3. 14: Evolution of permeability k∞ and volumetric deformation as a function of time during the cyclic triaxial compression test on Sample 11

3.6.3.2. Cyclic thermal fatigue

The impact of thermal cyclic fatigue on rock salt permeability is analysed from the experiment on Sample 12. Fig 3. 15 represents the evolution of volumetric deformation as a function of time during this test. The material deformation remains isotropic during the whole test. For each cycle, temperature increase induces obviously material dilatation and temperature decrease induces material contraction. The contraction is more significant than the dilatation and, at the end of the experiment, an irreversible positive (contractant) deformation is observed. The amplitude of deformation cycles increases progressively and stabilizes after a few hours, which is probably due to the thermal inertia of the material. Indeed, the temperature represented in Fig 3.15 is measured in the climatic chamber with a thermocouple positioned close to the sample but it doesn't represent the temperature in the sample's core. The gas permeability has been measured before and after this thermal treatment with different gas pressures (Fig 3.15). The apparent permeability increases a little after the cyclic thermal fatigue. For this sample, Klinkenberg effect is present, then the intrinsic permeability k_∞ is calculated from the exponential correlation equation (3.14). The intrinsic permeability increases also a little from 2.7×10^{-20} m^2 to 4.9×10^{-20} m^2 because of the cyclic thermal fatigue.

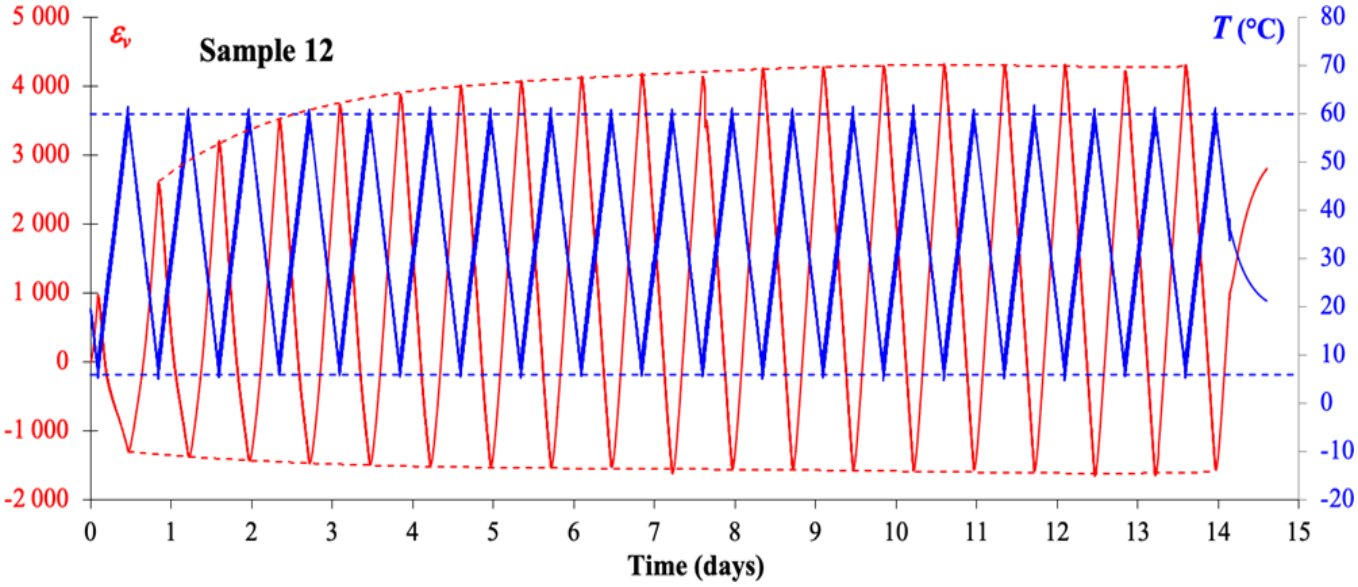

Fig 3.15: Evolution of volumetric deformation as a function of time during the thermal cyclic fatigue test on Sample 12

This increase can be attributed to the material damage induced by this treatment. First, it is worth emphasizing that, compared to the in-situ case (i.e., at the wall of a storage cavern), this experiment is an uncoupled thermo-mechanical problem since the sample can deform freely during the temperature variations. However, at the microscopic scale, cracking damage can develop. Indeed, rocks like rock salt are constituted by minerals which are anisotropic most of the time and whose coefficient of thermal expansion can therefore vary depending on the axis considered. The deformations induced by temperature variations (elongation or shortening of crystals) are therefore anisotropic, which can induce differential thermal stresses and thus microcracking. Moreover, rocks such as salt are generally formed by more than one type of rock forming minerals which can induce deformation heterogeneities from one grain to another and then (tensile and compressive) thermal stresses. If these stresses exceed the failure strength, intergranular and intragranular cracks can develop. A lot of similar laboratory experiments (cyclic thermal fatigue) can be found in the literature. Most of them (e.g., Feng et al. 2020; Yu et al. 2020, Hu et al. 2021) were performed on crystalline rocks such as granite within the framework of geothermal energy extraction and underground storage of high-level nuclear waste, and much larger thermal amplitudes are generally applied on samples in a furnace. Hu et al. (2021) showed that with increasing temperature, the uneven thermal expansion and thermal shock effect of minerals promote crack development, leading to increases in the porosity and permeability of granite, particularly at temperatures above 450°C. Although cycles with relatively small thermal amplitude (6-60 °C) were applied on our rock salt specimen, microcracking damage also developed and induced a (relatively small) permeability increase.

3.7. Conclusions

We performed a complete set of laboratory experiments on a rock salt specimen (salt bed of the Alsace potash mines in the East region of France) to study the very complex relation between the permeability evolution and the mechanical and thermal solicitations. The complexity is due to the specific features of the mechanical behaviour (large plastic deformation capacity, good creep properties, microcracking damage, cracks healing) of rock salt and gas flow in such unconventional reservoir (Klinkenberg effect). First, the initial microstructure of rock salt was identified with different porosity methods and with X-ray 3D tomography. Then, different short-term mechanical tests (hydrostatic compression tests, uniaxial and triaxial compression tests, uniaxial compression test with five ultrasonic P and S-wave velocities measurement) was performed on large core samples to characterize the poromechanical behaviour (deformation mechanisms, elastic properties, Biot's coefficient) of our rock salt specimen. The gas (helium) permeability was measured with the steady-state method under hydrostatic compression and under triaxial compression (with different confining pressures). Permeability measurements were performed at different stress levels and continuously to analyse the impact of the deformation mechanisms on the permeability evolution, and at different gas pressure to characterize the Klinkenberg effect. The impact of static (creep test) and dynamic (cyclic) mechanical fatigue and the impact of cyclic thermal fatigue on rock salt permeability were also analysed.

The porosity of rock salt is very low (~1%) and is composed predominantly of infrapores (of nanometric size) that connect dispersed cracks and macropores. This large porous spectrum corresponds to a multiscale porous network that impacts gas flow. The initial permeabilities of our rock salt samples are very scattered and vary over 4.5 orders of magnitude (10^{-16}-5×10^{-21} m^2). Some permeability values are very important compared to that conventionally expected for a healthy (i.e., undamaged) rock salt (from 10^{-20} to 10^{-21} m^2). This wide permeability range in the as-received samples is primarily due to the presence of cracks caused by the stress relaxation (induced by core drilling or cavity excavation) and sample preparation. The Klinkenberg effect (i.e., decrease of permeability with the increase in gas pressure) is only observed for the less permeable (and then less initially damaged) samples. When it appears, the exponential empirical correlation gives the better estimation of the intrinsic permeability, which means that gas flow falls in transitional regime in weakly damaged rock salt.

The mechanical behaviour of rock salt is isotropic and linear elastic (until 30 MPa) under hydrostatic loading. The hydrostatic loading induces the irreversible closure of initial voids, thus increasing material stiffness. The Biot's coefficient is equal to zero in a sample with high initial permeability (~10^{-18} m^2) and remains almost equal to zero after being damaged with a uniaxial compression test (until a deviatoric stress of 16 MPa). Then we consider that the poroelastic coupling is almost negligible in our rock salt specimens, which means that the effective mean stress is almost equal to the total mean stress. Under deviatoric loading, rock salt exhibits the following features: very low elastic limit (yield strength), crack initiation threshold and the unstable cracking threshold (dilatancy boundary) tends to increase with the confining pressure, dilatant and irreversible micro-cracking damage develops mainly at low confining pressures (0 and 1 MPa), the behaviour becomes almost fully plastic (ductile) from a confining pressure of 5 MPa. The measurement of five ultrasonic P and S-wave velocities during a uniaxial compression test showed the preferential closure of pre-existing micro-cracks and penny-shaped pores that are perpendicular, or almost perpendicular, to the uniaxial stress direction and the opening of axial micro-cracks, whose direction is parallel or almost parallel to the axis of the applied uniaxial stress. The closure of micro-cracks is almost irreversible which is very specific to the rock salt. Because of these deformation mechanisms, the rock salt, initially isotropic, becomes slightly anisotropic (transverse isotropy). The ultrasonic method allows a more precise determination of the dilatancy threshold (11 MPa under uniaxial loading condition) than with strain gages. Dilatancy threshold, which is a very important turning point from which important changes in halite property can happen, i.e. very important increase of permeability due to cumulated microcracking damage.

During deviatoric loading (up to 25 MPa), a moderate increase in gas permeability (up to one order of magnitude) has been measured for the lower confining pressure (1 MPa). Permeability starts to increase approximately from the dilatancy threshold identified from the compression tests. For higher confining pressure (5 MPa), no increase in permeability was measured because the material becomes fully plastic which practically eliminates microcracking damage process and then material dilatancy. If the test duration is too long, damage recovery restores the initial permeability. The moderate impact, compared to other studies in the literature, of deviatoric stress on permeability of our rock salt could be explained by its very plastic nature, even at low confining pressures and temperature. Under hydrostatic loading (up to 5 MPa), the gas permeability decreases (one order of

magnitude) because of the closure of voids (cracks and pores). This decrease of permeability is irreversible if the confining pressure and time of run are high enough, which can give rise for the restoration of the permeabilities of undisturbed natural rock salt. This can be explained by an irreversible closure of initial micro-cracks due to the healing mechanism. We showed that, even at a low confining pressure (1 MPa) and for a relatively short-term (2 days) experiment, a significant decrease (half an order of magnitude) of permeability was measured thanks to the cracks healing process. Static and dynamic (cyclic) mechanical fatigue tests with a confining pressure of 1 MPa showed that dilatancy develops and increases slightly the permeability during the dynamic stage due to microcracking damage, while self-recovery reduces damage and decreases slightly the permeability during the static stage. Then, the different mechanisms (viscoplasticity with strain hardening, microcracking damage and cracks healing) involved in the rock salt deformation during dynamic and static fatigue act in a competitive way to annihilate any significant permeability evolution. Cyclic thermal fatigue induced a small permeability increase due to the cracking damage that develops at the microscopic scale. This is due to the anisotropy of the thermal deformation of rock forming minerals and to the polycrystalline nature of rock salt, which can induce deformation heterogeneities and then differential thermal stresses and microcracking damage.

As a conclusion, for the purpose of underground hydrogen storage in deep salt caverns, fractures and associated permeability increase in the near field (i.e., close to the cavity wall) could promote hydrogen leakage because of the excavation that induces high deviatoric stress and because of the gas pressure (high-frequency) cycles that induce temperature and stresses changes. Fortunately, the thickness of this excavation damaged zone is relatively small and the increase of damage and permeability within this zone should be moderate especially for highly plastic type of rock salt as the one investigated in the present study. In addition, self-recovery from damage and good creep properties of rock salt prevent any significant long-term permeability increase. Therefore, the low permeability of rock salt and the integrity of the storage project will not be negatively impacted. All these experimental results support that advective gas leakage through cavern walls should be negligible and give more clue about future exploitation of salt caverns for hydrogen storage. More attention, however, should be paid to the contribution of other mechanisms of gas transport (see a recent review of AbuAisha and Billiotte, 2021, on this topic), especially by diffusion of dissolved hydrogen into pore brine. Further research should be also conducted to extend this study to various types of rock salt and determine the most appropriate rock salt formations for hydrogen storage.

3.8. Acknowledgements

This research was funded by the French Scientific Interest Group GEODENERGIES in the framework of the ROSTOCK-H project (Risks and Opportunities of the Geological Storage of Hydrogen in Salt Caverns in France and Europe).

3.9. References

AbuAisha, M. & Billiotte, J., 2021. A discussion on hydrogen migration in rock salt for tight underground storage with an insight into a laboratory setup. *Journal of Energy Storage*, 38 :102589.

Abuaisha, M. & Rouabhi, A., 2019. On the validity of the uniform thermodynamic state approach for underground caverns during fast and slow cycling. *International Journal of Heat and Mass Transfer*, 142:118424.

Alkan, H., Cinar, y. & Pusch, G., 2007. Rock salt dilatancy boundary from combined acoustic emission and triaxial compression tests. *International Journal of Rock Mechanics and Mining Sciences,* 44(1), pp. 108-119.

Aubertin, M., Sgaoula, J. & Gill, D.E., 1993. A damage model for rocksalt: application to tertiary creep. Proceedings of the 7th Symposium on Salt, Kyoto, Tokyo, vol. 1, 1993. pp. 117-25.

Ayling, M.R., Meredith, P.G., Murrel, S.A.F., 1995. Microcracking during triaxial deformation of porous rocks monitored by changes in rock physical properties, I. Elastic-wave propagation measurements on dry rocks. *Tectonophysics*, Volume 245, Issues 3–4, Pages 205-221.

Bernabé, Y. Gaseous flow through heterogeneous, partially connected networks of pipes. Sci Rep 8, 14956 (2018).

Beskok, A. & Karniadakis , G., 1999. Report: a model for flows in channels, pipes, and ducts at micro and nano scales. *MicroscaleThermophysical Engineering,* Volume 3, pp. 43-77.

Beskok, G., Karniadakis, E. & Trimmer, W., 1996. ASME. *J.Fluids Eng,* Volume 448, p. 118.

Bieniawski, Z.T. 1967. Mechanism of brittle rock fracture. Part I. Theory of the fracture process. *International Journal of Rock Mechanics and Mining Sciences & Geomechanical Abstracts*, 4(4): 395-406.

Biot M., 1941. General theory of three dimensional consolidation. Journal of Applied Physics; 12(2):155–164.

Blanco-Martín, L., Rouabhi, A., Billiotte, J., Hadj-Hassen, F., Tessier, B., Hévin, G., Balland, C. & Hertz, E., 2018. Experimental and numerical investigation into rapid cooling of rock salt related to high frequency cycling of storage caverns. *International Journal of Rock Mechanics and Mining Sciences*, 102, 120-130.

Brouard, B., Berest, P., Djizanne, H., & Frangi, A., 2012. Mechanical stability of a salt cavern submitted to high-frequency cycles. In Mechanical Behavior of Salt VII (pp. 381-390). Taylor & Francis Group.

Chen, J. et al., 2013. Self-Healing Characteristics of Damaged Rock Salt under Different Healing Conditions.. *Materials,* 6(8), p. 3438–3450.

Cui, X., Bustin, A.M.M. & Bustin, R.M., 2009. Measurements of gas permeability and diffusivity of tight reservoir rocks: different approaches and their applications. *Geofluids*, 9, 208–223.

De Las Cuevas, C., 1997. Pore structure characterization in rock salt. *Engineering geology,* 47(1-2), pp. 17-30.

Drury, M.R.& Urai, J.L., 1990. Deformation-related recrystallization processes. Tectonophysics, 172, 235–253.

Eberhardt, E. D., Stead, D. & Stimpson, B., 1999. Quantifying progressive pre-peak brittle fracture damage in rock during uniaxial compression. *International Journal of Rock Mechanics and Mining Sciences,* 36(3), pp. 361-380.

Eberhardt, E. D., Stead, D. & Stimpson, B. & Read, R.S., 1998. Identifying crack initiation and propagation thresholds in brittle rock. *Can. Geotech. J*., 35: 222-233.

Eslami, J., Grgic, D. & Hoxha, D., 2010. Estimation of the damage of a porous limestone from continuous (P- and S-) wave velocity measurements under uniaxial loading and different hydrous conditions. Geophysical Journal International, Vol. 183: 1362–1375.

Feng, G., Wang, X., Wang, M. & Kang, Y., 2020. Experimental investigation of thermal cycling effect on fracture characteristics of granite in a geothermal-energy reservoir. *Engineering Fracture Mechanics*, Volume 235.

Florence, F. A., Rushing, J. A., Newsham, K. E. & Blasingame, T. A., 2007. *Improved permeability prediction relations for low-permeability sands.* Denver, Colorado, SPE papers.

Freeman, C. J., Moridis, G. J. & Blasingame , T. A., 2011. A numerical study of microscale flow behavior in tight gas and shale gas reservoir systems. In: *Transport in Porous Media.* s.l.:s.n., pp. 253-268.

Gloyna, E. F. & Reynolds, T. D., 1961. Permeability measurements of rock salt. *Journal of geophysical research,* 66(11), pp. 3913-3921.

Grgic, D. & Amitrano, D., 2009. Creep of a porous rock and associated acoustic emission under different hydrous conditions. Journal of Geophysical Research B: Solid Earth, Vol. 114 (Issue B10), 19p.

Hoek, E. & Martin, C.D., 2014. Fracture initiation and propagation in intact rock – A review. *Journal of Rock Mechanics and Geotechnical Engineering*, 6, 287-300.

Hu, J., Xie, H., Li, C., & Sun, Q., 2021. Effect of Cyclic Thermal Shock on Granite Pore Permeability. *Lithosphere 2021*; 2021 (Special 5): 4296301.

Klinkenberg, L. J., 1941. The permeability of porous media to liquids and gases. In: *Drilling and Production Practice.*

Labaune, P., Rouabhi, A., Tijani, M., Blanco-Martín, L. & You, T., 2018. Dilatancy criteria for salt cavern design: a comparison between stress and strain-based approaches. *Rock Mechanics and Rock Engineering,* 51(2), pp. 599-611.

Letham, E. A. & Bustin, R. M., 2016. Klinkenberg gas slippage measurements as a means for shale pore structure characterization. *Geofluids ,* 16(2), pp. 264-278.

Li, W., Einstein, H. H., & Germaine, J. T., 2019. An experimental study of matrix dissolution and wormhole formation using gypsum core flood tests: 1. Permeability evolution and wormhole geometry analysis. *Journal of Geophysical Research: solid earth*, 124(11), 11055-11073.

Li, J. & Sultan, A., 2016. Klinkenberg slippage effect in the permeability computations of shale gas by the pore-scale simulations. In: s.l.:s.n.

Liu, J., Xie, H., Hou, Z., Yang, C. & Chen, L., 2014. Damage evolution of rock salt under cyclic loading in unixial tests. *Acta Geotechnica,* 9(1), pp. 153-160.

Lockner, D.A., 1993. The role of acoustic emission in the study of rock fracture. *Int. J. Rock Mech.Min. Sci. and Geomech. Abstr*., 30(7), 883–899.

Lv, Q., Wang, E., Liu, X. & Wang, S., 2014. Determining the intrinsic permeability of tight porous media based on bivelocity hydrodynetics. Microfluid Nanofluid 16, 841–848.

Martin, C.D. & Chandler, N.A., 1994. The Progressive Fracture of Lac du Bonnet Granite. *Int. J. Rock Mech. Min. Sci. & Geomech. Abstr*., Vol. 31, No. 6, pp. 643-59.

Ohnaka, M. & Mogi, K., 1982. Frequency characteristics of acoustic emission in rocks under uniaxial compression and its relation to the fracturing process to failure, *J. geophys. Res*., 87(B5), 3873–3884.

Pazdniakou , A. et al., 2018. Numerical efficiency assessment of the lattice Boltzmann model for digital nano-porous rock applications. *Advances in Water Resources,* Volume 121, pp. 44-56.

Peach, C. J., 1991. Influence of deformation on the fluid transport properties of salt rocks. *Geologica Ultraiectina,* volume 77, pp. 1- 238.

Peach, C. J. & Spiers, C. J., 1996. Influence of crystal plastic deformation on dilatancy and permeability development in synthetic salt rock. *Tectonophysics,* 1(4), pp. 101-128.

Popp, T., Kern, H. & Schulze, O., 2001. Evolution of dilatancy and permeability in rock salt during hydrostatic compaction and triaxial deformation. *Journal of Geophysical Research:Solid Earth,* 106(B3), pp. 4061-4078.

Present, R. D., 1958. Kinetic theory of gases. s.l.:McGraw-Hill.

Rouabhi A., Hévin G., Soubeyran A., Labaune P. and Louvet F., 2017. A multiphase multicomponent modeling approach of underground salt cavern storage. *Geomechanics for Energy and the Environment*, 12: 21-35.

Rouabhi, A., Labaune, P., Tijani, M., Gatelier, N. & Hévin, G., 2019. Phenomenological behavior of rock salt: On the influence of laboratory conditions on the dilatancy onset. *Journal of Rock Mechanics and Geotechnical Engineering*, 11, 723-738.

Schulze, O., Popp, T. & Kern, H., 2001. Development of damage and permeability in deforming rock salt. *Engineering Geology,* Volume 61, pp. 163-180.

Senseny P.E., Hansen F.D., Russell J.E., Carter N.L. & Handin J.W., 1992. Mechanical behaviour of rock salt: phenomenology and micromechanisms. *Int. J. Rock Mech. Min. Sci. & Geomech. Abstr*. Vol. 29, No. 4, pp. 363-378.

Smith, D.L. & Evans, B., 1984. Diffusional crack healing in quartz. J. Geophys. Res., 89 (B6): 4125-4135.

Sutherland, H. J. & Cave, S. P., 1980. Argon Gas permeability of New Mexico rock salt under hydrostatic compression. *International journal of rock mechanics and mining sciences & geomechanics abstracts.,* 17(5), pp. 281-288.

Tang, G. H., Tao, W. Q. & He, Y. L., 2005. Gas slippage effect on microscale porous flow using the lattice Boltzmann method. *Phys.Rev.E,* 72(8), p. 056301.

Tarkowski, R., 2019. Underground hydrogen storage: Characteristics and prospects. *Renewable and Sustainable Energy Reviews*, Volume 105, 86-94.

Thomsen, L., 1986. Weak elastic anisotropy. *Geophysics* 51 (10), 1954–1966.

Thorel , L., 1994. *Plasticité et endommagement des roches ductiles. Application au sel gemme,* s.l.: s.n.

Urai, J. L., Schléder, Z., Spier, C. J. & Kukla, P. A., 2008. Flow and transport properties of salt rocks. In: R. Littke, U. Bayer, D. Gajewski & S. Nelskamp, eds. *Dynamics of complex intracontinental basins: the Central European Basin system.* s.l.:Springer Science & Business Media, pp. 277-290.

Yahya, O.M.L., Aubertin, M. & Julien, M.R., 2000. A unified representation of the plasticity, creep and relaxation behavior of rocksalt. *International Journal of Rock Mechanics and Mining Sciences*, 37, 787-800.

Yu, P., Pan, P.-Z., Feng, G. Wu, Z. & Zhao, S., 2020. Physico-mechanical properties of granite after cyclic thermal shock. *Journal of Rock Mechanics and Geotechnical Engineering*, Volume 12, Issue 4.

Pages 693-706

Zhang, D., Skoczylas, F., Agostini, F. & Jeannin, L., 2020. Experimental Investigation of Gas Transfer Properties and Stress Coupling Effects of Salt Rocks. *Rock Mech Rock Eng,* 27 May, Issue 53, p. 4015–4029.

Zhu, C. & Arson, C., 2015. A Model of Damage and Healing Coupling Halite Thermo-mechanical Behavior to Microstructure Evolution. *Geotech Geol Eng ,* 33(2), p. 389–410.

Zhu, G. Y., Liu, L., Yang, Z.M., Liu, X.G., Guo, Y.G., Cui, Y.T., 2017. Experiment and Mathematical Model of Gas Flow in Low Permeability Porous Media. Proceedings of the Fifth International Conference on Fluid Mechanics, Aug.15-19, 2007, Shanghai, China.

Ziarani, A. S. & Aguilera, R., 2012. Knudsen's Permeability Correction for Tight Porous Media. *Transp Porous Med,* Volume 91, p. 239–260.

Zivar, D., Kumar, S. & Foroozesh J., 2021. Underground hydrogen storage: A comprehensive review. *International Journal of Hydrogen Energy*, Volume 46, Issue 45, 23436-23462.

4. Conclusions and perspective on storage in salt caverns

We performed a complete set of laboratory experiments on a rock salt specimen (salt bed of the Alsace potash mines in the East region of France) to study the very complex relation between the permeability evolution and the mechanical and thermal solicitations. The complexity is due to the specific features of the mechanical behavior (large plastic deformation capacity, good creep properties, microcracking damage, cracks healing) of rock salt and gas flow in such unconventional reservoir (Klinkenberg effect). First, the initial microstructure of rock salt was identified with different porosity methods and with X-ray 3D tomography. Then, different short-term mechanical tests (hydrostatic compression tests, uniaxial and triaxial compression tests, uniaxial compression test with five ultrasonic P and S-wave velocities measurement) was performed on large core samples to characterize the poromechanical behavior (deformation mechanisms, elastic properties, Biot's coefficient) of our rock salt specimen. The gas (helium) permeability was measured with the steady-state method under hydrostatic compression and under triaxial compression (with different confining pressures). Permeability measurements were performed at different stress levels and continuously to analyze the impact of the deformation mechanisms on the permeability evolution, and at different gas pressure to characterize the Klinkenberg effect. The impact of static (creep test) and dynamic (cyclic) mechanical fatigue and the impact of cyclic thermal fatigue on rock salt permeability were also analysed.

The porosity of rock salt is very low (~1%) and is composed predominantly of infrapores (of nanometric size) that connect dispersed cracks and macropores. This large porous spectrum corresponds to a multiscale porous network that impacts gas flow. The initial permeabilities of our rock salt samples are very scattered and vary over 4.5 orders of magnitude (10-16 - 5×10-21 m2). Some permeability values are very important compared to that conventionally expected for a healthy (i.e., undamaged) rock salt (from 10-20 to 10-21 m2). This wide permeability range in the as-received samples is primarily due to the presence of cracks caused by the stress relaxation (induced by core drilling or cavity excavation) and sample preparation. The Klinkenberg effect (i.e., decrease of permeability with the increase in gas pressure) is only observed for the less permeable (and then less initially damaged) samples. When it appears, the exponential empirical correlation gives the better estimation of the intrinsic permeability, which means that gas flow falls in transitional regime in weakly damaged rock salt.

The mechanical behaviour of rock salt is isotropic and linear elastic (until 30 MPa) under hydrostatic loading. The hydrostatic loading induces the irreversible closure of initial voids, thus increasing material stiffness. The Biot's coefficient is equal to zero in a sample with high initial permeability (~10-18 m2) and remains almost equal to zero after being damaged with a uniaxial compression test (until a deviatoric stress of 16 MPa). Then we consider that the poroelastic coupling is almost negligible in our rock salt specimens, which means that the effective mean stress is almost equal to the total mean stress. Under deviatoric loading, rock salt exhibits the following features: very low elastic limit (yield strength), crack initiation threshold and the unstable cracking threshold (dilatancy boundary) tends to increase with the confining pressure, dilatant and irreversible micro-cracking damage develops mainly at low confining pressures (0 and 1 MPa), the behaviour becomes almost fully plastic (ductile) from a confining pressure of 5 MPa. The measurement of five ultrasonic P and S-wave velocities during a uniaxial compression test showed the preferential closure of pre-existing micro-cracks and penny-shaped pores that are perpendicular, or almost perpendicular, to the uniaxial stress direction and the opening of axial micro-cracks, whose direction is parallel or almost parallel to the axis of the applied uniaxial stress. The closure of micro-cracks is almost irreversible which is very specific to the rock salt. Because of these deformation mechanisms, the rock salt, initially isotropic, becomes slightly anisotropic (transverse isotropy). The ultrasonic method allows a more precise determination of the dilatancy threshold (11 MPa under uniaxial loading condition) than with strain gages. Dilatancy threshold, which is a very important turning point from which important changes in halite property can happen, i.e. very important increase of permeability due to cumulated microcracking damage.

During deviatoric loading (up to 25 MPa), a moderate increase in gas permeability (up to one order of magnitude) has been measured for the lower confining pressure (1 MPa). Permeability starts to increase approximately from the dilatancy threshold identified from the compression tests. For higher confining pressure (5 MPa), no increase in permeability was measured because the material becomes fully plastic which practically eliminates microcracking damage process and then material dilatancy. If the test duration is too long, damage recovery

restores the initial permeability. The moderate impact, compared to other studies in the literature, of deviatoric stress on permeability of our rock salt could be explained by its very plastic nature, even at low confining pressures and temperature. Under hydrostatic loading (up to 5 MPa), the gas permeability decreases (one order of magnitude) because of the closure of voids (cracks and pores). This decrease of permeability is irreversible if the confining pressure and time of run are high enough, which can give rise for the restoration of the permeabilities of undisturbed natural rock salt. This can be explained by an irreversible closure of initial micro-cracks due to the healing mechanism. We showed that, even at a low confining pressure (1 MPa) and for a relatively short-term (2 days) experiment, a significant decrease (half an order of magnitude) of permeability was measured thanks to the cracks healing process. Static and dynamic (cyclic) mechanical fatigue tests with a confining pressure of 1 MPa showed that dilatancy develops and increases slightly the permeability during the dynamic stage due to microcracking damage, while self-recovery reduces damage and decreases slightly the permeability during the static stage. Then, the different mechanisms (viscoplasticity with strain hardening, microcracking damage and cracks healing) involved in the rock salt deformation during dynamic and static fatigue act in a competitive way to annihilate any significant permeability evolution. Cyclic thermal fatigue induced a small permeability increase due to the cracking damage that develops at the microscopic scale. This is due to the anisotropy of the thermal deformation of rock forming minerals and to the polycrystalline nature of rock salt, which can induce deformation heterogeneities and then differential thermal stresses and microcracking damage.

III – Hydrogen Storage in porous rock

5. Literature review

5.1. Challenges for hydrogen storage in porous rock

Storage in porous rocks is praised for its multiple benefits and ease of operation (Stone et al., 2009). It is acquainted for long-term storage over months or seasons to supply energy for urban heating or industrial needs. Porous saline aquifers and depleted hydrocarbon fields offer several orders of capacity larger than salt caverns and provide a geographically more independent and flexible solution for pumping and withdrawal cycles. However, porous media storage (aquifers, depleted reservoirs) is still on the scale of field trials or small projects even though it's the most promising technique on regional and global scales based on storage capacity and widespread geological distribution. A typical porous reservoir feature is familiar: a reservoir formation sealed by a caprock and a trapping structure. Thus, storage in porous rocks appears a more cost-effective option because this structure is familiar with well-developed infrastructure, easy to manage, and already proved its integrity to conserve the gas stock (Lord et al., 2014; Heinemann et al., 2021).

Injecting the hydrogen into the stable reservoir could cause bio-geochemical interactions between the gas, the medium, the present minerals, fluids, and indigenous microorganisms. Hence, gas loss in quantity and quality is inevitable (L. Paterson, 1983; Foh et al., 1979; Truche et al., 2013; Ebrahimiyekta, 2017). Hydrogen leakage is associated with the high mobility of the hydrogen molecule and diffusive phenomenon (describing the single-phase flow of a slightly compressible fluid) through the surrounding areas (salt, marl, clay). Injected hydrogen displaces the in-situ fluids originally present in pores (water, hydrocarbon) and spreads into the porous medium through multiphase fluid flow. Only trapping and sealing effects will prevent gas lateral escape (Heinemann et al., 2021). The hydrogen flow in such a multiphase system displays some mobility features like viscous fingering and gravity segregation. In addition, the injection point results in a highly saturated and homogenous hydrogen plume in the near well area where hydrogen is almost pure in the upper part of the reservoir. Hence, hydrogen purity and recovery potential increase with the increase of withdrawal cycles: it leads to an upcoming hydrogen accumulation in the upper part of the reservoir and water below. Therefore, the withdrawal from the top becomes easier (Sáinz-García et al., 2017; Hagemann, 2018; Luboń & Tarkowski, 2020). On the other hand, the interaction between hydrogen, the medium, and water stimulates mineral dissolution and precipitation. It could change the permeability and porosity of the media (Ganzer et al., 2013; Truche et al., 2013). It can affect the performance and the safety and stability of the storage $_{media}$ too. Batch experiments have shown significant changes in the porosity of Permian and Triassic sandstones on contact with pure hydrogen: dissolution and precipitation of anhydrite and carbonates filling the pores (Flesch et al., 2018). However, geochemical models estimated that hydrogen losses during the interaction with calcite are minor because the reaction is reversible (Bo et al., 2021). However, most hydrogen storage in porous formations is limited to gas mixtures; pure hydrogen is mainly stored in salt caverns. Hydrogen has specific physicochemical properties of density, energy, viscosity, thermal conductivity, and reactivity with other fluids and minerals in the subsoil compared to other gases like methane CH_4 and carbon dioxide CO_2. This could affect the potential of storage (Heinemann et al., 2021). Furthermore, porous media (aquifers and reservoirs) are predominantly a biotope for microorganisms. So the bio-consumption of hydrogen can also lead to significant stock alteration (Varjani & Gnansounou, 2017; Dopffel et al., 2021). It should be noted that if bacterial activity in salt has a low overall risk of H_2 conversion according to the literature, risk is higher in porous rocks. Indeed, the underground microbial life in aquifers and depleted reservoirs are found several kilometers into deep rock originated from natural sediment transport or has been anthropogenically introduced by mining, drilling, and pumping. Temperature and pressure conditions at these depths are said to be "extreme." Microorganisms capable of enduring it are called "extremophiles." Despite the presence of essential parameters of life (water, energy source, carbon, nutrients, and a variety of trace elements), cell number division in these extreme conditions is generally slow (Kirchman, 2018). Temperature, pressure, and salinity are also vital limiting factors. Other factors such as radiation, poisoning, poor permeability, and low water content also restrain bacterial proliferation (Payler et al., 2019; Dopffel et al., 2021). In anaerobic conditions of extreme environments, however, hydrogen can replace the electron donors for respiration of hydrogenothrophic bacteria producing cellular energy (Wait, 2011; Gregory et al., 2019; Dopffel et al., 2021). So, the artificial elevation of the H_2 concentration may stimulate their growth. They can consume the hydrogen stock or converted it to other forms and this could be positive or negative depending on the end use of the gas. The performance of hydrogen storage in porous rock and especially interaction with the community of microorganisms will be discussed in this chapter.

5.2. Flow and mass transport in porous rock:

5.2.1. Multiphase transport of hydrogen within the porous rock: relative permeability

To assess the hydrogen performance for storage in porous media, it's important to understand the rock-fluid interactions influencing gas flow behavior. So, we define the dynamic of fluids in the porous system considering gas permeability and relative permeability, capillary pressure, interfacial tension wettability, and contact angle of fluids (oil-hydrogen-water-sandstone). The different phases of fluids present in the porous rock can move independently in what we call a multiphase fluid transfer induced either by the difference of pressure or concentration.

Mass balance is directly related to fluid pressure and the elements concentration. The concept governs the flow law and any variation of pressure and concentration is stated directly in flow equations. Those variations are caused by mass transport via a considered volume surface when a pressure gradient is present. It can be also due to internal mass creation inside the considered volume (Boulin, 2008). The classical flow equation describing the mass conservation concept is the following (Ebrahimiyekta, 2017):

$$\frac{\partial\left(\Phi\Sigma_a S_a \rho_a X_{a,k}\right)}{\partial t} + \nabla.\sum_a (\rho_a X_{a,k} v_a + J_{\alpha,k}) = R_{a,k} + Q_{a,k} \qquad (5.1)$$

where the mass fraction is represented by $X_{\alpha,k}$ for species k in fluid phase α, Φ is the porosity, $R_{\alpha,k}$ is the reaction term (loss), $Q_{\alpha,k}$ is the source term, ρ_α is the molar density, S_α is the phase saturation, v_α is the Darcy velocity of fluid phase, $J_{\alpha,k}$ is the total diffusive and dispersive flux (Bear, 2013). This equation takes into consideration the total and the partial saturation of pores with each fluid phase. If $S\alpha$=1, the sample is assumed fully saturated. If $X\alpha,k$= 1, the medium is fully concentrated with the species. So, the absolute permeability can be determined under conditions of low stiffness. Below these values, and considering the residual water saturation (the irreducible volume of water), we need to introduce the concept of relative permeability changing Darcy's law equation (Ebrahimiyekta, 2017).

Therefore, first, we define the concept of relative permeability in presence of multiple fluids, which is the ratio between the effective permeability characterizing one fluid phase and the absolute permeability with respect to the saturation (Ahmed, 2018; Hagemann, 2018). The flow path is necessary considered as continuous and advective and Darcy's multi-phase flow equation becomes:

$$v_a = -\frac{K \times k_{ra}}{\mu_a}(\nabla P_a - \rho_a g) \qquad (5.2)$$

where K is the absolute permeability, $k_{r\alpha}$ is the relative permeability of the phase, μ_α is the phase viscosity, g is the gravity, P_α is the phase pressures. The relative permeability to gas is a dimensionless quantity between 0 and 1, if pores are saturated with gas $k_{r\alpha}$ =1.

Phase pressures are related by the absolute capillary pressure. For example, if the media contains water and gas the correlation equations will become according to Laplace law of equilibrium:

$$P_c(Sw) = P_g - P_w \qquad (5.3)$$

Where P_g the gas pressure and P_w the water pressure. Capillary pressure P_c is defined as the tension intrinsic stress induced by the liquid gas interfacial pressure created within pores. It's also locally related to the interfacial curvature at the contact between the two phases R_c and the tension stress σ of the surface by the equation:

$$P_c = \frac{\sigma}{R_c} \qquad (5.\ 4)$$

For a meniscus in a cylindrical pore with radius r, and a contact angle of δ, this same equation can be written:

$$P_c = \frac{2 \times \sigma \times \cos(\delta)}{r} \qquad (5.\ 5)$$

Pc is the capillary pressure, the contact angle for the hydrogen / water interface δ is considered 0° (assuming perfect non-wetting gas). The equilibrium between forces is secured by the pore pressure force compensating the tension. Capillary pressure closely affect the relative permeability in the porous rock storage conditions (Boulin, 2008; Ebrahimiyekta, 2017).

But the flow is not uniform and multiple chemical species can be transported within and between phases, which makes complex to express the flow gradient with respect to the advective flow only (driven by Darcy law) but requires to account for the dispersive flux also. Therefore, we define a new flux expressed as the sum of the molecular diffusion and mechanical dispersion due to the presence of multiple species and the interactions between each other:

$$J_{\alpha,k} = -\rho_\alpha (D^k_{diff,\alpha} + D^k_{disp,\alpha}) \nabla X_{\alpha,k} \qquad (5.\ 6)$$

where D_{diff} and D_{disp} are the effective molecular diffusion coefficient and effective mechanical dispersion coefficient respectively. In presence of different fluids, if a difference of concentration occurs in the stagnant conditions, it results into a random dispersive movement of suspended particles due to their collision with the fast-moving molecules in the fluid (friction): Brownian movement. This movement aiming to reduce the concentration gap is called diffusion expressed by Fick's law and the effective diffusion coefficient can be written according to the equation:

$$D_{diff,\alpha k} = \Phi S w \tau \overline{D}^k_{diff,\alpha} \qquad (5.\ 7)$$

Where α represents water phase , τ is the tortuosity of porous medium and $\bar{D}_{diff,\,\alpha k}$ is diffusion coefficient of components k in water (Loeb, 2004b; Boulin, 2008; Didier et al., 2012; Ebrahimiyekta, 2017). For non-dilute system such as multicomponent gas phase, Maxwell Stefan diffusion model can be more suited. Effective diffusion coefficient of hydrogen gas was measured in the argillite as 5 x 10^{-11} m^2/s (Boulin, 2008; Didier et al., 2012), and in saturated clay rock of 3 x 10^{-11} m^2/s (Krooss, 2008; Ebrahimiyekta, 2017). Diffusion of dissolved hydrogen in water is 4.5 x 10^{-9} m^2/s (Cussler, 2009). Diffusion of hydrogen is expected to be high in comparison with other gases. However, any major diffusive leakage was not observed in practice through the caprock of the reservoir even in case of helium, a smaller molecule and highly diffusive also (Hart, 1997; Panfilov, 2010).

On the other hand, mechanical dispersion is the flux property dependent on the structure and the heterogeneities of the porous medium and the velocity of the fluid. It's expressed by the following equation (Scheidegger, 1961):

$$D^k{}_{disp,,\alpha} = \Phi S_a \left(a_T \|\upsilon_i\| + \frac{a_L - a_\tau}{\|\upsilon_i\|} v_i v_i^T \right) \qquad (5.\ 8)$$

where a_L is the longitudinal dispersion and a_τ is the transverse dispersion. The mechanical dispersion coefficient depends on the velocity of the directional flow of the gas according to the equation above. In addition, the process is strongly influenced by the scale of measurements. Often, laboratory measurement doesn't reflect the real in-situ dispersion of gas. Tracer tests consider the longitudinal dispersion between 1m and 100m (TEK, 1989; Carriere et al., 1985; Laille et al., 1986). The transverse diversity is usually one to two orders less (Hagemann, 2018).

5.2.2. Effects of saturation, wettability and mobility of fluids in porous rock

Gas and water are non-wetting for each other in a binary multi-phase system. There is a certain equilibrium between phases. Each phase shares a part of the pore network, with gas preferring large pores and water preferring smaller pores. Phases interactions are provoked by interfaces forces between gas-water and the rock and fluids (Boulin, 2008). These forces occurring in multi-phase system form the capillary pressure.

The ability of a fluid to adhere to a surface is called wettability. It is represented by the contact angle between the phases. Water adherence to surfaces is stronger than that of gas. Thus, a multiphase system is considered to be water-wet in general: a thin film of adsorbed liquid molecules separates the solid surface from the gas in a considered pore. Hence, gas pressure is higher than water pressure (Ahmed, 2018). At a dynamic state, the flow of each phase must necessarily be advective in a very porous rock depending only on the capillary pressure. Thus, to have a continuous flow, the adhered phase is displaced under the effect of the surface tension gradients entrained by the gas phase. Eventually, the relative permeability becomes zero at a certain critical value of saturation also called residual saturation when the displacement process occurs (Hagemann, 2018). In the case of residual water saturation, gas transmissibility can be significantly reduced (Chen et al., 1977).

It is possible to find a relation between applied capillary pressure and saturation rate for porous medium. This curve is called the capillary characteristic curve during the flooding process. A porous medium is a complex structure made up of pores of various sizes, mostly connected. During imbibition, the wetting phase penetrates the larger pores or channels where gas resides and displaces it and vice versa during drainage. Hence, the capillary pressure-saturation relationship exhibits hysteresis between the imbibition and the drainage (Fig 5. 1):

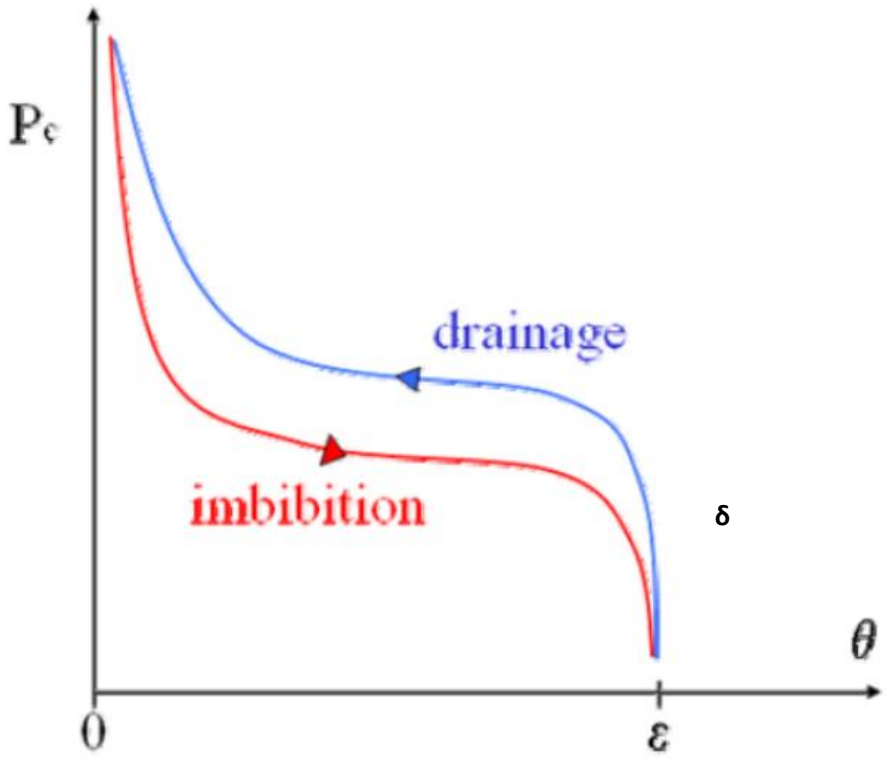

Fig 5.1: Characteristic of the capillary pressure PC curves during drainage and imbibition with respect to the contact-angle between water and gas δ (Boulin, 2008).

So, for the same capillary pressure, the saturation could be different. It depends on the initial saturation state and the connectivity between pores. For example, water in large pores connected to small pores won't be drained until small pores are drained first (Boulin, 2008). That's why a residual amount of the displaced fluid phase will be left behind (Helmig, 1997).

A viscous fingering phenomenon arises due to a contrast in mobility and an unstable interface occur between the displacing and displaced fluid phases. This behavior is observed in laboratory during flooding experiments (Buckley & Leverett, 1942). It's classically visualized in Hele-Shaw cell experiments which consists of two glass plates with a

small gap: a small injection of fluid induces strong destabilization forces and allow the perturbations to propagate as large fingers (Kueper & Frind, 1988; Fig 5. 2).

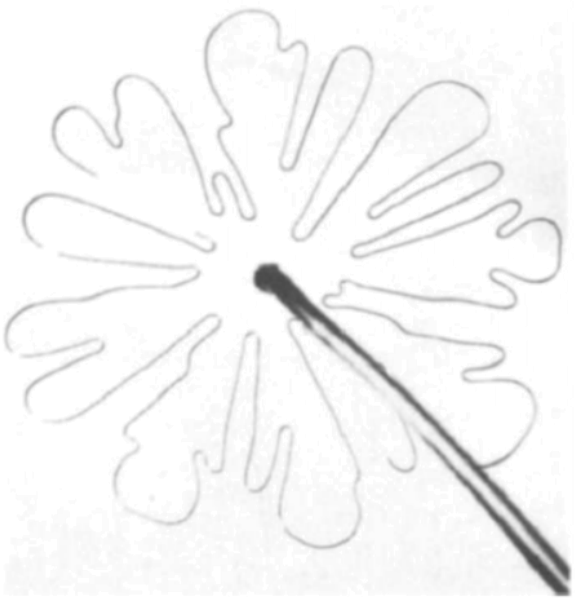

Fig 5.2: Viscous fingering around the injection point observed in Hele-Shaw(L. Paterson, 1983)

This mobility is considered according to the ratio:

$$M = \frac{K_{r1}\mu_2}{K_{r2}\mu_1} \qquad (5.\ 9)$$

where k_{r1} is relative permeability of the displacing fluid, kr_2 is relative permeability of the displaced fluid and μ_1 and μ_2 are their viscosities respectively. If this ratio is smaller than one, it results in a stable displacement, and if higher than one finger of fluids occurs in the displacement front (Ho & Webb, 2006). For hydrogen storage, the water mobility ratio is in the order of 2 to 5 allowing a viscous fingering displacement (Hagemann, 2018).The effect is also influenced by medium heterogeneities, anisotropy, destabilization forces, and fluid viscosity. Finger flow propagates in the direction of the high flow potential. So the gas injection at the top of underground reservoirs could lead to gas losses due to the uncontrollable spreading of fingers beyond the spill point of the structure. It's important to note that hydrogen spreads laterally faster than other gases like methane if present. To avoid this effect, the gas could be injected from the bottom of the reservoir so that the rising is retarded by geological barriers (Hagemann, 2018) .

Gravity segregation arises too due to the differences in density and mobility of the displacing and displaced fluid (TEK, 1989). The less-dense fluid flows at the top of the aquifer structure due to density difference. On the contrary, a denser fluid flows to the bottom of the structure in density underride conditions. In underground hydrogen storage, the less dense and more mobile phase is at the top of the aquifer. Water drops below the gas during the injection. The system becomes unstable at a certain critical water velocity. Above this velocity, a gravity override of water occurs. An opposite behavior of gravity underride is noticed during withdrawal. So in hydrogen storage, gravity segregation could be an unstable displacement (L. Paterson, 1983). Gas carried by buoyancy forces to flow up can be lost. For low injection rates, gravitational forces are dominant and water displacement is uniform. However, for higher injection rates, the displacement becomes unstable. Lateral gas fingers start to propagate to left and right reservoir boundaries below the caprock. So, to avoid losses by gravity segregation and fingering, it's important to control gas injection rates (Sáinz-García et al., 2017). On the other hand, fingers shape could enlarge the contact angle between water and hydrogen, resulting in gas dissolution in water, and a certain quantity is lost. Finally, a certain quantity of the mobile fluids could be left behind and recovered by the subsequent withdrawal process (Hagemann, 2018) (Fig 5. 3).

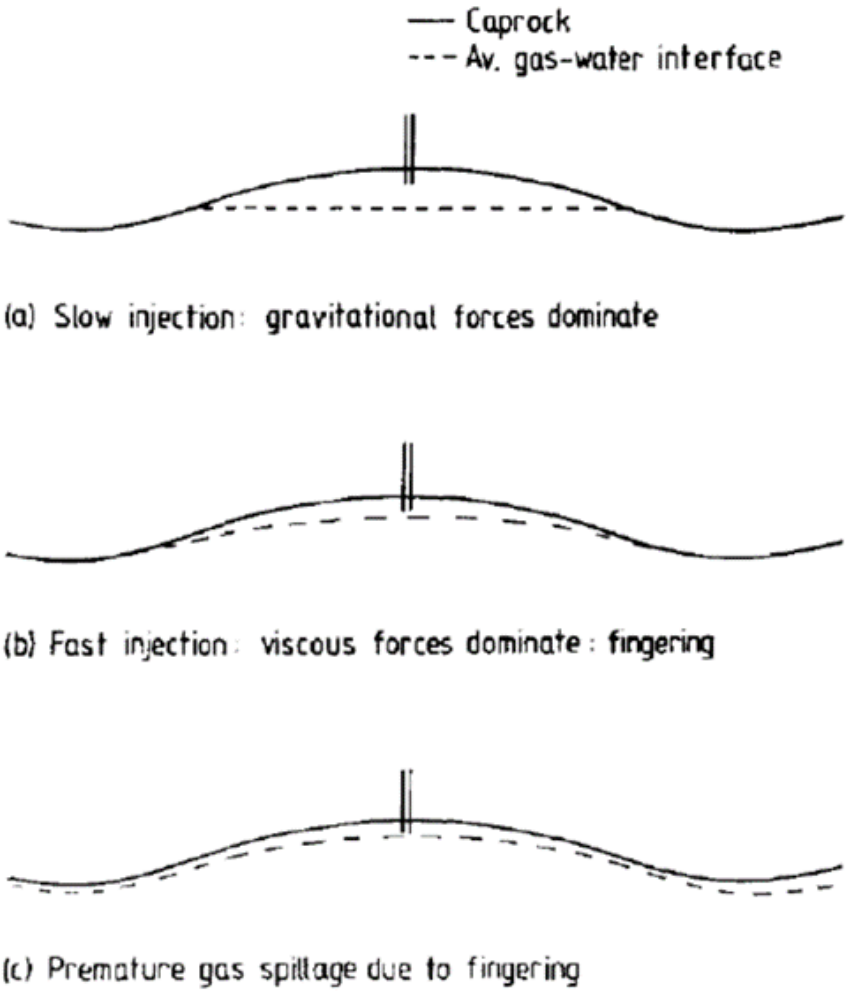

Fig 5.3: Injection of hydrogen gas into a trap and viscous and fluids displacement (L. Paterson, 1983)

5.2.3. Mixing phenomena in gas-gas interaction

Gas in underground hydrogen aquifer storage is stored in a mixture to increase the recovery rate of hydrogen. The rest of the gas elements are used as a cushion gas to ensure cavern stability. If pure hydrogen is stored solely, a large part of the injected volume is not recovered and remains in the site to become a cushion layer (Lysyy et al., 2021). On the other hand, the mixture can ensure the safety and security measurements related to the physico-chemical properties of hydrogen (mobility, flammability, energy density etc.) and increase the thermal capacity. In addition, the interaction between the gases in the mixture plays a major role in the hydraulic displacement and hydrochemical properties of the gas.

In a one-dimensional scale of flow-like pumping, all the gas is moved in a piston-like displacement. No initial gas is left behind the front because of the difference in the physical properties of elements. However, in the case of hydrogen, miscibility is much more important because of its very low density and viscosity. It involves a high tendency for an unstable displacement of diffusive and dispersive fluxes smearing out the front and racing the other gases provoking miscible viscous fingering observed mainly in 2D models (Becker & Kuznetsov, 2014; Hagemann, 2018). The behavior of a miscible gas displacement is represented for different Peclet numbers (Pe) by (Kantzas et al., 2012). The Péclet number (Pe) is a dimensionless number relevant to characterize continuous transport phenomenon. It is defined as the ratio of advection rate of advection to the diffusion rate of the same quantity of fluid driven by an appropriate gradient. A high Peclet number indicates that diffusion has a low influence on the transport and miscibility opposes to the piston displacement of fluids (Pe=320, Pe=80, Fig 5. 4).

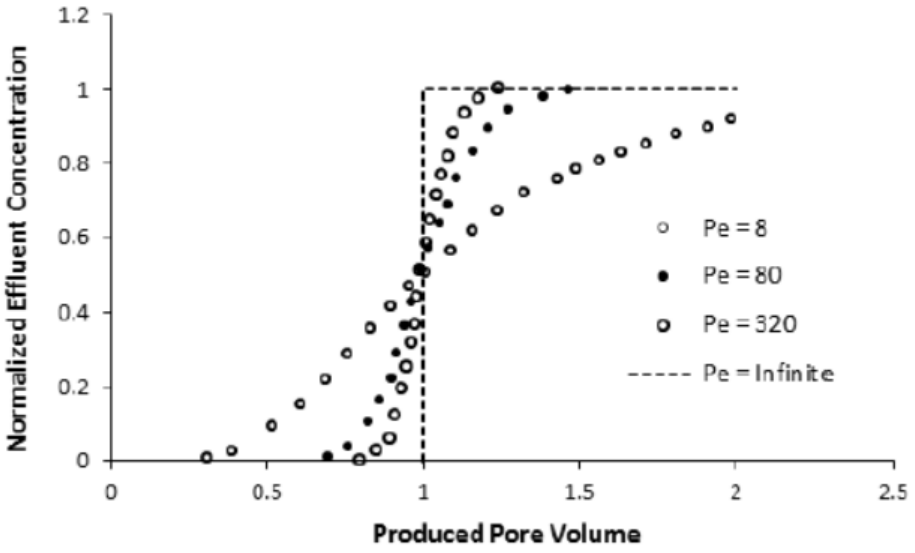

Fig 5.4: Injected tracer concentration with respect to the produced pore volume (Kantzas et al., 2012; Hagemann, 2018).

This process is influenced by heterogeneities and anisotropies of the porous medium, mobility ratio and density difference and fluids viscosities. So it differs when using a multi-scale approach for heterogeneous reservoirs, where the compartmentalization and lower permeability leads to higher contact allowing gas mixture (Hagemann, 2018). Hydrogen has a very low viscosity which results in a mobility ratio around 1.5 for the system H_2-CH_4 and 4 for the system H_2-CO_2. So at pumping, and the establishment of differential gradient of concentration, the mixing zone between the initial gas and injected gas becomes larger because it includes a mechanical dispersion (Hagemann, 2018). Gas mixing lowers the quality of recovered gas during withdrawal phase. Thus, gas requires a post-treatment to remove impurities which increases the production cost (Pfeiffer et al., 2017; Sáinz-García et al., 2017).

However, because of density difference between gas species, a separation between the mixture components could occur. This segregation can keep the mixture elements separated and it's beneficial when using another gas with hydrogen as a cushion gas or stabilizer like for instance methane (L. Paterson, 1983) and extract a pure hydrogen and preserve the hydrogen enrichment without dilution effect by another gas (Panfilov, 2010). This separation would need geological time scale in a porous medium, but it's only possible because of hydrogen high mobility and its ability to form quickly after the injection a top gas layer with a high share of the main gas isolated from the rest of the mixture. So mixing is a very minor problem and gas withdrawn from storage sites contains only 1% of the original elements (Pichler, 2019).

In case of gas-water segregation, gas injection leads to a dispersion of the gas front stabilizing the flow without affecting it quality (Ho & Webb, 2006). On the other hand, an excessive gas extraction leads to a pressure drop around the production well. The gas plume in the cavern contracts while the pressure gradient between the well and the denser underlying fluid increases. So, water migrates upward leading to the production of water with the gas at the production process. So, to keep the quality of extracted gas, production wells are shut down when gas saturation becomes below 0.4 (Sáinz-García et al., 2017).

5.2.4. Miscibility of fluids: effect of hydrogen solubility in water

In general, hydrogen is a gas with very little solubility in water (Ebrahimiyekta, 2017; Chabab, Théveneau, et al., 2020), unlike CH_4 with a solubility in the fluid pores of 0.4×10^3 mol/m^3 , and CO_2 with a solubility in millipore water of 0.3×10^3 mol/ m^3 in brine solution (Duan & Sun, 2003; Duan et al., 2006; Huq et al., 2015).

Nevertheless, even during steady-state conditions, one can't deny the presence of gas losses through a regular exchange of reservoir fluids, which might become severe with time. At standard conditions of temperature and pressure, hydrogen solubility in pure water is about 0.784 mol/m^3 and it increases to 37 mol/m^3 at 50 bar and 30°C (Ortiz et al., 2002) and reaches 80 mol/m^3 at 100 bar and 25°C (Crozier & Yamamoto, 1974). The little hydrogen dissolution in water could also affect pH-Eh condition of the system (Lassin et al., 2011).When oxidized, hydrogen loses its electron giving it a positive charge H^+ so that it resembles a proton dissolving the minerals of the medium

(Petrucci et al., 2012; Pichler, 2019). The amount of gas dissolved in a certain volume of water is linearly related to the partial pressure of that gas according to the thermodynamic equilibrium conditions. The chemical activity for both phases (gas-liquid) is balanced and this equilibrium is expressed according to Henry' law approximating the solubility of gases in liquids considering the gas as an ideal gas like in the case of hydrogen dissolution:

$$P_{H_2} = \frac{C_{H_2}}{K_H} \qquad (5.\ 10)$$

K_H is Henry's constant for the water-hydrogen couple, when water is the solvent and is equal to 7.6 x 10^{-6} mol. $Pa^{-1}.m^{-3}$. For hydrogen and helium, the Henry's constant varies by less than 1% for pressures ranging from 1 to 100 bar (Clever, 1979; Boulin, 2008; Pichler, 2010). However, dissolution of hydrogen into groundwater increases significantly at pressures between 30 and 400 bar reaching concentrations of several millimoles per liter groundwater due to the roughly linear correlation between increasing depth and pressure and solubility following Henry's law (Feldmann et al., 2016; Pfeiffer et al., 2017).

Pray et al., (1952) showed that hydrogen solubility in pure water decreases with respect to an increasing temperature while considering a constant pressure. However, it increases again when reaching an inflection temperature point at 60°C (Lassin et al., 2011). So temperature influence is minor and the equilibrium is reached with time. Also, he observed a decrease in the gas solubility with respect to increasing pore pressure, in isotherm conditions according to Henry's law. So, gas solubility mainly depends on the partial pressure of the hydrogen phase. Equilibrium between phases is rapidly reached with time (Pray et al., 1952).

On the other hand, it's known that salinity and alkalinity reduces gas solubility (Lassin et al., 2011). Equilibrium is reached more rapidly at higher temperature and in distilled water than at lower temperature and saline water (Crozier & Yamamoto, 1974). The injection of hydrogen gas leads also to the effect of vaporization of liquid water (Hagemann, 2018).

5.3. Hydrogen geochemical interactions in porous rock

5.3.1. Abiotic reactions of hydrogen

The hydrogen injection into a porous medium induces interactions between the rock and chemical and physical changes of the reservoir properties. Reactions are driven by contact with water and minerals under storage conditions of temperature, pressure, and chemical composition. The solubility of hydrogen in reservoir fluids changes the pH of the medium and the geochemical equilibrium and activates the redox reactions (Lassin et al., 2011). Furthermore, an eventual accidental leakage of hydrogen from the storage site and its diffusion to shallow water aquifers (140 m of depth) might enhance H_2 dissolution in shallow groundwater because of high gas pressure changing the water pH and probably initiating typical redox reactions associated with the oxidation of the gas (Evans, 2009).

The hydrogen molecule is a small and light molecule having a polar nature and a strong H-H binding (436 kJ/mol). It requires the overstepping of a high energetic barrier to participating in an efficient abiotic reaction (Truche et al., 2013). So, the abiotic reaction mechanisms require high energy and temperature. Most of the hydrogen abiotic reactions with rock minerals in porous rock storage sites are restricted to reservoir temperature between 50 °C and 100 °C and at maximum pore pressure of 100 bar range (Truche et al., 2013).

Truche et al., (2013) studied experimentally abiotic redox reaction by hydrogen in a nuclear waste storage site of a clay-rich host rock. He showed that hydrogen reduces pyrite minerals particularly present in the caprock into pyrrhotite, and releases sulfide anions in the solution, under hydrogen partial pressure above 30 bars and higher than 150°C, which is higher for the underground hydrogen storage (Reitenbach et al., 2015). This allows a variation of the porous structure leading to changes in petrophysical properties of porosity and permeability. The abiotic reactions are influenced by the alkalinity and the pH of the medium. It can even o ccur at low-temperature ranges. It's expressed by the relation below:

$$FeS_2 + (1-x)H_2 = FeS + x + (1-x) \quad H_2S, 0 \le x < 1 \quad \text{(5. 11)}$$

However, this experiment found that the hydrogen effect on the other minerals present in this rock (clay minerals, quartz, calcite, dolomite, and feldspars) is not significant even for a PH_2 of 30 bar and a temperature of 150 °C (Truche et al., 2013).

Hydrogen was found also to decrease structural Fe(III) in clays but in small proportions according to the experiment conducted by Didier et al., (2012) on the Callovo-Oxfordian formation at temperatures lower than 350 °C in the context of deep geological disposal of nuclear waste. For a temperature below 90 °C at a pressure of 1 bar of H_2 (g), the natural clay minerals are stable. In some cases, the decay of nuclear waste in the storage site generates heat allowing metallic corrosion in anaerobic conditions. This corrosion damages the containers but also generates quantities of hydrogen that can affect the safety of waste storage facility (Lassin et al., 2011; Ortiz et al., 2002). On the other hand, hydrogen could be absorbed by clay minerals replacing the water content. The rheological stiffness change and the clay becomes brittle. Eventually, this changes the anisotropy of the porous network and probably increases its permeability for hydrogen (Lassin et al., 2011; Ortiz et al., 2002).

It should be noted though that the minerals stability is directly related to the equilibrium in the medium with their dissolved species, for example, the quartz equilibrium with dissolved SiO_2 and clay minerals with brine. If any instability occurs, this leads to dissolution and precipitation activation in the storage site (Pichler, 2019). So, hydrogen gas is known to be chemically inactive in presence of minerals and gas losses by this way are restrained and easy to detect. It commonly originates from corrosion of casing or failure of the cement provoking a leakage through host rock and cap rock (Panfilov, 2010). It's unlike other gases like CO_2 that interact with the host rock changing it matrix, dissolving the matrix and cement minerals and allowing secondary minerals precipitation (Bachu, 2008).The dissolution of some evaporitic minerals like anhydrite may generate leakage pathways by weakening the mechanical strength of the caprock. This could largely enhance the rock permeability and so the leakage risk (Hangx et al., 2010; Huq et al., 2015).

Carbonate minerals of cements are highly influenced by hydrogen injection. Hydrogen tends to form metal hybrids when absorbing a negative charge. Therefore, oxidized hydrogen loses its electron and gives a positive H^+ proton and the rest of OH^- makes the solution basic (Foh et al., 1979). The change of water pH into alkaline direction leads to dolomite dissolution into carbonate minerals and calcite precipitation. This reaction could only occur in presence of pure hydrogen and the loss decrease with decrease of hydrogen concentrations. Nevertheless, these reactions are very slow under the pressure and the temperature of the storage site (Pichler, 2019).

5.3.2. Physical properties of sandstone: a typical rock reservoir

Sandstone reservoirs are the most widespread aquifers and reservoirs possess the largest volume available for storage due to their great porosity (Ngoc et al., 2011). The majority of the sandstone reservoirs have a high content of SiO2 and considered as quartz-rich/quartz-intermediate reservoirs following criteria of (Crook, 1974).They are mostly composed of nonreactive silicate minerals of quartz, feldspars, garnets and micas and other clay minerals like illite and chlorite. However, minor sulfide, sulfate, carbonate (mostly calcite) and oxide minerals often occur either as cementing materials, binding the grains and pore spaces or coating the surfaces of larger grains. These minerals could possibly react with the gas injected and the residual water in pores (Huq et al., 2015; Ebrahimiyekta, 2017). Sandstone displays also a low to moderate content of Fe_2O_3 and MgO. Other ions can be also present such as li, Rb, Sr and K, Ni, Cr, S, Ti, Al and many variable minerals. A sandstone can be Fe-rich, lithic sandstones, sulfuric or quartz arkoses according to the major element present in its minerals and this affect the type of geochemical reactions that can occur within the media.

Sandstone is a clastic sedimentary rock composed of sand-sized silicate grains, and other minerals. Grain size vary from medium-grained to fine-grained sand- and siltstone with point grain to suturated grain contacts, reflecting different stages of petrographic evolution during reservoir rock diagenesis. This mineralogy depends on the geological and deposition conditions of formation sediments. This affect the detrital and petrophysical features for each reservoir but also the contact surface allowing the geochemical reactions (Henkel et al., 2013). Its main mineralogical composition is of quartz, K-feldspars muscovite, hematite and other evaporitic mineral in less concentration (Ebrahimiyekta, 2017) vary due to differences in source areas, transport conditions and depositional environments at the investigated sites.

Because of the large amount of exposed surface minerals in sandstone-type reservoirs of quartz it allows possible reactions with hydrogen and alter the stock or could be used as substrate to catalyze biotic reactions. This could also produce toxic gases or change gases mixture by conversion. Under the hydrogen pore pressure, pore water can dissolve some parts of the quartz and dissolved silicate components tends to precipitate in other sites of the rock (Pichler, 2019). Only oxygen, Fe_2O_3 and sulfur could possibly react with hydrogen. Temperature doesn't significantly affect the kinetics of the reaction neither the pressure. However, these reactions require enough temperature as a catalyzer for the reaction (Ebrahimiyekta, 2017). On the other hand, the present of clay minerals in the composition of the rock, increases the surface of exposure to geochemical interactions. Water when interacting with clay minerals provoke their swelling and reducing pores diameter. Also, it stimulates geochemical reactions changing the properties of the reservoir in function of the composition of the formation water and the type of the reacting minerals (Henkel et al., 2013).

Additionally, post depositional, diagenetic burial evolution of the sandstones at different pressure, temperature and pH/Eh/fluid conditions strongly affect any fluid-rock interactions (Henkel et al., 2013). The large porous surface is suitable to be a medium for microbial development in presence of adsorbed water, nutrients and appropriate temperature and pressure. However, the spectrum of mechanical compaction, cementation and porosity proportions of each sandstone is very broad. Pores can be free for fluids residence (water, oil, gas) or already filled with cements which are carbonate minerals, anhydrite, quartz or even clay minerals illite, chlorite, and kaolinite and coating detrital grains and feldspar and other detrital components reducing the porosity and permeability of the rock for fluid/gas flow (Henkel et al., 2013).

5.4. Impact of bacterial activity on the storage in porous rock

5.4.1. Hydrogen biogeochemical Interactions and conversion

Several industries like oil and gas, geothermal, carbon storage, natural gas storage often experience significant microbial activity. In oil and gas storage, and CO2 storage, it provokes souring of the reservoir and corrosion problems. Storage sites display mineral plugging and permeability reduction induced by sulfate-reducing microorganism's activity (Morgan et al., 2017; Skovhus & Whitby, 2019). Microbial plugging could be positive to prevent CO_2 leakage for instance (Cunningham et al., 2009). In geothermal energy systems, a steep thermal gradient activates the microbial potential around the injection areas. Sulfate-reducing bacteria proliferate in the site because of their temperature tolerance provoking similar challenges like plugging (Bonte et al., 2013; Lienen et al., 2017). Similar challenges can be encountered with H_2 UGS. One of the most known examples is the storage of hydrogen gas in Russia, for aerospatial usage (Ponomarev-Stepnoi, 2004).The storage was successful in general. Nevertheless, an in-situ testing revealed an issue. A mixture of 55% of H_2, 20% of (CO_2 + CO) and 20% of CH_4 was injected for storage. After several months (5 to 7 months), the extracted gas contained 37% H_2, 12% (CO_2 + CO) and 40% CH_4. The methane content doubled while the acidic gases and CO decreased. This impoverishment in dihydrogen gas could be explained by the bacteria metabolism that consume the CO_2 carbon and use the electrons of H_2. Bacteria are the catalyzers of this reaction (slimane, 2015). This kind of alteration have a negative effect on gas quality needed for the storage and would require gas treatment depending on site conditions. Other sites also revealed this bacterial impact, like in town gas storages in Lobodice (Czech Republic) and also in Beynes (France) (Ebrahimiyekta, 2017). Most of the time, gas reinjection/pumping compensates this loss of H_2. However, due to the high diffusion within the porous media, this loss could increase by the mechanical effect of cycling. So, it's important to control bacterial activity by understanding their metabolism.

5.4.2. Hydrogenotrophic bacteria

Many microorganisms can use H_2 as an electron donor. Some studies show that certain bacteria belonging to different metabolic groups (methanogens, sulfate-reducing, ferroreductive and homoacetogenic) are capable of consuming hydrogen anaerobically or aerobically (Cord-Ruwisch et al., 1988; Libert et al., 2011).
In anaerobic ecosystems, H_2 is oxidized in presence of a mineral phase. Inorganic electron acceptors, like CO_2 and the oxidized forms of sulfur (ranging from SO_4 to elemental sulfur (S °)), are reduced with electrons produced from the oxidation reaction. CO_2 is reduced to methane for instance. The microorganisms using H_2 as an electron donor belongs to different metabolic groups, namely sulphate-reducing bacteria, iron-reducers, methanogens, homoacetogenic or thiosulfatoreducers (Cord-Ruwisch et al., 1988). So, four microbial processes could be

considered in geological hydrogen storage. The presence of residual water favors those bacteria to live and reduce hydrogen (Tab 5.1).

Tab 5.1: Types of hydrogen redox reactions in porous media storage

Metabolic Groups	Example	Reactions	ΔG0 Kj/mole electrons (25°C)
Iron reducing bacteria	*Shewanella*	H_2+ 2FeOOH+4H^+ = 2Fe^{2+} + 4H_2O	-91.25
Sulfato-reducing bacteria	*Desulfovibrio*	4H_2+ SO_4^{2-} +4H^+ = H_2S +4H_2O	-24
Methanogen bacteria	*Methanobacterium*	4H_2 + CO_2 = CH_4 + 2H_2O	-21.95
Thiosulfato-reducing bacteria	*Thermotoga*	4H_2+ SO_4^{2-} + 2H^+ = H_2S +4H_2O	-19.5

Iron reducers accept to use Fe^{III} in solid form (Fe^{3+} s) or aqueous form (Fe^{3+} in acidic or complex media such as Fe^{3+} citrate) as an electron and reduce it to Fe^{II} in presence of hydrogen. This reaction can produce energy too (Fredrickson & Gorby, 1996; Vargas et al., 1998; Slobodkin et al., 1999; Lovley et al., 2000). Bacteria like *Geobacter, Pelobacter*, *Pyrobaculum islandicum*, *Thermotoga maritima*, *Pyrococcus furiosus* and *Shewanella spp* are examples of such strains (Vargas et al., 1998; Zegeye et al., 2005; Libert et al., 2011; Hazotte, 2012). Many studies conducted on this metabolism used the strains of *Geobacter metallireducens* and *Shewanella putrefaciens*. The reaction produces some mixed iron oxides: magnetite (Fe_3O_4) or green rust ("Fe5OH12"). For example, in presence of different concentrations of iron oxides like lepidocrocite (γ-FeOOH) (from 30 to 100 mMoles) as electron acceptor and in presence of H_2 as the only electron donor, at atmospheric pressure and 30 ° C, *Shewanella putrefaciens* reduces Fe^{III} with a rate of 0.05 to 0.12 mMoles Fe^{II} h^{-1}. Lack of nutrients though, provokes a decrease in bacterial proliferation over time. The initial cell density in batch experiment decreased from 1.8 × 108 CFU mL^{-1} to 106 Cell per mL-1 after 14 days (Zegeye et al., 2005). Today, iron oxides are considered to be the most abundant electron acceptors for the oxidation of organic matter in anoxic sedimentary environments (Nealson & Saffarini, 1994). It places iron reduction as an important biogeochemical process in submerged soils and aquifers (Canfield et al., 1993; Lovley & Chapelle, 1995).

On the other hand, the activity of acetogens and methanogens can be directly detected with the CO_2 concentration decrease in a storage site. While on the other side, the methane concentration increases and the microbial community converges toward the methano-microbes (Basso et al., 2009; Enzmann et al., 2018). Note that some business models can benefit from this metabolism and thrive the mixture with CH_4 by boosting the stored hydrogen mixture with CO_2. CH_4 has a versatile end-use (industrial, district heating, electricity, mobility, etc.) and is also a green gas making it possible to diversify the energy mix (Sato et al., 2013; Strobel et al., 2020). The business model known to use this technique is the "power-to-gas" model. An example of this storage is the Underground Sun Storage Project in Lehen, Austria a pilot project for green hydrogen in aquifers. An in-situ test was carried out on this site to prove the efficiency of this method. A gas mixture of 10% hydrogen and methane was introduced in the site. After four months, H_2 was completely lost, CO_2 decreased to a scarce concentration of 0.2% to 0.05% while CH_4 increased. Simultaneously, water saturation decreases and permeability increases consequently. The DNA analysis has shown a rise in methanogens explaining the consumption of CO_2 and H_2. In addition, a sulfate reduction is observed over the withdrawal period but without H_2S production. It indicates an activation of acetogenesis and sulfate reducing bacteria but H_2S seemed to be fixed by dissolved iron forming FeS precipitates (RAG, 2017; Pichler, 2019). Other studies on these sites revealed the presence of methanogens transforming H_2 and CO_2 into methane to thrive the energy mix. Similar studies were conducted on the Argentinian HyChico project for hydrogen storage in a depleted gas reservoir generated from wind energy. The project focuses on underground methanation concept (Pérez et al., 2016; Dopffel et al., 2021). The methanogenic reaction is only possible if only biologically stimulated. An high concentration of methanogenic bacteria was for instance discovered in Lobodice site of aquiferous storage of hydrogen in Czech republic (103–104 cells/ml) (Amigáň et al., 1990; Buzek et al., 1994; Panfilov, 2010). This high concentration was responsible of methanogenic activity at the optimal temperature and pressure of the reservoir (Taconi, 2004).

It seems that methanogens compete with acetogens in presence of CO_2. Therefore, and because their high specific growth rate, they dominate the biofilm while acetogens and actetotrophs make less than 20% (Ebigbo et al., 2013). The microbial rate of H_2 and CO2 consumption and CH_4 production rate change when passing through the different domains of bacterial and gas concentration. So, the kinetics of microbial reactions underground depends on the amount and the activity of the biomass underground and the gas availability and the presence of a thick water film for biofilm growth (Ebigbo et al., 2013). Furthermore, acetogenesis also uses hydrogen in presence of high

concentration of acetate, produce fluids allowing bacterial growth. In general, the presence of acetate drop the pH of a medium but this can be masked by microbial consumption (Zabranska & Pokorna, 2018; Dopffel et al., 2021).

Sulphate-reducing bacteria metabolism also use sulfate (dissolved or sulphidic minerals like gypsum and anahydride) as acceptor of electrons (oxidant). This process is coupled to the oxidation of an organic substance considered as an electron donor (reducer). As a substrate, these bacteria use hydrogen as electron source in presence of a carbon source like organic acids or ethanol for development (Badziong et al., 1978; brandis & Thauer, 1981). The reaction leads to the formation of H_2S a toxic and corrosive gas and a decline in sulphate content (Kleinitz & Boehling, 2005; Wolicka & Borkowski, 2007). This process can be identified by a decrease in the dissolved iron and sulfide concentrations in the re-produced liquids.

5.4.3. Microbial Process

It is essential to understand the mechanisms governing the conversion of hydrogen by the bacterial biomass of the subsurface. Microorganisms live usually in communities of aggregated cells irreversibly attached to an interface or attached to each other, embedded in a matrix of extracellular polymorph substances. They are called biofilm and their presence in the pores reduce the throat size, increase tortuosity and decreases permeability (Pedersen, 2000; Donlan & Costerton, 2002; Coombs et al., 2010; Yin et al., 2019). The growth behavior of bacteria can be followed in the laboratory through batch experiment. Microorganisms are cultivated in flakes containing a nutrient solution and a fixed amount of a substrate (iron, sulphate, etc.). The number of cells is counted frequently and subsequently plotted against time. The resultant curve displays a semi-logarithmic behavior (Hagemann, 2018, Fig 5. 5):

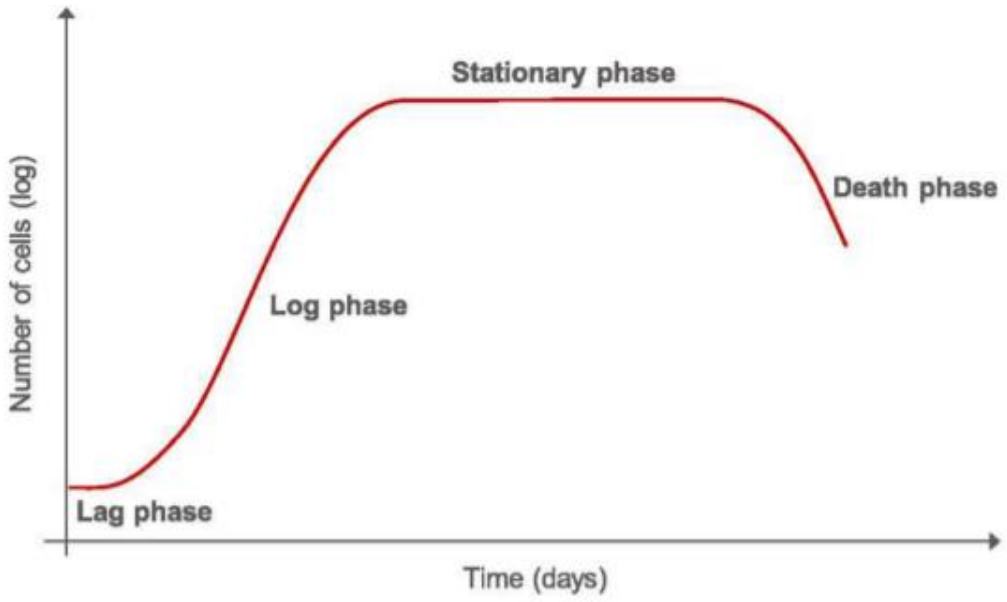

Fig 5. 5: Typical bacterial growth curve in batch culture (Straube & Müller, 2016; Hagemann, 2018)

Biofilm growth follows a sequence of events similar to that of planktonic bacteria (Fig 5. 5), with lag, log, stationary, and decline phases as detailed below:

5.4.3.1. The conditioning of the surface by the environment and bacteria adhesion

This step is responsible of the lag phase in the typical growth curve. In this phase no growth of microorganism occurs. It's only a physiological preparation for cells to adapt the conditions of the medium. The surface of the medium is a seat of irreversible adsorption of macromolecules such as humic, polysaccharides or proteins, leading to the formation of a "conditioning film". It can modify the properties of the material by creating a micro-environment adequate to bacteria stable adhesion (Baier, 1980; Little & Jacobus, 1985; Ishida & Griffiths, 1994).
The adhesion of bacteria to the surface depends on the physical and chemical properties of the medium like adsorption, porosity and fluid flow dynamics characteristics (Katsikogianni & Missirlis, 2004). It also involves moving the cells to the surface by different bacterial appendages such as flagella (O'Toole et al., 2000; Gavín et al., 2003). The adhesion of bacteria to the surface depends on the dynamic properties of the medium (fluid flow

velocity) and the physicochemical properties of the surface (Katsikogianni & Missirlis, 2004). It involves moving the cell to the hanging seat and adhering by the bias of different bacterial appendages such as flagella and lashes (O'Toole et al., 2000; Gavín et al., 2003).

Initially, the adhesion is weak because of the soft interactions between surface and biofilm (van der Waals and electrostatic interactions). The bacteria can desorb from the surface and return to its planktonic state. Adhesion is therefore reversible. At a second step, the adhesion becomes irreversible because of exopolymers secretion by bacteria consolidating the attachment. In this case, adhesion becomes strong between the bacteria and the surface with hydrophobic interactions. This stage is the lag phase on the typical bacterial growth curve (Fig 5. 5).

5.4.3.2. Bacteria growth

Once the bacterium is irreversibly adhered to the surface, multiplication leads to the formation of colonies covering the surface. Subsequently, the biofilm increases in thickness and becomes a three-dimensional heterogeneous film (Costerton et al., 1995; Davey & O'toole, 2000; Sauer et al., 2002). Its structure depends on environmental conditions such as the carbon source or the hydrodynamic regime (Stanley & Lazazzera, 2004; Klausen et al., 2006). Channels are formed into this 3D structure allowing the circulation of nutrients and oxygen and the evacuation of products from the bacterial metabolism (Costerton et al., 1995).

After the lag phase the growth behavior shifts into the exponential growth phase. Growth rate depends also on the medium physical conditions (Cypionka, 2010; Hagemann, 2018). Growth phase in batch conditions can takes a long period slower than in situ conditions (Maier et al., 2009). On the other hand, the growth rate is faster in batch than in environmental conditions. Mathematically, the growth during this phase can be described by the following differential equation (Cypionka, 2010; Hagemann, 2018):

$$\frac{dn}{dt} = \mu n \qquad (5.12)$$

where n is the number of microbial cells and μ is the maximum growth rate in (*1/s*) (Hagemann, 2018).

5.4.3.3. Growth stable phase and biofilm dispersion

Finally, the biofilm thickness stabilizes when carbon or energy source becomes limiting and compensates growth (Costerton et al., 1995).Therefore, no net growth occurs and cells do not duplicate. Microbial cells use dead cells as carbon source by an endogenous metabolism (Maier et al., 2009). The detachment of cells from the biofilm occurs when the environmental conditions become unfavorable: limitation of oxygen, hard shear forces due to hydrodynamics conditions, decrease in concentration of available nutrients (Sauer et al., 2002, 2004). The bacteria migrate in order to find a favorable environment for development.

5.4.3.4. The decay phase

Finally, the growth shifts into a decay phase. The curve shows a negative exponential decline. Cells duplication is slowed and inhibited with time (Maier et al., 2009).

5.4.4. H_2 consumption rate by biofilm degradation

Biofilms are described as heterogeneous porous medium in which bacteria represent the solid phase, and the water carrying the species flows and distributes the nutrients to the microorganisms. Thus, bacteria consume hydrogen for respiration to grow in a complex dynamic film at large scale (Ebigbo et al., 2013; Usher et al., 2015). Kinetics of the hydrogen conversion describes the rate of the electron transfer in the reaction. It is ranked according to the magnitude of their H_2 threshold and their standard free energy change (ΔG0) (Tab 5.1). The more negative ΔG0 values means more available free energy and lower threshold of H_2 to be used in the conversion process. H_2 oxidizing process is in general very slow in absence of any biological activity. In presence of bacteria, the sulfate reduction process has the fastest kinetics and homoacetogenesis, the lowest (Thaysen et al., 2020). In underground medium, microorganisms are capable of supporting their vital functions in extreme conditions. The consumption rate varies with medium physical parameters and other factors like the number of cells, nutrients availability, salinity, pH, and the elevated H_2 concentration in the storage site (Gregory et al., 2019). Hence, there is a difference

between the population kinetics of the microorganisms in enriched batch culture and that of the deep subsurface (Payler et al., 2019). Also, it's important to notice that each strain grow in proper optimum conditions and that varies between environments and strain type (Freitag & Prosser, 2009).

Microorganisms consume better dissolved H_2. Hence, the solubility of H_2 is an important factor for reaction functioning and influences directly the pH and the redox potential. In presence of a gas mixture, hydrogenotrophs consume better the hydrogen (Thaysen et al., 2020). Nutrients requirements for H_2 oxidation varies in function of the microorganism strain. Hydrogenetrophic bacteria requires water and thermodynamic activity for living , but also macro-elements like C, N, H, P, Ca, Mg, S and Fe and trace elements Co, Mn, Ni, Mo, Cu, Zn, W and Se for some metabolic groups (Choong et al., 2016; Pedersen, 2000). Also, it requires vitamins, yeast extract, and specific acids (Thaysen et al., 2020). Any limited concentrations of theses nutrients might limit kinetics of the conversion reaction of hydrogen with respect to the strain type. Storage temperature in aquifers and depleted reservoirs ranges between 22.5–80 °C or 20–100 °C based on a depth range of 500–2000 m (Thaysen et al., 2020). Each strain of microorganism has its own optimal range of tolerance because high temperature changes the solubility of substances and the redox potential. It can also damage the DNA structure of the bacteria and decreases the protein hydrolysis. (Ghosh et al., 2020). Nevertheless, in case of thermophiles, higher temperature increases the reaction rate and is considered as catalyzer (Miller et al., 1989; Thaysen et al., 2020). Salinity for H_2 storage is 0–2.5 M NaCl. This value is tolerated by most of the organic communities in aquifers and depleted reservoirs. Extreme halophile communities can grow in best at a concentration of 2.5–5.2 M NaCl (Oren, 2013; Thaysen et al., 2020). High salt concentration provokes osmotic stress cells and degrade it. Commonly, bacterial salt tolerance increases with temperature. pH can be also critical and the redox potential of the reaction is adapted at pH between 6.5 and 7.5 (Thaysen et al., 2020).

5.4.5. The Shewanella bacteria

Shewanella is a bacterial family known for its main phenotypic feature to reduce H_2. Many studies conducted on the metabolism of iron reduction used the strains of *Shewanella oneidensis* and *Shewanella putrefaciens*. Microbial activity of this specie that digests hydrogen and generates biogas in anaerobic conditions was investigated in lab-scale microbial electrolysis cells (MECs) (Abdalla et al., 2018; Yu et al., 2018). *Shewanella* is electively anaerobic and can live in extreme aquatic habitat but can also tolerate oxygen presence. In the absence of oxygen, it can use of a variety of other electron acceptors for respiration like thiosulfate, sulfite, or elemental sulfur or fumarate. Some members of the *Shewanella* have the ability to use wide range of metals species especially, manganese, chromium, uranium and iron.

In anaerobic conditions, several species of *Shewanella* are able to reduce a number of compounds as an electron acceptor including trimethylamine N-oxide, sulfur, manganese oxide, chromium oxide, iron, uranium, thiosulfate or iron oxide. For example, the study of the MR-1 strain (type strain of *Shewanella oneidensis*) demonstrated the energy production coupled with the reduction reaction of iron oxide or manganese oxide (Myers & Nealson, 1990; Hazotte, 2012). *Shewanella* is widely used in laboratory models to study anaerobic respiration of metals or other anaerobic extracellular electron acceptors.

Shewanella oneidensis MR-1 is one of the most characterized species of mesophilic iron-reducing bacteria living in aquifers or depleted reservoirs at some medium to deep environments under pressure conditions above 40 bars (Kato et al., 1999; Ikegami et al., 2000; Hazotte, 2012). It is consisting of non-sporulation gram-negative bacilli, 2 to 4 µm in length by 0.4 to 1 µm in diameter, mobile thanks to a single polar flagellum. Its optimum growth temperature is between 30 and 40°C and it has a neutrophilic pH. It is non-fermenting and requires breathing (Hazotte, 2012). If *Shewanella oneidensis* (108 cells $mL^{-}1$) incubated at 30 ° C in a complex medium in the presence of 5 mM, iron-citrate can reduce Fe^{III} under a pressure that goes around 1000 bars. In a culture medium based on peptone and yeast extract (electron donors), *Shewanella* completely reduces Fe^{III} up to 700 bars. Above this value, the reduction rate decreases with incremental pressure. The initial reduction rates vary from 0.33 to 1.62 $mM.h^{-1}$. However, growth rate of cells decreases with increasing pressure. At atmospheric pressure, 100% of the cells grow up in this conditions while at 500 bars, any bacteria develops (Picard et al., 2012). *Shewanella oneidensis*, considered as chimioorganotroph, has the ability to use organic substrates as an electron donor (formiate, lactate) and fix the hydrogen. Its outer membrane presents hydrogenases making it possible to fix and oxidize H_2 and to accept electrons during the reaction (Heidelberg et al., 2002; Lovley et al., 2000; Shi et al., 2011; Hazotte, 2012). If Fe^{III} is chosen as an electron acceptor can be in either in solid form or in soluble form. The solid form is in the form of lepidocrocite (-FeOOH). Fe^{III} oxyhydroxide is found almost exclusively in poorly drained hydromorphic soils with

a seasonal alteration of aerobic and anaerobic conditions. During the rainy season, anaerobic conditions develop and lead to the formation of Fe^{II} which is oxidized on contact with air and precipitates in the form of lepidocrocite. The soluble form is represented by Fe^{III}-citrate (Gaboriaud & Ehrhardt, 2003). The rate of hydrogen consumption by this process is calculated by measuring Fe^{II} concentration according to the stoichiometry of the equation below:

$$2Fe^{III} + H_2 = 2H^+ + 2Fe^{II} \qquad (5.1)$$

Hazotte, (2012) used this method to estimate the rate of hydrogen consumption by *Shewanella oneidensis* MR1. 5×10^{10} cells/mL of the bacteria were incubated for the experiment. The dose was estimated from the optical density measurement DO600 nm. DO is defined as the logarithm of the ratio of incident to transmitted radiant power through a sample. The cell density is so estimated according the relation:

$$1OD_{600} = 5.5\times10^{8}\, cells.mL^{-1} \qquad (5.\ 2)$$

The experiment took place first in batch at 2 bars to compare the reduction of H_2 by the bacteria to the reaction in situ conditions, reproduced in the autoclave.

First,100mL of substrate (nutrients and other vitamins) is prepared and added to the medium in presence of soluble Fe^{III} (Iron citrate) and solid γ lepidocrocite –FeOOH. The medium was distributed on several flakes each contains different concentration of lepidocrocite and 109 cells/mL of the bacteria were incubated with 79.4 mM of H_2 corresponds at 30°C. FeII was measured by H_2SO acid digestion frequently, in order to estimate consumed quantity of H_2 according to the stoichiometry of the equation (5.13) cited above. The bacterial concentration evolution was followed by counting traced cells marked by fluorochromes observed by epifluorescence microscope. This same bioreduction is also executed in autoclave at different pressures of hydrogen and the same bacterial concentrations. Gas was monitored by a sampling line over time and the pressure was then adjusted by an injection of Argon. Results showed that *Shewanella oneidensis* is able to use H_2 as electron donor for iron reduction in soluble and solid form. However, soluble iron is more available and easier to be fixed by the cells membrane (Hazotte, 2012). The kinetics of this reaction could be also influenced by the concentration of the reactors (iron, hydrogen) (Zegeye et al., 2005). It also appears that the hydrostatic pressure of the reservoir does not influence the consumption of H_2 but has an impact on the membrane integrity of the cells and the substance adherence (Hazotte, 2012).

Nevertheless, for our following study we will use the *Shewanella putrefaciens CIP 80.40.* The genus *Shewanella spp*., discovered in 1931, is composed of non-sporulating bacteria in the form of motile bacilli consisting of a single flagellum at one pole of the bacteria. These bacteria have a Gram negative stain and are 2 to 3 µm in length and 0.4 to 0.7 µm in diameter (Venkateswaran et al., 1999). The optimum temperature for growth of *Shewanella putrefaciens* is 35 °C. Thus bacteria is able doing the fermentation process, the respiration using iron as electron acceptor (Bowman et al., 1997). The *Shewanella* family consists of a particular skin and mucous pathogen with a circular genome of 4.6 Mbp. The *Shewanella putrefaciens CIP 80.40.* has two proteins, MrtB and C, driving the metabolism and the reaction of metals reduction to MtrA and MtrC proteins also present in the skin of the bacteria (Beliaev et al., 2001) (Fig 5. 6).

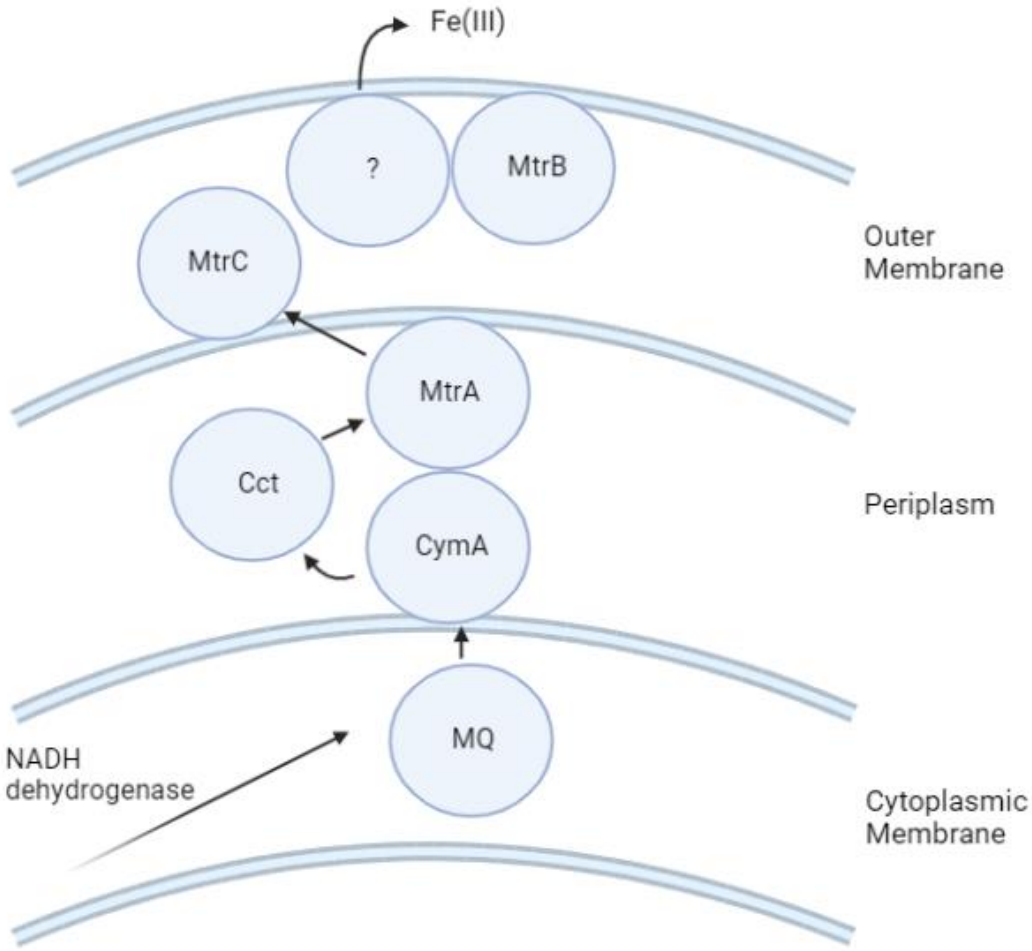

Fig 5. 6: Diagram describing to the reduction of Fe^{3+} by the S. putrefaciens membrane proteins (MtrB, MtrC and Cct involved in metal reduction, MtrA, CymA, MQ periplasmicdecahaemc-type cytochrome involved in electron transportation chain when uptaking an electron,(Beliaev et al., 2001).

5.4.6. Flow-through test in literature

The flow –through test method is used generally to study a gas flow performance through a porous network by mimicking the in-situ conditions of fluid-rock interaction, geochemical reactions, physico-chemical conditions. This laboratory method is used to simulate the reservoirs conditions on laboratory scale to interpret the gas behavior during gaseous storage (methane, CO_2, hydrogen) and all risks of leakage or biogeochemical alteration.

For hydrogen storage, very few studies have considered flow-through experimental method to evaluate the biogeochemical effects of hydrogen storage. Hydrogen oxidation can reduce electron acceptors such as nitrate, Fe^{III} and Mn^{IV} (hydro)oxides, sulfate, and carbonate present in the medium and can cause losses in the gas stock and provoke unwanted changes in the composition of the groundwater. So to evaluate the impact of these reactions and simulate the storage of hydrogen into shallow aquifers, Berta et al., (2018) conducted an experiment using filled columns of sediments from a pristine shallow quaternary aquifer preserved under anaerobic conditions to prevent redox reactions under a confinement pressure of 100 bar. The inflow solution was equilibrated and pressurized with H_2 in the mixing cell before it percolated through the experimental column at a pressure of 2 to 15 bar from the bottom to the top at constant flow. The H_2 gas was captured by the sampling unit repeatedly extracted by a 60-ml syringe to be chemically analyzed by gas chromatography. After this procedure, the fluid in the sampling unit was extracted at atmospheric pressure and the content of minerals is analyzed by the total inorganic carbon (TIC) analyzer (Haase et al., 2014; Berta et al., 2018, Fig 5. 7).

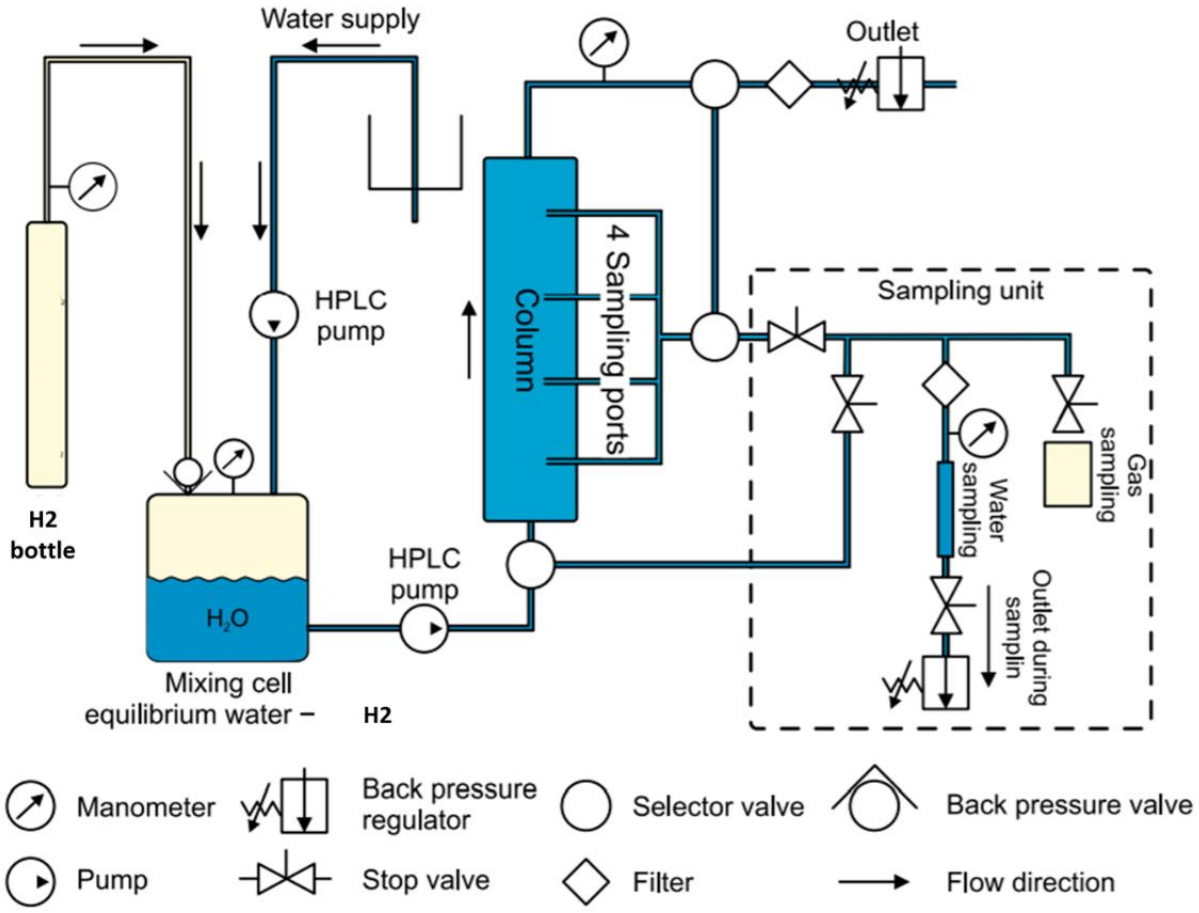

Fig 5.7: Set-up of the column experiment and the sampling unit edited from (Haase et al., 2014).

The results showed a continuous change between the in- and outflow of the column presenting a surplus of H_2 gas, regarding dissolved concentrations of sulfate, acetate, total inorganic carbon species (IC), calcium, and hydrogen, all over the experiment. Furthermore, a sulfidic content was identifiable in the solution flowing out of the column indicating sulfate reduction, and dark precipitates, most probably iron and manganese sulfides or carbonate were also detected indicating an acetogenesis reactions. These changes prove the assumption of an established hydrogenotrophic microbial community apparently oxidizing hydrogen mainly by reducing sulfate (sulfate-reducing bacteria) and reducing carbon dioxide through acetogenesis catalyzed by the microorganisms. This was also proved by the pH change and precipitation of calcite. The depletion of H_2 in the column by reducing the gas pressure to 2 bars, didn't stop acetate production, pH increase, or calcium precipitation, so apparently the microbial community depends only on a low concentration of the gas to be activated. However, this consumption could be inhibited by the increase of salinity (increase of TDS in the water) (Berta et al., 2018). This indicates the importance of the microbial activity as a catalyzer for geochemical interaction between the hydrogen and storage medium and requires further experiment and improved setups to study the process of stock alteration of hydrogen and estimate the kinetic of these reactions.

However, to the best of our knowledge, no flow-through experiment was performed to study H_2 consumption by bacteria in representative storage conditions both in terms of pressure and temperature (temperature controlled triaxial test) and multiphase behavior (water/gas system).

The following chapter will represent a first attempt to quantify the effective kinetics of hydrogen concentration evolution with respect to biogeochemical alteration in aquifers storage site with a new experimental study using the flow-through method we have conceptualized.

6. Flow-through experiments in porous rock on analog sandstone

6.1. Introduction

In order to study the phenomena of bio-geochemical alteration of hydrogen stock on an analog sandstone of a porous reservoir rocks, we have developed a new experimental device to simulate the biogeochemical activity under representative conditions (T = 35 ° C, p_{H2} = 50bar, Pconfinement = 200bar) of the aquifer in situ storage. This new experimental approach combines gas (hydrogen) injection tests in a triaxial compression cell with geochemical analytical methods to trace and quantify the biological processes of hydrogen conversion and alteration. We choose first the analog rock, the Vosges sandstone and the bacterial strain, we use Shewanella Putrefaciens, bacteria known in ultra-saline reservoirs and responsible for the reduction of iron and hydrogen respiration to grow. We then prepare a bacterial solution under optimal conditions for microbial growth similar to that in situ but enriched in iron. We first perform batch experiments to quantify hydrogen consumption by the model of iron-reducing bacteria Shewanella putrefaciens under anaerobic conditions and in the presence of H2 under very optimal conditions to estimate the kinetics of the iron reducing reaction by the bacteria, and finally we perform the new method in flow-through cell coupled to a special sampling valve and gas chromatograph to analyse the evolution of hydrogen while keeping the circuit cloased throughout the experiment in order to approach the in situ conditions. The paragraphs below detail the establishment of the process and some results obtained too.

6.2. Analog samples characterization: Vosges sandstone

We consider an analog rock to assess the storage capacity of underground hydrogen storage: The Vosges sandstone. The core samples used for the experiment are from the formation of red Vosges sandstones from Buntsandstein (inferior Trias). They have the following average mineralogical composition: 67.1% of quartz, a low amount of muscovite of 10.2% and a very low content of clay of about 4.8%.
Before the tests we characterized the geometry and porosity of the samples. The water porosity measurement was carried out on three cylindrical sandstone samples of the Vosges sandstone. The results are shown in Tab 6. 1. It can be seen that the samples show an average water connected porosity of 23.3% (Tab 6. 1)

Tab 6.1: Water porosity of samples from Vosges sandstone

Sample	Height (mm)	diameter (mm)	Weight (g)	Volume (m^3)	% water porosity
1	76.265	37.846	172.47	8.588E-05	23.52
2	76.445	37.81	173.12	8.58E-05	23.22
3	76.56	37.69	174.7	8.54E-05	23.26

6.3. Bacterial culture medium preparation

We work on optimal conditions for bacterial growth. So we prepare a solution for bacterial development similar to the one in-situ but enriched with iron. We used two solutions. The first one is an aqueous solution in equilibrium with the rock. A sample of Vosges sandstone was crushed and suspended in 1L of water for 10 days in order to achieve a state of equilibrium. This solution was then centrifuged at 5000g for 10min at 20°C and the resultant solution is called “sandstone solution”. The second solution is similarly prepared but was enriched with iron by the addition of 5 mM of Fe^{3+} citrate. A culture medium was added to support bacterial growth in combination with ferric citrate ($C_6H_5FeO_7$). This solution is called "Fe^{3+} citrate" and abbreviated FCm. Dihydrogen (H_2) is the only electron donor and ferric citrate the only electron acceptor in this solution (Tab 6. 2).

Tab 6.2:Composition of the FCM solution

Components	Molar weight (g/mol)	Concentration	Density (g/L)
KH_2PO_4	136	0,025 mM	0,0034
K_2HPO_4	174	0,015 mM	0,0027
NH_4Cl	53	4,49 mM	0,238
$NaHCO_3$	84	2 mM	0,168
$MgSO_4{\cdot}7H_2O$	246	1,016 mM	0,25
$CaCl_2{\cdot}2H_2O$	146	0,48 mM	0,070
EDTA ($C_{10}H_{16}N_2O_8$)	292	0,065 mM	0,019
H_3BO_3	62	0,056 mM	0,0035
L-Arginine ($C_6H_{14}N_4O_2$)	174	20 mg/L	0,02
Ac.L(+)/L(-) glutamic acid ($C_5H_9NO_4$)	147	20 mg/L	0,02
Sérine	105,1	20 mg/L	0,02
Fe^{3+} citrate ($C_6H_5FeO_7$)	263	40 mM	10,52

First, 10.52 g of ferric citrate were dissolved in 400 mL of water and heated until boiling to remove dissolved gas. The pH is then adjusted to 6 when cooled. Then the rest of the salts were added and the volume adjusted to 500 mL with deionized water at a pH of 7.0 ± 0.1. The salinity of the culture medium was balanced by adding a saline solution in order to obtain NaCl contents 50 g/L. The medium was boiled for at least 5 min to remove the dissolved gases, then was cooled under with nitrogen, and distributed in 100 mL flakes. The formiate solution of a pH around neutrality 7 and other vitamins were then added to the bioreduction medium in order to obtain the final concentrations of 4 mmol L-1. The flakes and the medium contained were eventually sterilized in the autoclave. This FCm solution enrich the sandstone solution with iron, nutrients, and carbone source in order to be used as a bacterial medium for incubation in the flow-through cell.

6.3.1. Batch experiments

6.3.1.1. Preparation of the bacterial culture solution

The objective of these experiments in batch conditions is to quantify the consumption of hydrogen by iron-reducing bacteria *Shewanella putrefaciens* in anaerobic conditions and in the presence of H_2 in the very optimal conditions. This part was accomplished in collaboration with the Laboratory of Physical Chemistry and Microbiology for the Environment (LCPME - UMR 7564, CNRS / Université de Lorraine) by the student Elodie Martet for her master's thesis project.

Three types of experiments were carried out using *Shewanella putrefaciens*:

- monitoring the growth of the strain under various salt concentrations (NaCl) in an enriched medium of Trypticase Soy Broth (TSB) adequate for bacterial growth
- measuring the consumption of dihydrogen in a non-saline environment
- measurement of the consumption of hydrogen in a saline environment (representative of storage conditions in saline aquifer)

For that, three media were used for bacterial culture in order to compare the kinetics of hydrogen consumption at different conditions concerning carbone concentration, presence or absence of hydrogen and salinity:

- a formiate-free medium with H_2 (non-limiting) as the source of electrons;
- a medium with 4 mM of non-limiting formiate and H_2: The formiate concentration is assumed to serve primarily as a source of carbon for growth and H_2 the main source of electrons
- a medium serving as a positive control, with formiate as the only source of carbon and electrons, 30 Mm without addition of H_2.

These media were produced in triplicate and also the ferric citrate medium and with the sandstone solution. Several control tests were carried out under similar conditions:

- a medium with 2 mM of lactate where it is expected that the lactate acts as a source of C and H_2 as the main source of electrons;
- a medium with 1 mM acetate where the acetate is expected to act as the source of C and H_2 as the main source of electrons;
- a control without a source of organic C (except for amino acids) and without H_2, therefore without an exogenous source of electrons;
- an abiotic control in triplicate for each concentration of formiate for which the inoculum has been sterilized by heat at 121 ° C for 30 min before injection.

For these three media, ferric citrate is excessive relatively to the electron donor, at a concentration of 40 mM. The concentration of lactate and acetate used were calculated to as equivalent of electron of 4 mM of formiate in order to facilitate the comparison.

The FCm media were inoculated under sterile conditions in flasks sealed with gas with a thick butyl stopper and crimped with an aluminum ring. The presence of aqueous Fe^{3+} gives a dark color to amber appearance. The culture media were incubated at 30 ° C at 150 rpm in the dark for 15 days. Then, they were reloaded with H_2 by 5 min of a cloud of H_2/N_2 mixture (5% / 95%), the sterilization of the media was ensured by a hydrophobic filter membrane having a 0.2 µm of pore size. The operation was repeated after each sample for the bottles with H_2 so as to also maintain a slight overpressure of the order of +1 bar and left to rest for at least 24 hours.

6.3.1.2. Preparation of the bacterial suspension

To measure growth in a saline medium, the bacterial strain used was *Shewanella putrefaciens* CIP 8040 (equivalent to ATCC 8071). First, the strain was cultivated on a solid trypticase soy (TSA) medium for 24 h at 30 ° C. The preculture was then carried out in a trypticase soy broth (TSB) and stirring at 150 rpm and a temperature of 30 ° C for 24 h. The OD_{600} of the preculture was measured and added to the volume of the suspension and to the culture media TSB to obtain an OD_{600} between 0.1 and 0.2 units.

To cultivate the bacterial serial in the iron citrate medium, 30 mL of the culture was centrifuged (5000 g for 10 min at 20 ° C), and lots were taken up in 30Ml of suspension of 9 ‰ sterile NaCl. The four lots were then combined for centrifugation, then the resultant solution was suspended again in 20 mL of sterile 9 ‰ NaCl. The N_2 gas (99.99%) was then introduced for 20 min in the suspension obtained under aseptic conditions. The OD_{600} of this suspension was measured and was added in a sufficient volume to the culture medium to obtain an OD_{600} between 0.1 and 0.2 units.

For the culture in the sandstone solution, the same protocol was applied but the culture of 1 L was taken in 20 mL and the target OD_{600} of the culture medium was 6.0 ± 0.2. These cultures were inoculated with a high cell concentration (rest in cells) as cell growth will not be measured and in order to be able to observe a reduction of Fe^{3+}.

6.3.1.3. Physicochemical analysis

Cell growth evolution was controlled by measuring the optical density for λ=600 nm (OD_{600}). One milliliter of a bacterial suspension was taken and placed in polycarbonate of spectrophotometry. The OD_{600} was measured with respect to a blank reference corresponding to the filtered culture medium at 0.2 µm. OD_{600} measurements greater than 1.0 units were diluted with the same filtered medium in order to obtain a reading between 0.1 and 0.9 units. The natural growth rate µ (h^{-1}) and the generation time G (h) were calculated from the equation:

$$\ln OD_{600} = f(t) \qquad (6.\ 1)$$

t being the time of culture (h). The natural growth rate (or specific growth rate) μ was obtained by calculating the slope of the linear part of the exponential growth phase on the representation ln (OD_{600}) = f (t). The generation time was obtained according to the relation:

$$G \propto \frac{\ln 2}{\mu} \qquad (6.2)$$

The total number of cells was determined by labeling with SYBR Green II. One milliliter of the bacterial suspensions diluted before and fixed with 4% formaldehyde was mixed with SYBR Green II stock diluted to 1/1000 and incubated for 15 minutes at room temperature. This mixture is then completed with 9 mL of pyrogen-free water, then filtered through a black polycarbonate filter (0.2 µm porosity and 25 mm in diameter) after adding 10 mL of pyrogen-free water to the filter. The filter is then rinsed with 10 mL of non-pyrogenic water before being placed on a clean sheet and finally dried on Petri plate. A slide cover is then deposited on the 30 µL of buffered glycerin previously added to the filter to be studied under a microscope of x100 immersion objective and UV epifluorescence excitation in order to count the labelled bacteria.

Measuring Fe^{2+} allows to estimate the rate of Fe^{3+} bioreduction. Measuring Fe^{2+} is done by colorimetric test by the phenanthroline method (Fadrus & Malỳ, 1975). Each sample was mixed volume / volume with 1 Mol of HCl solution and stored away from light at + 4 °C until analysis day. The acidic environment limits the oxidation of Fe^{II} by O_2 in the air. The buffer solution was prepared as indicated in (Tab 6. 3), phenanthroline complex with Fe^{2+} and forms a reagent reacting at a wavelength of 510 nm, the glycocolle is a buffer allowing the solution to be maintained at a pH of 2,9. Nitrilotriacetic acid (NTA) complexes this with Fe^{3+} to prevent it from reacting with phenanthroline so that only Fe^{2+} is measured. Ten milliliters of buffer solution with phenanthroline were added to a 50 mL polypropylene bottle containing the sample to be measured (from 1µL to 40 mL). The volume was then reduced to 50 mL with ultrapure water. The flasks were left in the dark for 30 minutes. The intensity of the coloration was then measured at 510nm against a blank produced under identical conditions but without Fe or even without phenanthroline. This absorbance was then related to a standard range previously obtained and calibrated by following the same protocol but not exceeding 1mg/L of Fe^{3+} so that the curve remains linear.

Tab 6.3: Composition of the buffer solution. TAN: nitrilotriacetic acid

Composition	Volume	Masse (g) for a v= 100 mL
Phenanthroline /HCl (0.025 M)	5	2.48
Glycocolle	5	18.67
NTA (added after dosage)	1	1.90

In order to calculate the production rates of Fe^{2+} the equation used is calculated according the first order of the kinetic law of Fe^{3+} reduction equation:

$$V = \frac{d[Fe^{3+}]}{dt} = \frac{d[Fe^{2+}]}{dt} = K_{obs}[Fe^{3+}] \qquad (6.3)$$

$$V = \frac{dx}{dt} = K_{obs}(a-x)$$

$$\frac{dx}{(a-x)} = k_{obs}dt \qquad (6.4)$$

The integration of the differential equation is:

$$-\ln(a-x) = K_{obs}t + C \qquad (6.5)$$

C is determined according to the initial state conditions: at t_0 x = 0

$$C = -\ln(a)$$

$$-\ln(a-x) = K_{obs}t - \ln(a)$$

$$\ln(\frac{a-x}{a}) = -k_{obs}t \qquad (6.\ 6)$$

$$a - x = ae^{-k_{obs}t}$$

Considering , $x = a(1-e^{-k_{obs}t})$, we can calculate the evolution of F^{2+} concentration during the reaction where K_{obs} the constant of production rate of the first order (t^{-1}):

$$\left[Fe^{2+}{}_t\right] = \left[Fe^{2+}\right]_{\max}(1-e^{-k_{obs}t}) \qquad (6.\ 7)$$

The rate of Fe^{3+} reduction is represented by the derivative of the first order equation of the mathematical function represented by the equation above with respect to time:

$$\frac{\left[Fe^{2+}{}_t\right]}{dt} = \left[Fe^{2+}\right]_{\max} K_{obs}e^{-k_{obs}t}) \qquad (6.\ 8)$$

The initial rate of Fe^{2+} production is obtained for t → 0:

$$V_0 = \frac{\left[Fe^{2+}{}_t\right]}{dt} = \left[Fe^{2+}\right]_{\max} K_{obs} \qquad (6.\ 9)$$

The maximum concentration of Fe^{2+} is obtained for t → ∞ and the rate of production become 0.
So in order to fit the experimental results and calculate the initial production rate of Fe^{2+}, the benchmark equation below i an exponential fit:

$$V_0 = \left[\left[Fe^{2+}\right] - \left[Fe^{2+}\right]_{\max}\right] \times e^{-K_{obs} \times t\,0} + C_1 \qquad (6.\ 10)$$

Where C_1 corresponds to the Fe^{2+} concentration at t = ∞ and C_2 corresponds to the concentration of iron at the considered time. C_1=0.01, Kobs=1.

6.3.2. Flow-through experiment mimicking the underground storage in aquifers

A special flow-through system was designed to simulate the reservoir conditions of lithostatic pressure of 200 bar and a temperature of 35°C, the optimal temperature for *Shewanella* growth. This mixture was chosen considering the optimal conditions at which the bacteria can convert the hydrogen according to the stoichiometry of the redox equation of respiration and the quantity of the present iron substrate.

6.3.2.1. Experimental apparatus

The major components of the experimental apparatus are:

Circuit components:

- At the upstream:
  - A precision syringe pump to inject hydrogen gas mixture in the system at 50 bar
  - A precision syringe pump to regulate the confinement oil pressure at 200 bars
- Triaxial compression cell in the oil bath: the cell contains the sandstone sample and allows the application of hydrostatic pressure as well as the injection of gases and other fluids. The cell is completely immersed in an oil bath equipped with temperature probes to regulate the temperature.

- At the downstream: another precision syringe pump for the outgoing fluids from the triaxial cell and to regulate the backup pressure at the outlet.

All components are connected with valves and circulation capillaries (Fig 6. 1).

Fig 6.1: Set-up of the circuit components

Sampling setup-components:

This triaxial cell is linked to a micro-gas chromatograph (micro-GC) allowing a chemical analysis of the interstitial gas by a controlled sampling system (high pressure-low pressure valve).

- The sampling valve: the high pressure-low pressure valve (HP-BP): this valve designed specifically by SRA instruments allows reducing the pressure of sampled gas from 50 bars to 2 bars in order to be analyzed in the micro-GC. The valve is an injection turret composed of two pneumatics valves. Gas is sampled at 50 bars when the high-pressure valve opens by a push of 5 bars of another gas. A loop of 113 mL fills up with the sample. Then, the low-pressure valve opens so gas pressure depressurizes to 2 bars by passing through another transfer line and being injected into the micro-GC. The lines are heated up to 35°C. The valve is connected to the micro-GC as well as the computer through the LaTep software of SRA instruments.
- Micro Gas chromatography is one of the most widespread geochemistry analytical tools used in laboratories and fields as a way to separate and analyze complex mixtures of gas. Sample is injected after heating into channels through which a carrier gas (helium or argon) circulates permanently. The gas mixture is separated into its individual components based upon relative retention time on the GC separation column with respect to their affinity with the stationary phase. For quantification, each surface obtained is attributed to a certain specific concentration value taking into consideration the nature of the gas separated and the retention time. Results appear on a plot as symmetrical Gaussian peaks, and peak shape and surface are function of the gas elution rate and concentration. A calibration curve is required before analysis. In our study we use a Micro-GC from Agilent solutions piloted by Soprane software from SRA instruments.

The setup valve-micro-GC works in sync according to a previously inserted program of sequences. A sampling sequence is made up of 6 analyses: the first 3 analyses are for purging the system and the last 3 ones are considered for measurements of gas evolution in sandstone samples. For each analysis, the valve uptakes 3 times 0.113 ml from the gas and discharges it into the micro-GC for analysis. Before the test, the gas mixture of hydrogen and nitrogen was analyzed by the setup. Several sequences of measurement were done at the same pressure of 50 bars, separated by 15 minutes each, in order to obtain a baseline for the analysis (Fig 6.2).

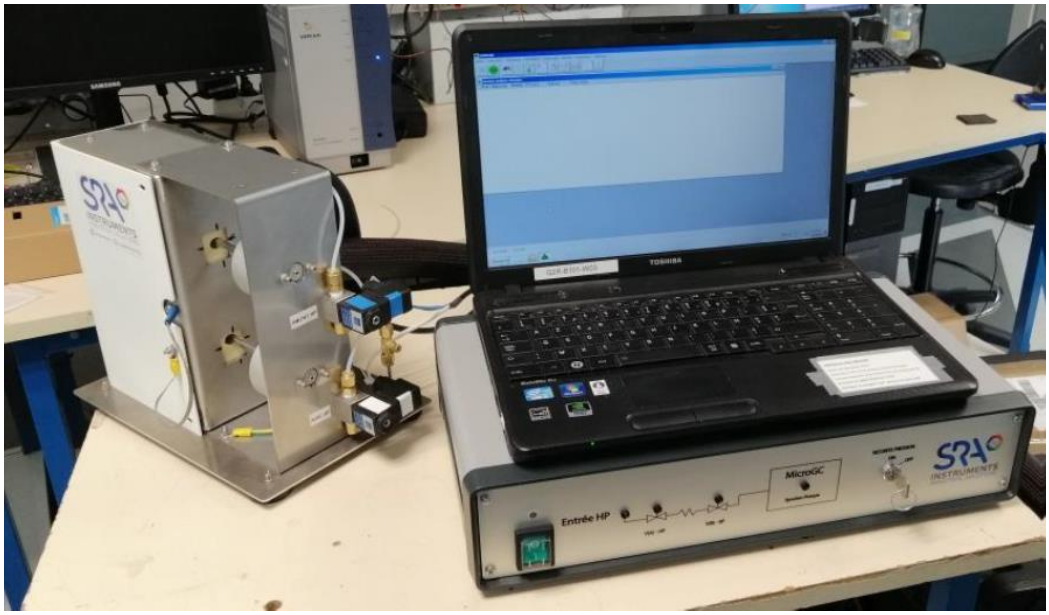

Fig 6.2: The sampling valve HP-LP components

6.3.2.2. Calibration of the micro-GC and the valve HP-LP

Six calibration standards with a specific composition of gas have been used to calibrate the micro-GC in order to quantify directly the concentration of hydrogen with respect to the peak surface obtained according to the gas retention time on the column of the micro-GC (). Some of the standards were passed in triplicates for repeatability purposes.

Tab 6.4: Gas standards mixtures used for calibration

Gas standard	H_2 concentration (%)	N_2 concentration (%)	Ar concentration (%)
H2_90_N_20	88%	10%	-
H2_80_N_20	80 %	20%	-
H2_50_N_50	50%	10%	-
H2_20_N_80	20%	80%	-
H2_5_ar_95	5%	-	95%
H2_5_ar_90	10%	-	90%

After conditioning the microGC columns to remove all external contamination and impurities, standards were injected to be analyzed into microGC channels by a capillary. Channel 1 having helium as carrier gas, was used to identify hydrogen content. The calibration curve was plotted for hydrogen considering the multiple point external standard method (Fig 6. 3).

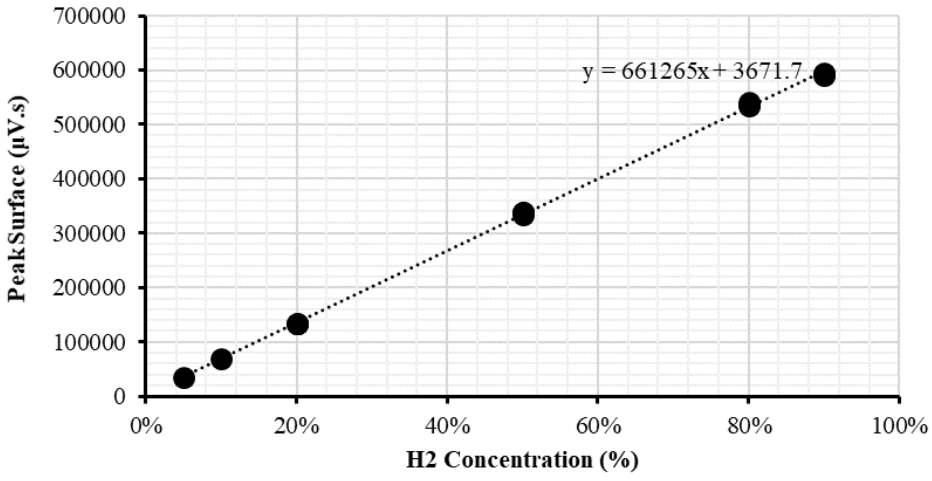

Fig 6.3: H_2 calibration curve with respect to the peak surfaces

It should be noted that the calibration curve was first conceived for high concentration of hydrogen (around 70%) to simulate the underground storage of pure hydrogen.

The valve is calibrated to work only for a pressure of 50bars of gas. In order to validate the calibration, we inject at different pressure, a gas mixture of 70% of H_2 and 30% of N_2 directly from the tank and by passing via the valve into the micro-GC. Hydrogen concentration measurements obtained by the microGC were plotted with respect to injection pressure (Fig 6. 4).

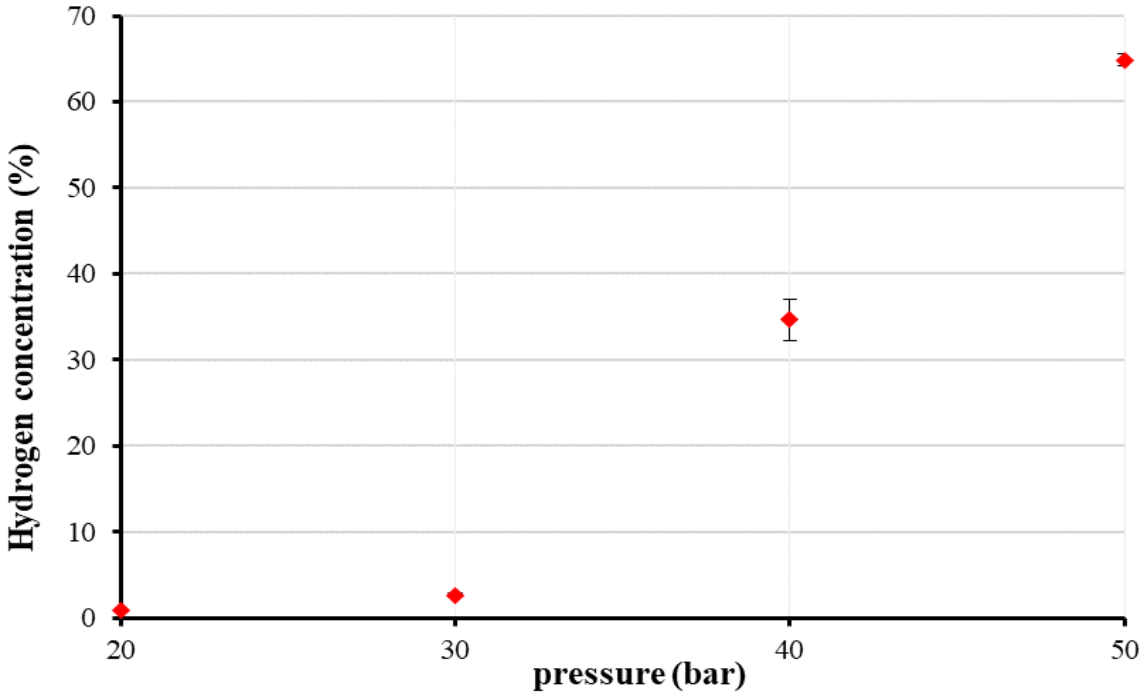

Fig 6. 4: Impact of gas injection pressure in the sampling valve HP-LP on measured hydrogen concentration values.

Hydrogen concentration decreases with the decrease of pressure. The valve recalibrates the sample volume by an injection of ambient air inducing a dilution of the gas mixture and disturbing the real values of the concentrations intended to be measured. The correct concentration value is recovered only for an injection pressure of 50 bars (Fig 6.4). So if we want to use this valve for lower or higher pressure it should be recalibrated. This sampling issue should be kept in mind in the analysis of our experimental results and will require to maintain a constant pressure within the cell during all the experiments.

6.3.2.3. Experimental procedure

Feasibility test of the system:

The cylindrical sample of sandstone is wrapped with aluminum foil and hooded with a Viton cover to properly insulate it. The sample is then placed at the base of the cell, the body is fixed and the cell is filled with confinement oil then closed by the top with a head fixed with 8 jacks. The hydrostatic pressure is settled up at 200 bars and the whole cell is moved to the thermal bath to be heated at 35°C and all necessary connections are established.

To test the feasibility of the system, the sample is filled at 50 bars of H_2 gas until equilibrium is reached. Several measurements were executed by the setup valve-microGC separated each by 15 minutes. The withdrawn volume is compensated every time by an upstream injection of gas to maintain the operating pressure value, hence a closed circuit in the cell. For the compensation we test different type methods:

- Compensation with the same mixture of hydrogen gas: For example, when using 70% of hydrogen gas mixture we compensate by an upstream injection with the same gas. This in order to maintain the same pressure.
- Compensation by an injection of argon gas, an inert gas and the vector gas present in the micro-GC column. We choose to work with an inert gas in order to better observe the bacterial alteration effect with respect to the initial hydrogen concentration present in medium. Argon provokes a concentration dilution of the

mixture inside the cell after every sampling. This factor of dilution should be determined in order to work in optimal conditions with respect to the stoichiometry of the hydrogen conversion equation.

Cell sterilization and establishment of anaerobic conditions:

The system is purged with argon to expel air in order to allow gas saturation in sample pores and avoid oxygenated conditions. Then, the system is decontaminated by introducing 103ml of distilled water and increasing the temperature to 100°C over a few hours. Temperature is then lowered back to 35°C and left to stand overnight. Eventually, water is flushed out of the system entirely with argon.

Bacterial solution inoculation and seeding on the sandstone sample in the cell:

100 ml of the bacterial solution is mixed with 1 bar of hydrogen gas and pushed inside the cell to be seeded on the sandstone sample. The bottle containing the substrates, nutrients, and bacteria was previously degassed at 0.1 ml/min and a pressure of 10 MPa to establish an anaerobic state inside. So, hydrogen gas was introduced through a syringe into the bottle and mixed with the solution. The gas is pressurized (1-2 bar) to pump the liquid inside the upstream liquid pump to be introduced into the cell. The objective of this process is to preserve the deoxygenated state of the bacterial solution and provide all the physical conditions necessary for bacterial seeding and growth (Fig 6.5).

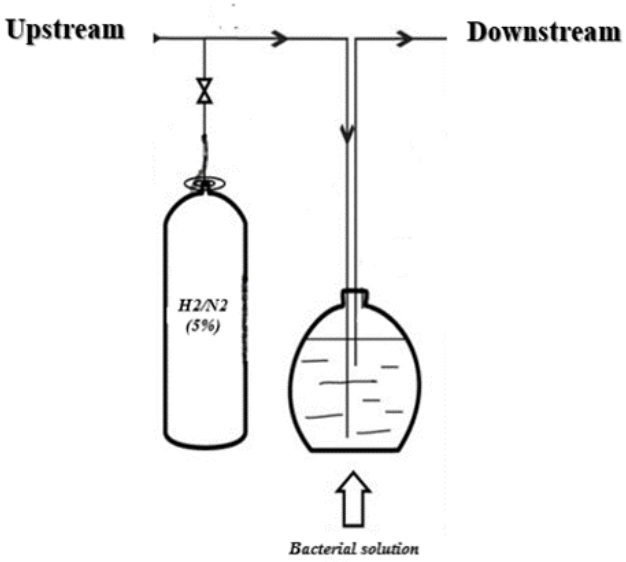

Fig 6.5: Bacterial seeding into the flow-through cell setup

The introduced solution circulates in the cell under a pressure of 50 bars in order to seed the bacteria on the sample. After 24 hours, water is collected from the dead volumes and the optical density is measured directly to determine the number of remaining cells in the system. Bacteria are allowed to incubate at rest for another 48 hours in the system.

Finally, gas is injected and the bacterial solution is flushed out. The volume of fluid is recuperated to calculate residual water saturation and the possible number of remaining cells in the system.

Experimental process:

H_2 gas is maintained at 50 bar pressure at the upstream. The downstream is then isolated in order to have a closed circuit. Every 72 hours, the valve-micro-GC system samples 3 ml of the gas from the system. The volume is compensated by an injection of gas at the upstream. The experiment was executed at different conditions of gas concentrations, iron concentrations, bacterial concentration and sampling rate:

Tab 6. 5: The different test conditions performed on the new experimental device

Test	Presence of bacteria	Hydrogen gas mixture	Compensation gas at the upstream	Sampling rate by the valve-microGC	Initial iron concentration	Saturation
1	Yes: OD_{600}=5	70%H_2, 30%N_2	70%H_2, 30%N_2	Every 1 day	40mmol	0.63
2	No	5%H_2, 95%N_2	Pure argon	Every 15 minutes	80mmol	0
3	No , blank test	5%H_2, 95%N_2	Pure argon	Every 3 days	80mmol	0.58
4	Yes, OD_{600}=10	5%H_2, 95%N_2	Pure argon	Every 3 days	80mmol	0.56

By this method, the evolution of the outlet gas concentration can be identified and so the possible microbial consumption if present in the medium (Fig 6. 6).

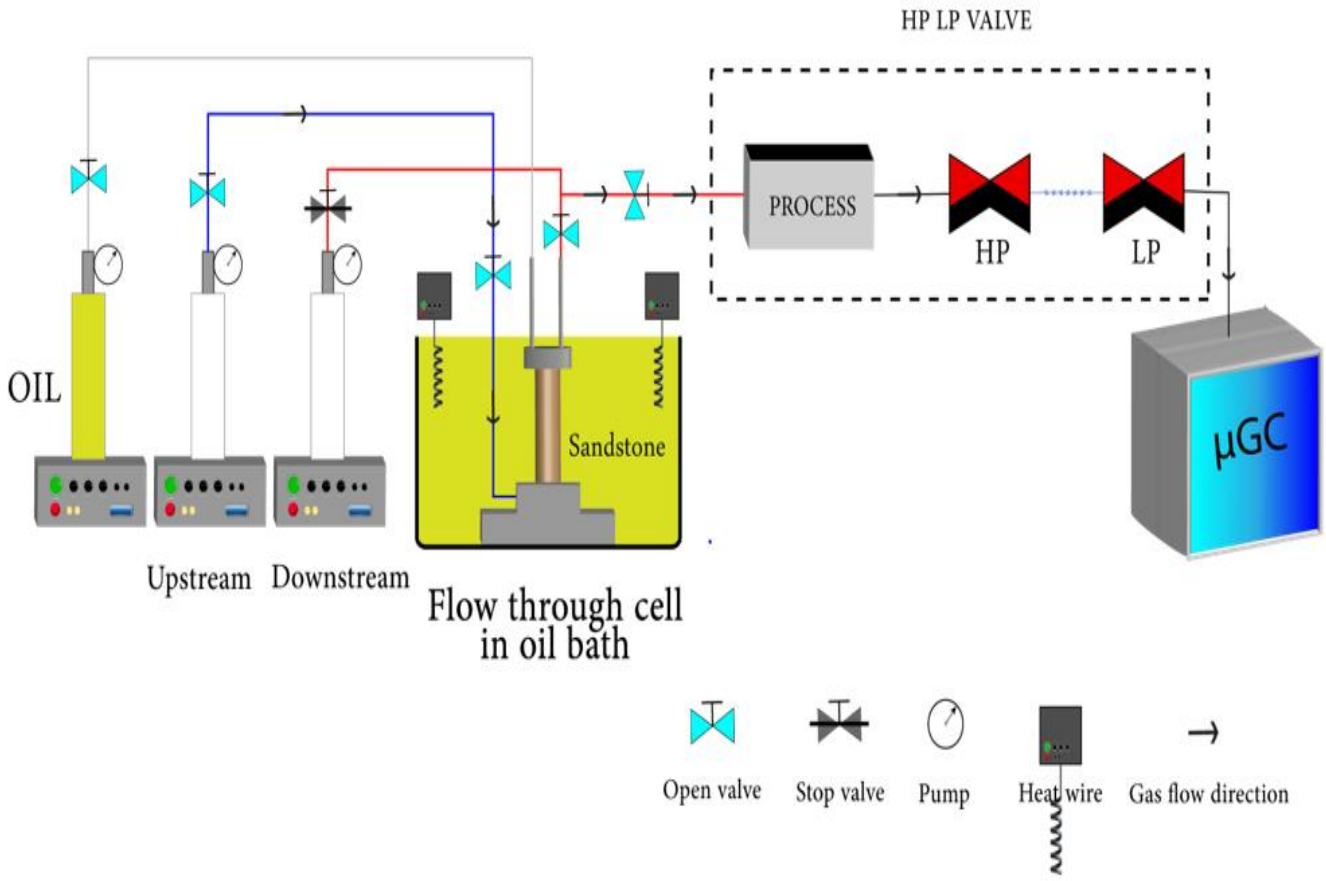

Fig 6. 5:Scheme of the set-up of the flow-through experiment in a closed circuit method

6.3.3. Results and discussion

6.3.4. Results in batch

6.3.4.1. Salinity impact on S. putrefaciens growth

First, the effect of salinity was observed in batch on the growth of *S. putrefaciens*. For this, bacteria were incubated in complete medium (TSB) with NaCl concentrations of 5g/L, 25 g/L, 50 g/ L and 100 g/L. The resultant curves of bacterial growth observed according to the optical density (OD_{600}) evolution with respect to incubation time shows an exponential behavior with a small lag phase at the first hours before a rapid growth. The curve at 5g/L enters the stationary phase of growth by the end of incubation time (48 h) faster than the other curves reaching the plateau later. Reaching this phase is function of nutrient availability by the end of incubation time. So, it is possible that, if the incubation time is extended, the OD_{600} of these cultures reach the same order of magnitude as the culture at 5 g/L of NaCl (Fig 6. 7).

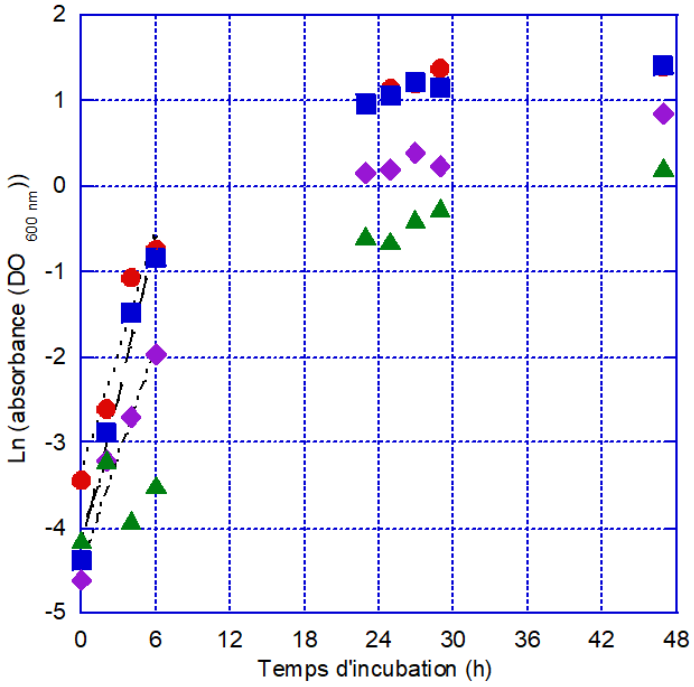

Fig 6. 6: Representations of the growth of S. putrefaciens measured by density of absorbance at 600nm optical wave in a rich medium (TSB) at different concentrations of NaCl: 5g/L (red circle), 25g/L (blue square), 50g/L (purple diamond) and 100g/L (green cross): OD600 = f (t) (a) and Ln (OD600) = f (t) (b). The natural growth rate μ (h-1) was calculated from linear regressions Ln(OD600nm) = f (t) (exponential trend). The experiment was performed in triplicates (three culture flasks per salt concentration).

In addition, the maximum OD_{600} logarithmic value of 1.3 doesn't show any variation with the increase of concentration to 25 g/L. However, for a higher concentration of salinity, OD_{600} show a proportional decrease with respect to the increase in NaCl concentration.

On the other hand, Tab 6.6 shows that specific growth rate μ (h^{-1}) decreases with the concentration of salt from 1.3 h^{-1} for 5 g/L of NaCl to 0.68h^{-1} for 100 g/L of NaCl. The time required for bacteria to divide, *i.e.* the generation time ***G* (h)**, increases with the concentration of salinity. The duration of generation time goes from 0.54 h for 5g/L to 1.02 h for 100 g/L of NaCl. This impact of salinity is much more visible at high concentrations of 25 and 50 g/L of NaCl. The threshold salinity value impacting *S. putrefaciens* growth is therefore between these two values. This negative impact of salinity on cell growth is due to the loss of energy in cells. In fact, *S. putrefaciens* is an opportunistic and halophilic bacterium but this halotolerance has an energetic cost. This species can tolerate living in seabeds at high salinity of 34.7g/L (Nogi et al., 1998) but beyond, for salinity close to 300 g/L of NaCl, *S. putrefaciens* become hardly active and their growth decelerates (Pagniez & Berche, 2005).

Tab 6.6: Specific natural growth rate µ(h-1) and generation time G (h) in a rich medium (TSB) at different NaCl concentrations

	μ (h^{-1}) (n=3)	***G* (h) (n=3)**	**Valeur maximale de OD_{600} (47h)**
5 g/L de NaCl	1,30 (± 0,16)	0,54 (± 0,06)	5.94
25 g/L de NaCl	0,92 (± 0,01)	0,75 (± 0,01)	4.87
50 g/L de NaCl	1,03 (± 0,03)	0,67 (± 0,02)	4.33
100 g/L de NaCl	0,68 (± 0,05)	1,02 (± 0,08)	3.57

6.3.4.2. Hydrogen consumption evolution by the measurement of Fe^{2+} production

The ability of *S. putrefaciens* to reduce Fe^{3+} to Fe^{2+} was measured under different conditions in FCm medium for the same intial concentration of 10Mm of Fe^{3+}. The reduction equation will make it possible to calculate the consumption of H_2. The first conditions tested for the production of Fe^{2+} by *S. putrefaciens* are buffer solutions with two compositions

- in the absence of formiate and without H_2
- with only H_2 as the exogenous source of electron.

A third control media was prepared in abiotic conditions, in absence of bacteria but with only presence of H_2 gas (Fig 6.8). In absence of any bacteria, no reduction in Fe^{3+} is observed (curve with orange diamonds). It proves that this reaction only occurs in presence of biological intervention. The concentration curve of Fe^{2+} for the medium in the absence of H_2 and without formiate (curve with black circles), shows an increase until reaching a plateau at aorund 10mM after 72h of incubation. The only responsible of this production of Fe^{2+} are the endogenous electrons of the bacteria accumulated during the culture preparation process. This was also verified later by calculating the estimated quantity of Fe^{3+} reduced by the amino acids present in the medium to 1.76 mM which cannot explain the 10mM Fe^{2+} produced.

The curve at 0 mM formiate and in the presence of H_2 (blue square) increases until it forms a plateau at 25mM Fe^{2+} produced after 216h until 312h of incubation. The difference between the two curves is only due to the presence of H_2. In other words, this production of Fe^{2+} is caused by the redox equation catalyzed by *S. putrefaciens* using only H_2 as electron donor (Fig 6.8).

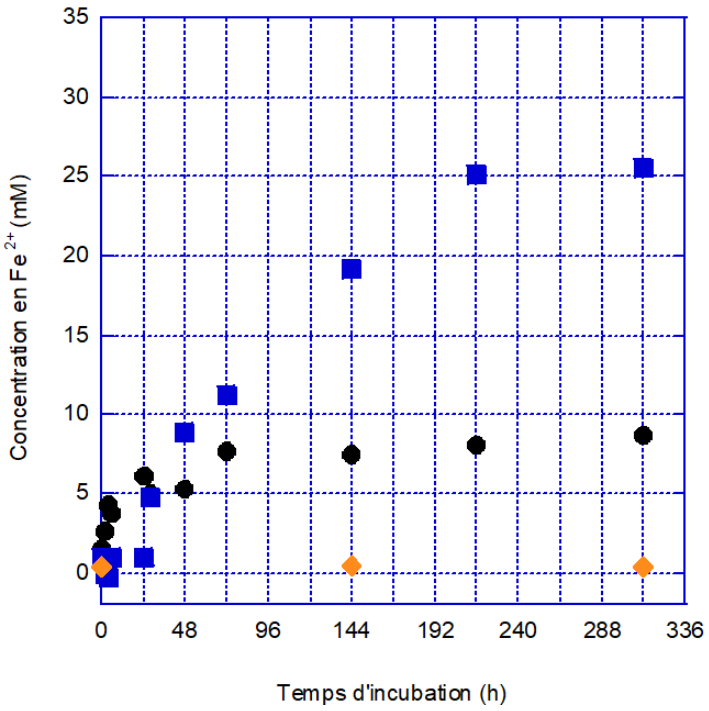

Fig 6. 7: Variation of Fe^{2+} concentrations during S. putrefaciens culture in FCm medium: culture without formiate and H_2 (black circle) and culture without formiate and with only H_2 (blue square) and culture in abiotic control conditions without bacteria in presence of H_2 (orange diamond).

Other conditions were also tested to observe whether *S. Putrefaciens* has the ability to use different carbon sources like acetate, lactate or formiate at different concentrations. The capability of *S. Putrefaciens* to regulate his consumption by using H_2 only as electron donor and formiate only as carbon source is also investigated.
Fig 6. 9 presents the variation of Fe^{2+} concentrations during *S. Putrefaciens* culture in FCm medium obtained with different carbon sources: 1mM acetate with H_2 (green circle), 2mM lactate with H_2 (blue square), 4mM formiate with H_2 (black cross) and 30mM of formiate without H_2 (pink triangle)

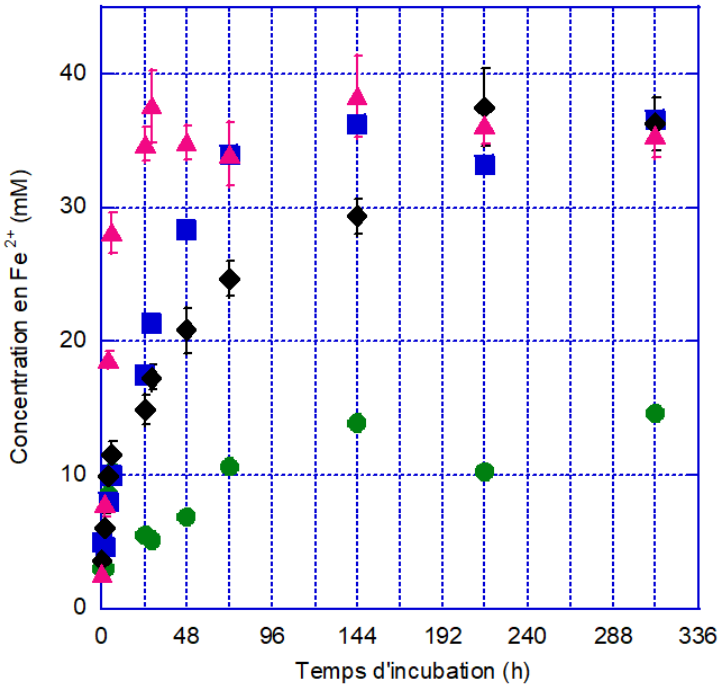

Fig 6. 8: Variation of Fe^{2+} concentrations during S. putrefaciens culture in FCm medium with different carbon sources: 1mM of acetate with H_2 (green circle), 2mM lactate with H_2 (blue square), 4mM formiate with H_2 (black cross) and 30mM of formiate without H_2 (pink triangle). Error bars represent standard deviations from the mean of three independent tests.

Note that the concentrations of 4mM formiate, 2mM lactate and 1mM acetate present in these experiments provide the same amount of electrons.

The concentrations of Fe^{2+}, in presence of hydrogen and, respectively of 4Mm of formiate (black cross) and of 2mM of lactate (blue square) increase until a plateau is formed at 35mM of Fe^{2+} produced after 72h of incubation for the lactate, after 216h of incubation for the 4mM formiate. So lactate, appears to be more suitable for a rapid growth of the bacteria and hydrogen consumption compared to the formiate.

However, the concentration curve in the presence of 1 Mm of acetate (green circle) and in presence of H_2, shows an increase until only reaching a plateau at 15mM Fe^{2+} after 72h of incubation less than the plateau of lactate and formiate. The acetate curve is similar to the control curve without an exogenous source of electron (formiate, Fig 6. 7). It indicates that bacteria are not able to use acetate as carbon source and that acetate partially inhibits the use of hydrogen to produce Fe^{2+} compared to formiate or lactate. On the contrary, lactate and formate are also used by bacteria as electron donor.

In addition, without the presence of hydrogen, the concentrations of Fe^{2+} in presence of 30mM of formiate (pink triangle) increase to reach the same plateau of the lactate curve and formiate curve of 4Mm. As the production rate is similar during the first 24h for the two conditions in presence of formiate (4mM formiate with H_2 and 30mM of formiate without H_2), it means that *S. Putrafaciens* cannot regulate growth for limiting conditions of formiate availability. So bacteria prefer to use formiate as a carbon and electron source for cell growth over the usage of H_2 as electron source.

Also, we test the differences between in Fe^{2+} production as a function of NaCl concentrations without formiate or with 30 mM of formiate (Fig 6. 10).

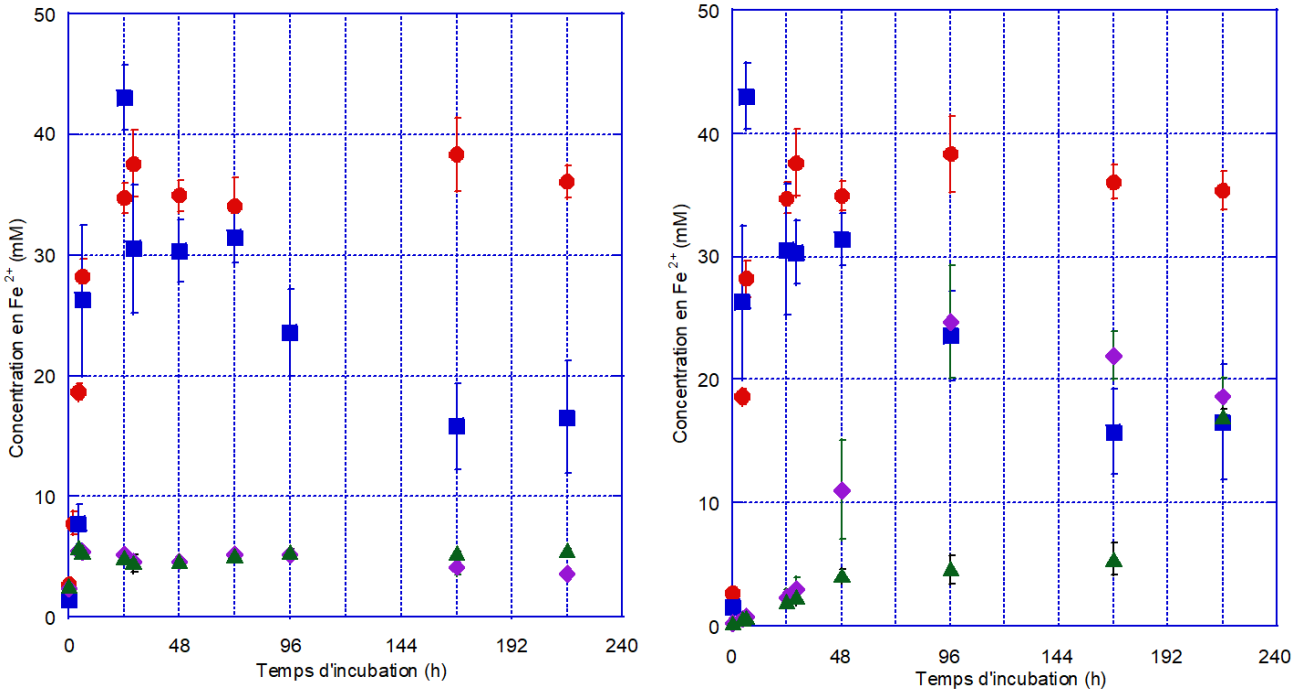

Fig 6.10: Variation of Fe^{2+} concentrations for S. putrefaciens culture in FCm medium with 0mM formate (a) or 30mM formate (b) at different NaCl concentrations: 0g/L with H_2 (red circle), 25 g/L with H_2 (blue square), 50g/L with H_2 (purple diamond) and 100 g/L with H_2 (green cross). Error bars represent standard deviations from the mean of three independent tests.

The Fe^{2+} concentration for S. putrefaciens culture in FCm medium with 0mM formiate shows a sharp increase in the Fe^{2+} concentration at 0 g/L NaCl (red circle) and reaches a plateau of 35mM of Fe^{2+} produced at 24h incubation. The Fe^{2+} concentration at 25 g/L of NaCl (blue square) increases to more than 40 mM produced at 24h of incubation, then decreases to 30 mM from 28h to 72h of incubation. The concentration of Fe^{2+} at 25 g/L of NaCl then decreases to reach about 25 mM of Fe^{2+} product from 168h to the end of the incubation time (216h). Finally, the concentrations of Fe^{2+} at 50 (purple diamond) and 100 g/L of NaCl (green cross) increase both to reach 5mM of Fe^{2+} produced after 2 hours of incubation. They will remain at this level until the end of the incubation time (216hrs) (Fig 6. 5, a).

In a similar way, variation of Fe^{2+} concentrations for *S. putrefaciens* culture in FCm medium with 30mM formiate shows a sharp increase in the Fe^{2+}concentration at 0g/L NaCl (red circle) until reaching a plateau of 35mM Fe^{2+} produced at 24h incubation. The Fe^{2+} concentration at 25 g/L of NaCl (blue square) increases to more than 40mM of Fe^{2+} produced at 8h of incubation, then decreases to 30mM at 24h to 48h of incubation. The Fe^{2+} concentration then decreases to about 25mM Fe^{2+} product from 168h to the end of the incubation time (216h). The concentration of Fe^{2+} at 50g/L of NaCl (purple diamond) increases slowly to reach 20 mM of Fe^{2+} produced at 168h of incubation and stagnates at this level until the end of the incubation time (216h). The Fe^{2+} concentration at 100g/L NaCl (green cross) increases to a plateau at 5 mM Fe Fe^{2+} produced from 48h to 168h of incubation. The Fe^{2+} concentration then increases to 20 mM at 216 hours of incubation (Fig 6. 5, b). For the same NaCl concentrations, for the medium at 0mM and 30mM of formate, the Fe^{2+} concentration has the same dynamics. Therefore, the presence of formiate doesn't seem to influence the production of Fe^{2+} by *S. putrefaciens*.

Finally, it was possible to calculate the initial rates of Fe^{2+} production using the curves under the various conditions. For the negative control (without hydrogen, formate or NaCl) reduction of Fe^{3+} without an exogenous electron donor (H_2) was used as a benchmark: this value was subtracted at all other initial rates in order to obtain the rate of reduction of Fe^{3+} without the endogenous donors. Eventually, the rate of consumption of hydrogen could be calculated by dividing the rate of production of Fe^{2+} by two according to the stoichiometry of the reduction equation of H_2 by *S. putrefaciens*:

$$H_2 + FeOOH + 4H^+ = 2Fe^{2+} + 4H_2O \qquad (6.\ 11)$$

For the production curve in FCm medium with 4 mM of formiate and hydrogen without NaCl, we obtain two distinct slopes. The first corresponds to the production of Fe^{2+} in the presence of formiate (used also as electron donor) and the second to the production of Fe^{2+} in the presence of H_2. Thus, the initial speed was calculated for these two slopes (Fig 6. 9).

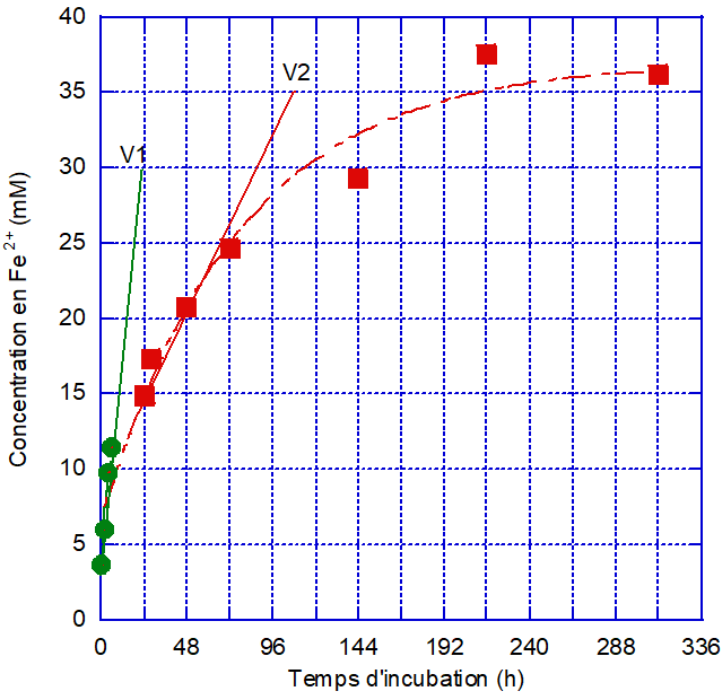

Fig 6.11: Initial rate of reduction of Fe^{3+} to Fe^{2+} based on the Fe^{2+} concentration curve produced by S. putrefaciens in FCm medium with 4 mM formate and without NaCl: green curve corresponds to the initial rate of reduction of Fe^{3+} in the presence of only formiate (V1), while the curve in red corresponds to the initial rate of reduction of F^{3+} in presence of formiate and H_2 (V2).

From these results we can observe several points (Fig 6. 7). First, the initial production rate of Fe^{2+} under control conditions, i.e. without H_2, NaCl or formiate is very close to the initial rate in the presence of 1mM acetate (respectively 0.20 and 0.14 mM/h). In addition, in the presence of 4 mM formate (3.20 mM/h) and 2 mM lactate (1.90 mM/h), the production rates are relatively close which validate the possible usage of different electron sources for the bacterial growth.

For the culture with 4 mM of formiate, *S. putrefaciens* consumes all the carbon to reduce Fe^{3+} despite the presence of H_2 in the first 24 hours (Fig 6.9, curve V1) then use the present hydrogen for growth (Fig 6.9, curve V2). Thus, for the part of the consumption only by the H_2 (V2 in Figure 6.9), this initial speed is (0.48 mM /h) close to that of V1, and with addition of H_2, it becomes 0.86 mM / h.

For conditions without NaCl in the Vosges sandstone solution VS, the initial rates of reduction are lower (1.99 mM/h without formiate and 0.04 mM/h in presence of 30 mM of formiate) than the initial rates of the FCm medium (0.86 mM/h without formate and 6.77 mM/h with 30 mM of formiate).

For the FCm medium, without formiate, the initial rate goes from 0.86 mM/h to 5 g/L of NaCl at 0.05 mM/h for 100 g/L of NaCl. For the FCm medium with 30 mM of formate, the initial rate goes from 6.77 mM/h to 5g/L of NaCl at 0.19 mM/h for 100 g/L of NaCl. For the VS solutions without formiate, the initial speed goes from 1.99 mM/h to 5 g/L of NaCl at 0.09 mM/h for 100 g/L of NaCl. For the VS solution medium with 30 mM of formate, the initial rate goes from 0.04 mM/h to 5 g/L of NaCl to 0.004 mM/h for 100 g/L of NaCl. These values clearly show a decrease for each condition when the NaCl concentration increases.

Tab 6.7: Table of initial velocities under different conditions of Fe3+ reduction, obtained graphically

Culture	**Fe^{3+} reduction velocity (mM/h)**	**Reduction velocity due to exogenous electron donor (mM/h)**	**H_2 consommation rate (mM/h)**
FCm (without H_2 and Formiate) benchmark	0.20 (± 0.00)	X	X
FCm with H_2 without formiate, NaCl =0 g/L	0.86 (± 4.41)	0.66	0.33
FCm with H_2 without formiate, NaCl =50g/L	3,46 (± 1.84)	3.26	1.63
FCm with H_2 without formiate, NaCl =100g/L	0.005 (± 106.85)	0	0
FCm with H_2, Formiate à 4 mM ,NaCl =0 g/L	X	3.20 (± 2.44)	3,00
FCm without H_2,Formiate 4 mM , NaCl = 0 g/L	3.20 (± 2.44)	3,00	X
FCm with H_2,Formiate 4 mM , NaCl = 0 g/L	0.48 (± 0.00)	0.28	0.14
FCm without H_2,Formiate 30 mM ,NaCl =0 g/L	6.77 (± 0,03)	6.57	X
FCm without H_2,Formiate 30 mM , NaCl 50 g/L	4.02 (± 3.20)	2.42	X
FCm without H_2,Formiate 30mM , NaCl =100 g/L	0.19 (± 1E308)	0	X
FCm with H_2, Lactate 2 mM , NaCl= 0 g/L	1.09 (± 0.00)	0.89	0.44
FCm with H_2, Acetate 1 mM , NaCl =0 g/L	0.14 (± 0.36)	0	0
VS with H_2,Formiate 0 mM , NaCl =0 g/L	1.99 (± 0.01)	1.79	0.89
VS with H_2,Formiate 0 mM , NaCl =25 g/L	2.96 (± 0.15)	2.76	1.38
VS with H_2, Formiate 0mM , NaCl =50 g/L	0.44 (± 0.00)	0.24	0.12
VS with H_2,Formiate 0 mM , NaCl =100 g/L	0.29 (± 0.01)	0.09	0.04
VS with H_2, Formiate à 4 mM, NaCl= 0 g/L	0.03 (± 0,47)	0	0
VS without H_2, Formiate à 30 mM , NaCl = 0 g/L	0.04 (± 3,20)	0	X
VS without H_2,Formiate 30 mM , NaCl =25 g/L	0.06 (± 10488,17)	0	X
VS without H_2,Formiate 30 mM , NaCl =50 g/L	0,01 (± 434.33)	0	X
VS without H_2, Formiate à 30 mM , NaCl=100g/L	0.004 (± 48.85)	0	X

6.3.4.3. *S. putrefaciens* bacterial cells count

In order to verify that cultures still display high bacterial concentration after incubation periods, we performed a cell count with SYBR Green II in several different cultures (25g/L of NaCl with 30 mM of formate and without formiate in FCm medium or in sandstone solution, 30 mM of formate without NaCl and without H_2, and without formate or NaCl with and without H_2) at three different times (0, 48 and 216 h of incubation). A sample was taken periodically to be traced in order to count the living cells. The cell concentration (cells / mL) of the cultures was calculated and shown in Fig 6. 10 below:

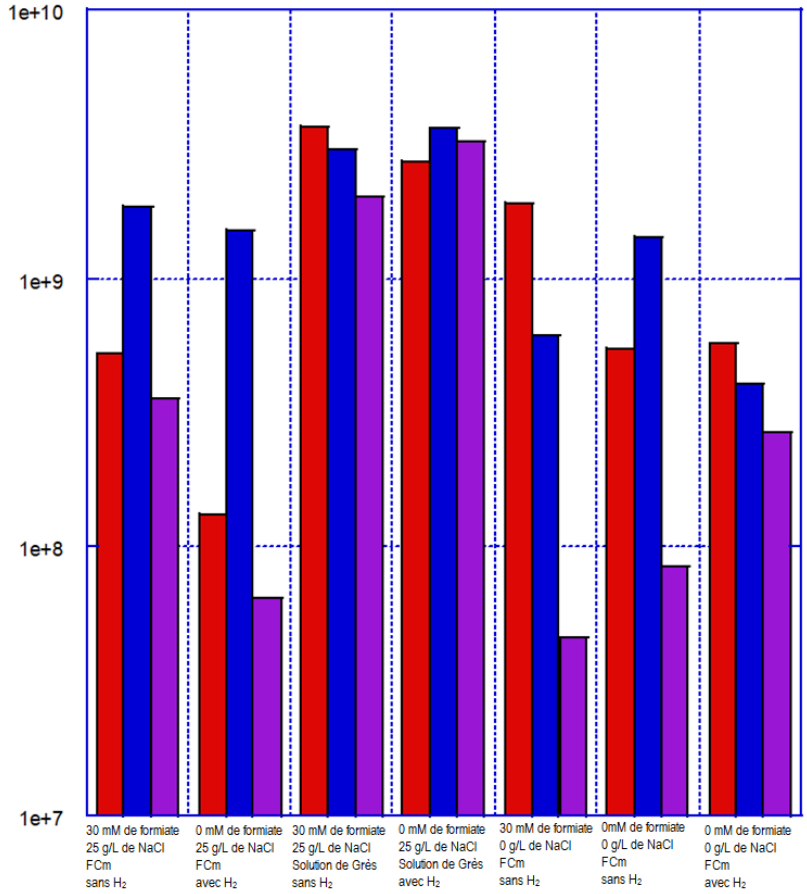

Fig 6.1: Evolution of cells number of cells (cells/mL) labeled with SYBR Green II for different cultures at three incubation times: 0 (red), 48 (blue) and 216 h (purple).

Cell counts do not seem to vary greatly either between different incubation times or between environmental conditions. Despite the lack of a standard deviation, the cell number remains relatively stable.

6.3.4.4. *Some observations on hydrogen bacterial consumption in batch*

Experiments carried out in batch have made possible to draw several conclusions. First, in the absence of an electron source in the medium, *S. putrefaciens* is able to reduce the Fe^{3+} present by endogenous electron source composed of reserves accumulated during culture preparation process. Second, *S. putrefaciens* is able to use lactate as well as formiate but is unable to use effectively the acetate (O'Loughlin et al., 2019). In addition, *S. putrefaciens* is not able to regulate the use of organic carbon when 4mM of formiate is present. Organic carbon is entirely consumed before the usage of hydrogen.

Concerning the solution culture of VS, the results cannot be used quantitatively, due to the fact that the initial concentration of Fe^{3+} present in the medium is very low. Thus, it's important to increase the concentration of iron in this medium to observe a bacterial activity by *S. putrefaciens* in conditions close to that of underground storage.

For medium presenting high concentration of NaCl, Fe^{2+} concentrations observed after 48 hours of incubation are non-coherent. Two hypotheses were suggested to explain this decrease of Fe^{2+} in the medium:

1- an input of O_2 that would have reoxidized Fe^{2+} into Fe^{3+}
2- the fluid samples taken for the measurement of Fe^{2+} are non-homogeneous and non-representative.

The first hypothesis of the entry of O_2 is less likely to occur because cultures were frequently purged with H_2 and also because the Fe^{2+} totally disappear which should be the case during in presence of O_2. The second hypothesis, a non-homogeneous sample, seems more probable. Some gas flocculations adhering strongly to the glass of flakes were observable in certain cultures. In addition, this hypothesis is verified by the fact that at 100 g/L of NaCl, the concentration of Fe^{2+} is too low to precipitate. These variations in Fe^{2+} concentration are therefore due to an analytical problem and the measurement after 48 hours should be carried out with another technique to overcome this flocculation issue. Also, hydrogen has a very low solubility in water of only 1.6 mg/L while oxygen has a maximum solubility of around 8mg/L (at 25°C and in pure water, Kolev, 2007). Thus, in our study model, the exchange surface between the hydrogen gas and the culture medium is very small and the transfers might be underestimated and hence, the hydrogen consumption rate.

S. putrefaciens growth has been reduced in saline environment. But other iron-reducing bacteria could grow at extreme concentrations of NaCl in aquifers. In addition, other metabolisms such as sulfate-reducing or carbon reducing bacteria such as *Desulfovibrio sp*. could be present and consume the present hydrogen.

In future studies, it should be possible to verify, for each metabolic type possibly present in storage sites, whether these metabolisms could develop there and to quantify the possible consumption of dihydrogen present by these various bacterial or archean strains.

6.3.5. Results of the feasibility tests of the experimental setup

6.3.5.1. Experimental tests with hydrogen concentration of 70% and hydrogen reinjection for maintaining pressure equilibrium in the closed circuit

First, we execute the flow through experiment using a gas inflow of solution of H_2/N_2 mixture of 70% of H_2 and 30% of N_2 to get as close as possible to in situ conditions for pure hydrogen storage. We incubate bacterial culture in presence of 40mmol of iron in the rock sample by the above-mentioned method described in section 6.3.2.3 until the OD_{600} reaches 5. The core sample is then saturated with the gas mixture at 50 bar. Sampling by the valve-micro-GC system is programmed every 24 hours. The volume taken by the valve is compensated at the upstream by an injection of the same gas mixture (70% H_2 / 30% N_2) is order to maintain the pressure in the closed circuit constant. Results were plotted according to the number of samples (Fig 6. 11). We compare the results to the those obtained by a blank test measuring gas concentration directly from the original gas tank without passing by the cell.

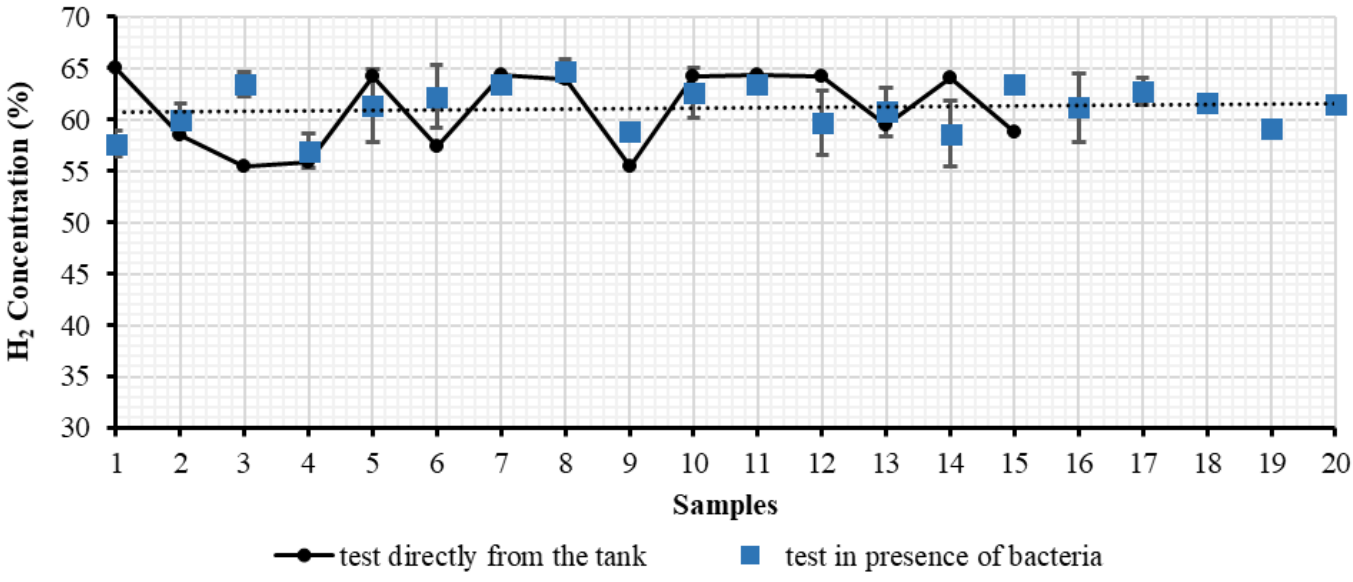

Fig 6. 2: Evolution Hydrogen concentrations in presence of S. Putrefaciens bacteria incubated on the Vosges sandstone in the flow-through cell with respect to the gas sample from the closed circuit. Each sampling is separated by 24 hours. Error bars represent standard deviations from the mean of three independent tests

Hydrogen concentration appears to be highly variable but remain constant around a mean value of 62% corresponds to the mean value measured directly from the hydrogen tank of 70% by the system valve-microGC despite the presence of *Shewanella* (Fig 6. 11). Unfortunately, no evidence of hydrogen consumption by bacterial can be exhibited.

Therefore, two hypotheses were suggested to explain this result. The first one is that reinjecting the same gas mixture at the upstream mask the H_2 consumption process by bacteria. Another concern is the time interval between two successive samples (and by extent the total duration of the experiment) which could be too short to observe a significant H_2 variation due to bacterial activity. The second main hypothesis is related to the stoichiometry of the redox reaction by *S. putrefaciens*:

$$2Fe^{3+} + H_2 = 2Fe^{2+} + 2H^+ \qquad (6.\ 12)$$

The solution of bacteria incubation, at a pressure of 50 bar and temperature T = 35°C, has a density ρ = 1.0053 g/cm^3. The mass of water recovered at the end of the test is 12.52g measured by weighing the sample before and after the flow-through test, so the volume of water recovered is 12.39 cm^3. The estimated residual water saturation of the sample is S_r = 0.68. And the water content, which is the mass of water over the mass of the dry sample, is 0.725%.

First, at initial conditions, the concentration of iron Fe^{3+} introduced into the medium is C_{Fe3+}=40 mM/L in the pores. So the quantity of Fe^{3+} reactant left in the porous rock with the bacteria after gas injection is 40mmol/L × 12.39×10^{-3}=0.49mmol.

The volume of gas present is the total pore volume minus the volume occupied by residual water so $Vg = V_{pores} - Sr \times V_{pores} = 19.73 - 0.63 \times 19.73 = 7.34cm^3$. Considering the law of ideal gas, we calculate the quantity of gas present in the media according to the partial pressure of hydrogen and the pressure and temperature conditions in the media so $n_{H_2} = \frac{P_{H2}V}{RT}$ for H_2=64.5% (the maximum value of concentration measured from directly from the gas tank via the valve-microGC system $n_{H_2} = 8.8mmol$ **.**

At equilibrium, according to the mass conservation balance and the stoichiometry of the equation above, the molar ratio of the reactants is:

$$R = \frac{2mol_{Fe^{3+}}}{1mol_{H_2}} \qquad (6.\ 13)$$

So, since we have 8.8mmol of hydrogen for 0.49 mmol of iron, the iron appears the limiting reactant compared to the high concentration of gas in the media inhibiting the biogeochemical reaction of iron reduction. Therefore, no significant alteration of gas by the bacteria can be observed.

For that we decide for the following tests to use higher concentration of iron (80 mmol of iron) and lower concentration of hydrogen (5%). We also decide to reinject pure argon gas instead of H_2/N_2 mixture to maintain gas pressure within the cell. Argon is an inert gas also considered as the gas vector of the micro-GC column, so it doesn't affect the measurements but only dilute progressively the H_2 concentration within the gas phase. In addition, we decide to assess the time interval separating each sample required in order to ensure the homogenization of the gas mixture after each argon injection.

6.3.5.2. Experimental test with hydrogen concentration of 5% and Argon reinjection for maintaining pressure equilibrium in the closed circuit

For this experiment we use a gas mixture H_2/N_2 with 5% of H_2. We first test the capability of our experiment to measure such low hydrogen concentration by injecting from the gas tank directly via the valve into the micro-GC. We perform several sequences separated each by 15 min. Gas concentration is constant for all the samples around 4.3%. We inject this same gas by the flow-through cell setup and we apply a steady-state closed circuit at 50 bars. We sample the gas into the setup by the valve-microGC system every 15 min and we equilibrate the pressure by reinjection of the same gas at the upstream after each sampling sequence. The measured concentration of hydrogen doesn't vary and stays constant around 4.3% of hydrogen (Fig 6. 12).

When reaching the steady-state in all over the system with the hydrogen gas (5%), we isolate the upstream and downstream in a closed circuit system. Then, sampling by the valve-microGC system is executed with reinjection of argon gas from the upstream. In order to determine the optimal sampling interval required to guarantee a homogenous gas mixture within the rock sample, two blank tests are carried out by changing the time period between two successive samples. H_2 measurements for respectively a sampling interval of 15 minutes and 3 days are compared in Fig 6. 12. We calculate in parallel the expected theoretical evolution of H_2 concentration only due to dilution effects when injecting argon. We assume for this purpose a mixture of ideal gas, constant volume sampling, isothermal mixing and a constant pressure of 50 bar. This comparison suggests that a sampling interval of 3 days is sufficient to ensure an ideal mixing within the cell and hence, representative and reliable concentration measurements of the gas mixture composition. In the following, we will keep this sampling methodology.

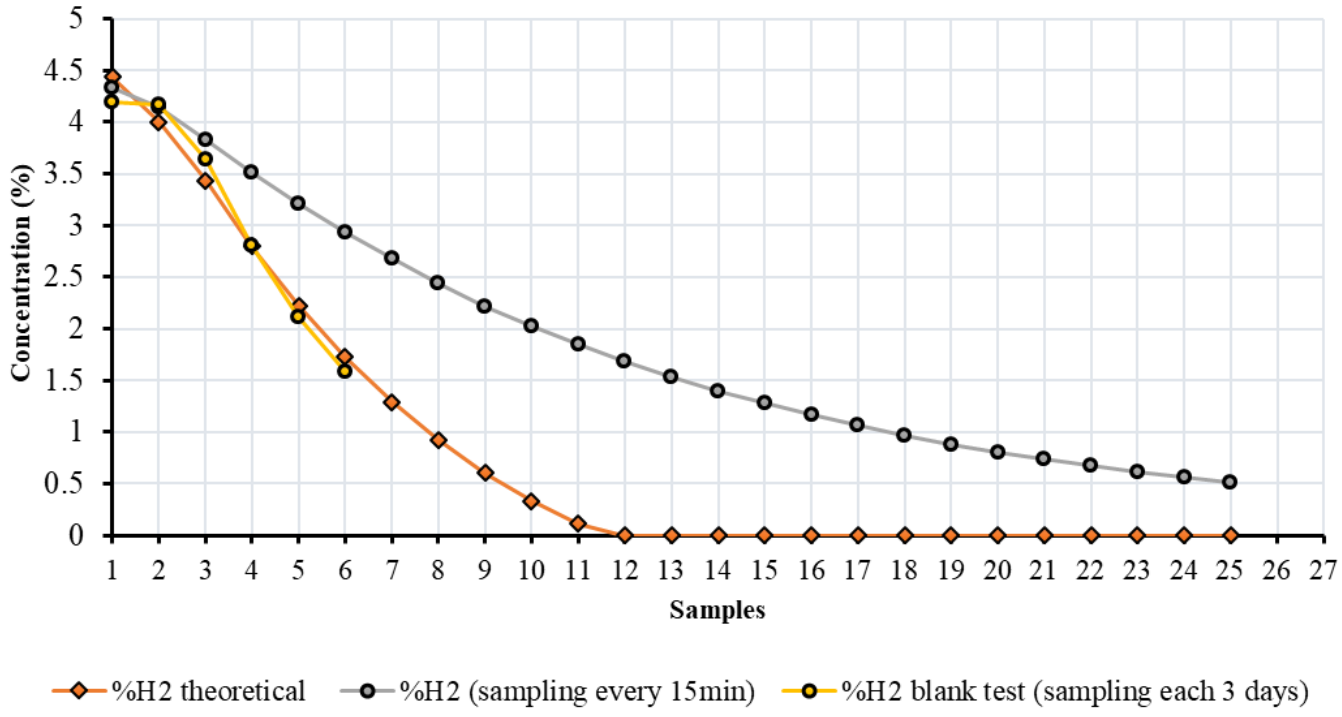

Fig 6.3: Evolution of hydrogen concentration during the feasibility test with respect to sequences of sampling (black and grey circles) compared to theoretical curve of hydrogen concentration evolution (orange squares) and the blank test performed at a sampling rate every 3 days (yellow circles)

At this point, we repeat the same experiment on two samples:

- The first one is considered as a blank sample. We inject into the porous rock the incubation solution with 80mmol of Fe^{3+} but without any bacteria. We follow the same procedure of injection and purging than previously detailed.
- In the second one, we add the bacterial culture of *S. putrefaciens* previously incubated in presence of 80mmol of Fe^{3+} until the OD_{600} is 8 and following the same procedure of seeding.

Sampling is done every three days in order to obtain a homogeneous mixture of gas. We plot results of both tests with respect to the sequence of sampling and we compare the curves to the theoretical curve of dilution calculated before. We show also the theoretical curve of hydrogen alteration calculated from the theoretical dilution curve assuming that all the injected iron in the media (80mmol) was reduced by the hydrogen (5%) with an instantaneous kinetics (Fig 6.13).

So at t_0, the concentration of iron Fe^{3+} introduced into the medium is C_{Fe}^{3+} = 80 mM/L in the pores. Considering the water saturation Sr=0.6, the volume of water recovered is 12.39 cm^3 and the poral volume 19.73 cm^3, the quantity of iron injected reactant in the system is 0.99 mmol at 50 bar and temperature T= 35°C. For a hydrogen concentration of 4.43% the maximum concentration measured by the system valve micro-GC from the gas tank, and for a volume of 7.8 cm^3, the initial quantity of hydrogen is of 0.67 mmol.

At equilibrium, according to the mass conservation balance and the stoichiometry of the equation above, the quantity of hydrogen needed to consume the total quantity of iron is 0.49 mmol/L. Hence, we may draw a

theoretical curve of H_2 depletion, considering we had a total consumption of iron in the medium before the first sampling (Fig 6.13). This curve represents the maximum consumption of hydrogen in optimal conditions for bacterial proliferation.

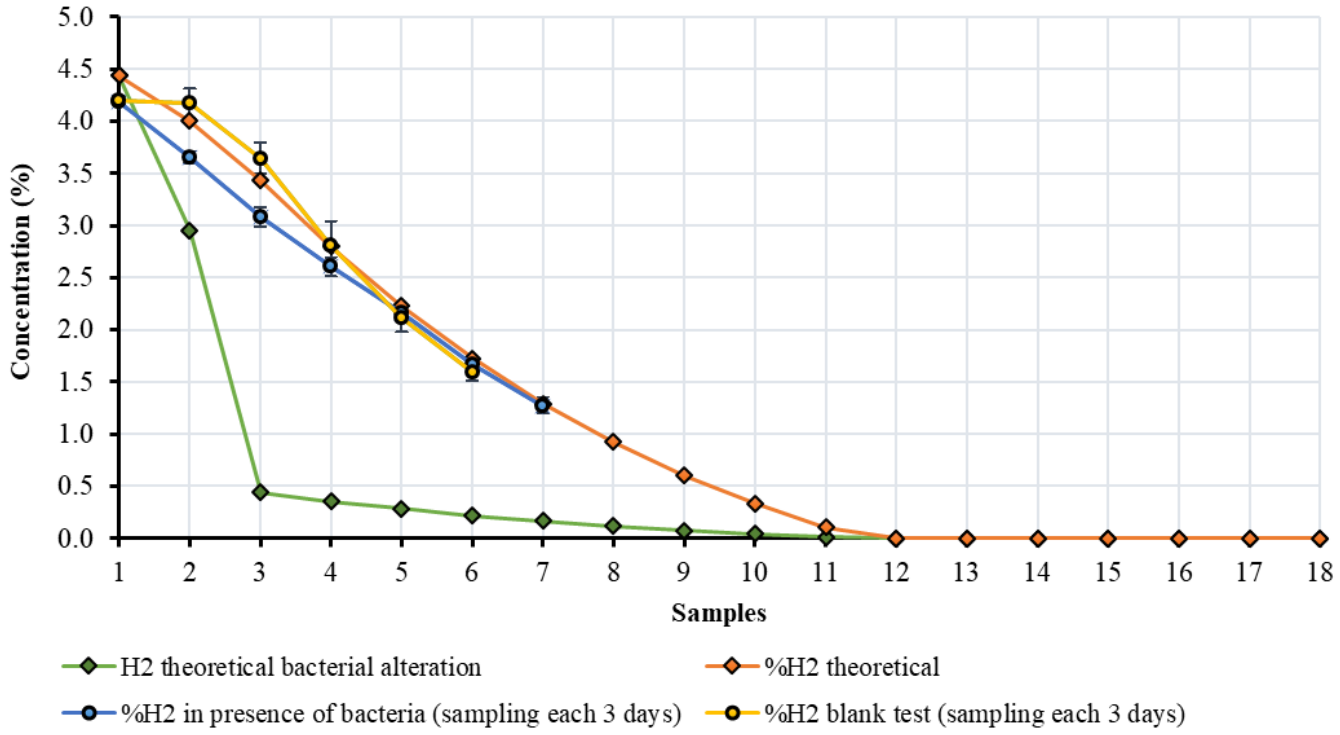

Fig 6. 4: Evolution of hydrogen concentration with respect to sequences of sampling for the blank test with a sampling rate each 3 days (yellow circles) compared to the curve of hydrogen concentration evolution for the test in presence of bacteria at sampling rate of 3 days (bleu circles). Error bars represent the standard deviation of three triplicates. Both curves are compared the theoretical curve of hydrogen concentration evolution (orange squares) and the theoretical curve of hydrogen concentration evolution assuming that all the quantity of Iron was reduced according to the stoichiometry of the redox equation (green squares).

Sample starts to decrease with sampling from similar concentrations of hydrogen of 4.3% measured by the micro-GC, almost in a linear trend. The blank test and the test executed in presence of bacteria display results very close to the theoretical curve of dilution. The reduction of hydrogen concentration on the sample without bacteria is due to the dilution by the fact of the continuous sampling and injection of Argon gas from the upstream for pressure equilibrium in the close circuit. However, Fig 6. 13 shows that the values of concentration reduction for the test in presence of bacteria are slightly below the ones of the blank test during the first 15 days of monitoring (5 sequences of sampling). Hydrogen concentration is lower of 0.5% in presence of bacteria than in abiotic conditions. However, both curves converge and intercept after 5 sampling sequences with the theoretical curve of dilution (orange squares). Error bars of the triplicates are very low for all tests, though. This indicates that repeatability of the test is reliable and the measurements are considerably precise. Both curves stay largely above the hypothetical curve of alteration, which, as we can see, drops practically to zero very quickly (but assuming reaction at equilibrium).

In order to find an explanation, the CO_2 production concentration was also monitored for the tests executed with a sampling rate of 3 days (Fig 6.14). CO2 production is almost zero during the whole duration of the blank test. However, the test in presence of bacteria shows a positive production of CO2 and an increase in CO2 concentration measured during each sampling. Shewanella Putrefaciens appears to be active and producing CO2 only by using the Formiate and/or endogenous source of carbon to reduce the iron and produce CO2, and not the provided hydrogen. It seems that *S. putrafaciens* prefers initially the carbon source as electron donor over the provided hydrogen. It matches with the kinetic of the bacteria activety in batch (fig 6.9). Hydrogen respiration kinetics could be slower in storage conditions than the value estimated in batch, and requires a longer period to finish all the carbon source and start depending on hydrogen.

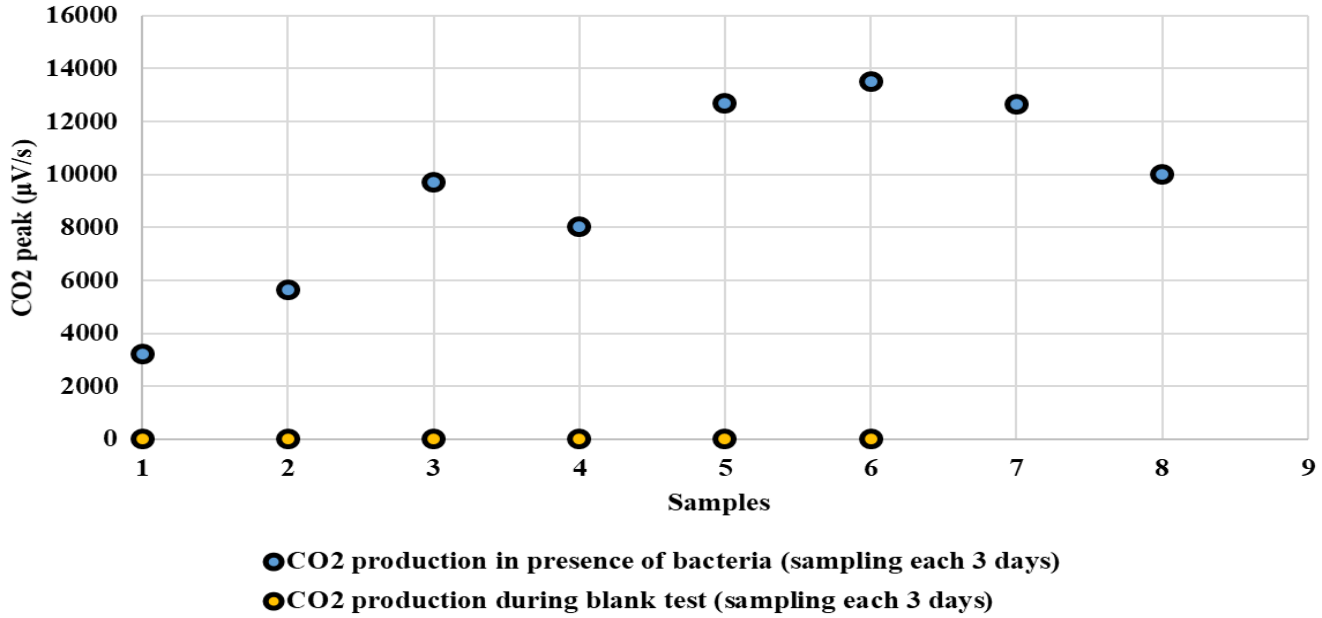

Fig 6.16: Evolution of CO_2 concentration peaks with respect to sequences of sampling for the blank test (yellow circles) compared to the curve of of CO_2 concentration peaks for the test in presence of bacteria (bleu circles), at sampling rate of 3 days.

However, it is hard to conclude about the evidence of bacterial activity or not. Post mortem microbiological analyses should be executed to count bacteria cells present within the system or iron dosage and estimate possible growth and biooogical activity during the experiement. It should give additional insights on bacterial dynamics in storage conditions. So, basically the kinetic of the iron reducing reaction of the shewanella is considered as a first hypothesis for such results.

However, in presence of many uncertainities, we can suggest also another hypothesis for such result.

It can be due to the difference in sandstone samples between the one for the blank test and the one used for the test in presence of bacteria. In spite that both samples were taken from the same formation of Vosges sandstone and have the same porosity and were tested in similar experimental conditions, there still difference residing in the architecture and pore distribution (tortuosity, shape, size) of the porous rocks. In other words, the variability observed betwwen both experiments could be only due to rock heterogeneity. So for further improvements, we need to test multiple samples of sandstone from the same depth to ensure the reproducibility of conditions.
Also, it can be due to the low activity of the *Shewanella Putrefaciens* in storage conditions simulated in this experiment. The purging of the incubation water was an indispensable step for the experimental performance because the micro-GC cannot sample liquid water. But the low residual water saturation essential for bacterial life limits the biofilm distribution within the porous rock. Solubility of gaseous hydrogen in the residual water is a very critical factor too. At 35°C, and at a pressure of 50 bars, the solubility of H_2 is less than 0.04mol of H_2/kg H_2O (Pichler, 2019). As a consequence, this low water saturation and the low availability of dissolved nutrients are not favorable for bacterial proliferation and effective hydrogen consumption.

7. Conclusion

The hydrogen solubility in pore water could change the pH of the present groundwater and residual water geochemical redox reactions between the fluids and minerals, e.g. dissolution of some minerals and cement and precipitation of others. This might change the porosity structure and permeability and increase leakage risks, and also induce an unwanted consumption of the hydrogen resource. Previous studies showed that these abiotic reactions in sandstone reservoir are minor. Yet, these reactions could be catalyzed by the biological activity. Indeed, microorganisms can tolerate the extreme conditions of deep saline aquifers and reservoirs. For example, iron-reducer bacteria like *Shewanella* reduce Fe^{3+} to Fe^{2+} in presence of hydrogen and produce energy. These types of bacteria are very abundant in anoxic sedimentary environments. Their growth requires the consumption of hydrogen present in the media or preferably dissolved in pores water.

To study these phenomena, we developed a new experimental device to simulate the biochemical activity under conditions (T=35°C, P_{H2}=50bar, $P_{confinement}$=200bar) representative of storage reservoirs on cylindrical core samples in a triaxial compression cell. This new experimental approach combines gas (hydrogen) injection tests under high mechanical stresses and gas pressure, with geochemical analytical methods in order to quantify biological processes of hydrogen alteration and conversion. We chose to work on the Vosges sandstone (formation of lower Triassic) which is considered as an analogue rock of underground saline aquifers and reservoirs. This rock is constituted by: 67.2% of quartz, 10.2% of muscovite and 4.8% of clays. The porosity is about 23% and the permeability is very important. The strain chosen for this purpose is the iron-reducing bacteria *Shewanella putrefaciens.*

Its metabolism and performance as a hydrogenotrophic bacteria were first tested in batch condition, in presence of different medium conditions of nutrients, hydrogen concentration, and iron concentrations. The bacteria growth was monitored by cell counting using a biological marker. The kinetic of iron reduction and hydrogen consumption was studied from measuring Fe^2 concentrations. Results showed that this type of bacteria can tolerate saline environments even if its growth is significantly reduced. This halophilic bacterium can live under a salinity density of 50g/L. It can depend on any carbon source like lactate or formiate but cannot use lactate. Even in absence of external electron donor, *S. putrefaciens* is capable of reducing the iron present in the medium probably using endogenous source of electrons. However, *S. putrefaciens* cannot regulate his consumption of organic carbon in the presence of several electron source (formiate and H_2).

However, under in-situ conditions, the dissolved quantity of hydrogen is not very important, the exchange surfaces for these kind of reactions are limited, and the nutrients and other carbon source are not always easily available. That's why we chose to work on a solid core of sandstone in a triaxial compression cell. The sample was confined in the triaxial cell with a confinement pressure of 200 bar, then heated at 35°C to permit the growth of bacteria. Before testing, anaerobic conditions were established in the setup. Then, the sample in the cell was filled with hydrogen gas with a pressure of 50 bar injected at the upstream. The downstream was connected to a micro-gas chromatograph allowing a chemical analysis of the outflow gas concentration by a controlled sampling system (HP-LP valve). Different experimental conditions were considered:

- High (70%) and low (5%) hydrogen concentration. Indeed, the use of low concentration of hydrogen can be a limiting factor for the redox reaction catalyzed by bacteria, according to the mass balance and stoichiometry of the redox reaction of iron reduction.
- With hydrogen or argon gas reinjection at the upstream to equilibrate the pressure (50 bar) after each gas sampling with the HP-LP valve. Using the same gas mixture (hydrogen) to equilibrate the gas pressure could mask the impact of hydrogen alteration, then argon (an inert gas) was also used.
- With and without bacteria incubation.
- Different sampling frequencies (one day and three days) to verify if the duration between each sampling is large enough to allow a homogenized gas mixture and to observe a significant difference in biological activity.
- CO_2 gas production monitoring to detect any biological activity

These tests allowed to choose the best conditions for bacterial proliferation according to the stoichiometry of the redox reactions in order to obtain and monitor the maximum biological alteration of hydrogen. The experimental

conditions can be considered as closed, which better represents the long-term storage conditions at steady-state. It resulted that the bacterial activity doesn't seem to impact significantly the hydrogen concentration in the system, whatever the initial hydrogen concentration (70% or 5%), the sampling frequency (one or three days) and the nature of the reinjected gas (hydrogen or argon). Many hypotheses are proposed to explain the observed differences between batch and triaxial conditions:

- The slow kinetics of hydrogen consumption by S. putrefaciens when reducing iron under triaxial conditions, which are closer to in-situ conditions. This kinetic being related to the consumption of carbone source (endogeneous or the added formiate) before starting the usage of disposable hydrogen in the media. Also, it can be related to the availability of water, nutrients, exchange surface.
- The scarcity of dissolved hydrogen in residual water which is preferentially consumed by bacteria.
- The low exchange surface for biogeochemical reactions in the case of solid core samples.
- The possibility of absence of gas homogenization in the sandstone sample provoked by the injection of gas after each sampling. The rate of sampling could be not enough to allow a homogeneous repartition of gas in pores and could mask partially the biological alteration effect.
- The detection limit of measuring instruments given the low reactivity of the biogeochemical reaction and the inherent variability between experiments due to heterogeneity between core samples.

IV – Conclusion and perspectives

8. General conclusions and perspectives

Within the framework of underground storage of hydrogen, two solutions are generally considered: salt caverns and porous rocks like saline aquifers and depleted reservoirs of oil and gas. The choice of storage is dictated by the geology and the end use of the gas. However, questions and concerns remain concerning the reliability, capacity and tightness of these types of repositories since mechanical, chemical and thermal constraints, related to in-situ conditions but also to the operating processes, apply. Thus, this thesis proposes an evaluation of gas leakage risk in the case of salt cavities under the influence of hydrogeomechanical stress, and the risk of biogeochemical alteration (in presence of hydrogenotrophic bacteria) of the gas stock in the case of porous reservoir rocks.

8.1. Hydrogen storage in salt cavern

To characterize the complex relationship between the permeability evolution and the mechanical and thermal solicitations, which is due to the specific features of the mechanical behaviour (large plastic deformation capacity, good creep properties, microcracking damage, cracks healing) of rock salt and gas flow in such unconventional reservoir (Klinkenberg effect), we performed a complete set of laboratory experiments on a rock salt specimen (salt bed of the Alsace potash mines in the East region of France). It resulted that:

- The porosity is very low (~1%) and the initial permeability varies over 4.5 orders of magnitude.
- The Klinkenberg effect is only observed for the less permeable and damaged samples.
- The poroelastic coupling is almost negligible in our samples even when damaged (Biot's coefficient ~ 0).
- Measurement of ultrasonic wave velocities during uniaxial compression test showed an almost irreversible closure of pre-existing microcracks and the opening of axial microcracks that are perpendicular and parallel, respectively, to the uniaxial stress direction, and allowed a precise determination of the dilatancy threshold.
- Deviatoric loading under low confining pressure (1 MPa) induces a moderate increase in gas permeability from the dilatancy threshold due to microcracking.
- Under higher confining pressure (5 MPa), no increase in permeability was measured because the material becomes fully plastic which practically eliminates microcracking and thus dilatancy.
- Under hydrostatic loading, gas permeability decreases because of cracks closure and this decrease is irreversible due to the time-dependent self-healing process.
- Permeability increases slightly during dynamic mechanical and thermal fatigue due to microcracking, while it reduces during static fatigue (creep) thanks to the self-recovery process.

Within the framework of underground hydrogen storage in deep salt caverns, fractures and associated permeability increase in the near field (i.e., close to the cavity wall) could promote hydrogen leakage because of the excavation that induces high deviatoric stress and because of the gas pressure (high-frequency) cycles that induce temperature and stresses changes. Fortunately, other deformation mechanisms, specific to rock salt, will act in a competitive way to annihilate any significant damage and long-term permeability increase: strong plasticity with strain hardening, good creep properties and self-recovery from damage.

Therefore, the low permeability of rock salt and the integrity of the storage project will not be negatively impacted, especially since the thickness of the excavation damaged zone is generally relatively small. All these experimental results support that advective gas leakage through cavern walls should be negligible and give more clue about future exploitation of salt caverns for hydrogen storage. More attention, however, should be paid to the contribution of other mechanisms of gas transport, especially by diffusion of dissolved hydrogen into pore brine. Further research should be also conducted to extend this study to various types of rock salt and determine the most appropriate rock salt formations for hydrogen storage.

To support and validate these conclusions at the scale of rock salt caverns, numerical simulations should be performed. For that, on the perspective of this thesis, we present below the modelling work of the postodoctoral fellowship of Ever-Dennys COARITA-TINTAYA.
Both the short-term model (a macroscopic elastoplastic and damage model) and the long-term behavior (considering the three creep phases) of the salt rock have been simulated at the scale of salt cavern.

Hydromechanical simulations were carried out under saturated conditions. The analysed scenarios were shallow and very depth caverns, as well as seasonal and daily hydrogen operating cycles. These simulations were conducted with the set of parameters listed in Tab 8. 1. The values of the elasticity and strength parameters were fitted from the experimental information of Thorel (1994) and Grgic *et al*. (2021). Biot coefficient equal to 0 (Grgic et al., 2021) means that there is no hydromechanical coupling. Finally, regarding hydrogen migration, hydrogen is assumed to be fully dissolved.

Tab 8. 1: Values used in the hydromechanical simulations. Short-term (shaded in yellow) and long-term (shaded in green) model parameters

Mechanical parameters								
Variable	**Value**	**Unit**	**Variable**	**Value**	**Unit**	**Variable**	**Value**	**Unit**
ρ_s	2100	kg/m^3	β_{m0}	1.1		k_2	-0.15	1/MPa
E	35	GPa	b_β	350		η_k	60000	MPa.d
ν	0.3		γ_{ult}	0.09		n_N	4	
c	8	MPa	d_{max0}	0.15		A	0.005	1/d
ϕ	36.8	°	b_d	100		B	4700	K
η_0^p	0.35		a_d	0.5	1/MPa	σ_{ref}	1	MPa
α_0^p	0.0024		k_1	-0.18	1/MPa	A_T	4E-08	1/d
β_0	-0.02		G_k	126000	MPa	n_T	5	
Hydraulic parameters								
k	1E-20	m^2/s	n	0.012[(1)]		K_f	2.2E+09	Pa
μ_f	0.001	Pa.s	b	0[(1)]		ρ_f	1000	kg/m^3
Hydrogen concentration								
D*	6E-09	m^2/s						

(1) Grgic *et al.* (2021)

The simulated operating conditions were:

- ***Phase 1: Initial:*** There is not salt cavern (t= 0). In this phase we have the hydromechanical initial conditions.
- ***Phase 2: Leaching:*** From the initial geostatic stress, the salt cavity is excavated by the dissolution of the salt. For modelling purposes, the initial stress is gradually replaced by the brine pressure (brine density = 1100 kg/m^3). The duration of this phase is assumed to be one year (t= 1 year).
- ***Phase 3: Brine:*** The cavity is filled with brine. This is a waiting period before injecting hydrogen. This phase is considered to last another year (t= 2 years).
- ***Phase 4: Debrining:*** Hydrogen injection and gradual replacement of the brine is carried out. The considered duration of this phase is 6 months (t= 2.5 years), during which it reaches 100% of the maximum hydrogen pressure considered.
- ***Phase 5: Cycling loading operation;*** After considering a period of 6 months of maximum hydrogen pressure (t= 3 years), hydrogen injection and withdrawal cycles are performed. The internal pressure in the cavern is reduced to the minimum operating pressure. Two scenarios were analysed: (i) seasonal and (ii) daily. The seasonal scenario considers 6 months of withdrawal and 6 months of injection, during 50 years of activity (t= 53 years). The daily scenario considers 4 hours of extraction, 6 hours of injection, another 4 hours of extraction and finally 10 hours of injection. Therefore, there were two cycles in one day. The operating time considered is 100 days (t= 3 years + 100 days). The maximum and minimum hydrogen pressures considered correspond to 80% and 20%, respectively, of the initial geostatic stress state.

In the following, one of the hydromechanical applications is shown. The cavity considered has a volume of 910 800 m^3 and is at a depth of -1350 m (Fig 8. 1, a). The cavern has a diameter of 70 m and a height of 260 m. The top and bottom have a spherical shape. The main equations, boundary conditions and initial hydromechanical conditions are illustrated in Fig 8. 1.

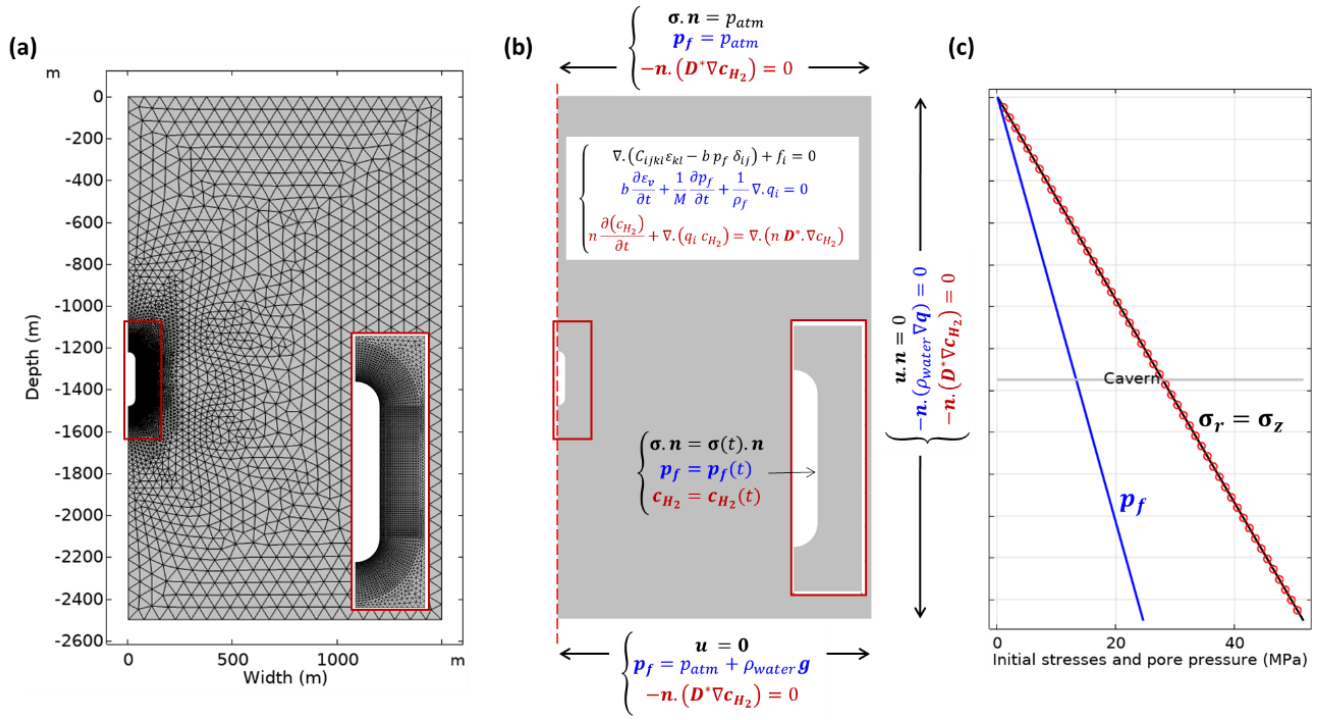

Fig 8. 2: (a) Geometry and mesh; (b) axisymmetrical model and boundary conditions; (c) initial conditions.

For the seasonal cycle scenario, at the first discharge of hydrogen pressure the cavity walls enter in plastic behaviour. The shape and extension of this plasticity zone is the same as shown at 53 years (Fig 8. 2.a), i.e., no evolution of the extension of the plastic zone was calculated. The plasticity zone has a maximum extension in the lateral part of the cavern. This extension is approximately 0.3 of the diameter of the cavern. It should be noted that no damaged zones were obtained. As for the maximum displacements, they reach 3.3 m in the lateral wall (Fig 8. 2.b) at 53 years. These displacements are significant due to mechanical creep. Due to the very low permeability of the salt rock, pore pressure dissipation is very slow when the internal pressure in the cavity is decreased. However, due to the maximum pressure of the cavity induced by confinement, this causes the pore pressure distribution to be modified up to an extension of 200 m in the horizontal direction (Fig 8. 2.c) at 53 years. The maximum considered internal pressure is 24 MPa, while the minimum is 6 MPa. Finally, the extension reached by the hydrogen is approximately 7.4 m from the cavity wall and at 53 years (Fig 8. 2.d). This extension represents 0.1 of the cavity diameter.

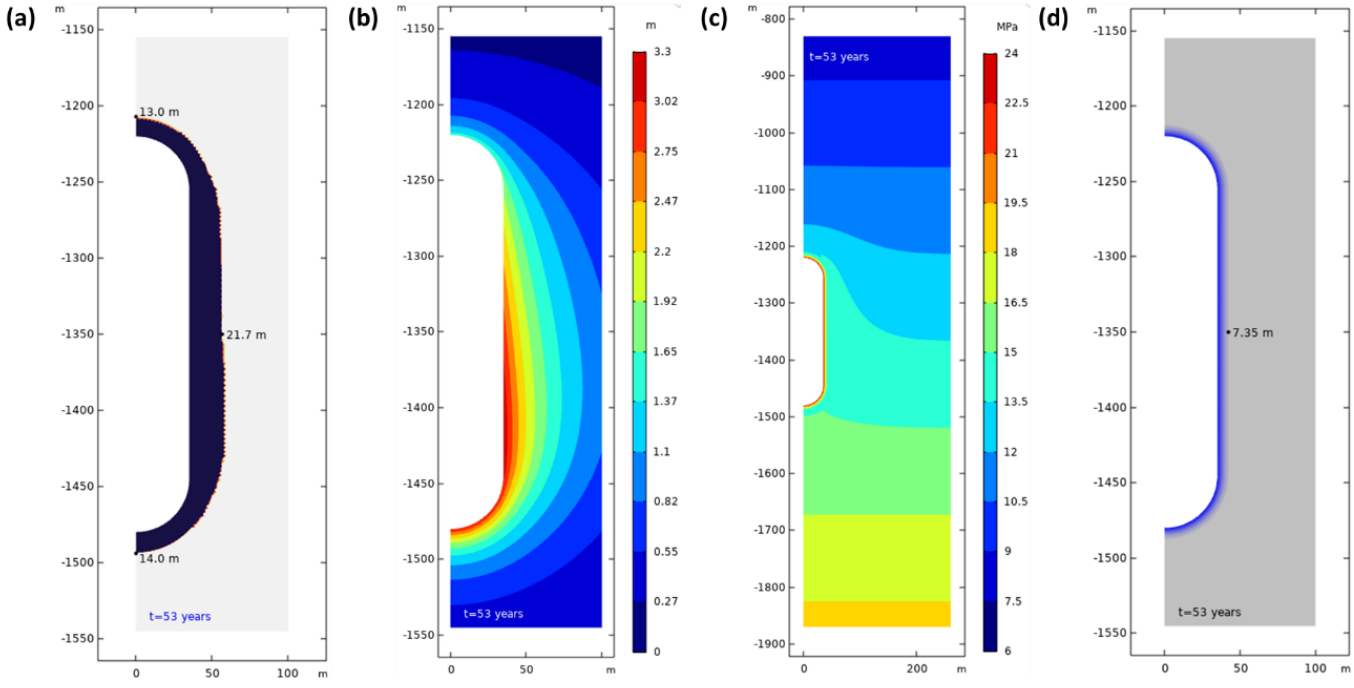

Fig 8. 3: (a) Plastic zone; (b) displacement isovalues; (c) Pore pressure isovalues and (d) hydrogen concentration and distribution at t=53 years.

Ongoing simulations take into account the decrease in material strength, the analysis with respect to transient creep and analyse a case with a non-zero value of the Biot coefficient. In the latter case, hydraulic coupling would be present in contrary to what we have already seen on MDPA salt. Perspectives of the model would be, among others, to consider material fatigue and the influence of temperature on the mechanical behaviour. This in order to monitor the gas leakage risk in any salt type caverns and under different conditions of stress damage.

Globally, simulations suggest the presence of a small restrictive damage zone and a very small extent of the H_2 plume even after several decades of the cavern lifetime. The integrity of the sealing is maintained.

8.2. Hydrogen storage in porous reservoir rocks

In the case of porous reservoir rocks, hydrogen injection can induce biogeochemical reactions between the fluids and minerals which could increase leakage risks and also induce an unwanted consumption of the hydrogen resource. Indeed, microorganisms can tolerate the extreme conditions of deep saline aquifers and reservoirs. To study these phenomena, we developed a new experimental device to simulate the biochemical activity under conditions (T=35°C, PH_2=50bar, Pconfinement=200bar) representative of storage reservoirs on cylindrical core samples containing bacteria in a triaxial compression cell. The outflow gas was automatically sampled with a HP-LP valve and the concentration was measured with a micro-gas chromatograph to quantify biological processes of hydrogen consumption. We chose to work on the Vosges sandstone (formation of lower Triassic), a very porous and permeable rock. The strain chosen for this purpose is *Shewanella putrefaciens* bacteria which reduces iron in the presence of hydrogen to produce energy. It resulted that:

- Under batch condition (preliminary test on a rock powder), *Shewanella putrefaciens* bacteria can tolerate anaerobic environments. It can reduce the iron present in the medium using endogenous source of electrons. However, it can also use the hydrogen in the medium to execute this reaction and prefers available dissolved hydrogen in the water pores rather than in gaseous phase.
- Under triaxial conditions (i.e., on a cylindrical rock sample) with our new experimental device, which better mimic in-situ conditions in terms of stresses and pressure, the bacterial activity doesn't seem to impact enough the hydrogen concentration in the system, whatever the initial hydrogen concentration (70% or 5%) and the sampling frequency (one or three days).

As a conclusion and despite the remaining uncertainties related to our experiments, we can consider that the underground storage of pure hydrogen in porous reservoir rocks is not drastically threatened by the activity of *Shewanella putrefaciens* bacteria. In-situ conditions are not favorable for the growth of such bacteria and for a significant deterioration of the hydrogen resource. Therefore, the hydrogen storage under these conditions can be considered safe. However, these results and hypotheses need to be validated by post-mortem analyzes, for example, counting the cells remaining in the sandstone core sample after testing and quantifying the reduced iron. In addition, other bacterial strains, such as sulfato-reducing or methanogens with greater kinetics in terms of hydrogen consumption, could be tested in the future. But this could only be done by adapting the experimental set-up to the culture conditions of these bacteria, like reducing the quantity of carbon in order to accelerate the kinetic of hydrogen consumption in order to reduce iron and taking into consideration the water saturation in pores and availability of dissolved hydrogen. The experimental method requires also improvement to reduce uncertainities by optimizing the homogenization time between sampling process, increasing the test duration, and optimizing the gas mixture.

V – References

9. References

1. Abdalla, A. M., Hossain, S., Nisfindy, O. B., Azad, A. T., Dawood, M., & Azad, A. K. (2018). Hydrogen production, storage, transportation and key challenges with applications: A review. *Energy Conversion and Management*, *165*, 602–627.

2. Ahmed, T. (2018). *Reservoir engineering handbook*. Gulf professional publishing.

3. Air Liquide. (2017). *Hydrogen could contribute to 20% of CO2 emissions reduction targets by 2050*. Hydrogen Could Contribute to 20% of CO2 Emissions Reduction Targets by 2050. https://newsroom.toyota.eu/hydrogen-could-contribute-to-20-of-co2-emissions-reduction-targets-by-2050/

4. Air Liquide. (2018). *Air Liquide et 12 partenaires publient une étude prospective sur le rôle de l'hydrogène décarboné pour la transition énergétique en France*. Air Liquide Energies. https://energies.airliquide.com/fr/air-liquide-12-partenaires-publient-etude-prospective-role-lhydrogene-decarbone-transition

5. Alkan, H., Cinar, Y., & Pusch, G. (2007). Rock salt dilatancy boundary from combined acoustic emission and triaxial compression tests. *International Journal of Rock Mechanics and Mining Sciences*, *44*(1), 108–119. https://doi.org/10.1016/j.ijrmms.2006.05.003

6. Amigáň, P., Greksak, M., Kozánková, J., Buzek, F., Onderka, V., & Wolf, I. (1990). Methanogenic bacteria as a key factor involved in changes of town gas stored in an underground reservoir. *FEMS Microbiology Ecology*, *6*(3), 221–224.

7. Amro, M., Haefner, F., & Freese, C. (2012). Modern in-situ and laboratory measurements of permeability and porosity to prove tightness of underground storage of hydrogen, natural gas and CO ${$sub 2$}$; Moderne In-situ- und Labormessung von Permeabilitaet und Porositaet zum Dichtheitsnachweis von Speichern fuer Wasserstoff, Erdgas und CO ${$sub 2$}$. *Erdoel Erdgas Kohle*, *128*.

8. ASM International. (1978). *Physical properties of carbon-and low-alloy steel* (Vol. 1).

9. Aufricht, W. R., & Howard, K. C. (1961). Salt characteristics as they affect storage of hydrocarbons. *Journal of Petroleum Technology*, *13*(08), 733–738.

10. Bachu, S. (2008). CO2 storage in geological media: Role, means, status and barriers to deployment. *Progress in Energy and Combustion Science*, *34*(2), 254–273.

11. Badziong, W., Thauer, R. K., & Zeikus, J. G. (1978). Isolation and characterization of Desulfovibrio growing on hydrogen plus sulfate as the sole energy source. *Archives of Microbiology*, *116*(1), 41–49.

12. Baier, R. E. (1980). Substrata influences on adhesion of microorganisms and their resultant new surface properties. In *Adsorption of microorganisms to surfaces* (pp. 59–104). John Wiley, New York.

13. Basso, O., Lascourreges, J.-F., Le Borgne, F., Le Goff, C., & Magot, M. (2009). Characterization by culture and molecular analysis of the microbial diversity of a deep subsurface gas storage aquifer. *Research in Microbiology*, *160*(2), 107–116.

14. Bear, J. (2013). *Dynamics of fluids in porous media*. Courier Corporation.

15. Bear, J., & Bachmat, Y. (2012). *Introduction to modeling of transport phenomena in porous media* (Vol. 4). Springer Science & Business Media.

16. Beauheim, R. L., & Roberts, R. M. (2002). Hydrology and hydraulic properties of a bedded evaporite formation. *Journal of Hydrology*, *259*(1–4), 66–88.

17. Becker, S., & Kuznetsov, A. (2014). *Heat transfer and fluid flow in biological processes*. Academic Press.

18. Beliaev, A. S., Saffarini, D. A., McLaughlin, J. L., & Hunnicutt, D. (2001). MtrC, an outer membrane decahaem c cytochrome required for metal reduction in Shewanella putrefaciens MR-1. *Molecular Microbiology*, *39*(3), 722–730.

19. Berest, P., Bergues, J., & Duc, N. M. (1979). Comportement des roches au cours de la. rupture: Applications à l'interprétation d'essais sur des tubes épais. *Revue Française de Géotechnique*, *9*, 5–12.

20. Berést, P., Brouard, B., & Durup, G. (1996). Behavior of sealed solution-mined caverns. *ISRM International Symposium-EUROCK 96*.

21. Berest, P., Brouard, B., & Durup, J. G. (2001). Tightness tests in salt-cavern wells. *Oil & Gas Science and Technology*, *56*(5), 451–469.

22. Bérest, P., Gharbi, H., Brouard, B., Brückner, D., DeVries, K., Hévin, G., Hofer, G., Spiers, C., & Urai, J. (2019). Very slow creep tests on salt samples. *Rock Mechanics and Rock Engineering*, *52*(9), 2917–2934.

23. Bérest, P., Karimi-Jafari, M., & Brouard, B. (2005). Transient creep in salt caverns. *Proceedings Of*.

24. Berta, M., Dethlefsen, F., Ebert, M., Schäfer, D., & Dahmke, A. (2018). Geochemical Effects of Millimolar Hydrogen Concentrations in Groundwater: An Experimental Study in the Context of Subsurface Hydrogen Storage. *Environmental Science & Technology*, *52*(8), 4937–4949. https://doi.org/10.1021/acs.est.7b05467

25. Bertuccioli, L., Chan, A., Hart, D., Lehner, F., Madden, B., & Standen, E. (2014). Study on development of water electrolysis in the EU. *Fuel Cells and Hydrogen Joint Undertaking*, 1–160.

26. Blanco-Martín, L., Rouabhi, A., Billiotte, J., Hadj-Hassen, F., Tessier, B., Hévin, G., Balland, C., & Hertz, E. (2018). Experimental and numerical investigation into rapid cooling of rock salt related to high frequency cycling of storage caverns. *International Journal of Rock Mechanics and Mining Sciences*, *102*, 120–130. https://doi.org/10.1016/j.ijrmms.2018.01.008

27. Bo, Z., Zeng, L., Chen, Y., & Xie, Q. (2021). Geochemical reactions-induced hydrogen loss during underground hydrogen storage in sandstone reservoirs. *International Journal of Hydrogen Energy*, *46*(38), 19998–20009.

28. Boggs Jr, S. (2014). *Principles of sedimentology and stratigraphy*. Pearson Education.

29. Bonte, M., Röling, W. F., Zaura, E., van der Wielen, P. W., Stuyfzand, P. J., & van Breukelen, B. M. (2013). Impacts of shallow geothermal energy production on redox processes and microbial communities. *Environmental Science & Technology*, *47*(24), 14476–14484.

30. Borns, D. J., & Stormont, J. C. (1989). The delineation of the disturbed rock zone surrounding excavations in salt. *The 30th US Symposium on Rock Mechanics (USRMS)*.

31. Boulin, P. (2008). *Expérimentation et modélisation du transfert d'hydrogène à travers des argiles de centre de stockage de déchets radioactifs* [PhD Thesis]. Institut National Polytechnique de Grenoble-INPG.

32. Bowman, J. P., McCammon, S. A., Nichols, D. S., Skerratt, J. H., Rea, S. M., Nichols, P. D., & McMeekin, T. A. (1997). Shewanella gelidimarina sp. nov. and Shewanella frigidimarina sp. nov., novel Antarctic species with the ability to produce eicosapentaenoic acid (20: 5$ømega$3) and grow anaerobically by dissimilatory Fe (III) reduction. *International Journal of Systematic and Evolutionary Microbiology*, *47*(4), 1040–1047.

33. Boyko, V., Garber, R., & Kossevich, A. (1997). *Reversible crystal plasticity*. Springer Science & Business Media.

34. Brace, W. F., Paulding, B. W., & Scholz, C. (1966). Dilatancy in the fracture of crystalline rocks. *Journal of Geophysical Research (1896-1977)*, *71*(16), 3939–3953. https://doi.org/10.1029/JZ071i016p03939

35. Brace, W., Walsh, J. B., & Frangos, W. T. (1968). Permeability of granite under high pressure. *Journal of Geophysical Research*, *73*(6), 2225–2236.

36. BRANDIS, A., & THAUER, R. K. (1981). Growth of Desulfovibrio species on hydrogen and sulphate as sole energy source. *Microbiology*, *126*(1), 249–252.

37. Bredehoeft, J. D. (1978). *Geologic disposal of high-level radioactive wastes: Earth-science perspectives* (Vol. 779). Department of the Interior, Geological Survey.

38. Brouard, B., Bérest, P., Durup, J. G., & de France, G. (2001a). In situ salt permeability testing. *Fall 2001 Meeting*, 7–10.

39. Brouard, B., Bérest, P., Durup, J. G., & de France, G. (2001b). In situ salt permeability testing. *Fall 2001 Meeting*, 7–10.

40. Buckley, S. E., & Leverett, Mc. (1942). Mechanism of fluid displacement in sands. *Transactions of the AIME*, *146*(01), 107–116.

41. Buzek, F., Onderka, V., Vančura, P., & Wolf, I. (1994). Carbon isotope study of methane production in a town gas storage reservoir. *Fuel*, *73*(5), 747–752.

42. Byron Bird, R., & Stewart, W. E. (1960). *Transport phenomena*. Lightoot, Edwin N.,.

43. Caglayan, D. G., Weber, N., Heinrichs, H. U., Linßen, J., Robinius, M., Kukla, P. A., & Stolten, D. (2020). Technical potential of salt caverns for hydrogen storage in Europe. *International Journal of Hydrogen Energy*, *45*(11), 6793–6805.

44. Canfield, D. E., Thamdrup, B., & Hansen, J. W. (1993). The anaerobic degradation of organic matter in Danish coastal sediments: Iron reduction, manganese reduction, and sulfate reduction. *Geochimica et Cosmochimica Acta*, *57*(16), 3867–3883.

45. Carden, P. O., & Paterson, L. (1979). Physical, chemical and energy aspects of underground hydrogen storage. *International Journal of Hydrogen Energy*, *4*(6), 559–569.

46. Carriere, J. F., Fasanino, G., & Tek, M. R. (1985). Mixing in underground storage reservoirs. *SPE Annual Technical Conference and Exhibition*.

47. Chabab, S., Théveneau, P., Coquelet, C., Corvisier, J., & Paricaud, P. (2020). Measurements and predictive models of high-pressure H2 solubility in brine (H2O+NaCl) for underground hydrogen storage application. *International Journal of Hydrogen Energy*, *45*(56), 32206–32220. https://doi.org/10.1016/j.ijhydene.2020.08.192

48. Chemin, P. (1990). *Etude du rôle des inclusions fluides dans les mécanismes de déformation des roches halitiques. Application aux formations salifères du bassin bressan* [PhD Thesis]. Ecole Nationale des Ponts et Chaussées.

49. Chen, J., Ren, S., Yang, C., Jiang, D., & Li, L. (2013). Self-healing characteristics of damaged rock salt under different healing conditions. *Materials*, *6*(8), 3438–3450.

50. Chen, L. L., Katz, D. L., & Tek, M. R. (1977). Binary gas diffusion of methane-nitrogen through porous solids. *AIChE Journal*, *23*(3), 336–341.

51. Choong, Y. Y., Norli, I., Abdullah, A. Z., & Yhaya, M. F. (2016). Impacts of trace element supplementation on the performance of anaerobic digestion process: A critical review. *Bioresource Technology*, *209*, 369–379.

52. Cinar, Y., Pusch, G., & Reitenbach, V. (2006). Petrophysical and capillary properties of compacted salt. *Transport in Porous Media*, *64*(2), 199–228.

53. Clever, H. L. (1979). *Krypton, xenon and radon-gas solubilities. Solubility Data Series*.

54. Coble, R. L. (1963). A model for boundary diffusion controlled creep in polycrystalline materials. *Journal of Applied Physics*, *34*(6), 1679–1682.

55. College of the Desert. (2001). Course Manual on Hydrogen Fuel Cell Engines and Related Technologies Module 1 Hydrogen Properties. *College of the Desert, Palm Desert, CA, USA*.

56. Coombs, P., Wagner, D., Bateman, K., Harrison, H., Milodowski, A. E., Noy, D., & West, J. M. (2010). The role of biofilms in subsurface transport processes. *Quarterly Journal of Engineering Geology and Hydrogeology*, *43*(2), 131–139.

57. Cord-Ruwisch, R., Seitz, H.-J., & Conrad, R. (1988). The capacity of hydrogenotrophic anaerobic bacteria to compete for traces of hydrogen depends on the redox potential of the terminal electron acceptor. *Archives of Microbiology*, *149*(4), 350–357.

58. Cosenza, P. (1996). *Sur les couplages entre comportement mécanique et processus de transfert de masse dans le sel gemme* [PhD Thesis]. Paris 6.

59. Cosenza, P., & Ghoreychi, M. (1999). Effects of very low permeability on the long-term evolution of a storage cavern in rock salt. *International Journal of Rock Mechanics and Mining Sciences*, *36*(4), 527–533.

60. Cosenza, P., Ghoreychi, M., Bazargan-Sabet, B., & De Marsily, G. (1999). In situ rock salt permeability measurement for long term safety assessment of storage. *International Journal of Rock Mechanics and Mining Sciences*, *36*(4), 509–526.

61. Costerton, J. W., Lewandowski, Z., Caldwell, D. E., Korber, D. R., & Lappin-Scott, H. M. (1995). Microbial biofilms. *Annual Review of Microbiology*, *49*(1), 711–745.

62. Cristescu, N., & Hunsche, U. (1998). *Time effects in rock mechanics* (Vol. 350). Wiley New York.

63. Crook, K. A. (1974). *Lithogenesis and geotectonics: The significance of compositional variation in flysch arenites (graywackes)*.

64. Crozier, T. E., & Yamamoto, S. (1974). Solubility of hydrogen in water, sea water, and sodium chloride solutions. *Journal of Chemical and Engineering Data*, *19*(3), 242–244.

65. Cunningham, A. B., Gerlach, R., Spangler, L., & Mitchell, A. C. (2009). Microbially enhanced geologic containment of sequestered supercritical CO2. *Energy Procedia*, *1*(1), 3245–3252.

66. Cussler, E. L., & Cussler, E. L. (2009). *Diffusion: Mass transfer in fluid systems*. Cambridge university press.

67. Cypionka, H. (2010). *Grundlagen der Mikrobiologie*. Springer-Verlag.

68. Da Gama, C. D. (1979). Rheologic behaviour of heterogeneous salt rocks. *4th ISRM Congress*.

69. Daim, T. U., Li, X., Kim, J., & Simms, S. (2012). Evaluation of energy storage technologies for integration with renewable electricity: Quantifying expert opinions. *Environmental Innovation and Societal Transitions*, *3*, 29–49.

70. Darcy, H. (1856). *Les fontaines publiques de la ville de Dijon: Exposition et application...* Victor Dalmont.

71. Davey, M. E., & O'toole, G. A. (2000). Microbial biofilms: From ecology to molecular genetics. *Microbiology and Molecular Biology Reviews*, *64*(4), 847–867.

72. Davison, J., Arienti, S., Cotone, P., & Mancuso, L. (2010). Co-production of hydrogen and electricity with CO2 capture. *International Journal of Greenhouse Gas Control*, *4*(2), 125–130.

73. De Marsily, G. (2004). Cours d'hydrogéologie. *Université Paris VI*.

74. Denholm, P., Ela, E., Kirby, B., & Milligan, M. (2010). *Role of energy storage with renewable electricity generation*. National Renewable Energy Lab.(NREL), Golden, CO (United States).

75. Didier, M., Talandier, J., & Berne, P. (2012). *Expériences de transfert de l'hydrogène gazeux à travers l'argilite du Callovo-Oxfordien*. 3.

76. Donaldson, E. C., & Tiab, D. (2004). *Petrophysics: Theory and practice of measuring reservoir rock and fluid transport properties*. Elsevier.

77. Donlan, R. M., & Costerton, J. W. (2002). Biofilms: Survival mechanisms of clinically relevant microorganisms. *Clinical Microbiology Reviews*, *15*(2), 167–193.

78. Dopffel, N., Jansen, S., & Gerritse, J. (2021). Microbial side effects of underground hydrogen storage–Knowledge gaps, risks and opportunities for successful implementation. *International Journal of Hydrogen Energy*.

79. Dullien, F. A. (2012). *Porous media: Fluid transport and pore structure*. Academic press.

80. Ebigbo, A., Golfier, F., & Quintard, M. (2013). A coupled, pore-scale model for methanogenic microbial activity in underground hydrogen storage. *Advances in Water Resources*, *61*, 74–85.

81. Ebrahimiyekta, A. (2017). *Characterization of geochemical interactions and migration of hydrogen in sandstone sedimentary formations: Application to geological storage* [PhD Thesis]. Université d'Orléans.

82. Energy.gov blog. (2021). *Hydrogen Storage*. Energy.Gov. https://www.energy.gov/eere/fuelcells/hydrogen-storage

83. Enzmann, F., Mayer, F., Rother, M., & Holtmann, D. (2018). Methanogens: Biochemical background and biotechnological applications. *Amb Express*, *8*(1), 1–22.

84. Escoffier, S., Homand, F., Giraud, A., Hoteit, N., & Su, K. (2005). Under stress permeability determination of the Meuse/Haute-Marne mudstone. *Engineering Geology*, *81*(3), 329–340.

85. EU_Eurostat. (2021). *Energy statistics—An overview*. https://ec.europa.eu/eurostat/statistics-explained/index.php?title=Energy_statistics_-_an_overview

86. European Association for the storage of energy. (2016). *Pumped Hydro Storage European Association for the storage of energy, 2016*

87. European Commission. Directorate-General for Energy. (2012). *Energy: Roadmap 2050*. Publications Office. https://data.europa.eu/doi/10.2833/10759

88. Evans, D. J. (2009). A review of underground fuel storage events and putting risk into perspective with other areas of the energy supply chain. *Geological Society, London, Special Publications*, *313*(1), 173–216.

89. Fadrus, H., & Malỳ, J. (1975). Suppression of iron (III) interference in the determination of iron (II) in water by the 1, 10-phenanthroline method. *Analyst*, *100*(1193), 549–554.

90. Fairhurst, C., St John, C. M., Midea, N. F., De Eston, S. M., Fernandes, A. C., & Bongiovanni, L. A. (1979). Rock mechanics studies of proposed underground mining of potash in Sergipe, Brazil. *4th ISRM Congress*.

91. Fan, J., Chen, J., Jiang, D., Ren, S., & Wu, J. (2016). Fatigue properties of rock salt subjected to interval cyclic pressure. *International Journal of Fatigue*, *90*, 109–115.

92. Feldmann, F., Hagemann, B., Ganzer, L., & Panfilov, M. (2016). Numerical simulation of hydrodynamic and gas mixing processes in underground hydrogen storages. *Environmental Earth Sciences*, *75*(16), 1–15.

93. Flesch, S., Pudlo, D., Albrecht, D., Jacob, A., & Enzmann, F. (2018). Hydrogen underground storage—Petrographic and petrophysical variations in reservoir sandstones from laboratory experiments under simulated reservoir conditions. *International Journal of Hydrogen Energy*, *43*(45), 20822–20835.

94. Foh, S., Novil, M., Rockar, E., & Randolph, P. (1979). *Underground hydrogen storage. Final report.[salt caverns, excavated caverns, aquifers and depleted fields]*. Brookhaven National Lab., Upton, NY (USA).

95. Fokker, P. A., Urai, J. L., Steeneken, P. V., Barends, F. B. J., Brouwer, F. J. J., & Schröder, F. H. (1995). Production-induced convergence of solution mined caverns in magnesium salts and associated subsidence. *Land Subsidence.*

Natural Causes, Measuring Techniques, the Groningen Gas Field: Proceedings of the Fifth International Conference on Land Subsidence, Den Haag, Netherlands, 281–289.

96. Fredrickson, J. K., & Gorby, Y. A. (1996). Environmental processes mediated by iron-reducing bacteria. *Current Opinion in Biotechnology*, *7*(3), 287–294.

97. Freitag, T. E., & Prosser, J. I. (2009). Correlation of methane production and functional gene transcriptional activity in a peat soil. *Applied and Environmental Microbiology*, *75*(21), 6679–6687.

98. Fuenkajom, K., & Daemen, J. J. (1988). Borehole closure in salt. *The 29th US Symposium on Rock Mechanics (USRMS)*.

99. Fuller, E. N., Schettler, P. D., & Giddings, J. C. (1966). New method for prediction of binary gas-phase diffusion coefficients. *Industrial & Engineering Chemistry*, *58*(5), 18–27.

100. Gaboriaud, F., & Ehrhardt, J.-J. (2003). Effects of different crystal faces on the surface charge of colloidal goethite (α-FeOOH) particles: An experimental and modeling study. *Geochimica et Cosmochimica Acta*, *67*(5), 967–983.

101. Gahleitner, G. (2013). Hydrogen from renewable electricity: An international review of power-to-gas pilot plants for stationary applications. *International Journal of Hydrogen Energy*, *38*(5), 2039–2061.

102. Ganzer, L., Reitenbach, V., Pudlo, D., Panfilov, M., Albrecht, D., & Gaupp, R. (2013). The H2STORE project-experimental and numerical simulation approach to investigate processes in underground hydrogen reservoir storage. *EAGE Annual Conference & Exhibition Incorporating SPE Europec*.

103. Gavín, R., Merino, S., Altarriba, M., Canals, R., Shaw, J. G., & Tomás, J. M. (2003). Lateral flagella are required for increased cell adherence, invasion and biofilm formation by Aeromonas spp. *FEMS Microbiology Letters*, *224*(1), 77–83.

104. Gevantman, L. H., & Lorenz, J. (1981). *Physical properties data for rock salt* (Vol. 167). US Department of Commerce, National Bureau of Standards.

105. Ghazali, A. (1995). *Etude par analyse texturale du rôle de l'humidité dans la déformation des roches salifères. Application au sel du Bassin Bressan et au sel de dôme de la mine d'Asse* [PhD Thesis]. Ecole Nationale des Ponts et Chaussées.

106. Ghosh, S., Lepcha, K., Basak, A., & Mahanty, A. K. (2020). Thermophiles and thermophilic hydrolases. In *Physiological and Biotechnological Aspects of Extremophiles* (pp. 219–236). Elsevier.

107. Gloyna, E. F., & Reynolds, T. D. (1961). Permeability measurements of rock salt. *Journal of Geophysical Research*, *66*(11), 3913–3921.

108. Gramberg, J., & Roest, J. P. A. (1984). *Cataclastic effects in rock salt laboratory and in situ measurements*. Commission of the European Communities.

109. Gregory, S. P., Barnett, M. J., Field, L. P., & Milodowski, A. E. (2019). Subsurface microbial hydrogen cycling: Natural occurrence and implications for industry. *Microorganisms*, *7*(2), 53.

110. Grgic, D. (2016). Constitutive modelling of the elastic–plastic, viscoplastic and damage behaviour of hard porous rocks within the unified theory of inelastic flow. *Acta Geotechnica*, *11*(1), 95–126.

111. Grgic, D., Al Sahyouni, Golfier, F., Moumni, M., & Schoumacker, L. (2021). Evolution of gas permeability of rock salt under hydrostatic and triaxial loadings and implications on the underground hydrogen storage in salt caverns. *Rock Mechanics and Rock Engineering*, *.To be published*.

112. Gueguen, Y., & Dienes, J. (1989). Transport properties of rocks from statistics and percolation. *Mathematical Geology*, *21*(1), 1–13.

113. Haase, C., Dahmke, A., Ebert, M., Schäfer, D., & Dethlefsen, F. (2014). Suitability of existing numerical model codes and thermodynamic databases for the prognosis of calcite dissolution processes in near-surface sediments due to a CO 2 leakage investigated by column experiments. *Aquatic Geochemistry*, *20*(6), 639–661.

114. Haeseldonckx, D., & D'haeseleer, W. (2011). Concrete transition issues towards a fully-fledged use of hydrogen as an energy carrier: Methodology and modelling. *International Journal of Hydrogen Energy*, *36*(8), 4636–4652.

115. Hagemann, B. (2018). *Numerical and analytical modeling of gas mixing and bio-reactive transport during underground hydrogen storage* (Vol. 50). Cuvillier Verlag.

116. Hangx, S. J., Spiers, C. J., & Peach, C. J. (2010). Mechanical behavior of anhydrite caprock and implications for CO2 sealing capacity. *Journal of Geophysical Research: Solid Earth*, *115*(B7).

117. Hansen, J. E., Cowan, R. D., Carter, S. L., & Kelly, H. P. (1984). Analysis of resonance structure in the photoionization of atomic chlorine. *Physical Review A*, *30*(3), 1540.

118. Hart, D., & Financial Times Energy Publishing, L. (United K. (1997). *Hydrogen power The commercial future ofthe ultimate fuel'*.

119. Hassanpouryouzband, A., Joonaki, E., Farahani, M. V., Takeya, S., Ruppel, C., Yang, J., English, N. J., Schicks, J. M., Edlmann, K., & Mehrabian, H. (2020). Gas hydrates in sustainable chemistry. *Chemical Society Reviews*, *49*(15), 5225–5309.

120. Hatzor, Y. H., & Heyman, E. P. (1997). Dilation of anisotropic rock salt: Evidence from Mount Sedom diapir. *Journal of Geophysical Research: Solid Earth*, *102*(B7), 14853–14868.

121. Haupt, M. (1991). A constitutive law for rock salt based on creep and relaxation tests. *Rock Mechanics and Rock Engineering*, *24*(4), 179–206.

122. Hazotte, A. (2012). *Cinétique de l'utilisation microbienne du di-hydrogène sous hautes pressions* [PhD Thesis]. Université de Lorraine (Nancy).

123. Heard, H. C. (1972). Steady-state flow in polycrystalline halite at pressure of 2 kilobars. *Flow and Fracture of Rocks*, *16*, 191–209.

124. Heidelberg, J. F., Paulsen, I. T., Nelson, K. E., Gaidos, E. J., Nelson, W. C., Read, T. D., Eisen, J. A., Seshadri, R., Ward, N., & Methe, B. (2002). Genome sequence of the dissimilatory metal ion–reducing bacterium Shewanella oneidensis. *Nature Biotechnology*, *20*(11), 1118–1123.

125. Heinemann, N., Alcalde, J., Miocic, J. M., Hangx, S. J., Kallmeyer, J., Ostertag-Henning, C., Hassanpouryouzband, A., Thaysen, E. M., Strobel, G. J., & Schmidt-Hattenberger, C. (2021). Enabling large-scale hydrogen storage in porous media–the scientific challenges. *Energy & Environmental Science*, *14*(2), 853–864.

126. Helmig, R. (1997). *Multiphase flow and transport processes in the subsurface: A contribution to the modeling of hydrosystems.* Springer-Verlag.

127. Henkel, S., Pudlo, D., & Gaupp, R. (2013). Research sites of the H2STORE project and the relevance of lithological variations for hydrogen storage at depths. *Energy Procedia*, *40*, 25–33.

128. Ho, C. K., & Webb, S. W. (2006). *Gas transport in porous media* (Vol. 20). Springer.

129. Houpert, A. (1959). Revue de L'Institut Francais du Petrole. *On the Flow of Gases in Porous Media*, *14*(11), 1468–1684.

130. Hunsche, U., & Hampel, A. (1999). Rock salt—The mechanical properties of the host rock material for a radioactive waste repository. *Engineering Geology*, *52*(3–4), 271–291.

131. Huq, F., Haderlein, S. B., Cirpka, O. A., Nowak, M., Blum, P., & Grathwohl, P. (2015). Flow-through experiments on water–rock interactions in a sandstone caused by CO2 injection at pressures and temperatures mimicking reservoir conditions. *Applied Geochemistry*, *58*, 136–146.

132. Hyne, N. J. (2019). *Nontechnical guide to petroleum geology, exploration, drilling & production*. PennWell Books, LLC.

133. Ikegami, A., Nakasone, K., Kato, C., Nakamura, Y., Yoshikawa, I., Usami, R., & Horikoshi, K. (2000). Glutamine synthetase gene expression at elevated hydrostatic pressure in a deep-sea piezophilic Shewanella violacea. *FEMS Microbiology Letters*, *192*(1), 91–95.

134. International energy agency. (2020). *2020 Inventory of U.S. Greenhouse Gas Emissions and Sinks: 1990-2018*

135. International energy agency. (2021). *Global Energy Review 2021 – Analysis*. IEA. https://www.iea.org/reports/global-energy-review-2021

136. Ishida, K. P., & Griffiths, P. R. (1994). Theoretical and experimental investigation of internal reflection at thin copper films exposed to aqueous solutions. *Analytical Chemistry*, *66*(4), 522–530.

137. Jockwer, N., MoÈnig, J., Hunsche, U., & Schulze, O. (1992). Gas release from rock salt. In *Gas generation and release from radioactive waste repositories*.

138. Jockwer, N., & Wieczorek, K. (2008). *ADDIGAS. Advective and diffusive gas transport in rock salt formations. Final report*. Gesellschaft fuer Anlagen-und Reaktorsicherheit mbH (GRS).

139. Kantzas, A., Bryan, J., & Taheri, S. (2012). Fundamentals of fluid flow in porous media. *Pore Size Distribution*.

140. Karaiskakis, G., & Gavril, D. (2004). Determination of diffusion coefficients by gas chromatography. *Journal of Chromatography A*, *1037*(1–2), 147–189.

141. Kato, C., Qureshi, M. H., & Horikoshi, K. (1999). Pressure response in deep-sea piezophilic bacteria. *Journal of Molecular Microbiology and Biotechnology*, *1*(1), 87–92.

142. Katsikogianni, M., & Missirlis, Y. F. (2004). Concise review of mechanisms of bacterial adhesion to biomaterials and of techniques used in estimating bacteria-material interactions. *Eur Cell Mater*, *8*(3), 37–57.

143. Kern, H. (1977). Preferred orientation of experimentally deformed limestone marble, quartzite and rock salt at different temperatures and states of stress. *Tectonophysics*, *39*(1–3), 103–120.

144. Kirchman, D. L. (2018). *Processes in microbial ecology*. Oxford University Press.

145. Klausen, M., Gjermansen, M., Kreft, J.-U., & Tolker-Nielsen, T. (2006). Dynamics of development and dispersal in sessile microbial communities: Examples from Pseudomonas aeruginosa and Pseudomonas putida model biofilms. *FEMS Microbiology Letters*, *261*(1), 1–11.

146. Kleinitz, W., & Boehling, E. (2005). Underground gas storage in porous media–operating experience with bacteria on gas quality (spe94248). *67th EAGE Conference & Exhibition*, cp-1.

147. Klinkenberg, L. J. (1941). The permeability of porous media to liquids and gases. *Drilling and Production Practice*.

148. Klotz, I. M., & Young, T. F. (1964). *Introduction to chemical thermodynamics*. Wa Benjamin.

149. Knudsen, M. (1995). The laws of molecular flow and of inner friction flow of gases through tubes. *Journal of Membrane Science*, *100*(1), 23–25.

150. Koelemeijer, P. J., Peach, C. J., & Spiers, C. J. (2012). Surface diffusivity of cleaved NaCl crystals as a function of humidity: Impedance spectroscopy measurements and implications for crack healing in rock salt. *Journal of Geophysical Research: Solid Earth*, *117*(B1).

151. Kolev, N. I. (2007). Solubility of O2, N2, H2 and CO2 in Water. In *Multiphase Flow Dynamics 3* (pp. 185–214). Springer.

152. Krooss, B. (2008). Evaluation of database on gas migration through clayey host rocks. *Belgian National Agency for Radioactive Waste and Enriched Fissile Material (ONDRAF-NIRAS)*.

153. Kruck, O., Crotogino, F., Prelicz, R., & Rudolph, T. (2013). Assessment of the potential, the actors and relevant business cases for large scale and seasonal storage of renewable electricity by hydrogen underground storage in Europe. *KBB Undergr. Technol. GmbH*.

154. Kueper, B. H., & Frind, E. O. (1988). An overview of immiscible fingering in porous media. *Journal of Contaminant Hydrology*, *2*(2), 95–110.

155. Kuntsman, A. (2007). 6. Belonging through Violence: Flaming, Erasure, and Performativity. *Queer Online: Media Technology & Sexuality*, *40*, 101.

156. Kyle, J. R., Ulrich, M. R., & Gose, W. A. (1987). Textural and paleomagnetic evidence for the mechanism and timing of anhydrite cap rock formation, Winnfield salt dome, Louisiana. In *Dynamical geology of salt and related structures* (pp. 497–542). Elsevier.

157. Laille, J. P., Coulomb, C., & Tek, M. R. (1986). Underground storage in Cerville-Velaine, France: A case history in conversion and inert gas injection as cushion substitute. *SPE Annual Technical Conference and Exhibition*.

158. Langer, M. (1982). *The rheological behaviour of rock salt*.

159. Langer, M. (1991). General report: The rheological behavior of rock salt. *7th ISRM Congress*.

160. Lassin, A., Dymitrowska, M., & Azaroual, M. (2011). Hydrogen solubility in pore water of partially saturated argillites: Application to Callovo-Oxfordian clayrock in the context of a nuclear waste geological disposal. *Physics and Chemistry of the Earth, Parts A/B/C*, *36*(17–18), 1721–1728.

161. Le Guen, C. (1991). *Mesure de la permeabilite de roches tres peu permeables et etude de son evolution sous sollicitaitons thermomecaniques. Application aux roches saliferes du bassin bressan* [PhD Thesis]. Paris, ENMP.

162. Lebrun, P. (1993). *Evolution des caractéristiques pétrophysiques de roches salifères sous sollicitations thermomécaniques* [PhD Thesis]. Paris, ENMP.

163. Lefebvre, R. (2006). *Écoulement multiphase en milieux poreux. Graduate course notes, 6e éd*. GEO-9602/GLG-65146, Joint Graduate program, Laval University/INRS-ETE, INRS ….

164. Lemaitre, J. (1985). *A continuous damage mechanics model for ductile fracture*.

165. Lemaitre, J., & Chaboche, J.-L. (1978). Aspect phénoménologique de la rupture par endommagement. *J Méc Appl*, *2*(3).

166. Letham, E. A., & Bustin, R. M. (2016). Klinkenberg gas slippage measurements as a means for shale pore structure characterization. *Geofluids*, *16*(2), 264–278.

167. Lewis, S., & Holness, M. (1996). Equilibrium halite-H2O dihedral angles: High rock-salt permeability in the shallow crust? *Geology*, *24*(5), 431–434.

168. Li, S.-Y., & Urai, J. L. (2016). Rheology of rock salt for salt tectonics modeling. *Petroleum Science*, *13*(4), 712–724.

169. Liang, W., Yang, C., Zhao, Y., Dusseault, M. B., & Liu, J. (2007). Experimental investigation of mechanical properties of bedded salt rock. *International Journal of Rock Mechanics and Mining Sciences*, *44*(3), 400–411.

170. Liang, W., Zhang, C., Gao, H., Yang, X., Xu, S., & Zhao, Y. (2012). Experiments on mechanical properties of salt rocks under cyclic loading. *Journal of Rock Mechanics and Geotechnical Engineering*, *4*(1), 54–61.

171. Libert, M., Bildstein, O., Esnault, L., Jullien, M., & Sellier, R. (2011). Molecular hydrogen: An abundant energy source for bacterial activity in nuclear waste repositories. *Physics and Chemistry of the Earth, Parts A/B/C*, *36*(17–18), 1616–1623.

172. Lide, D. R. (1994). *CRC Handbook of Chemistry and Physics. 75. Hrsg., 1994*. CRC Press Inc.

173. Lienen, T., Lüders, K., Halm, H., Westphal, A., Köber, R., & Würdemann, H. (2017). Effects of thermal energy storage on shallow aerobic aquifer systems: Temporary increase in abundance and activity of sulfate-reducing and sulfur-oxidizing bacteria. *Environmental Earth Sciences*, *76*(6), 261.

174. Lindblom, U. E. (1997). Design criteria for the Brooklyn Union gas storage caverns at JFK airport, New York. *International Journal of Rock Mechanics and Mining Sciences*, *34*(3–4), 179-e1.

175. Little, B., & Jacobus, J. (1985). A comparison of two techniques for the isolation of adsorbed dissolved organic material from seawater. *Organic Geochemistry*, *8*(1), 27–33.

176. Liu, J., Xie, H., Hou, Z., Yang, C., & Chen, L. (2014). Damage evolution of rock salt under cyclic loading in unixial tests. *Acta Geotechnica*, *9*(1), 153–160.

177. Loeb, L. B. (2004a). *The kinetic theory of gases*. Courier Corporation.

178. Loeb, L. B. (2004b). *The Kinetic Theory of Gases*. Courier Corporation.

179. Looff, K. M., & Rautman, C. (2010). Inferring the geologic significance and potential impact of salt fabric and anomalous salt on the development and long-term operation of salt storage caverns on Gulf Coast salt domes. *Solution Mining Research Institute Spring Conference*, 26–27.

180. Lord, A. S., Kobos, P. H., & Borns, D. J. (2014). Geologic storage of hydrogen: Scaling up to meet city transportation demands. *International Journal of Hydrogen Energy*, *39*(28), 15570–15582.

181. Lovley, D. R., & Chapelle, F. H. (1995). Deep subsurface microbial processes. *Reviews of Geophysics*, *33*(3), 365–381.

182. Lovley, D. R., Kashefi, K., Vargas, M., Tor, J. M., & Blunt-Harris, E. L. (2000). Reduction of humic substances and Fe (III) by hyperthermophilic microorganisms. *Chemical Geology*, *169*(3–4), 289–298.

183. Luboń, K., & Tarkowski, R. (2020). Numerical simulation of hydrogen injection and withdrawal to and from a deep aquifer in NW Poland. *International Journal of Hydrogen Energy*, *45*(3), 2068–2083.

184. Lysyy, M., Fernø, M., & Ersland, G. (2021). Seasonal hydrogen storage in a depleted oil and gas field. *International Journal of Hydrogen Energy*.

185. Mahlia, T. M. I., Saktisahdan, T. J., Jannifar, A., Hasan, M. H., & Matseelar, H. S. C. (2014). A review of available methods and development on energy storage; technology update. *Renewable and Sustainable Energy Reviews*, *33*, 532–545.

186. Maier, R. M., Pepper, I. L., & Gerba, C. P. (Eds.). (2009). *Environmental microbiology* (2nd ed). Elsevier/Academic Press.

187. Mansouri, H., & Ajalloeian, R. (2018). Mechanical behavior of salt rock under uniaxial compression and creep tests. *International Journal of Rock Mechanics and Mining Sciences*, *110*, 19–27.

188. Mansouri, H., Ajalloeian, R., Elyaszadeh, R., & Mansouri, A. (2018). Investigation of mechanical properties of salt rock based on its microstructure. *Scientific Quarterly Journal of Iranian Association of Engineering Geology*, *11*(1), 95–115.

189. Marbán, G., & Valdés-Solís, T. (2007). Towards the hydrogen economy? *International Journal of Hydrogen Energy*, *32*(12), 1625–1637.

190. Martin-Clave, C., Ougier-Simonin, A., & Vandeginste, V. (2021). Impact of second phase content on rock salt rheological behavior under cyclic mechanical conditions. *Rock Mechanics and Rock Engineering*, 1–23.

191. McTigue, D. F. (1986). Thermoelastic response of fluid-saturated porous rock. *Journal of Geophysical Research: Solid Earth*, *91*(B9), 9533–9542.

192. Merar, J. (1999). *Elaboration d'une loi de comportement pour le sel gemme* [PhD Thesis]. Centre de Géotechnique et d'Exploitation du Sous-sol-Ecole des Mines de Paris.

193. Meyers, R. A. (2010). *Extreme environmental events: Complexity in forecasting and early warning* (Vol. 1). Springer Science & Business Media.

194. Michalski, J., Bünger, U., Crotogino, F., Donadei, S., Schneider, G.-S., Pregger, T., Cao, K.-K., & Heide, D. (2017). Hydrogen generation by electrolysis and storage in salt caverns: Potentials, economics and systems aspects with regard to the German energy transition. *International Journal of Hydrogen Energy*, *42*(19), 13427–13443.

195. Miller, J. F., Nelson, C. M., Ludlow, J. M., Shah, N. N., & Clark, D. S. (1989). High pressure-temperature bioreactor: Assays of thermostable hydrogenase with fiber optics. *Biotechnology and Bioengineering*, *34*(7), 1015–1021.

196. Morgan, H., Large, D., Bateman, K., Hanstock, D., & Gregory, S. (2017). The effect of variable oxygen impurities on microbial activity in conditions resembling geological storage sites. *Energy Procedia*, *114*, 3077–3087.

197. Morton-Thompson, D., & Woods, A. M. (1993). *Development geology reference manual: AAPG methods in exploration series, no. 10*. AAPG.

198. Muhammad, N. (2015). *Deformation and transport processes in salt rocks: An experimental study exploring effects of pressure and stress relaxation* [PhD Thesis]. UU Dept. of Earth Sciences.

199. Munson, D. E., & Dawson, P. R. (1981). *Salt-constitutive modeling using mechanism maps*. Sandia National Labs.

200. Murray, G. E. (1966). Salt structures of Gulf of Mexico basin—A review. *AAPG Bulletin*, *50*(3), 439–478.

201. Myers, C. R., & Nealson, K. H. (1990). Respiration-linked proton translocation coupled to anaerobic reduction of manganese (IV) and iron (III) in Shewanella putrefaciens MR-1. *Journal of Bacteriology*, *172*(11), 6232–6238.

202. Nealson, K. H., & Saffarini, D. (1994). Iron and manganese in anaerobic respiration: Environmental significance, physiology, and regulation. *Annual Review of Microbiology*, *48*(1), 311–343.

203. Nogi, Y., Kato, C., & Horikoshi, K. (1998). Taxonomic studies of deep-sea barophilic Shewanella strains and description of Shewanella violacea sp. Nov. *Archives of Microbiology*, *170*(5), 331–338.

204. O'Loughlin, E. J., Gorski, C. A., Flynn, T. M., & Scherer, M. M. (2019). Electron donor utilization and secondary mineral formation during the bioreduction of lepidocrocite by Shewanella putrefaciens CN32. *Minerals*, *9*(7), 434.

205. Ordin, P. M. (1997). *Safety Standard for Hydrogen and Hydrogen Systems Guidelines for Hydrogen System Design, Materials Selection, Operations, Storage and Transportation*.

206. Oren, A. (2013). Life at high salt concentrations, intracellular KCl concentrations, and acidic proteomes. *Frontiers in Microbiology*, *4*, 315.

207. Orowan, E. (1940). Problems of plastic gliding. *Proceedings of the Physical Society*, *52*(1), 8–22. https://doi.org/10.1088/0959-5309/52/1/303

208. Ortiz, L., Volckaert, G., & Mallants, D. (2002a). Gas generation and migration in Boom Clay, a potential host rock formation for nuclear waste storage. *Engineering Geology*, *64*(2–3), 287–296.

209. Ortiz, L., Volckaert, G., & Mallants, D. (2002b). Gas generation and migration in Boom Clay, a potential host rock formation for nuclear waste storage. *Engineering Geology*, *64*(2–3), 287–296.

210. O'Toole, G., Kaplan, H. B., & Kolter, R. (2000). Biofilm formation as microbial development. *Annual Reviews in Microbiology*, *54*(1), 49–79.

211. Ozarslan, A. (2012). Large-scale hydrogen energy storage in salt caverns. *International Journal of Hydrogen Energy*, *37*(19), 14265–14277.

212. Pagniez, H., & Berche, P. (2005). Opportunistic infections caused by Shewanella, new emergent bacteria. *Medecine et Maladies Infectieuses*, *35*(4), 186–191.

213. Panfilov, M. (2010). Underground storage of hydrogen: In situ self-organisation and methane generation. *Transport in Porous Media*, *85*(3), 841–865.

214. Paterson, L. (1983). The implications of fingering in underground hydrogen storage. *International Journal of Hydrogen Energy*, *8*(1), 53–59.

215. Paterson, M. S. (1983). The equivalent channel model for permeability and resistivity in fluid-saturated rock—A re-appraisal. *Mechanics of Materials*, *2*(4), 345–352.

216. Payler, S. J., Biddle, J. F., Sherwood Lollar, B., Fox-Powell, M. G., Edwards, T., Ngwenya, B. T., Paling, S. M., & Cockell, C. S. (2019). An ionic limit to life in the deep subsurface. *Frontiers in Microbiology*, *10*, 426.

217. Peach, C. J. (1991). *Influence of deformation on the fluid transport properties of salt rocks*. Facultiet Aardwetenschappen der Rijksuniversiteit Utrecht].

218. Peach, C. J., & Spiers, C. J. (1996a). Influence of crystal plastic deformation on dilatancy and permeability development in synthetic salt rock. *Tectonophysics*, *256*(1–4), 101–128. https://doi.org/10.1016/0040-1951(95)00170-0

219. Peach, C. J., & Spiers, C. J. (1996b). Influence of crystal plastic deformation on dilatancy and permeability development in synthetic salt rock. *Tectonophysics*, *256*(1), 101–128. https://doi.org/10.1016/0040-1951(95)00170-0

220. Pedersen, K. (2000). *Microbial processes in radioactive waste disposal*. Swedish Nuclear Fuel and Waste Management Co.

221. PERAMI, R., CALEFFI, C., ESPAGNE, M., & PRINCE, W. (1993). Fluage et microfissuration du sel dans les stockages souterrains. *Géologie et Confinement Des Déchets Toxiques (Montpellier, 8-11 Juin 1993. Volume 1)*, 99–104.

222. Pérez, A., Pérez, E., Dupraz, S., & Bolcich, J. (2016). Patagonia wind-hydrogen project: Underground storage and methanation. *De 21st World Hydrogen Energy Conference*.

223. Petrucci, E., Montanaro, D., & Di Palma, L. (2012). A feasibility study of hydrogen peroxide electrogeneration in seawater for environmental remediation. *CHEMICAL ENGINEERING*, *28*.

224. Pfeiffer, W. T., Beyer, C., & Bauer, S. (2017). Hydrogen storage in a heterogeneous sandstone formation: Dimensioning and induced hydraulic effects. *Petroleum Geoscience*, *23*(3), 315–326.

225. Picard, A., Testemale, D., Hazemann, J.-L., & Daniel, I. (2012). The influence of high hydrostatic pressure on bacterial dissimilatory iron reduction. *Geochimica et Cosmochimica Acta*, *88*, 120–129.

226. Pichler, M. (2010). *ASSESMENT OF HYDROGEN – ROCK INTERACTIONS DURING GEOLOGICAL STORAGE OF CH4 – H2 MIXTURES*. 97.

227. Pichler, M. (2019). Underground Sun Storage Results and Outlook. *EAGE/DGMK Joint Workshop on Underground Storage of Hydrogen*, *2019*(1), 1–4.

228. Pierre Duffaut. (2004). *Manuel de mécanique des roches* (Vol. 2). Presses des MINES.

229. Ponomarev-Stepnoi, N. N. (2004). Nuclear-hydrogen power. *Atomic Energy*, *96*(6), 375–385.

230. Popp, T., Kern, H., & Schulze, O. (2001). Evolution of dilatancy and permeability in rock salt during hydrostatic compaction and triaxial deformation. *Journal of Geophysical Research: Solid Earth*, *106*(B3), 4061–4078.

231. Pouya, A. (1991). *Comportement rheologique du sel gemme. Application a l'etude des excavations souterraines* [PhD Thesis]. Marne-la-vallée, ENPC.

232. Prachi R., P., Mahesh M., W., & Aneesh C., G. (2016). A Review on Solid State Hydrogen Storage Material. *Advances in Energy and Power*, *4*(2), 11–22. https://doi.org/10.13189/aep.2016.040202

233. Pray, H. A., Schweickert, C. E., & Minnich, B. H. (1952). Solubility of hydrogen, oxygen, nitrogen, and helium in water at elevated temperatures. *Industrial & Engineering Chemistry*, *44*(5), 1146–1151.

234. Present, R. D. (1958). *Kinetic theory of gases* (Vol. 222). McGraw-Hill.

235. RAG. (2017). *Underground SUN storage—Chemical storage of renewable energy in porous subsurface reservoirs with exemplary testbed*. https://www.underground-sun-storage.at/en/?saveOptinHistory=&cHash=97c4ddd3f66a7671d0c83b04c40314f3

236. Reitenbach, V., Ganzer, L., Albrecht, D., & Hagemann, B. (2015). Influence of added hydrogen on underground gas storage: A review of key issues. *Environmental Earth Sciences*, *73*(11), 6927–6937.

237. Robinius, M., Otto, A., Heuser, P., Welder, L., Syranidis, K., Ryberg, D. S., Grube, T., Markewitz, P., Peters, R., & Stolten, D. (2017). Linking the power and transport sectors—Part 1: The principle of sector coupling. *Energies*, *10*(7), 956.

238. Roedder, E. (1984). The fluids in salt. *American Mineralogist*, *69*(5–6), 413–439.

239. Sáinz-García, A., Abarca, E., Rubí, V., & Grandia, F. (2017). Assessment of feasible strategies for seasonal underground hydrogen storage in a saline aquifer. *International Journal of Hydrogen Energy*, *42*(26), 16657–16666.

240. Sato, K., Kawaguchi, H., & Kobayashi, H. (2013). Bio-electrochemical conversion of carbon dioxide to methane in geological storage reservoirs. *Energy Conversion and Management*, *66*, 343–350.

241. Sauer, K., Camper, A. K., Ehrlich, G. D., Costerton, J. W., & Davies, D. G. (2002). *Pseudomonas aeruginosa displays multiple phenotypes during development as a biofilm*. Am Soc Microbiol.

242. Sauer, K., Cullen, M. C., Rickard, A. H., Zeef, L. A. H., Davies, D. G., & Gilbert, P. (2004). Characterization of nutrient-induced dispersion in Pseudomonas aeruginosa PAO1 biofilm. *Journal of Bacteriology*, *186*(21), 7312–7326.

243. Scheidegger, A. E. (1961). General theory of dispersion in porous media. *Journal of Geophysical Research*, *66*(10), 3273–3278.

244. Schelling, T. C. (1992). Some economics of global warming. *The American Economic Review*, *82*(1), 1–14.

245. Schiebahn, S., Grube, T., Robinius, M., Tietze, V., Kumar, B., & Stolten, D. (2015). Power to gas: Technological overview, systems analysis and economic assessment for a case study in Germany. *International Journal of Hydrogen Energy*, *40*(12), 4285–4294.

246. Schoenherr, J., Urai, J. L., Kukla, P. A., Littke, R., Schléder, Z., Larroque, J.-M., Newall, M. J., Al-Abry, N., Al-Siyabi, H. A., & Rawahi, Z. (2007). Limits to the sealing capacity of rock salt: A case study of the infra-Cambrian Ara Salt from the South Oman salt basin. *AAPG Bulletin*, *91*(11), 1541–1557.

247. Schofield, A. N., & Wroth, P. (1968). *Critical state soil mechanics* (Vol. 310). McGraw-hill London.

248. Schultze, O. (2007). Investigations on damage and healing in rocks. *Proceedings of 6th Conference on the Mechanical Behavior of Salt. Taylor & Francis, London*, 33–44.

249. Schulze, O., Popp, T., & Kern, H. (2001a). Development of damage and permeability in deforming rock salt. *Engineering Geology*, *61*(2–3), 163–180.

250. Schulze, O., Popp, T., & Kern, H. (2001b). Development of damage and permeability in deforming rock saltq. *Engineering Geology*, 18.

251. Shi, L., Belchik, S. M., Plymale, A. E., Heald, S., Dohnalkova, A. C., Sybirna, K., Bottin, H., Squier, T. C., Zachara, J. M., & Fredrickson, J. K. (2011). Purification and characterization of the [NiFe]-hydrogenase of Shewanella oneidensis MR-1. *Applied and Environmental Microbiology*, *77*(16), 5584–5590.

252. Skovhus, T. L., & Whitby, C. (2019). *Oilfield Microbiology*. CRC Press.

253. Ślizowski, J., Smulski, R., Nagy, S., Burliga, S., & Polański, K. (2017). Tightness of hydrogen storage caverns in salt deposits. *AGH Drilling, Oil, Gas*, *34*(2).

254. Slobodkin, A. I., Jeanthon, C., L'haridon, S., Nazina, T., Miroshnichenko, M., & Bonch-Osmolovskaya, E. (1999). Dissimilatory reduction of Fe (III) by thermophilic bacteria and archaea in deep subsurface petroleum reservoirs of Western Siberia. *Current Microbiology*, *39*(2), 99–102.

255. Smil, V. (2010). *Energy transitions: History, requirements, prospects*. ABC-CLIO.

256. Spiers, C. J., Urai, J. L., Lister, G. S., Boland, J. N., & Zwart, H. J. (1986). *The influence of fluid-rock interaction on the rheology of salt rock*. Commission of the European Communities.

257. Srinivasan, B. S. (2006). *The impact of reservoir properties on mixing of inert cushion and natural gas in storage reservoirs*. West Virginia University.

258. Stanley, N. R., & Lazazzera, B. A. (2004). Environmental signals and regulatory pathways that influence biofilm formation. *Molecular Microbiology*, *52*(4), 917–924.

259. Stone, H. B., Veldhuis, I., & Richardson, R. N. (2009). Underground hydrogen storage in the UK. *Geological Society, London, Special Publications*, *313*(1), 217–226.

260. Stormont, J. C. (1990). *Gas permeability changes in rock salt during deformation* [PhD Thesis]. The University of Arizona.

261. Stormont, J. C. (1997). In situ gas permeability measurements to delineate damage in rock salt. *International Journal of Rock Mechanics and Mining Sciences*, *34*(7), 1055–1064.

262. Stormont, J. C., & Daemen, J. J. K. (1992a). Laboratory study of gas permeability changes in rock salt during deformation. *International Journal of Rock Mechanics and Mining Sciences & Geomechanics Abstracts*, *29*(4), 325–342. https://doi.org/10.1016/0148-9062(92)90510-7

263. Stormont, J. C., & Daemen, J. J. K. (1992b). Laboratory study of gas permeability changes in rock salt during deformation. *International Journal of Rock Mechanics and Mining Sciences & Geomechanics Abstracts*, *29*(4), 325–342.

264. Straube, T., & Müller, C. (2016). How to do a Proper Cell Culture Quick Check: Workflow for Subculture of Adherent Cells. *Dostopno Na: Https://Www. Leicamicrosystems. Com/Science-Lab/How-to-Do-a-Proper-Cell-Culture-Quick-Check/[Citirano 10. 1. 2020]*.

265. Strobel, G., Hagemann, B., Huppertz, T. M., & Ganzer, L. (2020). Underground bio-methanation: Concept and potential. *Renewable and Sustainable Energy Reviews*, *123*, 109747.

266. Suri, P., Azeemuddin, M., Zaman, M., Kukreti, A. R., & Roegiers, J.-C. (1997). Stress-dependent permeability measurement using the oscillating pulse technique. *Journal of Petroleum Science and Engineering*, *17*(3–4), 247–264.

267. Sutherland, H. J., & Cave, S. P. (1980). Argon gas permeability of New Mexico rock salt under hydrostatic compression. *International Journal of Rock Mechanics and Mining Sciences & Geomechanics Abstracts*, *17*(5), 281–288.

268. Taconi, K. A. (2004). *Methanogenic generation of biogas from synthesis-gas fermentation wastewaters*. Mississippi State University.

269. Takeuchi, S., & Argon, A. S. (1976). Steady-state creep of single-phase crystalline matter at high temperature. *Journal of Materials Science*, *11*(8), 1542–1566. https://doi.org/10.1007/BF00540888

270. Tarkowski, R. (2019). Underground hydrogen storage: Characteristics and prospects. *Renewable and Sustainable Energy Reviews*, *105*, 86–94.

271. TEK, M. (1989). HUNTSMAN AND WEST ENGELLAND FIELDS A CASE HISTORY OF GAS MIGRATION MR TEK. *Underground Storage of Natural Gas: Theory and Practice*, *171*, 429.

272. Ter Heege, J. d, De Bresser, J. H. P., & Spiers, C. J. (2005). Dynamic recrystallization of wet synthetic polycrystalline halite: Dependence of grain size distribution on flow stress, temperature and strain. *Tectonophysics*, *396*(1–2), 35–57.

273. Thaysen, E. M., McMahon, S., Strobel, G., Butler, I., Ngwenya, B., Heinemann, N., Wilkinson, M., Hassanpouryouzband, A., McDermott, C., & Edlmann, K. (2020). *Estimating Microbial Hydrogen Consumption in Hydrogen Storage in Porous Media as a Basis for Site Selection*.

274. Thorel, L. (1994). *Plasticité et endommagement des roches ductiles. Application au sel gemme*. 316.

275. Thorel, L., & Ghoreychi, M. (1996). Plasticité et endommagement du sel gemme. *Revue Française de Géotechnique*, *77*, 3–17.

276. Todorescu, A. (1986). *Reologia rocilor cu aplicaţii în minerit*. Editura Tehnică.

277. Tol, R. S. (2009). The economic effects of climate change. *Journal of Economic Perspectives*, *23*(2), 29–51.

278. Torres, R., De Hemptinne, J.-C., & Machin, I. (2013). Improving the modeling of hydrogen solubility in heavy oil cuts using an augmented Grayson Streed (AGS) approach. *Oil & Gas Science and Technology–Revue d'IFP Energies Nouvelles*, *68*(2), 217–233.

279. Tran Ngoc, T. D., Konstantinovskaya, E., Lefebvre, R., & Malo, M. (2011). *Caractérisation hydrogéologique et pétrophysique des aquifères salins profonds de la région de Bécancour pour leur potentiel de séquestration géologique du CO2.*

280. Truche, L., Jodin-Caumon, M.-C., Lerouge, C., Berger, G., Mosser-Ruck, R., Giffaut, E., & Michau, N. (2013). Sulphide mineral reactions in clay-rich rock induced by high hydrogen pressure. Application to disturbed or natural settings up to 250 C and 30 bar. *Chemical Geology*, *351*, 217–228.

281. Tzimas, E., Filiou, C., Peteves, S. D., & Veyret, J. B. (2003). Hydrogen storage: State-of-the-art and future perspective. *EU Commission, JRC Petten, EUR 20995EN*.

282. Urai, J. L., Spiers, C. J., Peach, C. J., Franssen, R., & Liezenberg, J. L. (1987). Deformation mechanisms operating in naturally deformed halite rocks as deduced from microstructural investigations. *Geologie En Mijnbouw*, *66*(2), 165–176.

283. US EPA, O. (2020, February 4). *Inventory of U.S. Greenhouse Gas Emissions and Sinks: 1990-2018* [Reports and Assessments]. https://www.epa.gov/ghgemissions/inventory-us-greenhouse-gas-emissions-and-sinks-1990-2018

284. Usher, K. M., Kaksonen, A. H., Bouquet, D., Cheng, K. Y., Geste, Y., Chapman, P. G., & Johnston, C. D. (2015). The role of bacterial communities and carbon dioxide on the corrosion of steel. *Corrosion Science*, *98*, 354–365.

285. Van Hasselt, B. (1991). *Evaluation qualitative du rôle de la texture dans le fluage du sel bressan* [Doctoral Dissertation].

286. Vargas, M., Kashefi, K., Blunt-Harris, E. L., & Lovley, D. R. (1998). Microbiological evidence for Fe (III) reduction on early Earth. *Nature*, *395*(6697), 65–67.

287. Varjani, S. J., & Gnansounou, E. (2017). Microbial dynamics in petroleum oilfields and their relationship with physiological properties of petroleum oil reservoirs. *Bioresource Technology*, *245*, 1258–1265.

288. Venkateswaran, K., Moser, D. P., Dollhopf, M. E., Lies, D. P., Saffarini, D. A., MacGregor, B. J., Ringelberg, D. B., White, D. C., Nishijima, M., & Sano, H. (1999). Polyphasic taxonomy of the genus Shewanella and description of Shewanella oneidensis sp. Nov. *International Journal of Systematic and Evolutionary Microbiology*, *49*(2), 705–724.

289. Wait, A. F. (2011). *Novel aspects of the reactions of hydrogenases with small molecule inhibitors* [PhD Thesis]. Oxford University, UK.

290. Wallner, M., BraÈuer, V., & Bornemann, O. (1998). Geoscientific characterization and evaluation of the suitability of the Gorleben repository site. *Proceedings of the Distec*, *98*, 75–81.

291. Walsh, J. B. (1965). The effect of cracks on the uniaxial elastic compression of rocks. *Journal of Geophysical Research*, *70*(2), 399–411.

292. Wawersik, W. R., & Hannum, D. W. (1980). Mechanical behavior of New Mexico rock salt in triaxial compression up to 200 C. *Journal of Geophysical Research: Solid Earth*, *85*(B2), 891–900.

293. Weiguo, L., Suguo, X., & Yangsheng, Z. (2004). Experimental study on heating recrystallization effect on shear characteristics of damaged rock salt. *Chinese Journal of Rock Mechanics and Engineering*, *23*(20), 3413–3417.

294. Weisz, P. B. (2004). Basic choices and constraints on long-term energy supplies. *PHYSICS TODAY.*, *57*(7), 47–52.

295. Wolicka, D., & Borkowski, A. (2007). The geomicrobiological role of sulphate-reducing bacteria in environments contaminated by petroleum products. *Geomicrobiology Journal*, *24*(7–8), 599–607.

296. Yin, W., Wang, Y., Liu, L., & He, J. (2019). Biofilms: The microbial “protective clothing” in extreme environments. *International Journal of Molecular Sciences*, *20*(14), 3423.

297. Yu, Z., Leng, X., Zhao, S., Ji, J., Zhou, T., Khan, A., Kakde, A., Liu, P., & Li, X. (2018). A review on the applications of microbial electrolysis cells in anaerobic digestion. *Bioresource Technology*, *255*, 340–348.

298. Zabranska, J., & Pokorna, D. (2018). Bioconversion of carbon dioxide to methane using hydrogen and hydrogenotrophic methanogens. *Biotechnology Advances*, *36*(3), 707–720.

299. Zegeye, A., Ona-Nguema, G., Carteret, C., Huguet, L., Abdelmoula, M., & Jorand, F. (2005). Formation of hydroxysulphate green rust 2 as a single iron (II-III) mineral in microbial culture. *Geomicrobiology Journal*, *22*(7–8), 389–399.

300. Zhang, D., Skoczylas, F., Agostini, F., & Jeannin, L. (2020). Experimental Investigation of Gas Transfer Properties and Stress Coupling Effects of Salt Rocks. *Rock Mechanics and Rock Engineering*, *53*(9), 4015–4029. https://doi.org/10.1007/s00603-020-02151-x

301. Zimmerman, R. W., Haraden, J. L., & Somerton, W. H. (1985). The effects of pore pressure and confining pressure on pore and bulk volume compressibilities of consolidated sandstones. In *Measurement of rock properties at elevated pressures and temperatures*. ASTM International.

302. Zivar, D., Kumar, S., & Foroozesh, J. (2021). Underground hydrogen storage: A comprehensive review. *International Journal of Hydrogen Energy*, *46*(45), 23436–23462.

303. Züttel, A. (2003). Materials for hydrogen storage. *Materials Today*, *6*(9), 24–33.